Rock–Water Interaction Group
Institute of Geological Sciences,
University of Bern
Baltzerstrasse 1–3, 3012 Bern, Switzerland

Pre-study of the geological heat storage and utilisation project Geo-speicher Forsthaus (Bern): Geological and geochemical aspects

August, 2021

This final version replaces the preliminary version of 31 May, 2020.

Authors:
Dr. Daniela B. van den Heuvel, Dr. Peter Alt-Epping, Joshua P. Richards,
Dr. Christoph Wanner, Prof. Larryn W. Diamond

Conducted within the European Heatstore (GEOTHERMICA – ERA NET) research project (2018–2021).

Acknowledgments

The authors would like to thank the following people for helping with the setting up of the experiments, analyses and other technical aspects: Urs Mäder, Priska Bähler, Christopher Pichler, Fulvio di Lorenzo, Alannah Brett, Lukas Aschwanden, Christine Lemp, Wolfgang Jan Zucha, Raphael Kuhn, Julijana Krbanjevic, Thomas Aebi, Nadine Lötscher, Thomas Siegenthaler and Dominik van den Heuvel. We would also like to thank our MSc-student Ahathian Manikkapoody and BSc-student Kai Kraus for their contributions as part of their thesis research related to the *Geospeicher Forsthaus*.

We also appreciate fruitful discussions with current and former members of Geo Energie Suisse AG: Florentin Ladner, André El-Alfy, Dieter Ollinger and Peter Meier.

This work was funded by the European Heatstore project (GEOTHERMICA – ERA NET Cofund) and the Swiss Federal Office of Energy (SFOE). We appreciate management support by the scientific coordinator for Heatstore Switzerland, Luca Guglielmetti.

Executive Summary

Context and aims of report

The Forsthaus heat-storage project (*Geospeicher Forsthaus*) aims to store excess heat generated during the summer months by the *ewb* power plant (Energiezentrale Bern), which combusts municipal waste, wood and natural gas at Forsthaus, Bern. The heat will be stored in a geological reservoir at several hundred metres depth beneath the site. During the winter months the heat will be recovered and fed into the local district-heating network. This report presents an assessment of geological and geochemical issues that may arise during operation of the Geospeicher. This assessment serves to verify the planned drilling and operational scheme and it provides a scientific basis for further geological and geochemical investigations during the drilling and testing phases of the project. The understanding gained in this study will also support problem-solving during development and operation of the Geospeicher.

***Geospeicher* heat injection/extraction scheme**

The target heat reservoir is a sequence of water-saturated porous and permeable sandstones and interlayered low-permeability claystones that were deposited by ancient meandering rivers as part of the Lower Freshwater Molasse (USM). The summer heat-loading cycle entails extracting formation water from the sandstones through supporting wells.

Information sources

In the absence of subsurface data from the site itself, this report is based on five sources of information: (1) scientific literature documenting experience in similar projects; (2) scientific literature on the regional geology, which provides a basis to estimate reservoir properties at the Forsthaus site; (3) analyses of drill core and formation waters from shallow wells 2 km from the site, which provide material for experiments; (4) laboratory experiments involving heating of the sandstones and formation water to identify the governing water–mineral reac-

tions and to calibrate their rates; (5) 3D numerical simulations of the coupled thermal–hydraulic–chemical processes during the heat loading and unloading cycles at the reservoir scale, to assess the influence of water–mineral reactions on pore clogging and rock-cement dissolution, and on the thermal evolution and feasibility of the storage concept.

Information gaps

The geological literature shows that the reservoir properties of the target sandstones are site-specific. Without drillhole data it is not possible to accurately predict the response of the Forsthaus reservoir to fluid injection/extraction. Key missing information on the sandstones includes whether they are even present under Forsthaus, their geometries and dimensions, their porosity, permeability, mineralogy and degree of cementation, and the extent to which they are hydraulically connected. Likewise, the characteristics of the *in-situ* groundwaters are site-specific. Missing information includes their salinity, flow rates, microbial activity, and solute composition including corrosive components. Many of these properties will be determined during drilling and testing. In the meantime, properties extrapolated from other sites have been used in this study to assess potential issues with the *Geospeicher* scheme.

Critical issues

Within this context of incomplete information, our evaluation so far has revealed no critical issues that imply the project will fail or that a completely different storage strategy is required.

Cautionary issues

The following risks and complications are viewed as non-critical but they require consideration:

- Preferential flow paths may develop between the main and supporting wells due to heterogeneous permeability of the sandstones. This could reduce the volume of rock swept by the injected hot water, lowering the efficiency of heat storage below previous expectations.
- Calcite is predicted to precipitate in some regions of the reservoir and to dissolve in others during the water injection/extraction cycles. Regions clogged by calcite may become barriers to the injection/extraction flow regimes. Regions of moderate calcite depletion may focus flow and thereby leave other regions of the reservoir unswept by the injected hot water. Thus, both calcite clogging and dissolution may contribute to lowering the heat-storage efficiency of the reservoir.

- Extreme dissolution of calcite cement may induce local mechanical disintegration and compaction of the sandstones, and mobilise fines that clog pore throats, reducing permeability and hence further lowering the efficiency of the water injection/extraction cycles.
- Microbes may form biofilms and clog the casings of the supporting wells, where temperatures are < 50 °C. Microbial activity is expected to diminish as the reservoir heats up to 90 °C.
- The evolving thermal plume and the water–rock reaction zone around the main well are predicted to remain within a 50 m radius from the well. However, the influence of the entire heat storage reservoir, if defined by the distance to which non-reactive solutes injected or released from the rock can travel in the USM groundwater system, is much larger. There is therefore a possibility that unwanted chemical compounds are transported over large distances.
- Significant carbonate scaling is expected in the surface installations during the heat-loading cycle. This could impede flow and exchange of heat in the surface installations.

List of Contents

List of Figures

List of Tables

List of Acronyms and Abbreviations

APW	Artificial porewater
(HT-/LT-)ATES	(High-temperature-/low-temperature-) Aquifer thermal energy storage
BTES	Borehole thermal energy storage
CEC	Cation exchange capacity
CNS	Carbon-nitrogen-sulphur analyses
CS	Crevasse channel and splay sandstones
CPL	Cross-polarised light
CTES	Cavern thermal energy storage
DOC	Dissolved organic carbon
EMPA	Electron Microprobe Analysis
EZF	Power station Bern Forsthaus (German: Energiezentrale Forsthaus)
IC	Ion chromatography
ICP-OES	Inductively coupled plasma optical emission spectrometry
ISE	Ion-selective electrode
LS	Levee sand- and siltstones
MW	Main well
OMM	Upper Marine Molasse (German: Obere Meeresmolasse)
OPS	Overbank fines and palaeosol deposits
OSM	Upper Freshwater Molasse (German: Obere Süsswassermolasse)
PTES	Pit thermal energy storage
LAC	Lacustrine silts
MB	Meander belt sandstones
MIC	Microbially-induced or –influenced corrosion
MTES	Mine thermal energy storage
PFLOTRAN	Massively parallel multiscale and multiphysics numerical simulation code
PL	Plane-polarised light
RBS	Regionalverkehr Bern-Solothurn
SelFrag	Selective fragmentation of solid materials

SMB	Swiss Molasse Basin
SOB	Sulphur-oxidising bacteria
SRB	Sulphate-reducing bacteria
SW	Supporting well
TC	Total carbon content (solids)/concentration (liquids)
TDS	Total dissolved solids
TES	Thermal energy storage
TN	Total nitrogen content
TIC	Total inorganic carbon content (solids)/concentration (liquids)
TOC	Total organic carbon content (solids)/concentration (liquids)
TS	Total sulphur content
TTES	Tank thermal energy storage
UBELIX	High-performance computing cluster at the University of Bern
UMM	Lower Marine Molasse (German: Untere Meeresmolasse)
USM	Lower Freshwater Molasse (German: Untere Süsswassermolasse)
UTES	Underground thermal energy storage
XRD	X-ray diffraction analysis
XRF	X-ray fluorescence analysis

1 Introduction

Thermal energy for space heating and cooling accounted for around 50% of global energy consumption and around 40% of global CO_2-emissions in 2018 (iea.org). As global temperatures and standards of living continue to increase, demand for heating and especially cooling is expected to rise in the coming years. Thermal energy is primarily produced from fossil fuels with only slightly more than 10% originating from renewable sources (iea.org). Major challenges in increasing the share of renewables are posed by the fluctuation of certain energy sources (e.g. solar and wind) and by the seasonality of demand for heating and cooling. In order to mitigate the source issue, thermal energy storage (TES) solutions need to be found.

1.1 Underground thermal energy storage (UTES)

One of the main areas of research in TES is underground thermal energy storage (UTES), which is ideal for long-term storage due to its high efficiency and storage capacity (Caliskan et al., 2012; Li et al., 2016). UTES can be achieved by different techniques (modified after Fleuchaus et al., 2018):

- Aquifer Thermal Energy Storage (ATES): Thermal energy is stored in an open-loop system by injection/removal of hot/cold groundwater into/from an aquifer with suitable hydrogeological conditions.
- Borehole Thermal Energy Storage (BTES), Tank Thermal Energy Storage (TTES) or Pit Thermal Energy Storage (PTES): Thermal energy is stored in engineered structures such as boreholes, underground storage tanks or dug pits filled with gravel, respectively. These systems are all closed-loop.
- Cavern Thermal Energy Storage (CTES) or Mine Thermal Energy Storage (MTES): Thermal energy is stored in natural cavities/caves or abandoned underground mines. Open- or closed-loop systems depending on the presence or absence of engineered barriers (e.g. shotcrete).

According to Dincer and Rosen (2010), ATES is the storage option with the highest storage capacity and thus the highest potential. ATES can be implemented in both shallow (unconsolidated) and deep (consolidated) geological formations, as long as the aquifers have a large enough volume for storage and sufficient porosity and permeability to allow injection/production of fluid from the aquifer. In addition, the groundwater flow has to be low or absent so the heat can be stored without significant loss. Besides storage efficiency, the open-loop nature of ATES can cause problems with respect to mineral scaling and/or corrosion due to aquifer material-water-interactions taking place. Therefore, more in-depth investigations are needed to evaluate the suitability of any potential storage site (Fleuchaus et al., 2018).

The capacities of an ATES system not only depend on the volume of the aquifer but also the temperature of the injected water. In low-temperature ATES systems (LT-ATES), water is injected at temperatures below 40 °C, usually into relatively shallow aquifers. Despite their limited storage capacity, they make up over 99% of all ATES systems worldwide, with over 2,500 LT-ATES systems installed in the Netherlands alone (Fleuchaus et al., 2018). In high-temperature ATES (HT-ATES) systems, the injection temperatures are higher than 40 °C, leading to much higher energy storage capacities. At present, there are only five HT-ATES systems in operation around the world. This is due to substantial operational challenges encountered in pilot projects in the 1970s and 1980s, mostly related to scaling in wells and surface installations, corrosion, surface uplift (e.g. due to swelling of clay minerals), thermohydraulic problems (e.g. stratification due to buoyancy or thermal breakthrough) and low recovery rates (Fleuchaus et al., 2018). For an in depth discussion of problems encountered in HT-ATES pilot projects, see Section 2.1. ATES systems can be subdivided not only by injection temperature but also by other properties (Figure 1.1).

1.2 Context of the *Geospeicher Forsthaus* project

Switzerland is a small, densely populated country with several deep aquifers that contain non-potable waters (Chevalier et al., 2010) and thus it presents ideal conditions for developing HT-ATES systems. In 2018 a pilot project of the Swiss Office of Energy was started to support development of HT-ATES within Switzerland. This project, known as "Heatstore – De-risking and optimization of high temperature aquifer thermal energy storage in the Swiss Molasse Basin", is embedded in the European GEOTHERMICA ERA NET Cofund research project (www.heatstore.eu/project.html). Within this framework, the *Geostorage Forsthaus* pilot project (referred to hereafter by the German form *Geospeicher Forsthaus*) is being developed in the city of Bern. The aim of this project is to install an HT-ATES within the Tertiary sandstones of the

Lower Freshwater Molasse. The site was selected owing to its immediate proximity to a heat source, the Forsthaus Energy Centre (*Energiezentrale Forsthaus*) operated by *ewb* (*Energie Wasser Bern*), a commercial energy provider for the City of Bern. The consultancy *Geo Energie Suisse* is charged with implementing the project.

1.3 System parameters of the *Geospeicher Forsthaus*

The planned *Geospeicher Forsthaus* will be located in the immediate vicinity of the "Energiezentrale Forsthaus" (EZF; Figure 1.2). The EZF is a modern power plant, combining municipal waste incineration, burning of biomass (wood) and a combined cycle (gas/steam turbine) module to produce electricity, steam and district heating. The EZF provides around a third of the electricity and 12% of the thermal energy needed by the city of Bern (www.ewb.ch). The planned HT-ATES system will allow storage of the excess heat generated during the warm summer months, so that it can be retrieved during winter and fed into the district heating network. This will reduce the number of days during which the gas turbine is needed to generate additional hot water for district heating. The HT-ATES system will and thus reduce the amount of CO_2 released during energy production in the city of Bern.

The layout of the planned HT-ATES consists of a central injection/production well (= main well #1) and up to five peripheral supporting wells (= auxiliary wells #2 – 6; Figure 1.2). The optimal layout (e.g. number of wells, distance to central well) will be adapted as needed once results on the local geological and hydrogeological conditions are available from the first well(s). Inclined but straight drilling will allow the wells to reach the target depth of 550 m to the southwest of the EZF (Figure 1.2). The target formation at this depth is the Lower Freshwater Molasse, an alternating sequence of medium- to coarse-grained fluviatile channel sandstones and surrounding, fine-grained floodplain deposits (Figure 1.3, Section 2.2.4). On a regional scale, and especially in the vertical direction, these fine-grained sequences prevent circulation of groundwaters, resulting in the Lower Freshwater Molasse being considered a regional aquitard (Chevalier et al., 2010). At the local scale, the individual sandstone channels represent bodies with substantial porosity (6 – 25 vol.%) and permeability (0 to 5660 mD; Keller et al., 1990, Ammann et al., 1993) but limited spatial extent (thickness of 2 to 15 m). According to preliminary simulations, a combined thickness of 20 to 30 m of sandstones layers with high enough permeabilities distributed over the entire length of the wells (ca. 350 m of USM) is required for successful seasonal storage of warm water.

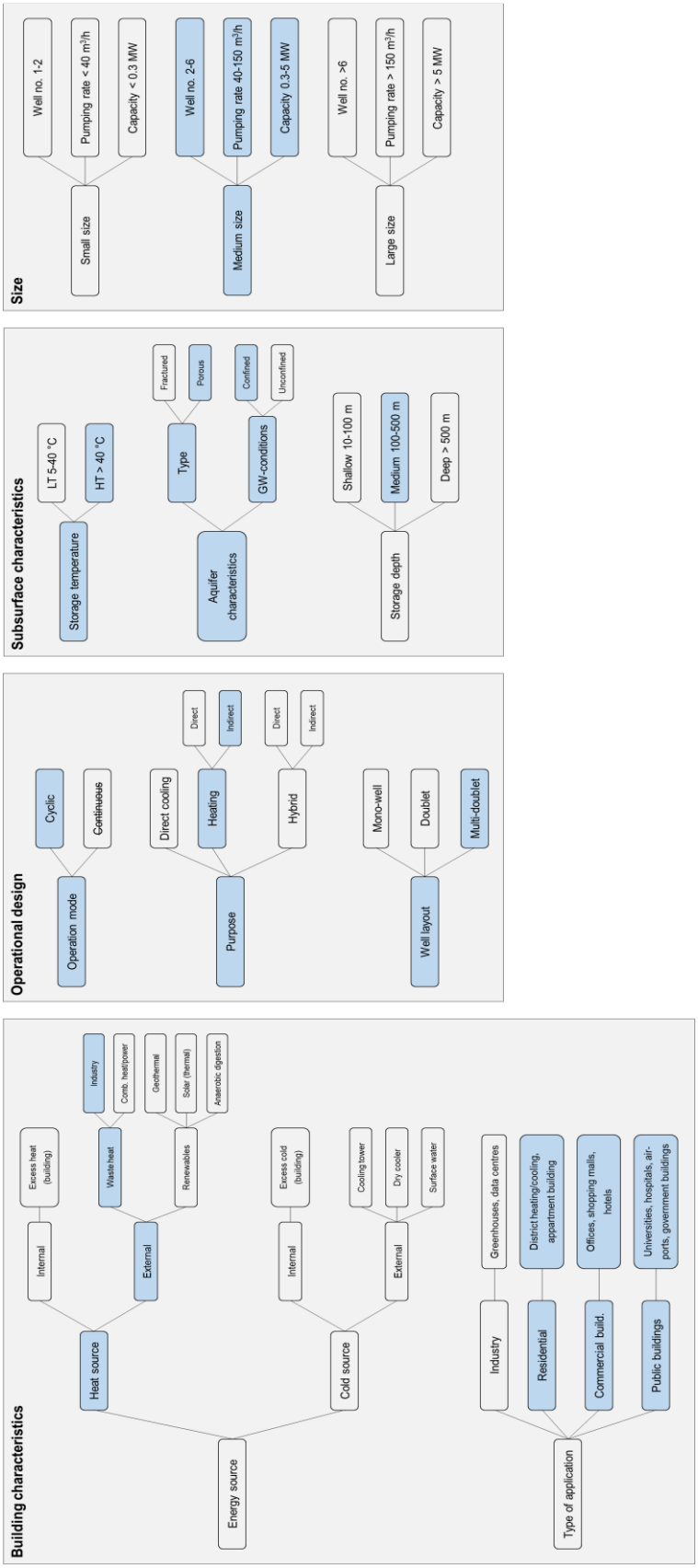

Figure 1.1: *ATES system characterisation according to Fleuchaus et al. (2018). The characteristics applying to the planned HT-ATES project at Bern Forsthaus are highlighted in blue.*

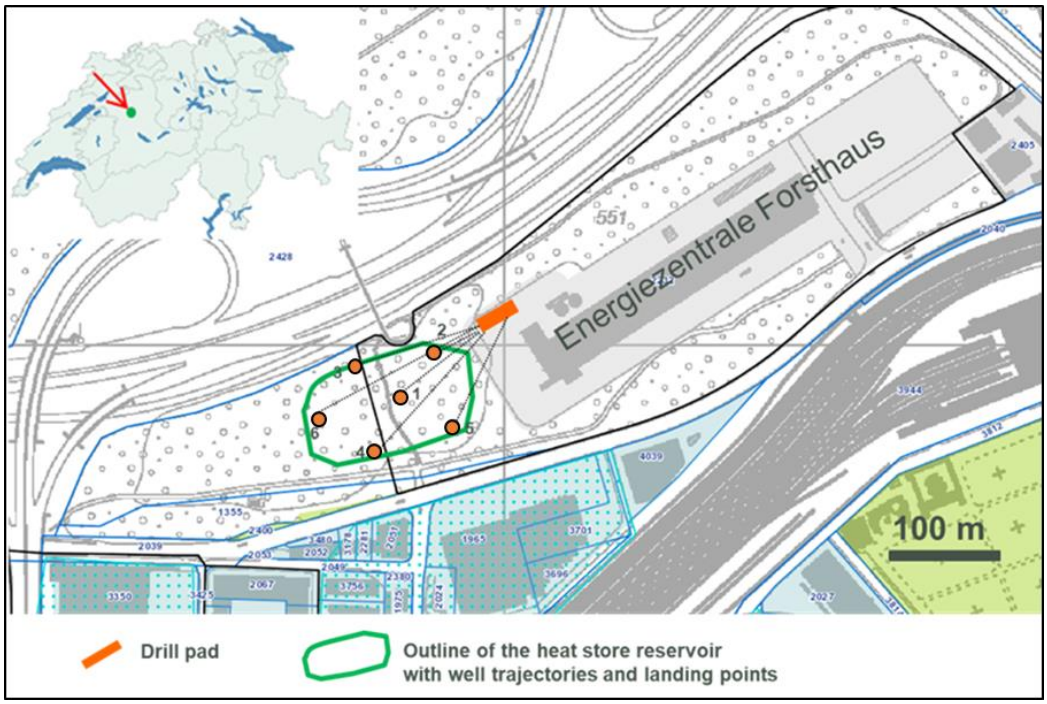

Figure 1.2: *Location and planned layout of the HT-ATES pilot project* Geospeicher Forsthaus *next to the Forsthaus Energy Centre (Energiezentrale Forsthaus, EZF).*

The current plan (Geo Energie Suisse) is to inject waters with a temperature of 90 °C at a rate of 25 L/s or 90 m^3/h (Figure 1.3). This temperature allows for a higher storage capacity and the feeding of the stored thermal energy into the district heating network without needing a heat pump in winter. However, operation of an HT-ATES system becomes more challenging at higher injection temperatures. It is thus possible that the injection temperature will have to be reduced to between 60 and 90 °C. Injection of hot water (= loading cycle) will take place over ca. 200 days through the main well in the centre of the system. This corresponds to an estimated 20 GWh/yr of heat stored. During the unloading cycle, the same central well will be used to produce warm water with temperatures between 90 °C (initially) and 50 °C (later stages; owing to mixing of the injected hot water with cooler *in-situ* water and to heat conduction into intercalated clay layers). Over time, the entire reservoir volume (incl. clay layers) will heat up, resulting in higher average production temperatures. Overall, it is estimated that about 13 GWh/yr of thermal energy will be produced from the reservoir. Concurrent pumping from/into the supporting wells will help to regulate flow at the system boundaries and thus balance pressure in the reservoir during injection and production. A lifetime of 20 years is assumed for the HT-ATES system *Geospeicher Forsthaus*.

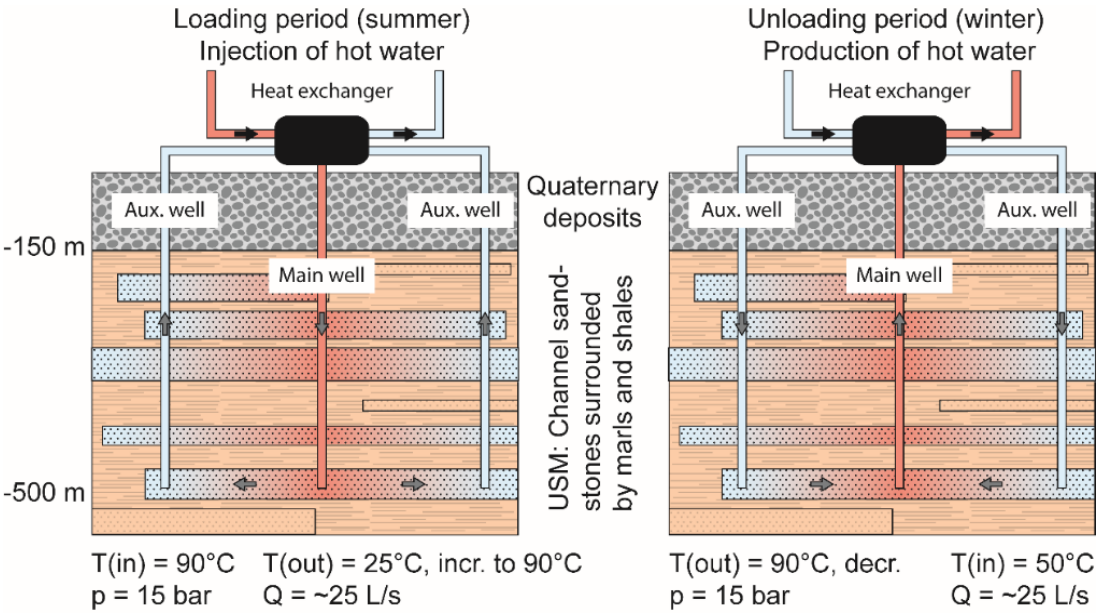

Figure 1.3: *Schematic depiction of the operational design and planned operational parameters of the HT-ATES pilot project* Geospeicher Forsthaus.

1.4 Aims of the pre-study and structure of the report

In preparation for the planned start of drilling operations in November 2021, a geological and geochemical pre-study (including water–rock experiments, scaling experiments and numerical simulations) was commissioned by Geo Energie Suisse and *ewb*. The following aims were defined:

(1) Understand which challenges might be encountered during operation of the *Geospeicher Forsthaus* based on problems encountered in previous projects. This knowledge also informs the conditions for the experiments presented here and planned in the future.

(2) Aquire as much knowledge as possible about the geology and hydrogeology of the target formation (Lower Freshwater Molasse, USM) and the heterogeneity of the properties before drilling starts to judge if (a) the drill cores and groundwater compositions used during the experiments are representative for the USM and (b) find reasonable input values for different parameters to be included in the numerical simulations.

(3) Assess potential mineral reactions at the site through experimental work by (a) investigating mineral reactions in the reservoir through core and batch experiments and (b) assessing the potential for carbonate scaling during heating of the formation fluid.

(4) Conduct numerical modelling simulations of the thermal-hydraulic-chemical (THC) processes expected to occur during operation of the system, so as to identify potential red flags before drilling starts.

Reflecting these aims, this report is subdivided into several chapters. Chapter 2 is a two-part summary of the available literature on HT-ATES and problems encountered in previous systems as well as the available geological and hydrogeological data on the target formation (meander belt sandstones of the Lower Freshwater Molasse). In Chapter 3, the newly obtained data from drill cores and groundwater wells close to the main train station of Bern are presented and compared to the USM data discussed in Chapter 2. These materials were also used in the laboratory experiments described in Chapter 4. Chapter 5 reports on the results of the site-specific, numerical THC model. Chapters 6 contains a summary of the results presented as well as an assessment of which problems, based on the data available so far, are most likely to occur during operation of the *Geospeicher Forsthaus*.

2 Literature Review

2.1 Problems observed in previous HT-ATES systems

In order to identify problems that could potentially affect the successful operation of the *Geospeicher Forsthaus*, problems encountered in previous HT-ATES were evaluated (Appendix A). Special attention was paid to problems that have led to projects being abandoned. Understanding which of these problems might be encountered and assessing their potential impact is thus vitally relevant to the success of the *Geospeicher Forsthaus*.

2.1.1 Mineral reactions

When water is injected into an aquifer, it will interact with the minerals present. Despite the wealth of studies published on HT-ATES, the number of studies evaluating mineral reactions in detail is relatively small. Out of the early projects, the HT-ATES site at the University of Minnesota was the only one where the chemistry of injection and recovery waters was evaluated as a function of time (Holm et al., 1987, Perlinger et al., 1987, Hoyer et al., 1991, Hoyer et al., 1994). Geochemical reactions in later projects, especially the ones in operation in northern Germany and planned in Bavaria, have been investigated in much more detail (Lerm et al., 2013, Ueckert and Baumann, 2019, Ueckert et al., 2020).

The most important reactions in an HT-ATES reservoir are dissolution, precipitation, adsorption/desorption, oxidation/reduction and ion exchange. They all change the composition of the fluid and by measuring compositional changes and physico-chemical parameters (e.g. temperature) as a function of time mineral reactions can be identified. Quantification of mineral reactions is often difficult as mixing with *in-situ* groundwater, especially in systems with detectable regional flow, also affects the composition of the formation water (e.g. Holm et al., 1987).

Dissolution and precipitation are controlled by mineral solubilities. Minerals show either a normal solubility (increasingly soluble with increasing temperature) or a so-called retrograde or inverse solubility (decreasingly soluble with increasing temperature). While many silicate minerals show normal solubility, carbonate minerals show a retrograde solubility (Stumm and Morgan, 2012). Thus, not all minerals are expected to dissolve or precipitate in the same area of an HT-ATES system: when a formation water is extracted, it is often saturated with respect to most minerals present in the reservoir as it has been in contact with these minerals for long time periods (unless the aquifer is characterised by substantial regional flow or is very young and shallow). When the cool formation water is pumped to the surface and heated inside the heat exchanger, minerals with a retrograde solubility may precipitate. If the precipitation rate is high, the deposited minerals ("scales") may, at least partially, clog the heat exchanger. If the rates are low, precipitation will may occur further downstream, reducing the permeability of the pipelines, injection well or the reservoir. Upon reinjection, the hot water from the heat exchanger is not in equilibrium with respect to the reservoir minerals and it will tend to dissolve minerals with a normal solubility until equilibrium is reached or until the water is produced at the end of the storage cycle. When the hot fluid is produced and cooled within the heat exchanger, minerals with normal solubility can become supersaturated and might precipitate. Again, such precipitation will occur in the heat exchanger for minerals with high precipitation rates and further downstream for minerals with a slower precipitation rate. If the cooled fluid is reinjected into the reservoir, minerals with a retrograde solubility are undersaturated and dissolution takes place until equilibrium is reached or the water is being produced for the next cycle.

In order to determine which minerals can dissolve or precipitate, the saturation index (SI) of a mineral is calculated according to

$$SI = log\left(\frac{IAP}{K}\right) \qquad (2.1)$$

with IAP representing the ion activity product and K the equilibrium constant of the reaction under the physico-chemical conditions of interest. An $SI < 0$ indicates undersaturation with respect to the mineral of interest (and the potential to dissolve this mineral), while an $SI > 0$ indicates supersaturation and the potential for mineral precipitation. An $SI = 0$ indicates saturation and neither dissolution nor precipitation occurs (Anderson, 2005). While the saturation index indicates which minerals can dissolve or precipitate, it does not indicate how fast a mineral reacts. Crystalline phases generally have relatively slow dissolution and even slower pre-

cipitation kinetics. They dissolve slowly when in contact with water but often do not precipitate even if supersaturation has been reached. Sometimes amorphous or poorly crystalline phases form instead. The exception are carbonate minerals which, despite their fully crystalline structure, show rapid dissolution and precipitation rates. Unfortunately, reaction rates for many minerals are notoriously poorly constrained, making predictions of the speed of mineral reactions difficult.

2.1.1.1 Changes in fluid chemistry (major elements) during HT-ATES

Changes in fluid chemistry during HT-ATES depend on the mineralogical composition of the reservoir and the physico-chemical parameters of the injected hot water (e.g. temperature, *pH*) and are therefore site- and project-specific. However, most dissolved components are qualitatively controlled by the same dissolution or precipitation reactions (e.g. Holm et al., 1987, Perlinger et al., 1987, Hoyer et al., 1994, Müller and Regenspurg, 2017). During heating of the formation fluid from a sandstone reservoir within the heat exchanger to the desired injection temperature, most chemical components behave conservatively as they are controlled by minerals with normal prograde solubilities (i.e. no precipitation). If the reservoir sandstones contain limestone or dolomite fragments or if they are cemented by such minerals, then calcium and alkalinity will not behave conservatively as they are controlled by retrograde solubility of the carbonate minerals. Magnesium often follows the same trend as it may also be controlled by carbonate solubility (dolomite or Mg-calcite). Scaling in the heat exchanger thus reduces the concentration of these components during heating. During the storage phase, most components show an increase in concentration due to dissolution of mineral phases in the reservoir, e.g. quartz (increasing Si concentration), feldspars or clay minerals (increasing K, Al and Si concentration) or pyrite (increasing Fe concentration). Generally, the increase shows a positive correlation with injection temperature as all of these minerals show normal prograde solubilities. In addition, ion exchange reactions, primarily involving clay minerals, affect the concentrations of sodium, calcium, magnesium and potassium. Certain components, such as chloride, are expected to remain constant throughout the storage period as their composition is not controlled by incorporation in or liberation from any mineral phases. During cooling of the produced fluid in the heat exchanger, a decrease in certain components can be observed if the solubility limit with respect to a mineral phase with normal solubility is reached. Besides minerals, other compounds such as organic matter can also be dissolved or, more precisely, decomposed during storage. This process produces CO_2, which leads to a higher alkalinity and lower *pH* of the reservoir water (Brons et al., 1991, Griffioen and Appelo, 1993).

A commonly used mitigation strategy to prevent carbonate scaling from occurring in the heat exchanger, is the use of ion exchange resins to treat the cold formation water before heating (e.g. at the HT-ATES systems at the University of Utrecht or the University of Minnesota, Appendix A). By passing through these resins, the calcium in solution is exchanged for sodium. This prevents carbonate minerals from precipitating and changes the behaviour of calcium and sodium accordingly: calcium (and to some degree also magnesium and potassium) decreases during the injection phase as it is removed from the solution by the ion exchange resin. This results in a fluid that is undersaturated with respect to carbonates. Thus, despite their retrograde solubility, carbonates are dissolved during the storage period, increasing the calcium concentration. The concentration is increased further by ion exchange on clay minerals in the reservoir. The concentration of sodium on the other hand increases during injection due to the ion exchange resin and slowly decreases during storage as it is exchanged for calcium and potentially magnesium and potassium on clay minerals (Holm et al., 1987, Perlinger et al., 1987).

In order to get an idea on the rate of mineral reactions during storage, it is interesting to compare the results from Holm et al. (1987) and Perlinger et al. (1987). Both investigated HT-ATES in the same aquifer, a quartz sandstone with potassium feldspar, dolomite, glauconite, and other clay minerals. The tests described by Holm et al. generally lasted ~ 30 days each and injection temperatures varied between 60 and 115 °C. The long-term test described by Perlinger et al. lasted for 60 days with an injection temperature of 109 °C. Despite the differences in the cycles, the identified mineral reactions were identical. The similarities between the short term tests discussed by Holm et al. and Perlinger et al. indicate that at least some mineral reactions are fast enough to reach equilibrium within 30 days (e.g. dissolution of quartz during storage) while other reactions are still far from equilibrium after 90 days (e.g. dissolution of feldspars).

If the observed changes in fluid chemistry cannot be fully explained by processes in the surface installations (e.g. scaling or ion exchange resin) or mineral reactions during storage, mixing with *in-situ* groundwaters is often inferred (Perlinger et al., 1987, Ueckert and Baumann, 2019). The complexity of a system involving a range of precipitation, dissolution and exchange reactions, all with different rates, as well as mixing of different waters, explains why it so challenging to identify the reactions controlling the chemical composition of the circulating waters.

2.1.1.2 Effect of organic acids on mineral reaction rates

Mineral reaction rates can be affected by the presence of organic acids in solution. Numerous studies, especially within the framework of soil science, have investigated the effects of these molecules on mineral reaction rates. These include (Drever & Stillings, 1997):

(1) Changing the speciation of ions in solution (e.g. formation of organic complexes and changing degree of dissociation as a function of *p*H).
(2) Influencing the solution saturation with respect to the mineral.
(3) Perturbing the dissolution reaction far from equilibrium as polyvalent cations react with the mineral surface to form surface complexes.

For a given system, the actual effect of organic acids on the dissolution rates depends the structure and composition of the minerals in question, the type of organic acid and its concentration and the solution composition (especially *p*H). For most alumosilicates (e.g. feldspars, micas, clay minerals), the effect on mineral dissolution is controlled by the interactions between the organic ligands and Al-species in solution and at the mineral surfaces. However, even if the rate of dissolution is enhanced by the presence of organic acids, the activity of Al in solution cannot increase substantially as it is controlled by the low solubility of Al-hydroxide. Thus, the overall effect of organic acids on silicate mineral dissolution is relatively small (around 1 order of magnitude; Drever & Stillings, 1997).

The effect of organic ligands on several carbonate minerals has primarily been studied within the framework of CO_2 sequestration in sedimentary basins. Pokrovsky et al. (2009) and Oelkers et al. (2011) found that most organic species at concentrations of < 0.05 M have only a small inhibitory effect (less than a factor of 2.5) on calcite dissolution rates. Exceptions are citrate and EDTA which enhance calcite dissolution rates substantially (up to 500x). Pokrovsky et al. (2009) and Veetil et al. (2018) observed identical effects on magnesite and dolomite dissolution rates, respectively. The slight inhibitory effect of most organic ligands could be associated with the adsorption of organics on the mineral surface which limits the area of contact between water and the mineral surface. This is in line with the findings of Thomas et al. (1993), who showed substantial inhibition of dissolution when calcite was pre-treated, i.e. a monolayer of organics was established prior to the experiments. Alternatively, the inhibition of carbonate dissolution can be explained by the complexes formed between cations (e.g. Ca and Mg) and organics in solution. This affects the saturation state of the fluid with respect to carbonate minerals and can, at least near equilibrium where dissolution rates are controlled by the saturation state, noticeably affect dissolution rates. As most natural waters under unperturbed reservoir conditions are near equilibrium, the inhibitory effect in natural waters might be higher than the values derived from laboratory experiments.

Pokrovsky et al. (2009) and Oelker et al. (2011) conclude that it is not necessary to take the inhibitory effect of organics into account when modelling carbonate dissolution in natural systems over long time spans (i.e. carbon sequestration) as it is only minor. However, for the short time-scales considered in HT-ATES (months to a few years), even small changes in dissolution rates could have a marked impact on the predictability of the system by geochemical modelling.

Organic acids also affect precipitation rates of minerals. Huang and Violante (1986) found that the formation of Al-organic-complexes hinder the precipitation of Al-hydroxide. The Al-hydroxides that do precipitate are the polymorphs gibbsite and nordstrandite and not bayerite (Kwong & Huang, 1979). The resulting precipitates also show distorted structures and significantly modified surface properties. In addition, incorporation of Al-species into pre-existing or newly formed clay minerals is hindered by the organic ligands (Huang and Violante, 1986). As diagenesis progresses (at temperatures > 100 °C), the Al-organic-complexes can be converted to diagenetic clay minerals as the complexes break down (Small et al., 1992). Any additional silicate precipitation reactions will take place at even higher temperatures or over geological time spans and are therefore not of interest for HT-ATES and will not be discussed here. Carbonate minerals on the other hand precipitate both at low temperatures and rapidly. Their inhibition in the presence of organic molecules has been recognised for decades and is due to adsorption of the organic ligands on the calcite surface, masking growth sites (e.g. Inskeep & Bloom, 1986, Lebron & Suarez, 1996, Gautier et al., 2016). This explains why many natural waters are actually slightly supersaturated with respect to calcite. Gautier et al. (2016) showed that magnesite precipitation is inhibited by the increase in its solubility due to complexation of Mg by organic ligands in solution.

The amount of organic acids present in natural formation waters is low. Values of dissolved organic carbon (DOC) of ≤ 2.2 mg/L have been reported for Tertiary and shallow Mesozoic units in the Swiss Molasse Basin (Section 2.2.5). Thurman (1985) reported that only about 1.5 % of DOC is organic acids. Thus, their total concentration in natural waters is very low – substantially lower than the concentrations where effects on mineral reactions were observed in laboratory experiments. However, in microenvironments (e.g. the pore space in the vicinity of degrading organic material or (micro)biological activity), the concentration can be increased locally and a significant effect on mineral reaction rates might be observed.

2.1.1.3 Mobilisation of toxic substances during HT-ATES

As discussed above, injection of heated water perturbs the water-rock equilibrium in the reservoir. Most studies have focused on the changes in main elements in the produced water as the difference in their concentrations reflects on mineral reactions in the reservoir. However, in recent years mineral dissolution in the reservoir has also been investigated as a potential source for heavy metals, some of which are toxic, and also of toxic organic substances. This is especially crucial when considering regional groundwater flow (Section 2.1.4) or hydrofracturing (Section 2.1.5) as both of these processes could lead to contamination of areas outside of the HT-ATES reservoir. This is especially detrimental if the same or the overlying aquifer is used for drinking water or for agricultural or industrial purposes.

Huenges (2011) described low but highly variable contents of heavy metals, especially Cu, Pb, Zn, Ni and Cd during operation of the HT-ATES at the German Reichstag (Appendix A). These metals primarily accumulated in fine material which was trapped in the filters. The authors assume that the heavy metals are all derived from corrosion of metal fittings within the system. However, no analyses were done in order to confirm this.

Only one study has been performed expressly to understand mobilisation of toxic elements from a HT-ATES reservoir. Müller and Regenspurg (2017) performed leaching tests on Jurassic sandstones from Northern Germany and found that the release of heavy metals was controlled by the following minerals and physico-chemical parameters:

- Fe: Dissolution of pyrite under oxic conditions and Fe-(hydr)oxides under anoxic conditions. Enhanced release with increasing temperature and decreasing *pH*.
- Mn: Ion exchange on Fe-hydroxides and dissolution of Mn-oxyhydroxides under oxic and anoxic conditions. Enhanced release with increasing temperature and decreasing *pH*.
- Cu: Dissolution of native copper and chalcopyrite. Enhanced dissolution under oxic conditions but relatively independent of temperature and *pH*.
- Ni: Release mechanism unclear but potentially related to hydroxide or sulphide dissolution. Enhanced release under oxic conditions.
- Pb: Release mechanism unclear but potentially related to hydroxide or sulphide dissolution. Enhanced release under oxic conditions.
- As: Remained immobile under the conditions tested.

Additional studies on the release of toxic metals from different rock types and under different physico-chemical conditions were done within the framework of CO_2 sequestration (e.g. Wang and Jaffe, 2004, Lu et al., 2010, Karamalidis et al., 2013). In all cases, the release of heavy metals was caused by a reduction of the solution *pH* due to addition of CO_2. As *pH* effects are also

common in HT-ATES, especially if the water is acidified by addition of HCl or CO_2 to prevent carbonate scaling (Section 2.1.1.3), the results obtained by these studies are relevant to HT-ATES systems. Unfortunately, many of these studies have only assessed total release of heavy metals and not tried to identify the exact dissolution or desorption processes responsible. Therefore, the significance of the results when trying to predict the release of heavy metals from other formations and under different conditions is strongly limited.

Acidification of the reservoir by injecting CO_2 or other acids is also known to enhance the solubility of the toxic BTEX (butane, toluene, ethylbenzen, xylene) group of organic molecules (e.g. Kharaka et al., 2009). This risk is highest in sandstones that include significant amounts of bitumen or petroleum.

2.1.1.4 Mineral scaling

As described above, minerals precipitate if the solution is supersaturated under the given physico-chemical conditions and if the precipitation rates are in the range of the residence time of the fluid. Generally, precipitates are detrimental to the successful operation of an HT-ATES system. They are thus often called "scales" which describes unwanted mineral precipitates. Scales can form in different places: (1) on available equipment surfaces (e.g. the inside of a heat exchanger or the well casing), (2) as suspended particles in the fluid and (3) on mineral surfaces in the reservoir. Precipitates formed on surfaces can become dislodged and end up as particles in solution, leading to clogging of filters and possibly even the reservoir (Mercer et al., 1982).

Depending on the chemistry of the fluid in question and the location within a HT-ATES system, different scaling minerals are expected to precipitate, e.g. carbonates during heating of the reservoir water before injection or silicates during cooling at the end of the storage period. The most common ones encountered in HT-ATES in sandstone or carbonate reservoirs are discussed below. However, for reservoirs and groundwaters with a more unique composition, other minerals could be encountered as well.

Carbonate minerals

There are several common carbonate minerals: (1) The three Ca-carbonate polymorphs calcite, aragonite and vaterite (e.g. Plummer and Busenberg, 1982) as well as amorphous calcium carbonate, a generally short-lived precursor phase and (2) the Ca-Mg-dolomite ($CaMg(CO_3)_2$). Ca-carbonates, especially calcite, are extremely common in reservoir formations considered for HT-ATES (as a main component or cement phase in sandstones). Due to the rapid dissolution and precipitation kinetics, fluids often reach equilibrium with respect to calcite during heating,

storage and cooling. Therefore, the amounts of calcite dissolved and precipitated often reach the maximum values predicted by thermodynamic data (= worst case scenario). The other Ca-carbonate polymorphs are rarely discussed within the framework of HT-ATES (e.g. Ueckert and Baumann, 2019). However, there is a plethora of laboratory studies investigating the mechanism of carbonate precipitation showing that, depending on supersaturation, temperature and the presence of ions such as Mg or SO_4, different polymorphs are precipitated preferentially. Such foreign ions (e.g. Mg, Fe, SO_4 or PO_3) are often incorporated into the precipitating carbonate minerals, especially calcite. While the impurities are generally below 10 wt.%, their effects on solubility cannot be described sufficiently by the thermodynamic and kinetic properties of pure calcite (e.g. Jenne et al., 1989), especially as many of the impurities act as inhibitors, slowing down or even preventing the precipitation of calcite despite substantial supersaturation (e.g. Andersson and Sellberg, 1992; Griffioes and Appelo, 1993). Nevertheless, calcite scaling during heating of reservoir waters is very common due to the retrograde solubility of carbonates. In addition, degassing due to reduced pressure (e.g. during pumping) can lead to substantial carbonate precipitation (Alt-Epping et al., 2014; Wanner et al., 2017).

Calcite scaling has been observed in many of the early HT-ATES test sites (SPEOS, University of Minnesota, Plaisir, Appendix A). However, these studies have generally not investigated the mechanisms and rates of calcite scaling but simply evaluated the success or failure of the implemented water treatment (see below). Detailed investigations on the factors controlling carbonate precipitation in HT-ATES are relatively rare. The study by Griffioen and Appelo (1993) investigating carbonate precipitation in a sediment core heated to 90 °C aimed to determine which of the several factors (e.g. degree of supersaturation, *pH*, partial pressure of CO_2, Mg-inhibition; Plummer et al., 1979) controls the precipitation rate. The authors showed that upon heating, supersaturation with respect to calcite was reached quickly and as expected. This led to the precipitation of small amounts of a partly amorphous, partly crystalline Ca-(Mg)-Fe-carbonate, containing Mn ± P in the first few centimetres of the core. In the remainder of the core and during the rest of the experiment (~ 45 h), no carbonate precipitation was observed despite substantial supersaturation and rapid theoretical precipitation kinetics (2.5 min to reach equilibrium according to the model by Plummer et al., 1979). Magnesium inhibition is a well-known effect delaying carbonate precipitation (Morse, 1983). However, under the conditions studied, Mg inhibition should increase the equilibration time twofold, i.e. to 5 min. This is clearly not sufficient to explain the experimental results. Another option discussed by the authors is the complexation of Ca^{2+} by the organic acids abundant in solution, such that less Ca^{2+} available for the precipitation of calcite. While this effect likely played a role

in reducing calcite precipitation, it is not sufficient to explain the minimal carbonate precipitation observed. However, the concentrations of organic acids are high enough to inhibit the precipitation of Ca-carbonates through sorption onto mineral surfaces (Berner et al., 1978, Inskeep and Bloom, 1986, Zullig and Morse, 1988). The same applies for phosphate, which is also present in high enough concentrations to inhibit Ca-carbonate precipitation (de Kanel and Morse, 1978). The results indicate that precipitation of carbonates at 90 °C under the conditions studied by Griffioen and Appleo (1993) does not proceed to equilibrium due to inhibition by organic acids and dissolved phosphate and thus cannot be predicted currently by theoretical calculations or geochemical models.

The second study investigating the mechanisms and rates of carbonate mineral precipitation during HT-ATES was conducted by Ueckert et al. (2020) using field tests and autoclave experiments at 45 – 110 °C. In the autoclave experiments using groundwaters, aragonite was generally the dominant Ca-carbonate polymorph that formed, while in the field experiments, calcite dominated. The results suggest that, despite evidence from previous studies, temperature and the Mg/Ca ratio showed no effect on which Ca-carbonate polymorph precipitated, and supersaturation alone was the controlling factor (higher in laboratory experiments). This shows that when investigating systems with either complex fluid chemistries (e.g. natural waters instead of simple Ca-carbonate solutions as commonly done in laboratory experiments) or with dynamic boundary conditions, predictions of which carbonate polymorph(s) form are challenging. It also indicates the precipitation mechanisms and the relevant kinetics remains unclear despite decades of work on the carbonate system.

Besides $CaCO_3$ minerals, dolomite commonly becomes supersaturated during heating of groundwater in a HT-ATES system. While dolomite is a common mineral in many reservoirs and thus affects the solution composition when it dissolves, it is unlikely to precipitate below 100 °C despite substantial supersaturation (e.g. Usdowski, 1989; Gregg et al., 2015) and to our knowledge has not yet been observed as a scaling mineral in HT-ATES heat exchangers.

As described previously, carbonate scaling during heating of formation waters has been observed in many of the pioneering HT-ATES sites. While not investigating the problem from a mechanistic point of view, a lot of time and effort went into designing and optimising water treatment strategies to mitigate the scaling problem:

- Acidification by addition of acids or CO_2 to prevent supersaturation upon heating
- ion exchange (i.e. replacing Ca^{2+} by Na^{+}) to prevent supersaturation upon heating
- Different types of heat exchangers (e.g. tubular, plate, fluidised bed) or Teflon coatings
- Controlled precipitation by electromagnetic conditioning or increasing the *pH*

Only the first two approaches showed successful mitigation of carbonate scaling upon heating

(Jenne et al., 1992, Jollien et al., 1992). Acidification (using HCl) was used in one of the earliest projects (SPEOS, Appendix A). While it successfully prevented carbonate scaling in the heat exchanger, it lead to strongly increased chloride concentrations, which caused substantial corrosion of metal parts (Jollien et al., 1992). Other acids (e.g. HNO_3, H_2SO_4 or H_3PO_4) should not be used (Sanner and Knoblich, 1999) as they could act as nutrients for microbes, enhancing microbial activity and thus clogging through biofouling and microbially-influenced corrosion (Section 2.1.3). At a later stage, CO_2 addition was tested at the SPEOS plant and described as an "economical, effective and environmentally beneficial water treatment method" (Koch and Ruck, 1992). However, as the project was shut down to lack of interest by the owner shortly after, no large scale test was performed. The first large scale application of CO_2 addition to prevent scaling was performed recently at a HT-ATES test site close to Munich (Ueckert and Baumann, 2019). The approach was very successful in preventing scaling in the heat exchanger. However, geochemical modelling showed that the efficiency of CO_2 addition decreases over time or the amount of CO_2 needed to prevent scaling has to be increased due to the ever increasing hardness of the water. While an increase in CO_2 addition is definitely needed, the increase of CO_2 calculated by the authors is likely too high, as their model did not take mixing with less hard *in-situ* groundwater into account.

Ion exchange resins, replacing calcium in solution with sodium, was the most commonly used water treatment technique in other early HT-ATES tests (e.g. University of Minnesota or Mobile, Appendix A). It was shown to be effective, easily realised and did not exacerbate any other issues such as corrosion. However, the increased Na concentration could potentially lead to swelling and dispersion of clay minerals in the reservoir (Section 2.1.1.4). In addition, the efficiency of the ion exchange treatment will decrease with every cycle as the water is (partly) reused, increasing the sodium concentration in the reservoir over time (Willemsen et al., 1992). Furthermore, the costs for NaCl used to regenerate the ion exchanger are relatively high, impacting the economic feasibility of HT-ATES projects (e.g. Molz et al., 1983a).

SiO_2 and silicates

Silica (SiO_2) and silicate minerals show normal prograde solubilities. They are thus undersaturated in the hot water injected, which leads to dissolution during storage (Section 2.1.1.1). When the fluid is cooled at the end of the storage period to produce thermal energy, the *SI* of silica and silicates increases. It is possible that this leads to supersaturation with respect to some minerals and subsequent precipitation. However, many of the crystalline silica and silicate minerals show relatively slow precipitation rates and their precipitation may therefore be

kinetically hindered. Quartz is one example. The mineral is abundant in most sand and sandstone reservoirs. Due to its normal solubility, it is dissolved during storage of hot water until equilibrium ($SI = 0$) is reached (Holm et al., 1987, Perlinger et al., 1987). Upon production and cooling of the hot water at the end of the storage cycle, it will become supersaturated ($SI > 0$). However, quartz scaling is not observed in any HT-ATES systems. Problems with the precipitation of SiO_2 phases will only occur if enough quartz is dissolved during storage to reach supersaturation with respect to the more soluble and rapidly precipitating amorphous silica (Sjöberg, 1996, Gunnarsson and Arnórsson, 2000). This is only observed in high-temperature geothermal systems. The temperature range for the operation of HT-ATES (generally < 100 °C) prevents the dissolution of high enough volumes of quartz in the reservoir. However, studies show that impurities, especially Fe and Al, are often incorporated into amorphous silica precipitates and lower the solubility of the entire phase (Thórhallsson et al., 1975, Gallup, 1989, Gallup, 1998). It is therefore conceivable that amorphous silica scaling could occur in HT-ATES systems with injection temperatures below 100 °C.

Other silicates which could potentially precipitate are Mg-(Al-)silicates. Precipitation of such phases has been observed in low-temperature geothermal fluids (< 100 °C) in Iceland (Kristmannsdottir, 1989, Kristmannsdottir et al., 1989, van den Heuvel et al., 2018). The exact identity of the phases is unknown but they are likely poorly crystalline sheet silicates related to clay minerals, sepiolite or talc. Holm et al. (1987) suggested precipitation of talc in the HT-ATES at the University of Minnesota but no other sites have reported similar observations.

Other scaling minerals

Metal (hydr)oxides or sulphides are the most common scaling minerals in HT-ATES besides carbonates. They are primarily composed of Fe, but Mn-, Ni-, Cu- and Zn-rich phases have been encountered as well. These metal phases were observed as fine grained particles transported in the fluid at numerous HT-ATES sites, e.g. Reichstag, Neubrandenburg (Appendix A). They are generally not interpreted to be derived from dissolution/precipitation reaction in the reservoir but instead from microbial activity including microbially-influenced corrosion (MIC, Lerm et al., 2013) and/or chemical corrosion of metal fittings (e.g Huenges, 2011) and thus cannot be considered scaling minerals *sensu stricto*. However, if concentrations of redox sensitive metals are high enough and oxygen enters the fluid circulation system, e.g. during maintenance or due to a leak, direct precipitation of metal phases (primarily Fe- and Mn-(hydr)oxides) is possible (Jenne et al., 1992, Vail et al., 1992). These precipitates represent "real" scales.

2.1.1.5 Clogging due to other mineral reactions

Clogging of pores in the reservoir and of wells and surface installations is not only the result of mineral precipitation. It can also occur when minerals swell and when mineral floccules are mobilised and redeposited in pore throats, thus reducing permeability of the formation. This is especially common in sand and sandstone reservoirs.

The main culprits for both these effects are clay minerals. Kaolinite, smectite and illite are the three main groups of clay minerals which differ with respect to their layer structures and thus their swelling properties (Grim, 1942). Smectites (and especially montmorillonites) are considered as swellable clays because they incorporate water molecules within their interlayer structure, upon changing salinity of the formation water and/or the type of cations available in solution. Especially the contact with less saline waters and the exchange of interlayer cations for sodium will result in smectite minerals swelling to several times their initial size (Hewitt, 1963; Mohan et al., 1999). This can reduce the size of adjacent pores and affect porosity and, often more strongly, permeability. In addition, swelling often leads to disintegration of the mineral grains and to subsequent dispersion of smectite floccules, which can further clog the reservoir. Kaolinite is a non-swellable clay mineral but it has been shown to readily disperse during fluid migration and thus contribute to formation clogging as well (Mungan, 1989). Kaolinite dispersion is enhanced at elevated temperatures and/or higher salinities as both changes lead to a larger electrical double layer which forces the kaolinite grains apart (Rosenbrand et al., 2014).

Formation damage due to clay swelling and dispersion has been observed in several HT-ATES systems (e.g. Mercer et al., 1982, Jenne et al., 1992). Especially during the early tests at the Mobile site, swelling, dispersion and migration of clay minerals (smectites and kaolinite) caused extensive formation damage as clay floccules became trapped in the narrow pore throats (Molz et al., 1979). The reason for the swelling of clay minerals was the injection of waters with a lower salinity compared to that of the formation water. No effect of temperature was found. Regular backwashing dissociated the clay floccules and enhanced permeability again temporarily (Molz et al., 1979, Molz et al., 1981). In later heat storage cycles, the issue was mitigated by not injecting freshwater but formation water enriched with NaBr instead. This water had a slightly higher TDS than the formation water and thus no swelling and dispersion of clay minerals was observed (Molz et al., 1983b).

Besides clay minerals, very small (sub-µm to several µm in size), loose particles of quartz, amorphous materials and other minerals (e.g. feldspars, clays, carbonates, mica) are abundant in most sandstones. These particles are called "formation fines" (Muecke, 1979) and can date back to the formation of the reservoir unit or be introduced later, e.g. during drilling.

As they are not cemented, they can be mobilised by any fluid migrating through the pore space and result in clogging of narrow pore throats (Figure 2.1). The likelihood for formation fines to clog pores increases with decreasing size of pore (throats), increasing particle size and concentration and flow velocity. High flow velocities additionally result in clogging which is harder to dissipate as the particles are packed more closely. Clogging can be reduced or reversed by pulsating flow or regular backwashing (Muecke, 1979).

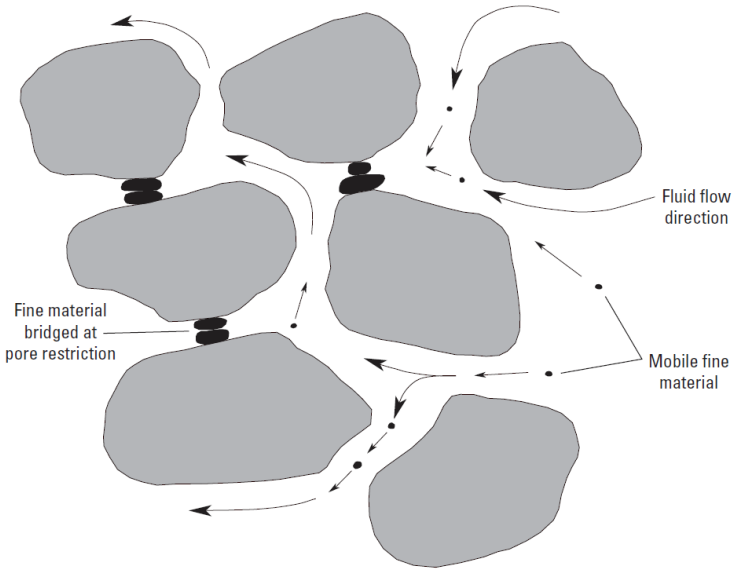

Figure 2.1: *Bridging of pore throats by fine material, leading to a significant reduction in permeability (from Miller and Delin, 2000).*

Clogging by mobilisation of fines can be strongly enhanced if the carbonaceous or siliceous cement in a sandstone is dissolved due to mineral reactions (Section 2.1.1.1) and additional particles are released (Subcasky, 1978). This process is especially common close to the injection/production well, where both the chemical disequilibrium (and thus mineral reactions) and the flow rates are highest (Miller and Delin, 2002).

Besides minerals and formation fines, gas bubbles can also cause clogging of the reservoir formation (Vail et al., 1979, Vuataz et al. 1989). This happens when a free gas phase forms due to pressure reduction in the surface installations. If this two-phase fluid is reinjected into shallow aquifers, bubbles can become trapped in the pore space and lead to clogging. A possible mitigation strategy is degassing of the fluid in the surface installations to reduce the concentration of dissolved gases and prevent bubble formation. However, degassing will also remove CO_2, which affects the carbonate equilibrium and can lead to enhanced carbonate scaling (Section 2.1.1.3). Maintaining a high enough back pressure in the system is thus a better option to mitigate clogging through bubble formation.

2.1.2 Microbial activity

Microbes are abundant in all shallow subsurface environments but the type of microbial community that thrives, strongly depends on the local physico-chemical conditions such as temperature, *pH*, fluid composition (e.g. oxygen, sulphate, nitrate), concentration of organic matter, salinity, porosity, depth and rock type (Hicks and Steward, 1988, Griebler and Lüders, 2009). Aquifers are considered to be environments that are relatively poor in nutrients and organic carbon (Griebler et al., 2002). Especially in deep aquifers, oxygen is often limited or absent and microbes need to use alternative energy sources such as oxidised species (e.g. sulphate, nitrate or iron). Due to the limited availability of nutrients, microbes prefer to grow attached to surfaces (e.g. mineral grains) and extract the required constituents from the water flowing past (Adinolfi and Ruck, 1992). These microbes often form synergistic biofilms where many different cells, often belonging to many different species, are joined together by sticky extracellular polymeric substances and create a unique micro-environment (Costerton et al. 1995, van Loosdrecht et al. 1995). Both spatial and temporal heterogeneities in physico-chemical conditions of the aquifer and nutrient availability can strongly affect the microbial diversity and distribution as they can make conditions more or less favourable for certain species. Some microorganisms can survive detrimental changes to their living conditions by entering a dormant state and returning to normal activity as soon as the conditions have improved again (e.g. Amy, 1997).

Due to their abundance and diversity, microbes commonly affect industrial usage of aquifers, e.g. geothermal energy production or ATES. Common problems associated with microbial activity are microbially-influenced corrosion (MIC; Section 2.1.3) and clogging due to scaling or biofouling. Certain species are more likely to negatively affect installations. For example, sulphate-reducing bacteria (SRB) have been found to strongly enhance corrosion. They produce H_2S as part of their metabolic pathway, which rapidly reacts with available steel surfaces to form Fe-sulphides (Hamilton, 1985, Lee et al., 1995, Javaherdashti, 2011). Other species such as fermentative and sulphur-oxidizing bacteria (SOB) produce inorganic acids (e.g. sulphuric acid) as part of their metabolism, which also contributes to corrosion of steel surfaces (Javaherdashti, 2008). The effects of these microbes are particularly detrimental as they often form biofilms directly on steel surfaces (wells, pumps, pipelines and heat exchangers; Lerm et al., 2013), precluding removal or dilution of the corrosive species by the adjacent fluid flow. When such biofilms grow large enough to affect the hydraulic characteristics of the flow path (e.g. clogging filters), the issue is described as biofouling. Biofouling can also occur in the reservoir, when changing conditions, e.g. increasing temperature, results in enhanced microbial growth and subsequent clogging (Howsam, 1988, Adinolfi and Ruck, 1992). Clogging can also

occur if the corrosion products formed are transported through the system and end up blocking filters or even the pores in the reservoir. Especially Fe-sulphide is observed as a common scaling mineral in many HT-ATES operations (Section 2.1.1.4).

Microbial activity was not investigated from most of the HT-ATES projects conducted in the 1970s and 1980s and most sites did not report major issues (Adinolfi and Ruck, 1992). Some studies investigated the potential for HT-ATES increasing the number of pathogenic microorganisms, such as *Legionella* in an aquifer, which could represent a health hazard (e.g. Hicks and Steward, 1988; Jolien et al., 1992). The only HT-ATES site where detailed microbial investigations were performed is Neubrandenburg (Appendix A). Lerm et al. (2013) identified the microorganisms present at both the hot (68 – 73 °C) and cold side (~ 46 °C) of the system during normal operation and the detrimental effects (corrosion and scaling) that the microbes can have. Westphal et al. (2016) focused on the effect of downtimes (i.e. (non-) scheduled maintenance) on the microbial community and how this changes corrosion and scaling processes. The following findings can be summarised for the HT-ATES system at Neubrandenburg:

- Distinctly different microbial communities on the hot and cold side of the system despite relatively similar fluid composition. Higher species diversity on cold side, which further increases during downtimes.
- Number of microbes on the hot side is substantially lower and less diversity. Downtimes dramatically increase the number of cells due to better growth conditions (e.g. higher DOC) and lack of removal by the passing fluid.
- Biofilms developed in heat exchangers and pipes of the surface installations. During downtimes, biofilms extended into the upper well-bore on the cold side.
- Microbial groups identified:
    - Sulphate-reducing bacteria (SRB) were encountered in all settings but were especially abundant on the cold side. The presence and activity of such bacteria are indicated by increased concentration of H_2S, strongly positive sulphur isotopic signatures and abundant precipitation of sulphides.
    - Fermentative *Halanaerobiaceae* producing for example acetate, ethanol, H_2 or CO_2 from carbohydrates.
    - After plant shutdowns (= stagnant conditions), sulphur-oxidizing bacteria (SOB) were also encountered on the cold side, indicating the ingress of oxygen.
- Corrosion was found to be much more substantial on the cold side of the HT-ATES system, i.e. microbes were involved in or even primarily responsible for the pump failure (= MIC; Section 2.1.3) and for the following 8-month shutdown required to fix

the problem. During other, shorter shutdowns, corrosion and subsequent formation of Fe-sulphides strongly increased on the cold side due to higher bacterial numbers and the presence of SOB which produce sulphuric acid as part of their metabolism.

The effect of shutdowns or stagnant conditions investigated by Westphal et al. (2016) could be of great importance for HT-ATES systems where an extended storage time is planned between injection of hot water in summer and production of cold water during winter. The results of that study suggest that microbial activity and accompanying corrosion and scaling could be strongly enhanced during such stagnant times.

As sampling at Neubrandenburg was started only after the heat storage site was commissioned, no information on the pre-existing microbial community under *in-situ*, pre-storage conditions are available. Thus, the findings from this site cannot be used to predict the microbial evolution of other sites under consideration for HT-ATES systems. However, the Neubrandenburg studies highlight the serious problems that can be caused by microbial activity. In fact, microbial diversity might even be higher in other, less saline systems as the high salinity at Neubrandenburg (~ 130 g/L) likely limits the number of species that can thrive.

2.1.3 Corrosion

Corrosion of metal well casings, pumps and surface installations is a common problem in many water handling industries and can be subdivided into three types which have all been observed in HT-ATES systems:

(1) Chemical corrosion, related to acidic *pH*, high TDS values and the presence of dissolved gases (O_2, H_2S, CO_2) and other corrosive compounds such as HS^-/S^{2-}, Cl^- or SO_4^{2-}.
(2) Microbially influenced corrosion (MIC) caused by or related to the metabolic activity of microbes.
(3) Electrochemical corrosion due to different metallic materials being in close proximity or imperfections within a stressed monometallic part.

Chemical corrosion is minor in most HT-ATES systems as they are often situated in shallow reservoirs with carbonate minerals present (e.g. sands and sandstones) where the *pH* is near-neutral (due to the buffering capacity of the carbonate system) and the TDS concentrations as well as the concentration of dissolved gases and corrosive species are relatively low. Extensive chemical corrosion has primarily been observed in HT-ATES systems where leaky fittings were observed and allowed the ingress of atmospheric oxygen or where HCl was added prior to heating of the water in order to prevent carbonate scaling in the surface instal-

lations (Section 2.1.1.3). The increased chloride concentrations in such systems have led to increased pitting corrosion (Jollien et al., 1992). This is the main reason why acidification as a mitigation strategy to prevent carbonate scaling has fallen out of favour over recent years (Jollien et al. 1992, Vail et al., 1992). An increase in chemical corrosion would also be expected in systems where the salinity of the water is increased in order to reduce thermal stratification (Section 2.1.3), thus limiting the applicability of this measure to real HT-ATES projects.

Corrosion related to microbial activity, i.e. microbially-influenced corrosion (MIC) is a much more common phenomenon. It has been shown that sulphate-reducing bacteria (SRB) are the most common culprits causing MIC (Hamilton 1985; Lee et al. 1995; Valdez et al. 2009; Javaherdashti, 2011). In addition, bacteria such as fermentive and sulphur-oxidising bacteria (SOB) produce organic and inorganic acids as part of their metabolic activity, which can indirectly enhance corrosion of steel surfaces by reducing *pH* (Javaherdashti, 2008). Extensive MIC has been observed in one of the only HT-ATES currently in operation, the geothermal heat store in Neubrandenburg (Section 2.1.2).

The third type of corrosion, electrochemical corrosion, has also been observed in previous HT-ATES systems. Jenne et al. (1992) even described it as more common than chemical corrosion. However, no publications are available on the occurrence of electrochemical corrosion in HT-ATES settings. A likely reason is that, once identified, problems with electrochemical corrosion can be resolved relatively easily by replacing the affected parts with parts made from a different, more corrosion-resistant material or by applying a cathodic protection system (e.g. a sacrificial anode).

Besides reducing the lifetime of parts installed in an HT-ATES system, corrosion can also lead to clogging if the corrosion products (Fe (hydr)oxides, Fe-/Cu-/Zn-sulphides and amorphous particles containing high concentrations of metal ions) are transported into the pore space of the reservoir (Potter et al., 1980, Vuataz et al., 1989), resulting in reduced permeability of the sandstones. In Neubrandenburg, MIC lead to the formation of FeS-particles (mostly below 1 μm in size). During normal plant operations, the particle load was around 0.01 g/L while this value increased by a factor of 5,000,000 upon restarting circulation after plant downtimes (Westphal et al., 2016). Luckily, filters were installed in the surface installations to prevent these colloids from being injected into the subsurface and thus no permeability reduction was observed.

2.1.4 Hydrogeological issues

2.1.4.1 Regional flow

In aquifers with a regional pressure gradient and sufficient permeability for HT-ATES, regional groundwater flow is commonly observed. This is detrimental to the successful operation of an HT-ATES site as it results in substantial mixing of the hot injected water with the cold *in-situ* groundwater and dispersion of the thermal energy. In addition, regional groundwater flow moves the thermal plume away from the injection site. Thus, the injection well cannot be used as a production well but one or several production wells need to be drilled into the displaced thermal plume. In order to change the flow field, the upstream pressure can be modified by pumping or a low-permeability screen can be established surrounding the entire storage volume (Mercer et al., 1982, Jenne et al., 1992). However, both of these strategies are relatively costly. It is thus easier to avoid aquifers with substantial regional flow altogether and focus on formations with more stagnant conditions (Mercer et al., 1982).

Regional flow can also be limited to certain sections of the aquifer. During a recent HT-ATES test in the Munich basin (Ueckert und Baumann, 2019), a narrow zone (~ 3 m) at the top of the Malm aquifer showed much higher porosities and permeabilities compared to the rest of the aquifer, probably due to karstification. Thus, the injected hot water mixed with large volumes of cold groundwater that was moving laterally through the karst network, resulting in over 50% energy loss during the storage test.

2.1.4.2 Preferential flow

Most aquifers exhibit a heterogeneous permeability distribution due to lithological variations (e.g. grain size difference or zones with a variable degree of sorting in sandstone aquifers) or heterogeneous fracture networks. It is thus possible that injection and production of hot water is concentrated in certain sections of the aquifer rather than homogeneously distributed across the entire thickness of the reservoir formation. This leads to a thermal plume with a wavy front instead of straight vertical front, and hence with a higher surface area, which increases the contact with colder areas of the aquifer. Thermal conduction between the more permeable "fingers" and the less permeable areas results in higher thermal losses (Buscheck et al., 1983, Jenne et al., 1992). Permeability heterogeneities can also affect the recovery of the energy stored as water is pumped primarily from the more permeable zones while the energy in less permeable zones is more difficult to extract (Molz et al., 1983a). Such aquifer heterogeneities can vary strongly over short lateral distances as shown by the difference between the 2nd and 3rd cycle

at the Mobile HT-ATES site. While the aquifer was homogeneous at the site of the 2nd cycle (Molz et al., 1981), a zone with a higher intrinsic permeability was encountered in the middle of the aquifer at the site of the 3rd cycle just over 100 m away (Molz et al., 1983a).

Permeability heterogeneities can easily be recognised during the (test) operation of an HT-ATES system, based on temperature profiles along individual wells and the temperature evolution during production. Ideally, they should be identified early during site characterisation so that their existence can be included in the planning of the injection and production parameters. Molz et al. (1983a) therefore consider detailed hydrological testing (i.e. tracer test instead of just pumping tests) to be crucial during site characterisation.

While often limiting the efficiency of HT-ATES, a heterogeneous permeability distribution can also prevent substantial buoyancy flow, thus resulting in a higher energy recovery compared to a homogeneous aquifer (Section 2.1.4.3).

2.1.4.3 Buoyancy flow or free thermal convection

When hot water is injected into an aquifer containing a colder groundwater, the density difference between the two can lead to the hot water rising to the top of the aquifer while the colder formation water accumulates at a lower level, a phenomenon known as thermal stratification. The temperature difference also results in a viscosity difference, which further facilitates the rising of hot water within the aquifer (Hellstrom et al., 1979). This movement of water has been termed buoyancy flow or free thermal convection and results in the tilting of the initially vertical hot water front and the establishing of a mushroom-shaped thermal plume rather than a cylindrical one (Figure 2.2). The water produced from the entire thickness of a thermally stratified aquifer represents a mix of hot water from the top and cold water from the bottom of the aquifer, resulting in low production temperatures. In addition, a substantial volume of hot water remains in the uppermost part of the aquifer, resulting in an overall low energy recovery from such a system (Molz et al., 1983b). The effect of buoyancy flow is more pronounced in thick or highly permeable aquifers (with a homogeneous permeability distribution), for high injection temperatures and long storage times (Mercer et al., 1982). According to Hellstrom et al. (1979), the maximum thickness of an aquifer to avoid thermal stratification can be estimated based on the planned injection temperature and the permeability of the aquifer.

Extensive buoyancy flow was observed during the third cycle at the HT-ATES test site in Mobile (Buscheck et al., 1983, Molz et al., 1983b) which resulted in a very low recovery of 45% for the injected heat. In order to increase the recovery for the second part of the cycle, a

dual recovery well system was constructed (Molz et al., 1983a). One well primarily produced the hot water from the top of the reservoir while a second well (rejection well) pumped the colder water from the bottom of the aquifer. It was expected that energy recovery could be maximised by finding an optimal pumping ratio between the two wells. Unfortunately, this was not achieved due to stronger lateral spreading of the thermal plume caused by flow along a high permeability zone at the centre of the aquifer. In addition, the large area of contact between the thermal plume in the uppermost part of the aquifer and the cold overlying aquitard resulted in substantial heat loss due to thermal conduction.

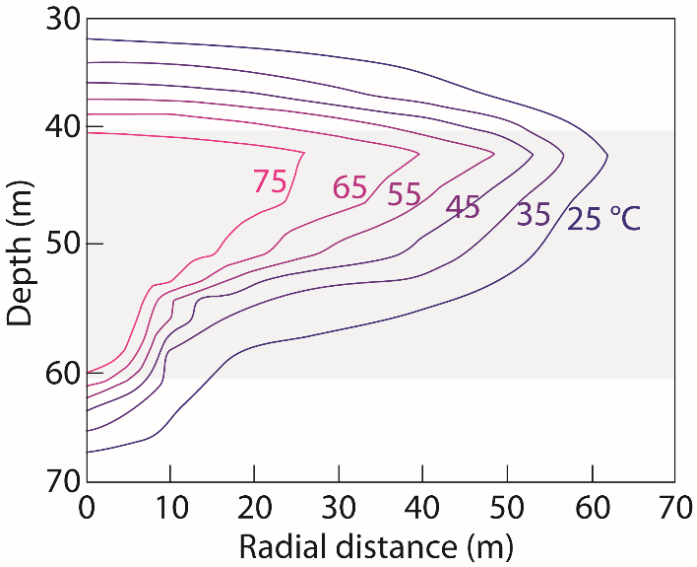

Figure 2.2: *Calculated temperature distribution at the end of the second-cycle injection period (137 days) at the HT-ATES test site in Mobile, Alabama, indicating substantial thermal stratification within the reservoir. Grey area indicates aquifer formation (modified after Buscheck et al., 1983).*

Despite a thicker aquifer and higher injection temperature (Appendix A), only limited buoyancy flow was observed in the HT-ATES site at the University of Minnesota (Hoyer et al, 1991). Convection was likely inhibited due to the marked horizontal permeability anisotropy of the FIG aquifer, which consists of interbedded sand- and clay-rich sections, limiting vertical buoyancy flow. Producing hot water from the top of the aquifer as was tried at Mobile, would therefore have led to reduced energy recovery. Thus, ideally the permeability distribution across the entire reservoir should be understood before designing the extraction scheme.

In order to prevent buoyancy flow and the associated reduction in recovery efficiency, HT-ATES are often situated in lower permeability aquifers and lower storage temperatures (Doughty et al. 1982; Schout et al. 2014). However, this limits both the maximum efficiency and storage capacity of HT-ATES as well as the number of storage sites considered suitable. A

possible mitigation strategy to prevent buoyancy flow and increase recovery efficiency of an HT-ATES system has been presented by van Lopik et al. (2016). They investigated the compensation of the thermally induced density difference by numerically simulating an increase in the salinity of the injected water, thus preventing stratification and increasing the recovery factor. In their models, they could show that the compensation improved recovery factors drastically, approaching the maximum possible values for a system with no thermal stratification (> 70%). While the compensation of the density difference works very well in theory, it is unclear if it can be applied in a real HT-ATES system as several questions remain unanswered:

- What is the lifetime of such an HT-ATES system as the amount of salt needed to correct for the density difference continuously increases as the salinity of the reservoir increases?
- What is the effect of higher salinity on mineral reactions (Section 2.1.1), microbial communities (Section 2.1.2) and corrosion (Section 2.1.3)?
- Additional costs of large quantities of NaCl (up to 46.5 kg/m^3 of injected water)?
- Environmental impact of injecting large amounts of brackish to saline water into the subsurface?

However, if successfully realised, density compensation would allow HT-ATES systems to be established in aquifers that are considered too thick and/or too permeable for normal HT-ATES operations and at higher temperatures than currently possible. It would thus help to increase overall potential of the HT-ATES concept.

2.1.5 Hydraulic fracturing and surface uplift

During the active phases of HT-ATES operations, i.e. injection and production, the pressure within the reservoir and the surrounding formations is strongly affected. Reducing the pressure could result in land subsidence while increasing the pressure could potentially cause surface uplift, at least in shallow aquifers with limited overburden. In deeper aquifers, where the lithostatic pressure is higher, uplift is less likely and increasing pressures are can result in hydrofracturing of the overlying formation (Mercer et al., 1982). As this formation general represents a less permeable seal confining the reservoir aquifer, breaking this seal could be highly detrimental to the successful operation of HT-ATES: It would provide the warm water with pathways into shallower aquifers where the heat cannot be recovered and leads to thermal and potentially chemical as well as microbial contamination of other formations. However, as pressure management of the reservoir is relatively easy by adjusting pumping rates of injection and/or production wells accordingly, unintentional hydrofracturing has occurred only at

Horsholm and, potentially, at the HT-ATES test site in Mobile (Molz et al., 1978, Jenne et al., 1989).

During a later test at a second test site in Mobile, an average surface uplift of ~ 4 mm (maximum value 12.4 mm) around 55 m from the injection site was observed. However, this was not related to insufficient pressure management but rather to thermal expansion and contraction of the subsurface due to injection and production of large volumes of hot water. Calculation of expected thermal expansion of both the quartz sandstone and the overlying clay formation showed that surface uplift was largely due to thermal expansion of the aquitard, i.e. the low-permeability water-saturated clays that constitute the caprock but not the reservoir formation itself (Molz et al., 1981). A later, hotter injection cycle confirmed the results as the pressure was lower but surface uplift higher (Molz et al., 1983a). Depending on the local geology, injection temperatures and the size of the HT-ATES reservoir, it is estimated that surface uplift of up to 3 cm is possible, which would make it impossible to operate such a system near buildings or other infrastructure.

2.2 Geology and hydrogeology of the Lower Freshwater Molasse

The target horizon for the *Geospeicher Forsthaus* project is the highly heterogeneous sequence of the Lower Freshwater Molasse (abbreviated USM after the German "Untere Süsswassermolasse"), more specifically the distal Aquitanian USM. The same formation is also considered as a potential horizon for HT-ATES in the Geneva Basin (Collignon et al., 2020).

The USM is part of the sedimentary filling of the Swiss Molasse Basin (SMB) that derived from erosion of the uplifting Alps during Upper Oligocene to Early Miocene times. The Swiss National Cooperative for the Disposal of Radioactive Waste (Nagra) investigated the USM in the 1980s to 2000s as part of the search for a repository for low- and intermediate-level nuclear waste. While these studies showed that the USM was not suitable to host a nuclear waste repository due to the abundance of permeable sandstones intercalated between the more clay-rich lithologies, they also provided a detailed understanding of the sedimentary structure and lithotypes comprising the USM. These findings will be summarised in the following sections.

2.2.1 Geological background

The USM is part of the sequence of Molasse sediments, which can be subdivided into two marine stages and two continental (freshwater) stages (Table 2.1). The transgressions/regressions separating the different stages were controlled by global sea level changes but also local

changes in the uplift rate of the Alps and the subsidence of the SMB, respectively (e.g. Trümpy, 1985). After the regression of the sea towards the East in the late Rupelian (~30 Ma), a flat alluvial plain was exposed across the SMB. In the south of the SMB, braided rivers resulted in the deposition of large coarse-grained alluvial fans. These transitioned to anastomosing river systems as the slope decreased. Eventually, they formed meandering rivers draining the flat basin northwards, turning NE along the base of the Jura Mountain bulge (= axial channel system) and eventually flowing into the Parathetys ocean in the area of Munich (Figure 2.3; Paulus, 1963). These rivers left behind a succession of sand- and siltstones as well as fine-grained clay-rich overbank sediments and even lacustrine deposits on the alluvial plain. The deposition of the USM came to an end during the rapid transgression in the early Burdigalian (~ 20 Ma), which marked the onset of the deposition of the Upper Marine Molasse (OMM). Together with the sediments of the Upper Freshwater Molasse (OSM), they buried the USM to about 1.5 to 3 km (Kälin et al., 1992).

Uplift during the Late Miocene and Pliocene caused the complete erosion of the OSM west of the River Aare and the OMM west of the River Noxon/Venoge. Pleistocene and Holocene glaciations have further eroded the Molasse sequence. In many areas across the SMB, the USM is thus exposed or directly overlain by up to 500 m of unconsolidated Quaternary deposits.

Table 2.1: *The four Molasse lithostratigraphic groups deposited in the Swiss Molasse Basin (SMB) during the Oligocene and early Miocene.*

Name[1]		**Age (Ma = million years)**	**Thickness**
Upper Freshwater Molasse	OSM – "Obere Süsswassermolasse"	Langhian/Seravallian (12 – 16 Ma)	Decreasing from 1500 m (S) to 100 m (N)
Upper Marine Molasse	OMM – "Obere Meeresmolasse"	Burdigalian (16 – 20 Ma)	Maximum thickness 1300 m
Lower Freshwater Molasse	USM – "Untere Süsswassermolasse"	Aquitanian (20 – 23 Ma) Chattian (23 – 28 Ma)	Decreasing from 4000 m (S) to 100 m (N)
Lower Marine Molasse	UMM – "Untere Meeresmolasse"	Rupelian (28 – 34 Ma)	Approx. 500 m thick

[1]By convention, German abbreviations are used for the lithostratigraphic groups of the Molasse deposits (Matter et al., 1980).

[2]In the area of Bern at least 800 m thick but likely up to 2000 m (Isler, 2005).

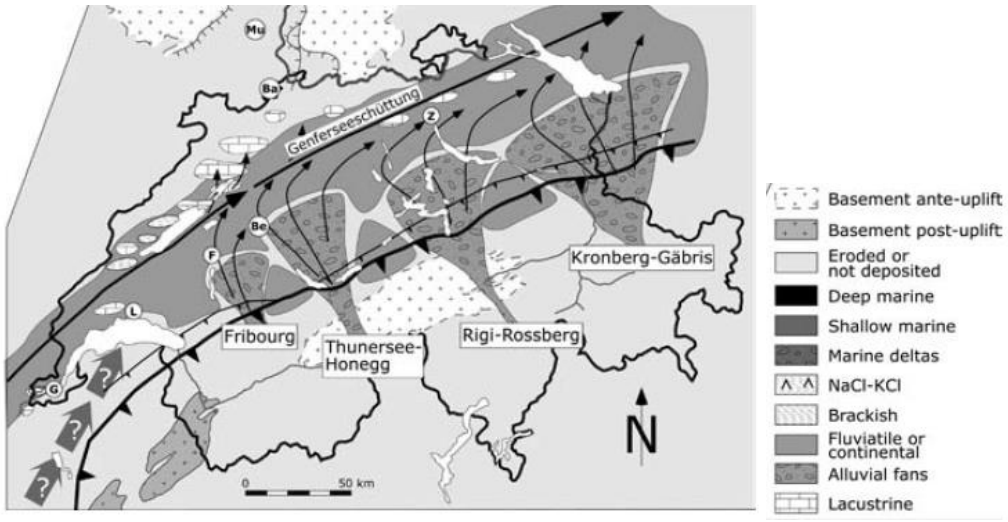

Figure 2.3: *Palaeographic situation during the deposition of the USM in the early Aquitanian (from Berger et al., 2005).*

2.2.2 Subdivison and nomenclature of the USM deposits

According to the Swiss Stratigraphic Commission, the USM can be subdivided into three units: USM-I, USM-II and USM-III (Berger et al., 2010). According to this classification, the USM-I corresponds to the more carbonate-rich Chattian (exposed in the western parts of the SMB) while USM-II represents the "granitic" (i.e. richer in quartz and feldspars) Aquitanian. USM-III represents freshwater deposits, which were deposited concurrently with the oldest deposits of the OMM in Eastern Switzerland. Each of the USM units can be further subdivided into different formations (e.g. Gümmenen formation or Molasse grise de Lausanne) with local to regional distribution. This allows the deposits of the flat-lying Molasse ("mittelländische Molasse") to be distinguished from those affected (e.g. tilted and fractured) by the formation of the Alps or the Jura Mountains ("subalpine" or "subjurassic Molasse"). However, the boundaries between these formations are often unclear and seem to be based on geographical (and language) considerations rather than lithological differences (e.g. Keller et al., 1990). They will thus be avoided and we will only refer to the "Chattian USM" or "Aquitanian USM" instead. As only the distal parts of the Aquitanian USM are considered as a target horizon for the *Geospeicher Forsthaus*, the following descriptions will focus exclusively on these units.

2.2.3 Exposure of USM deposits in the region of Bern

The Aquitanian USM forms the bedrock in large parts of the western and central SMB (Figure 2.4). Towards the East, the USM is only exposed as a narrow strip along the Alpine front

("subalpine USM") and the foot of the Jura Mountains ("subjurassic USM"). In the area of Bern, the USM is exposed in the city centre as well as towards the north and west of the city. In the south and east (e.g. Köniz, Ostermundigen, Ittigen) the sandstones of the OMM overlie the USM. In most places, a (generally thin) layer of Quaternary deposits and recent soils covers the USM (Figure 2.4). Thus, natural outcrops can primarily be found along river- and stream banks (e.g. along the River Aare north of Bern or the River Emme at Gerlafingen) as well as along road or rail cuttings (e.g. near the train station of Gümmenen). Sandstones mostly dominate these outcrops. As these deposits are more resistant to erosion than the other, more fine-grained lithologies within the USM, they form relatively steep banks. The banks with a gentler slope, generally covered in vegetation and soil, likely represent areas where fine-grained and less erosion-resistant elements are more abundant.

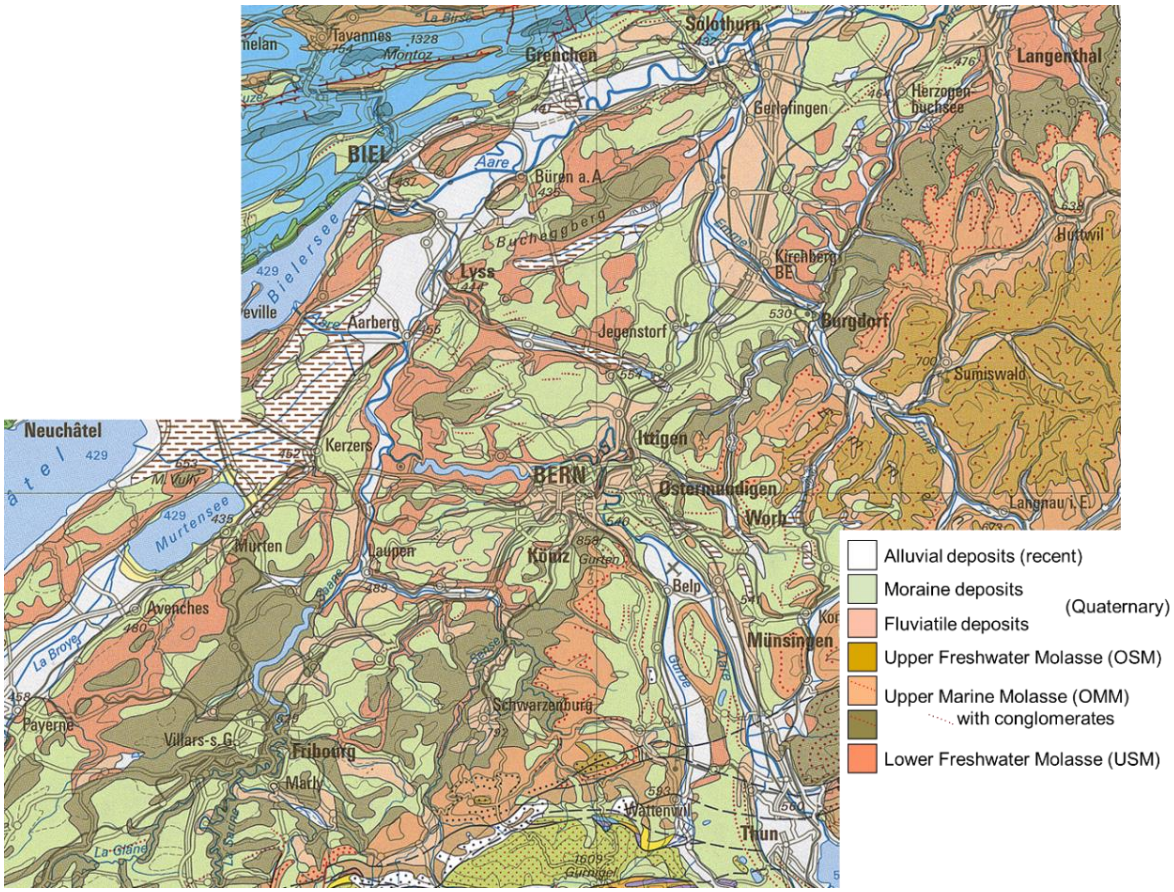

Figure 2.4: *Section of the Geological Map of Switzerland 1:500000 for the area surrounding Bern (modified after the Federal Office of Topography swisstopo).*

Well-exposed sections of USM dominated by the fine-grained deposits are primarily found in the former or active commercial clay pits of the SMB. Several of those are located in the north to northeast of Bern (e.g. Schüpfen, Rapperswil, Radelfingen, Roggwil). Much of the

information presented in this Chapter is based on investigations made on the sections exposed in these clay pits. Overall, the natural and artificial outcrops primarily show sections which are dominated by one of the two endmembers (natural outcrops = sandstones vs. quarries = fine-grained deposits) but they do not necessarily represent the average composition of the USM.

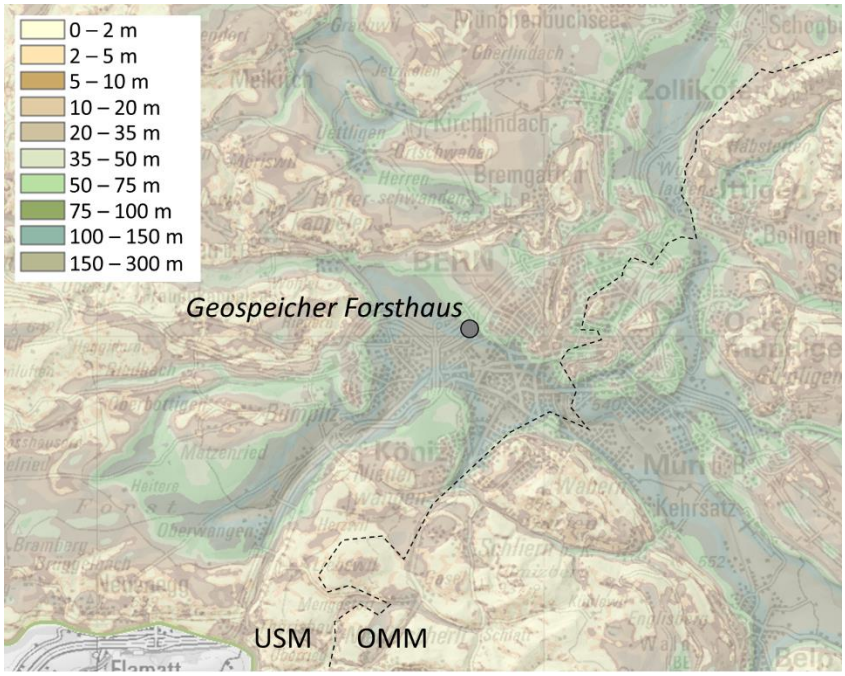

Figure 2.5: *Map showing the thickness of the unconsolidated deposits overlying the Molasse bedrock in the Bern area. The boundary between the Aquitanian USM and the younger OMM is indicated by the dashed line (modified after Geoportal Kanton Bern, version 16 January 2020).*

The USM is also encountered in many tunnels and galleries in the area of Bern. Detailed information is only available for the rail tunnel at Grauholz and not for the more recent construction projects e.g. the road tunnel Neufeld or the ongoing extension of the main train station of Bern. The only exception are the samples presented in Chapter 3. Another source of data are the numerous wells drilled in the central SMB. They were primarily drilled in the 1960s for hydrocarbon exploration and the data (lithological and petrophysical logs) as well as the drill core samples have, as of yet, largely remained confidential. The deep wells (> 500 m) closest to Bern were drilled in Tschugg, Hermrigen, Ruppoldsried, Fendringen, Kirchberg, Linden and Thun (from NW to SE). Around 1990, 16 shallow wells (100 to 250 m) were drilled in Lotzwil and Burgdorf (supported by Nagra). These sites were investigated in detail and the results (including drill core samples and petrographic thin sections) are publicly

available. In recent years, a plethora of additional shallow wells (several tens to a few hundreds of meters) have been drilled in and around the city of Bern for geotechnical investigations and to install ground-source heat pumps. Geological profiles have been compiled for most of them and are publicly available online on the *Geoportal* of the Canton of Bern. The destructive drilling unfortunately limits the resolution of the obtained geological profiles as only a single sample of cuttings is collected for every 2 m interval.

These shallow wells have also been used to reconstruct the bedrock top in the area of Bern. In the city centre as well as towards the north and west of the city, the top bedrock corresponds to the contact between Quaternary or more recent deposits and the USM (Figure 2.5). The data shows that the top surface of the bedrock is not flat but that it has substantial topography caused by glacial and fluvial erosion during uplift of the SMB in the late Miocene.

2.2.4 Meander belt sandstones and other lithotypes of the USM

The distal Aquitanian USM (for the remainder of this section simply termed "USM") was deposited by a system of meandering rivers distributed across the flat-lying alluvial plain north of the Alpine front. In such a fluviatile system, different depositional environments can be distinguished. This results a highly heterogeneous lithological assemblage consisting of different lithotypes with different geometries, mineralogical compositions and petrophysical properties (Figure 2.6). For the distal USM, the following lithotypes can be distinguished (Keller et al., 1990, Keller, 1992, Platt and Keller, 1992):

(1) Meander belt sandstones (MB) deposited in the main river channel.
(2) Levee sand- and siltstones (LS) deposited on the river levees.
(3) Crevasse channel and splay sandstones (CS) deposited during flooding events when the levees were breached.
(4) Overbank fines and palaeosols (OPS) deposited during minor flood events and partly altered by subsequent soil formation processes
(5) Lacustrine silts (LAC) deposited in small temporary lakes in poorly drained parts of the alluvial plain

2.2.4.1 Characterisation of meander belt sandstones (MB)

The central element in a meandering fluviatile system are the river channels themselves, preserved in the sedimentary record as meander belt sandstones (MB; Figure 2.6). They represent the target horizons for the *Geospeicher Forsthaus* and will thus be discussed in detail. Unless other sources are cited, the information below is summarised from Keller et al. (1990), Keller

(1992), Platt and Keller (1992) and Ammann et al. (1993). For further information on the geometries, compositional and petrophysical properties of the other lithotypes shown in Figure 2.6, please refer to these cited studies as well.

The MB are generally 2 – 8 m thick but can occur as amalgamated sequences of up to 50 m thickness. They are made up by medium- to coarse-grained sandstones with a mostly homogeneous grain size. Sedimentary structure such as trough cross-lamination, large scale low-angle/epsilon cross bedding and weak fining-upward can be observed. However, most MB are massive, giving no indication of the depositional or palaeoflow conditions. Many channels show a wavy erosive base with generally clay-rich, rip-up clasts or a pebble lag.

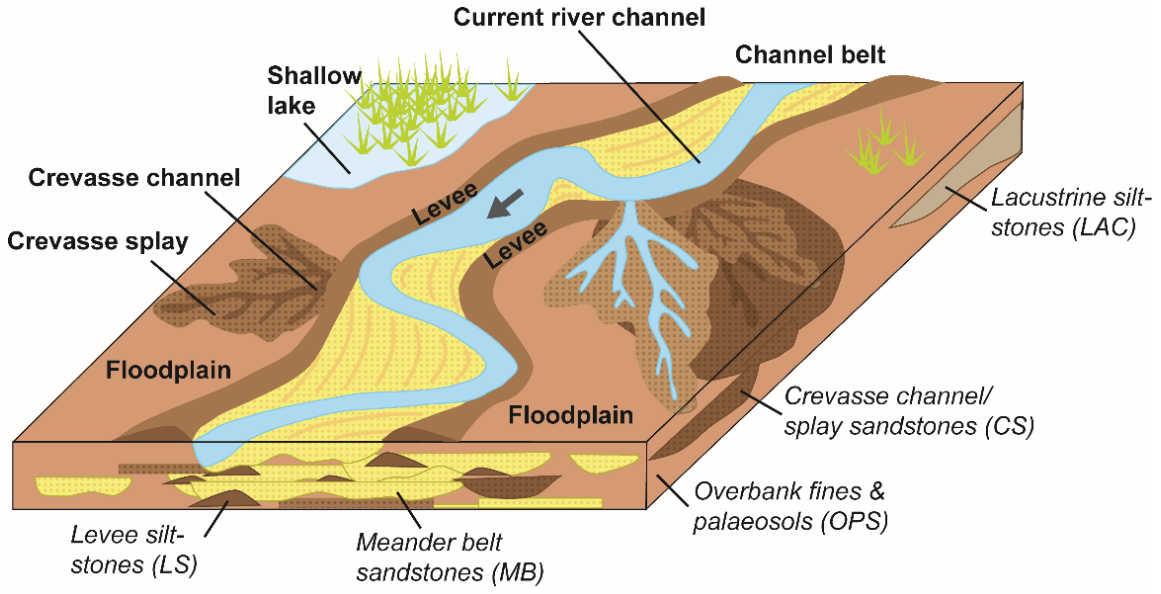

Figure 2.6: *Depositional environments and lithotypes of the distal Aquitanian USM (modified after Galloway, 1981, Keller et al., 1990).*

The MB can be classified as well-sorted feldspathic litharenites to lithic subarkoses, with a few samples falling into the sublitharenite, litharenite and lithic arkose fields (Figure 2.7). They are generally beige but can be slightly greenish in colour due to the presence of pyrite. Organic components (plant material, animal remains, microbial residues) were commonly deposited as part of the USM sequence. This is indicated by the presence of body- and trace-fossils (e.g. Becker & Rauber, 2007; Jost et al., 2015; Mennecart et al., 2016; Buatois et al., 2020) and a number of coal samples found within the deposits (Schegg, 1992). However, the high porosity of MB and CS deposits and abundant bioturbation in CS, LAC and OPS deposits have facilitated the degradation of organic matter. Thus only some LAC and OPS deposits preserve organic-rich dark grey to black horizons related to swamps or shallow lakes as well

as mature palaeosols associated with reducing conditions (Keller et al., 1990; Platt & Keller, 1992).

The same authors have also found a relationship between the abundance of MB sandstones and the maturity of palaeosols: at locations with abundant MB sandstones, palaeosols are immature and organic-poor. This indicates a setting close to the main channel belt. More mature and OM-rich palaeosols are present where channel sandstones are sparse, indicating a more distal floodplain setting. Thus, in a section with abundant and thick MB sandstones - as required for the *Geospeicher Forsthaus* - the concentration of organic matter, even within the OPS deposits, is expected to be low.

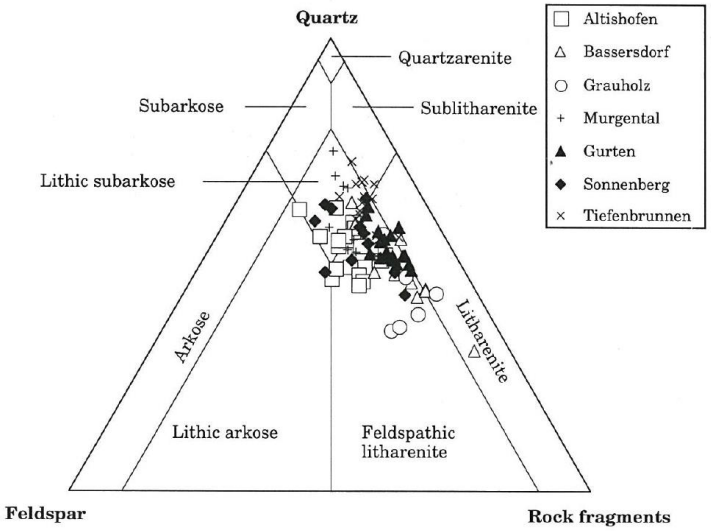

Figure 2.7: *Detrital composition of sandstones from the USM and OMM. USM sandstones were obtained from the wells at Altishofen, Bassersdorf and Murgental as well as the Grauholz and Sonnenberg tunnels (from Mátyás, 1998)*

On average, the sandstones consist of around 35 vol.% quartz, 30 vol.% feldspars, 20 vol.% clay minerals and 15 vol.% carbonates (calcite >> dolomite). This mineralogical composition is comparable to the other lithotypes but the fine-grained LS and OPS show higher clay contents that can be attributed to hydrodynamic sorting. This difference becomes even more pronounced when considering that most of the clay minerals in MB and CS are contained within the lithic fragments (e.g. alteration of feldspars). Three types of sediment components can be distinguished: detrital mineral grains, detrital lithic fragments and cements. The dominant detrital minerals are monocrystalline quartz of magmatic/metamorphic origin (19 to 50 vol.%), plagioclase and alkali feldspars (4 to 21 vol.%) as well as small amounts of sheet silicates. The lithic fragments make up 9 to 41 vol.% of the sandstones. They largely consist of

dolomites and metamorphic rocks but igneous clasts, micritic limestones and various types of shales also occur (Mátyás, 1998).

The individual grains were partially cemented by authigenic clay minerals during compaction and later, during early diagenesis, by Fe-calcite. Other, very localised cements include (Fe-)dolomite and ankerite alkali feldspar, quartz, sulphates and pyrite (Mátyás, 1998). The clay minerals form pore-lining cements and are common but volumetrically not very abundant (generally ≤ 3 vol.%). Their composition ranges from nearly pure smectites to smectite/chlorites and smectite/illites. In addition, filamentous illite has been observed in some open pores, locally being very abundant (e.g. Grauholz). Kaolinite is rare. Fe-calcite is present as sparry to microsparry cement and as small euhedral crystals attached to the surfaces of detrital grains. The calcite cement has partially filled the intergranular pore space and in some cases it has completely replaced some lithic fragments. In some samples, calcite cementation seems linked to organically derived CO_2, which led to a higher degree of cementation and thus lower porosity.

The early cementation has prevented stronger compaction, preserving a large proportion of the intergranular porosity originally present. Based on the diagenetic maturity, it is assumed that the cementation took place at around 40 to 50 °C, at a depth of 1 to 5.2 km and at around 17 to 13 Ma ago. The calcite precipitated from a pore fluid that represented a mixture between the original formation water released during compaction (partially marine from the overlying OMM) and fresh pore waters of meteoric origin infiltrating at the basin scale. Calcite cementation was not homogeneous, leading to a large spread in measured porosity values with a median of 20 vol.%, minimum value of 6 vol.% and maximum value of 25 vol.% in both the samples from Langenthal and Burgdorf. Most of the porosity is due to open intergranular pores (60%), the rest is porosity due to microfractures. At greater depths and towards the Alpine front, porosities are generally lower as shown by decreasing seismic velocities (Büchi and Bodmer, 1983). This is due to the greater compaction and/or cementation at greater depth (thicker stack of sediments close to the alpine front). At shallow depths (tens of meters), secondary porosity has been created in some samples as they were affected by circulation of meteoric waters leading to dissolution of carbonate cement and often oxidation of Fe-minerals. Towards the Alpine front, where the USM has been deformed, the importance of fractures and joints on porosity can increase the porosities of all lithotypes substantially.

The hydraulic conductivity of the MB sandstones in samples from the Langenthal wells (Keller et al., 1990) is between 10^{-4} and 10^{-10} m/s, with a median value of around 10^{-5} m/s. Given as permeability values, this corresponds to between < 10^{-17} and $2 \cdot 10^{-12}$ m^2. The samples from the Burgdorf wells (Ammann et al., 1993) showed average and maximum permeabilities up to

three times higher due to lower volumes of calcite cement. In samples showing secondary porosity, the conductivities can be up to 100 times higher. In addition, fissures and joints can further increase the hydraulic conductivity by several orders of magnitude, potentially linking aquifers at different depth levels. Most of these conductivity and permeability measurements were obtained from cm-sized core plugs and it is unclear how well the data can be extrapolated to the entire MB sandstones due to variations in grain size/shape/sorting as well as compacting or clay mineral deposition. Ammann et al. (1993) report the highest permeability values in the centre of each meander belt sandstone with lower values towards the top and base. The same was observed for amalgamated sandstones, where permeabilities were lower at the base of each unit.

Table 2.2: *Average values and standard deviation of whole-rock densities, thermal conductivities and heat capacities determined on water-saturated USM core samples as well as derived from well logs (from Leu et al., 2006).*

	Whole-rock-density ρwr (kg/m3)	**Thermal conductivity λws (W/mK)**	**Heat capacity Cws (J/kg/K)**
(Silty) Mudstones	2492 ± 202 (n = 75)	2.27 ± 0.40 (n = 115)	873 ± 44 (n = 86)
Siltstones	2435 ± 131 (n = 9)	2.68 ± 0.47 (n = 24)	881 ± 21 (n = 19)
Fine-grained sandstones	2447 ± 136 (n = 46)	2.49 ± 0.37 (n = 70)	1002 ± 96 (n = 37)
Medium-grained sandstones	2535 ± 184 (n = 32)	2.67 ± 0.49 (n = 44)	1037 ± 130 (n = 23)
Coarse-grained sandstones and conglomerates	2420 ± 215 (n = 9)	2.74 ± 0.41 (n = 13)	1031 ± 160 (n = 8)

Extrapolations to other MB units are unreliable as shown by the different pore pressures encountered for each sandstone layer in the Burgdorf wells (Ammann et al., 1993). Thus, in order to determine the hydraulic properties of the entire sequence, individual units should be tested separately. In addition, it has been shown that single MB layers have higher permeabilities than amalgamated units which often contain several thin horizons with low permeabilities. While the CS sandstones show similar hydraulic conductivities (10^{-6} and 10^{-8} m/s) and thus likely act as secondary aquifers or link between MB sandstones. The other lithotypes show much lower conductivities. The OPS element is especially important in this regard, because it occurs as laterally extensive deposits with low hydraulic conductivities (10^{-8} to 10^{-11} m/s), thereby limiting the permeability of the entire USM sequence in the vertical direction.

Besides petrophysical properties, the geothermal properties (e.g. whole-rock density, thermal conductivity and thermal capacity) of the USM have been studied (Leu et al., 2006). These properties were derived from both direct measurements as well as evaluation of gamma, sonic and density well logs. As these values are crucial for heat storage in the USM, they are briefly summarised in Table 2.2. Unfortunately, the samples were distinguished based on their lithology rather than the lithotypes they represent. However, the lithologies can be attributed to the different lithotypes based on grain size: (silty) mudstones = OPS ± LS, siltstones = LS ± CS, fine-grained sandstones = CS, medium-grained sandstones = MB, coarse-grained sandstones/conglomerates = alluvial fan deposits ± MB. Overall, the properties are identical (within the standard deviation) for all lithologies, but for the thermal conductivity and heat capacity a trend towards slightly higher values can be observed with increasing grain size. In addition, density and thermal conductivity show a slight increase with increasing depth as well as towards the Alpine front, both of which can be attributed to decreasing porosities of the rocks due to stronger compaction. The heat capacity shows the opposite trend as it increases with increasing water-saturated porosities.

2.2.4.2 Characterisation of palaeo-channels and their distribution

Based on grain size, sedimentary structures and the geometries of the MBs (see above), the original river channels were of coarse-grained, mixed-load channel type with high bed-load proportions. The sedimentary structures indicate that the deposition primarily took place during lateral channel migration, resulting in the observed laterally extensive tabular sandstone bodies. Thus, during the lifetime of the parent rivers, the channels were highly mobile, i.e. with frequent lateral displacement, which is in line with the flat and wide alluvial plain present during the Aquitanian (Platt and Keller, 1992; Galloway and Hobday, 2012). The abundance of amalgamated sequences hints at more stable channel positions, which can be attributed to their position within the axial channel system or structural control of channel positions at a local level (Figure 2.8). The distance of the axial channel system from the Alpine front was likely variable throughout the deposition of the USM sequence and shifted from more proximal to more distal areas as a function of Alpine uplift and subsidence in the SMB as well as climatic factors (Schlunegger et al., 1997). However, the exact position of the axial channel at any given time is unknown as, until now, no basin-wide facies reconstruction of the USM has been attempted.

Individual MBs are 2 – 8 m thick. This largely corresponds to the depth of the palaeochannel according to Lorenz et al. (1985). For amalgamated sequences, Fielding and Crane

(1987) assumed that the depth of the palaeo-channel can be approximated as 0.55 times the thickness of amalgamated sequence. Based on the data compiled by Keller et al. (1990), the average depth of USM palaeo-channels was 4 ± 1.6 m. The calculated depth values can then be used to estimate the width of the channel belt (Collinson, 1978, Fielding and Crane, 1987), which corresponds to the maximum lateral extension of the tabular sandstone bodies. These calculations indicate that the channel belts were possibly up to 1.6 km wide. Unfortunately, the generally small size of the USM outcrops (tens of meters) in the SMB does not allow confirmation of these estimates. The extent of the MBs in the third dimension (i.e. along the flow direction) is unknown but assumed to be many kilometres, as these rivers crossed the entire SMB which was over 35 km wide at this point (Figure 2.3; Schlunegger et al., 1997).

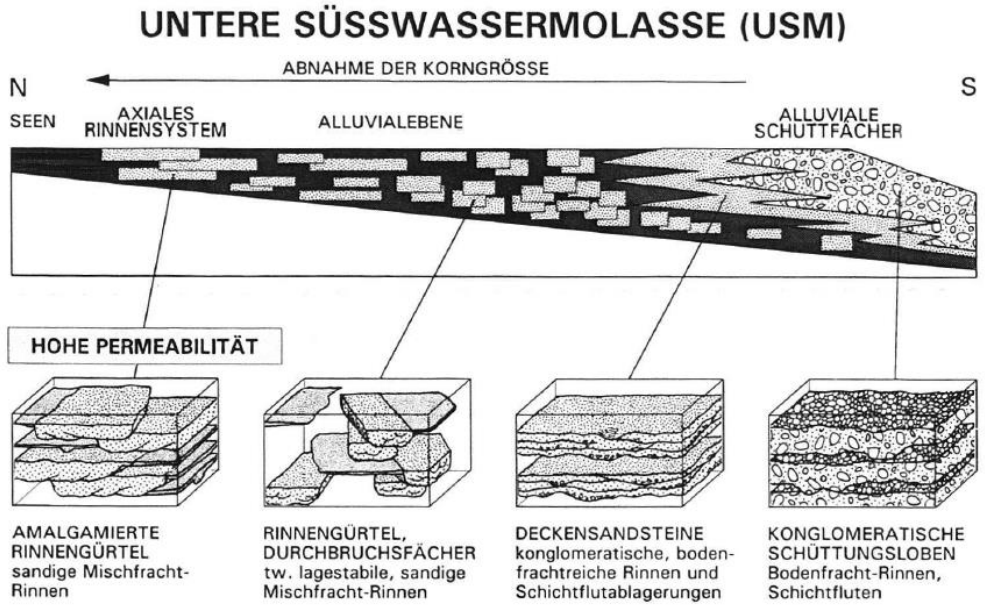

Figure 2.8: *Schematic north-south cross-section through the Swiss Molasse Basin showing the predicted distribution of single and amalgamated MBs in the distal part of the Aquitanian USM (black: lithotypes with low permeabilities, i.e. OPS and LS). In the more proximal, southern areas, the higher proportion of sandstones and coarser grained sediments (i.e. conglomerates) is due to deposition by high-energy, braided rivers instead of meandering rivers (from Keller, 1992).*

Besides their dimensions, the distribution of the MBs across the Swiss Molasse Basin is also not well constrained. Most of the work done in the 1990s has focused on distinguishing the different architectural elements as well as determining their geometries and chemical and petrophysical properties. Therefore, a relatively small number of boreholes and outcrops were studied in great detail and no basin-wide facies reconstruction of the Aquitanian USM was attempted. Such a reconstruction is highly challenging as the internal structure of the USM is

sub-seismic and is thus only revealed in outcrops and borehole profiles. The architectural elements revealed in outcrops depend on how the outcrops formed: in natural outcrops, erosion-resistant sandstones (= MB) dominate while in artificial outcrops, which are often created during quarrying for raw materials for the brick industry, fine-grained OPS deposits dominate (Section 2.2.3). Even without any MB sandstones present, information on the proximity to MB-rich sequences can be obtained from the presence and characteristics of other architectural elements:

(1) In sequences rich in MB deposits, other lithotypes deposited in close proximity to the main channels (e.g. LS and CS) are also more abundant while a decrease in grain size (i.e. increase in proportion of OPS) can be observed with increasing distance away from the channels.
(2) The maturity of palaeosols within the OPS increases with increasing distance away from the main channel (discussed in more detail by Platt and Keller, 1992). Thus, sequences containing thin and immature palaeosols are more likely to be close to MB-rich sequences.

However, in the central part of the SMB, outcrops are generally small in size, providing no more than a glimpse into the 3D structure of the USM, both laterally and, especially, vertically. Boreholes on the other hand provide a much better insight into the vertical structure of the USM. The number of boreholes with publicly available profiles are increasing every year as the Canton of Bern mandates that well profiles be collected for all wells drilled for geotechnical and energy purposes. However, these boreholes are typically drilled using destructive methods, limiting the spatial resolution of the obtained profile based on cuttings to 2 m. Nevertheless, this collection of borehole profiles represents a valuable resource to help identify zones within the USM where MBs are or are not abundant (Section 3.5.1).

2.2.5 Hydrogeology and hydrochemistry

Unless stated otherwise, the information presented in this section is derived from Küpfer (2005) who presented the latest compilation on the hydrogeology of the SMB. The hydrochemistry is summarised based on the compilations by Schmassmann et al. (1984) and Traber et al. (2014).

In order to understand the hydrogeology of the Aquitanian USM in the SMB, the hydrogeology of the entire Molasse sequence as well as the Malm aquifer in the footwall and the unconsolidated Quaternary deposits in the hanging wall has to be understood. Therefore, the hydrogeology of these six units will be summarised briefly:

(1) Quaternary: Unconsolidated aquifers with great importance as drinking water and water for agricultural and industrial use; very heterogeneous with respect to geometries (i.e. thickness), composition and hydrogeological properties.
(2) Upper Freshwater Molasse (OSM): Heterogeneous and anisotropic permeabilities due to different facies; largely limiting regional flow, especially in the vertical direction.
(3) Upper Marine Molasse (OMM): Relatively permeable and homogeneous lithology of regional extent. Only used as an aquifer locally.
(4) Lower Freshwater Molasse (USM): Heterogeneous and anisotropic permeabilities due to different lithotype and their heterogeneous distribution; MB relatively permeable and potentially allowing local to regional groundwater flow. The CS units likely act as secondary aquifers. LS and OPS act as aquitards and strongly limit regional flow, especially in the vertical direction across the USM.
(5) Lower Marine Molasse (UMM): Primarily limiting groundwater flow but individual units have aquifer properties.
(6) Upper Malm: Karstified and fractured limestone important as regional aquifer and used for example for geothermal production.

Depending on the location within the SMB, one or several of the Molasse units have been eroded during late Miocene uplift of the SMB (the further west, the more the Molasse sequence has been eroded). In addition, the Quaternary glaciations have carved a strong topography into the exposed Molasse bedrock (Figure 2.5) and draped it with significant moraine deposits. Thus, the often highly permeable and unconsolidated Quaternary sediments are in direct contact with relatively permeable units in the OMM as well as the MB of the USM, leading to mixing of shallow groundwater with older formation waters.

The above infiltration has led to a distinct hydrochemical stratification of groundwater types across the SMB (Figure 2.10). At the shallowest levels (tens of meters), the formation water can be characterised as Ca-(Mg)-HCO_3-type infiltrated during modern times (^3H-bearing, 340 – 770 mg/L TDS). At greater depths (several tens up to several hundreds of meters) a Na-HCO_3 water (320 – 1,540 g/L TDS) is present, which infiltrated during colder climates in the Pleistocene. At even greater depths, older Na-Cl, Na-Cl-HCO_3 or Na-Cl-SO_4 waters (2,300 – 30,000 mg/L TDS) can be found. These latter deep, saline formation waters are of great interest as their salinity is not derived from mineral reactions but suggests the downflux of marine formation waters from the OMM into the underlying USM. This process likely took place due to compactional dewatering during subsidence around 15 Ma ago, as the marine OMM signature can also be observed in the calcite cements (Mátyás, 1998). Today this trend has been

reversed and current pressure differences point to an upward flow trend across the SMB. Together, these findings suggest that, at least during certain periods since the deposition of the Molasse sequence, formation waters have been moving across the SMB, both laterally and vertically, irrespective of lithological boundaries. These findings support a high degree of interconnectedness of MBs across the otherwise relatively impermeable USM. Vertical flow paths can also be created along major fractures which link the different lithological units of the SMB. However, not many such fractures are known in the SMB, suggesting that the interconnections between MBs is a more likely control on regional groundwater movements. The old ages of the Na-Cl-type waters (> 100,000 to several million years) indicate that these groundwater movements take place over long geological periods and are not relevant at short timescales. The geochemical data suggest substantial groundwater movements in the shallow parts of the USM, at least over geological times, but no measurements of flow rates and/or directions are available for formation waters anywhere within the USM.

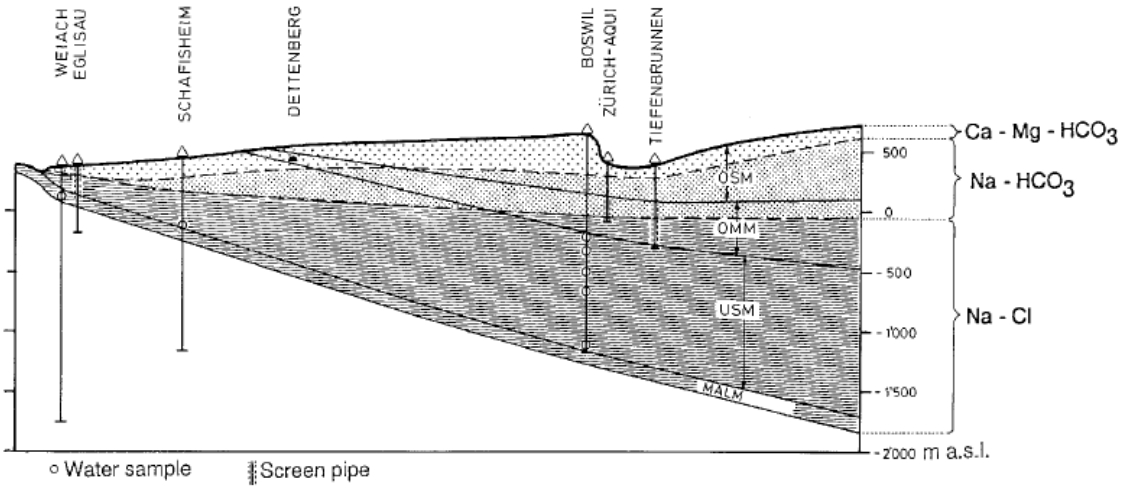

Figure 2.9: *Schematic representation of the different formation water types across the SMB, discordantly crosscutting the individual Molasse units (Nagra, 1988).*

Data on dissolved organic carbon from USM groundwaters are relatively rare. Schmassmann (1990) reports values of 0.5 to 2.2 mg/L DOC from four USM springs in Kanton Solothurn, Aargau and Basel-Landschaft. Similar values were reported from USM groundwater samples taken in the Eglisau and Schafisheim wells (0.4 to 2.0 mg/L, n = 5). Groundwater analyses from the other Molasse units (OSM, OMM, UMM) as well as the underlying Mesozoic units (Malm, Dogger) also show the same ranges of DOC concentrations (0.21 to 2.2 mg/L, n=14). Most samples show values of less than 1.2 mg/L. The elevated values can be associated with the presence of coal (OSM sample Schwarzenberg) or methane (Weiach and Schafisheim),

or with contamination by drilling fluid or microbial activity (Attisholz). Similar values of up to 1.2 mg/L were also found for shallow groundwaters of different lithologies across the USA (Leenheer et al., 1974), suggesting that low concentrations of DOC in shallow groundwaters are common not only across the SMB. Yellow UV-induced fluorescence in carbonate cements in OMM samples indicates the presence of organic matter during cementation (Mátyás, 1998). This suggests that DOC is not only common across shallow groundwaters today but that has been so over geological times, including during the cementation of the USM sandstones.

The temperatures of the formation waters in the USM are largely unknown. According to the GeoMol15 Temperature Model (Allenbach et al., 2017) for the region of Bern, the 60 °C isotherm is at a depth of -720 m a.s.l. below Forsthaus. Based on the elevation of the Forsthaus site (500 m a.s.l.) and the average surface temperature of 15 °C, a geothermal gradient of 36.9 °C/km can be calculated. As the thickness and depth of the flat-lying Molasse deposits increase towards the Alpine front (up to 3 km thick and 3.8 km deep), formation temperatures increase as well, with temperatures of up to 80 °C in the 2.4 km deep Aquitanian of the abandoned geothermal well St. Gallen GT-1 (pers. comm. Th. Bloch).

2.3 Implications for the *Geospeicher Forsthaus*

By combining the problems encountered in previous HT-ATES systems with the geological and hydrogeological information about the USM, we can assess, which problems are most likely to be encountered during commissioning and operation of the *Geospeicher Forsthaus*:

- Mineral reactions:
  - Based on the average composition of MB (quartz > feldspars > clay minerals > carbonate minerals), the expected mineral reactions during storage are comparable to what was observed at the HT-ATES site of the University of Minnesota. The exact reactions will depend on the exact mineral composition of the reservoir, the *in-situ* fluid composition, the injection temperature and duration of the storage period.
  - Pyrite is present in some MB's and its dissolution (especially if oxygen penetrated the aquifer) could potentially release heavy metals. However, both the pyrite content and the heavy metal concentration within the pyrite are unknown.
  - Due to the substantial concentration of carbonates (calcite >> dolomite) in MBs (~10 vol.%) the formation water will be saturated with respect to calcite, which will lead to carbonate scaling in the heat exchanger. Ions which could inhibit precipitation slightly (e.g. Mg and SO_4) are present. The concentrations of strong

inhibitors (organic acids, phosphates) are unknown but likely low due to the distance to the surface and any soils.

- Precipitation of pure amorphous silica is not expected. However, Al and Fe could be released during feldspar/clay mineral dissolution and pyrite oxidation, respectively, potentially leading to precipitation of impure amorphous silica.
- Precipitation of metal oxyhydroxides and sulphides is likely if microbial activity is high or if, periodically, oxygen enters the aquifer.
- Clay minerals are abundant in MB (but also the finer grained LS and OPS lithotype) and dominated by the smectite group. Swelling of clays when in contact with less saline fluids or fluids with higher Na concentrations than the *in-situ* formation water is possible but relatively easy to mitigate.
- Clogging due to transport of formation fines and loosened sand grains is likely due to the likely small pore size of the MBs. Clogging due to gas bubbles is unlikely if adequate pressure management is ensured.

- Microbial activity (and associated MIC) is likely but might be restricted to the cold wells due to the high injection temperature planned. During storage periods (equivalent conditions to shutdown periods), microbial activity is expected to increase, especially if oxygen is entering the upper wellbore.
- Chemical and electrochemical corrosion are likely minimal, unless a more saline groundwater than expected is encountered at reservoir depth. MIC is likely.
- Hydrogeological issues
  - Regional flow is probably limited due to the relatively low permeability and limited lateral extent of the MBs as well as the surrounding, low permeability LS and OPS lithotype. However, the unknown degree of vertical and lateral interconnection as well as the *in-situ* pressure distribution introduces a high degree of uncertainty.
  - The development of preferential flow paths, e.g. along a single, more permeable MB across the storage volume is likely due to the high degree of heterogeneity within the USM and the intercalation of sandy and clay-rich units.
  - Buoyancy flow/thermal stratification is not expected in individual MBs due to the relatively low permeability and limited thickness of the sandstone layers. Even for amalgamated sequences, the likelihood of buoyancy flow is relatively low due to the expected heterogeneous permeability distribution caused by differences in grain size, cementation and/or clay content.
- Hydrofracturing is unlikely if adequate pressure management is employed. Surface uplift due to thermal expansion could play a role due to the abundance of clay-rich,

water-saturated formations (LS and OPS). However, the planned reservoir depth of 500 m may reduce the observable effect at the surface.

However, there is a wide range of open questions that cannot be answered based on the knowledge gained from compiling previously published literature alone. Most of these problems are associated with the lack of knowledge about the site-specific *in-situ* conditions. The geological and hydrogeological data available for the USM is based on detailed studies of a few outcrops and wells distributed across the entire central and eastern SMB and it is unclear how representative these sites are with respect to the entire USM sequence in general and the Forsthaus site specifically. The issue is complicated further by the high degree of heterogeneity within the USM. Nevertheless, a couple of general statements can be made with respect to the expected geological conditions at the Forsthaus site:

- The USM was deposited by dynamic fluviatile systems where changes in channel position were very common. This has resulted in a highly heterogeneous unit, consisting of different lithotypes with different properties. The spatial distribution of these lithotypes is unknown. However, at the regional scale their distribution is relatively homogeneous (Figure 2.8) making large areas devoid of MBs unlikely.
- The mineralogical composition of the MB sandstones presented in Section 2.2.4.1 is expected to be an accurate representation of the sandstones which will be encountered at reservoir depth as USM and OMM sandstones from across the SMB show very similar compositions (Figure 2.7). This indicates that the composition of the sediment was relatively constant over a large area and over several Million years.

  Compaction and cementation during burial potentially resulted in vertical gradients with respect to porosities and permeabilities (decreasing with increasing depth) as well as friability (deeper = more cement = less friable). These gradients are likely exacerbated by dissolution of calcite cement close to the surface during modern times. As most properties of the MB reported in Section 2.4 are based on samples from surface outcrops or shallow wells, the extent of these vertical gradients cannot currently be assessed and the literature values can therefore not be extrapolated to the planned reservoir depth. These issues are discussed in more detail in Section 3.6.

3 Investigations of new drill core and groundwater samples from the USM

As described in Chapter 2, little published information is available on the properties of the target sandstones in the area of Bern City. As a means of filling this gap for the *Geospeicher Forsthaus* project, drill core samples were obtained from a new (2017) borehole that was drilled by Regionalverkehr Bern-Solothurn RBS, approximately 2 km to the southeast of the planned HT-ATES (well P7, Figure 3.1). Analyses of groundwaters from six nearby wells (GW1-GW6; Figure 3.1) were also obtained. These samples constitute the closest first-hand indications on the geology and hydrogeology of the USM to the planned HT-ATES site. Accordingly, detailed evaluations were carried out for this report, as summarised in the following. In addition, the drill core material form borehole P7 was used to conduct a range of laboratory experiments to assess possible mineral reactions (Chapter 4).

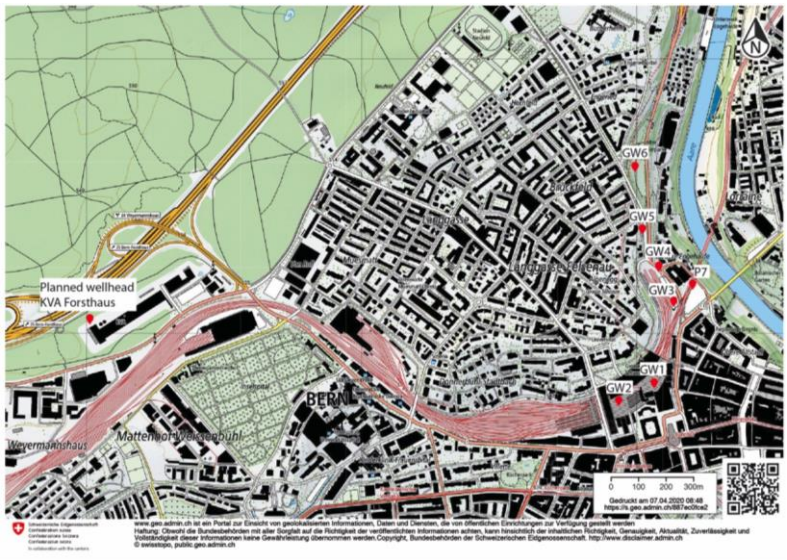

Figure 3.1: *Map showing the locations of the boreholes, from which USM drill core samples were obtained (P7) and for which USM groundwater analyses are available (GW1-GW6). Also shown is the location of the* Geospeicher Forsthaus *around 2 km further to the west.*

In addition, the distribution of meander belt sandstones in the area of Forsthaus/Inselspital/Länggasse were assessed. In order to do this, the geological profiles of 10 wells that penetrate 5 m or more into the USM were compiled from the online *Geoportal* of the Canton of Bern.

3.1 Materials

3.1.1 Drill core samples

Drill core samples from MBs were obtained from the 35 m deep P7 borehole. The well was drilled in January 2017 into the subsurface below the Schützenmatte car park, located to the NNE of the main railway station of Bern (Figure 3.1). All experiments and analyses were conducted on samples taken from the coarse-grained sandstone unit making up the bottom 5 m of the retrieved core (30 – 35 m depth; Figure 3.2). The unit was described as follows by the on-site drill core loggers:

- *29.40 – 32.95 m:* Sandstone, coarse-grained; moderately to weakly cemented; grey to beige, slightly rusty at 32.40 m; joints (90° to well axis) at 29.60 – 29.80 m
- *32.95 – 33.20 m:* Marl, sandy, finely laminated at the mm-scale, weakly cohesive; varicoloured, primarily red
- *33.20 – 33.95 m:* Sandstone, coarse-grained; moderately cemented; grey beige; joints (parallel to well axis) at 33.18 – 33.40 m
- *33.95 – 35.00 m:* Sandstone, very coarse-grained; moderately to weakly cemented, partly crumbly; massive; grey to grey beige; coarse bedding at the dm-scale

The exposure of the samples to air during sampling and storage was minimised by hermetically sealing the cores in bags made up of several layers of PVC and plastic coated Al-foil and storing them at 5 °C until preparation for the analytical work or the experiments. This was important in order to minimise oxidation of sulphide minerals (e.g. pyrite) potentially present as well as evaporation of the *in-situ* pore water, which can potentially cause precipitation of minerals in the pore space.

The analyses and experiments were performed on samples from the very bottom of the drill core (= sample A, Ø ≈ 9.5 cm, length ≈ 40 cm). The chosen sandstone unit is situated at an altitude of around 500 m a.s.l. For comparison, the target depth of the *Geospeicher Forsthaus* is much deeper, at approximately 50 m a.s.l. (Section 1.3). In a first step, a 25 cm piece was cut off to be used for the core experiments (Section 4.2.2). Two blocks (4.5 x 2.5 x 1 cm) for the preparation of petrographic thin sections were cut from the remaining material (Section 3.2.1).

To obtain rock fragments for conducting the batch experiments, (Section 4.2.3), additional core material was broken into cm-sized fragments using a hammer. Half of the fragments were ground to a fine powder in a tungsten carbide disk mill. The other half was separated into the individual sand grains using SelFrag.

SelFrag is a high-voltage disintegration method (SelFrag AG, Kerzers, Switzerland), which allows rock fragments to be disintegrated along grain boundaries (i.e. without damaging the grains) by passing a short-pulsed electrical discharge through the sample immersed in deionised water (Gnos et al., 2006). For the P7 sample, two sets of ten pulses at 140 kV and a frequency of 3 Hz, were employed. As a result, the sample was completely disintegrated into its component sand grains without fracturing individual grains. The deionised water was evaporated over night at 40 °C. The dried sample was then transferred to a plastic container without further washing to avoid losing any fine grains (i.e. the clay fraction) and stored until used in the experiments. For the analysis of porosity and permeability (Sections 3.2.4 and 3.2.5), a plug (Ø = 2.52 cm, length = 5.11 cm) was cut from sample A.

A third core from the same section (= sample B, Ø ≈ 9.5 cm, length ≈ 30 cm) was sent to Wintershall Dea GmbH in Germany, where the following parameters were measured: a) mineral phase composition, b) porosity and permeability, c) compressive strength and d) grain size distribution. These analyses will not be discussed in depth in the present report. However, the results will be compared to the results from sample A.

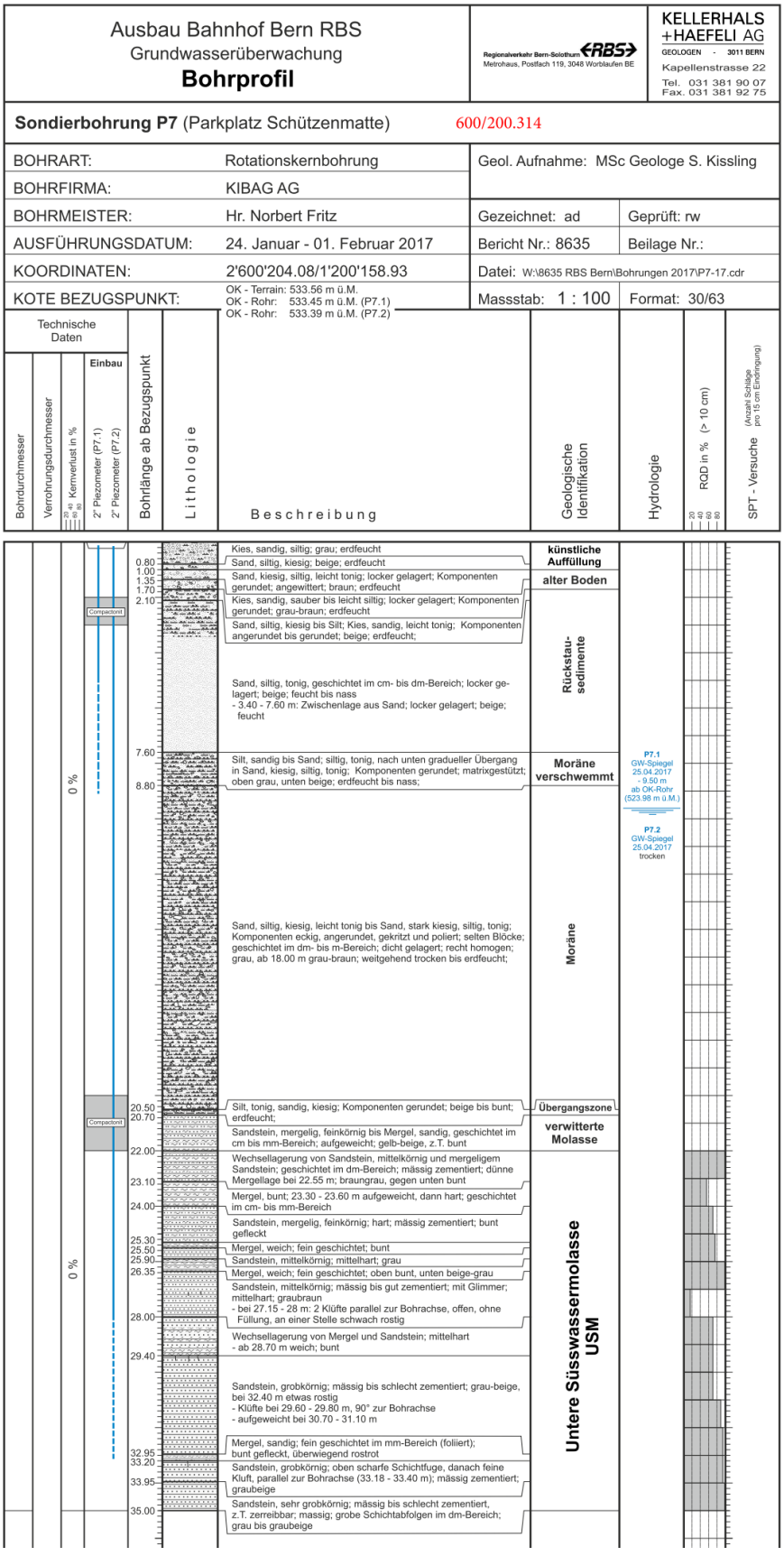

Figure 3.2: *Geological log of borehole P7 from the Geoportal of the Canton of Bern. The samples investigated were taken from the coarse-grained sandstone unit at 30 to 35 m depth.*

3.1.2 Analyses of USM formation waters

Knowledge on the chemical composition of the USM groundwater in the Bern area is mainly based on a groundwater survey carried out by a local consulting company at the planning stage of the new RBS railway station in Bern in 2016. Groundwaters from six wells drilled by rotary core drilling in 2008 and 2011 were sampled (Figure 3.1, Table 3.1). Access to drill core samples was not possible. However, the geological profiles are available online on the *Geoportal* of the Canton of Bern. For each well drilled in 2011, a packer was installed at the top of the bedrock, hydrologically separating the Quaternary from the USM. It is assumed that the same was done for the wells drilled in 2008 but no details are available.

Details of the groundwater sampling and analytical methods are unknown. However, the survey was carried out by an experienced consulting company and analysed at an accredited analytical laboratory. Therefore, the data are expected to accurately and reliably represent the USM groundwater composition in the six wells studied.

Table 3.1: *Details of the six wells from which USM groundwaters were sampled and analysed. For the location of the wells, see Figure 3.1. GW3 (highlighted) is considered to be the most representative groundwater sample for the USM (Section 5.4).*

		GW1	GW2	GW3	GW4	GW5	GW6
Drilling date		04/2008	04/2008	09/2011	09/2011	10/2011	09/2011
GW sampling date		06/2016	06/2016	06/2016	06/2016	06/2016	06/2016
Top well	m a.s.l.	532.9	533.0	539.5	539.6	544.1	540.3
Length well	m	25.0	25.2	30.3	30.5	40.4	40.4
Top bedrock	m a.s.l.	532.9	533.0	524.9	523.2	536.2	535.8
GW table1	m a.s.l.	514.9	522.4	521.2	519.0	513.7	510.8

[1]Equals the depth at which the groundwater samples were taken.

Discrete groundwater inflow points were not identified in any of the wells. However, it is unlikely that the water originated from all the layers penetrated, as there is a huge variability in the permeabilities of the different lithotypes of the USM (Section 2.2.4.1). It can thus be assumed that the groundwater sampled was dominated by water originating from the more permeable fine- to very coarse-grained sandstones corresponding to the MB and CS lithotypes. For each well the sandstone intervals with thicknesses over 0.5 m were noted (Table 3.2). A cut-off of 0.5 m was chosen as Keller et al. (1990) showed that CS lithotypes generally range from 0.5 to 2 m in thickness while MB range from 2 – 8 m (or more, if amalgamated). In addition, thinner units are unlikely to substantially contribute to the overall groundwater inflow.

Some of the sandstone intervals listed in Table 3.2 are cut by one or several marly or silty layers (< 0.5 m). These layers were ignored for this compilation and not used to further subdivide the sandstone units as their effect on lateral groundwater flow is assumed to be very limited. Based on the thickness and the grain size, the sandstones were interpreted as CS, MB or a mixture of the two (MB/CS).

Table 3.2: *Sandstone units more than 0.5 m thick and their position, thickness and grain size as indicated in the lithological well logs available from the online* Geoportal *of the Canton of Bern. GW3 is highlighted as the most representative groundwater sample (Section 3.4).*

	Sst > 0.5 m thick[1] (%)	**Top layer (m a.s.l.)**	**Bottom layer (m a.s.l.)**	**Thick-ness[1] (m)**	**Grain size[2]**	**Litho-type[3]**
GW1	79.8	531.35	511.40	19.95 (3)	mg – vcg	MB
GW2	60.7	531.00	528.20	2.8 (0)	fg	CS
		527.20	526.70	0.5 (0)	fg – mg	CS
		526.25	521.75	4.5 (0)	mg – cg	MB
		517.2	509.7	7.5 (1)	mg – cg	MB
GW3	25.5	522.88	521.03	1.85 (0)	mg	CS
		517.38	515.23	2.15 (0)	mg	CS
GW4	74.5	523.21	513.21	10 (3)	fg – vcg	MB/CS
		510.06	509.56	0.5 (0)	mg	CS
GW5	81.4	534.91	528.36	6.55 (1)	mg – cg	MB
		527.41	526.76	0.65 (0)	mg	CS
		524.01	508.41	15.6 (3)	fg – cg	MB/CS
		507.31	503.66	3.65 (0)	fg – cg	MB/CS
GW6	48.8	531.29	527.74	3.55 (0)	mg	MB
		525.49	521.44	4.05 (2)	fg – cg	MB/CS
		519.61	515.19	4.42 (2)	fg – cg	MB/CS
		509.79	508.33	1.46 (1)	mg – cg	CS
		507.69	505.99	1.7 (1)	fg – mg	CS
		503.69	501.34	2.35 (0)	fg – cg	MB

[1]Proportion based on length of USM penetrated and not the entire length of the well.

[2]Number in brackets indicates the number of marly to silty units < 0.5 m within each sandstone layer.

[3]fg: fine-grained, mg: medium-grained, cg: coarse-grained, vcg: very coarse-grained

[4]Interpretation of lithotypes as in Figure 2.6 based on thickness (0.5 – 2 m → CS, > 2 m → MB) and grain size (fine- to medium-grained → CS, medium- to very coarse-grained → MB). Some units likely represent MB with interlayered CS units (MB/CS).

3.2 Methods

3.2.1 Petrography

A cm-sized blocks cut from sample A was used to prepare a polished, uncovered thin section (~ 25 μm thick). Upon completion, half of the thin section was dyed using the following solutions:

- Solution A: 1 g potassium hexacyanidoferrat III is dissolved in 100 mL of 1 vol.% HCl
- Solution B: 0.1 g Alizarin dissolved in 100 mL of 1 vol.% HCl

Solutions A and B were then mixed with a ratio of 2:3 to produce solution C. The thin sections were dipped into solution 2 for one minute, followed by dipping into solution 3 for 10 seconds and rinsing with ultra-pure water. The dyed samples were then air-dried. This process stains the different carbonate minerals depending on their crystal structure and their Fe-content: calcite → red, Fe-calcite → purple, dolomite → colourless, Fe-dolomite (ankerite) → blue green (Dickson, 1966). Thereafter, the different carbonate minerals can be distinguished using a petrographic microscope.

Petrographic observations were made by transmitted light microscopy (Olympus BX51 polarizing microscope) equipped with an Olympus UC90 digital camera (software Stream Essential).

3.2.2 Mineralogical composition

Both the main minerals and clay mineral fraction were identified and quantified using X-ray diffraction (XRD). For quantifying the main mineralogy (quartz, plagioclase, K-feldspar, calcite, dolomite), the previously prepared powder was mixed with 20 wt.% corundum powder (internal standard) in a McCrone XRD mill. Two aliquots (a and b) were prepared. Both were analysed using a PANalytical CubiX3 diffractometer (CuKα1; 5-60° 2θ; 0.02°/step) and quantification was done by Rietveld refinement using the PANalytical software *High-Score Plus*.

For the quantification of the clay mineralogy (illite/biotite/muscovite, smectites, kaolinite, chlorite), the rock powder was dispersed in water using an ultrasonic bath. Subsequently, the clay minerals were separated using an Atterberg-cylinder. The thus obtained fines (< 2 μm) were used to prepare three different oriented aliquots: one by air-drying, one by ethylene glycol saturation and one by firing at 550 °C. All aliquots were analysed using a Philips PW3710 diffractometer (CuKα1; 2-40° 2θ; 0.02°/step). The relative concentrations of the clay minerals were quantified based on the relative intensity method (Poppe et al., 2001). Quantification by XRD is accurate to about ± 5 wt.%.

3.2.3 Chemical composition

The main and trace elements in the sample were determined by X-ray fluorescence (XRF) and total elemental carbon, nitrogen and sulphur (TC, TN and TS, respectively) were determined using a CNS-Analyser. For both analyses, aliquots of the previously prepared powdered sample was used (Section 3.1.1). In addition, the composition of the carbonate minerals was analysed by electron microprobe analysis (EMPA) on the same thin section as that used for petrography (Section 3.2.1).

Approximately 1.5 g of rock powder was used for XRF analysis. In a first step, weight loss on ignition (LOI) was determined by heating the milled rock powder for exactly 2 h at 1050 °C. The cooled samples were then mixed with Fluxana FX-X65-2 (Lithium Tetraborate : Lithium Metaborate 66:34; sample to flux ratio of 1:5). The homogenised mixture was fused in an PANalytical Eagon 2 oven at 1080 °C and the resulting glass beads were analysed on a PANalytical™ Axios wavelength-dispersive X-ray fluorescence (XRF) instrument with a rhodium source tube at voltages of 20–60 kV and beam currents of 40–100 mA at the ETH Zürich. Data processing was done using the SuperQ software package.

For CNS analyses, a 30 mg aliquot of fine rock powder was weighed into a small tin capsule. The sample was then combusted inside the combustion tube (filled with WO_2 and Cu shavings) at ~ 1320 °C with the addition of O_2 inside the elemental analyser (Thermo Fisher Elemental Analyzer FlashSmart NCS). The produced CO_2, NO_2 and SO_2 are passed through a water separation tube filled with Mg-perchlorate and are transported to the thermal conductivity detector using helium as a carrier gas, where TC, TN and TS are measured. Detection limits are 0.02 wt.% for TC, 0.01 wt.% for TN and 0.02 wt.% for TS. In order to also determine the contents of total inorganic carbon TIC and total organic carbon TOC of the sample, additional aliquots are weighed in. These aliquots are placed in silver capsules, 1 M HCl is added and left to react at 50 °C for 15 h. This completely removes inorganic carbon from the sample. The leached aliquot is then dried and analysed using the same approach as described above, yielding the TOC content of the material. TIC can then be calculated by subtracting TOC from TC determined in the previous step.

For EMPA, the previously prepared polished thin section was coated with 18 nm of carbon. Carbonate mineral compositions were then measured on a JEOL JXA-8200 electron-microprobe (EMPA) using a 15 kV, 10 nA focused beam. The elements Na, Mg, Ca, K, S, Mn and Fe were measured on wavelength-dispersive spectrometers (WDS) and were calibrated against different internal standards: albite (Na), dolomite (Mg), calcite (Ca), orthoclase (K), clinopyroxene (S), pyrolusite (Mn) and magnetite (Fe).

3.2.4 Porosity

Porosity was determined on plugs drilled from sample A. The porosity was calculated as follows:

$$\phi = \frac{V_{pore}}{V_{bulk}} = \frac{V_{bulk} - V_{matrix}}{V_{bulk}} \qquad (3.1)$$

with ϕ the porosity, V_{pore} the total pore volume, V_{bulk} the bulk volume of the sample and V_{matrix} the total volume of the solid fraction of the sample. The bulk volume was calculated from the dimensions of the core plugs as measured with a calliper (± 0.02 mm). Measurements of V_{matrix} were performed using a Micromeritics™ AccuPyc II 1340 helium gas displacement pycnometer (± 0.1 vol.%).

3.2.5 Permeability

Permeability measurements were performed on the same plugs used for the porosity determination at CoreLab Ltd in Aberdeen, Scotland using a CMS™-300 Core Measurement System. This is an automated, unsteady-state pressure decay permeameter that measures permeability at variable confining pressures (Klinkenberg corrected). For our samples, the analyses were performed at 800 psi (~ 55 bar) which corresponds to the expected confining pressure in the reservoir (z = 500 m) of around 55.5 bar, calculated from

$$P_{conf} = P_{lith} - P_{pore} = [(\rho_{sst} * g * z) - (\rho_{water} * g * z)] * 10^{-5} \qquad (3.2)$$

where P is pressure in bar, ρ_{sst} is the density of the MB sandstone (2130 kg/m^3; Keller et al., 1990), ρ_{water} is the density of water (1000 kg/m^3), g is the gravitational acceleration (9.8 m/s^2) and z is depth (m).

3.3 Characterisation of drill core samples

3.3.1 Petrography

The MB cores investigated consist of massive, coarse to very coarse grained grey-beige sandstones. They are weakly cemented, relatively friable and highly porous. Several zones (visible

as slightly lighter areas in Figure 3.3, left) are enriched in lighter coloured, finer grained components. However, it is unclear if this is a surficial feature, possible related to drilling or if it is a primary sedimentary feature. Similar zones with fine-grained components but more abundant and interspersed with coarse sandstone zones at the cm-scale, were observed on the drill core analysed by Wintershall Dea GmbH (Figure 3.3, right). The regular sequence of these more fine-grained zones and the coarser sandstone indicates that the texture is more likely related to sedimentological processes rather than the drilling operation.

Figure 3.3: *USM MB sandstone samples from P7 (sample A on the left, sample B on the right) used for the characterisation of the lithology. Cores are 9.5 cm wide. Both photographs were taken immediately after removing the samples from the hermetically sealed bags and before the samples were fully dry. Therefore, the surface appears relatively dark, especially for sample B.*

Under the microscope, the following components can be distinguished (Figure 3.4):

(1) Detrital components (monomineralic): Quartz (Figure 3.4 C) is the dominant monomineralic component (~ 20 vol.%). The grains range from < 200 to 700 µm. Extinction is sometimes undulose and linear fluid inclusion trails are abundant. Monomineralic feldspar grains are also common. Alkali feldspar (~ 10 vol.%) can be easily recognised due to the microcline twinning. In some grains, perthitic exolution was also observed. The grains are around 200 to 400 µm in size. Individual plagioclase grains were very rare and general strongly sericitised and difficult to recognise. Their amount is estimated at below 5 vol.%. The above features points to a mixed magmatic and metamorphic origin of quartz and feldspars. Other accessories include small flakes (40 µm) of chlorite with a dark green pleochroitic colour, idiomorphic flakes of muscovite (up to 300 µm) and biotite (40 µm) with a dark green pleochroism, an

unidentified accessory with a high refractive index and high birefringence (epidote?) as well as a small number of opaque grains (up to 200 μm).

(2) Detrital components (polymineralic): Rock fragments are abundant (~ 40 vol.%) in the thin section studied. They range from 50 to 500 μm in size. The most abundant fragments are polycrystalline quartz fragments (15 vol.%). Most of them are of metamorphic origin based on the irregular and interlocked nature of individual quartz grains (Figure 3.4 D). Some also show stretched metamorphic quartz, indicating ductile deformation (Figure 3.4 E). These fragments often contain sheet silicates (primarily muscovite). The second most abundant types of rock fragments are very fine grained and rich in sheet silicates (Figure 3.4 F). They likely have two different origins: (a) volcanic rocks which were strongly altered during erosion and transport and often contain substantial amounts of fine-grained opaque minerals in addition to the sericite (= fine-grained muscovite) and clay minerals and (b) low-grade metasediments such as slates and shales. Non-metamorphic sedimentary fragments such as limestone (micrite; Figure 3.4 F), dolomite (possibly Figure 3.4 E) and chert were also found as were other metamorphic fragments (serpentinite, gneiss (Figure 3.4 E) and schists).

(3) Porosity is estimated to be around 15 vol.% based on the macroscopic description of the sample. Fluoresce microscopy will help to better evaluate this value as well as differentiate between different types of pores.

(4) Authigenic minerals/cementation: Two types of carbonate cement were encountered (a) pore-filling Fe-calcite cement and (b) uneven, equant-bladed cement growing onto carbonate grains (rare). The pore filling cements show the typical polysynthetic lamellae and 120° cleavage of calcite and stained pink, purple or blue, indicating variable Fe-contents. Most cements show a degree of colour variation within the same pore space, either indicating heterogeneous staining or different stages of cementation (Figure 3.4 G-I). In addition, authigenic clay (smectite, illite or mixed-layer clay) was found. It is spatially limited, heterogeneously distributed and can be described as a fine grained, relatively opaque material with a brown to greenish colour under plane polarised light (Figure 3.4 J). Together, these authigenic minerals make up around 10 vol.% of the sample.

Texturally, the sample can be described as a medium- to coarse-grained and well-sorted sandstone with primarily angular clasts. Based on the composition, the sample is classified as a mature feldspathic litharenite according to McBride (1963).

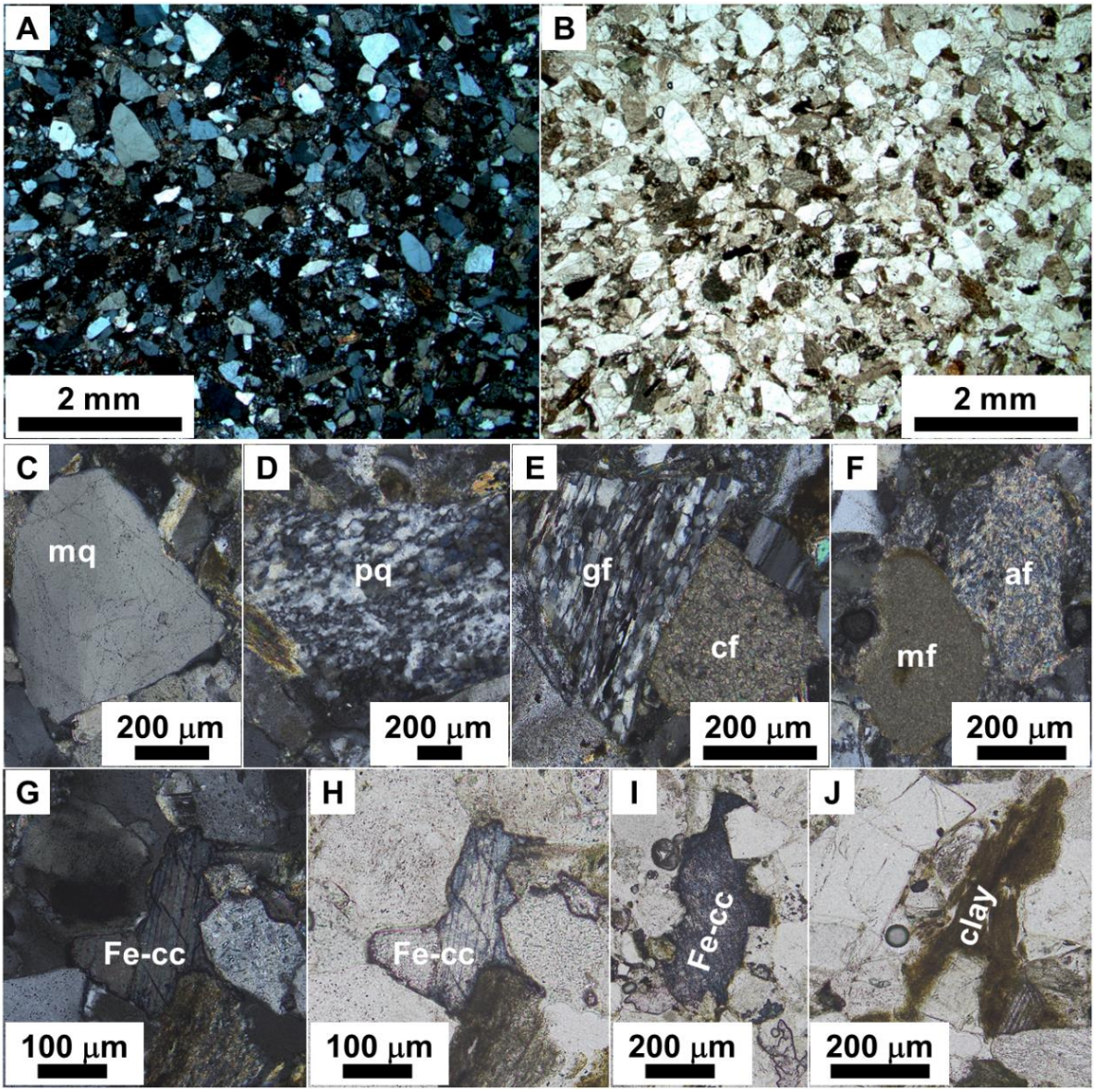

Figure 3.4: *Microphotographs of sample A. Overview of sample in (A) cross-polarised (CPL) and (B) plane-polarised (PL) light and higher resolution images showing (C) a monomineralic quartz grain (mq) with weak wavy extinction (CPL), (D) a polymineralic quartz grain (pq) of metamorphic origin as indicated by the interlocked grain boundaries (CPL), (E) a gneiss fragment (gf) showing elongated quartz and minor sheet silicates next to a coarse-grained carbonate fragment, possibly dolomite (cf; CPL), (F) a fine-grained micritic fragment (mf) next to an altered (possibly former volcanic) fragment (af; CPL), (G & H) pore-filling Fe-calcite cement with a light blue core and a more strongly tinted rim suggesting possibly suggesting several stages of cementation (CPL, PL) , (I) a Fe-cc cement with a higher iron content compared to plate H (PL) and (J) authigenic fibrous clay minerals, possibly illite (PL).*

3.3.2 Mineralogical composition

The mineralogical composition of sample A and B is shown in Table 3.3. The XRD measurements done on the two different core sections are in good agreement (analytical uncertainty: ± 5 wt.%), suggesting a relatively low degree of compositional heterogeneity of USM MBs, at least at the m-scale.

Table 3.3: *Quantitative XRD-analyses (reported as wt.%) performed at the University of Bern and by Wintershall Dea GmbH on drill core samples from P7. For comparison, the median, minimum and maximum composition of MBs from the Langenthal wells, as determined by Keller et al. (1990), are given.*

	Uni Bern (sample A)	**Wintershall (sample B)**	**Median/ Min/Max**
Quartz	41	44	35/14/55
K-feldspar	8	14	11/4/17
Plagioclase	20	19	18/5/25
Calcite	8	7	12/6/18
Dolomite	3	3	2/1/4
Illite/Musc./Biotite	6	9	
Smectites	12	Not analysed	22/2/54
Kaolinite	0	3	
Chlorites	2	1	

Due to the importance of swellable clays (i.e. smectites) in the operation of HT-ATES (Section 2.1.1.4), the measurements done at the University of Bern provide valuable additional information compared to the Wintershall-analyses. Unfortunately, the differentiation between individual sheet silicates (e.g. illite vs. muscovite vs. biotite or montmorillonite vs. saponite) or their chemical composition (e.g. Ca- vs. Na-rich varieties) is not possible with the applied XRD approach. However, thin section petrography combined with data from literature allow for the following conclusions: Muscovite is the dominant sheet silicate as it occurs in lithic clasts, either as a primary mineral (e.g. Figure 3.4 E) or alteration product of feldspars (e.g. Figure 3.4 F). In addition, a small number of detrital muscovite flakes were found. Biotite is less abundant, found only as a primary mineral in magmatic and metamorphic rock fragments (e.g. Figure 3.4 F) and rarely as detrital flakes. Chlorite has also been identified as a rare detrital component. It is likely also contained in some lithic metamorphic fragments derived from the Penninic ophiolite units. Their erosion during the deposition of the USM is evidenced by the presence of serpentinite grains. The clay minerals occur in lithic clasts (e.g. shales or altered

volcanic rocks; Figure 3.4 F) as well as authigenic cements (Figure 3.4 J). Mátyás (1998) identified smectites and mixed-layer clays (smectite-illite and chlorite-smectite) as well as small amounts of authigenic illite in different USM samples. Smectites are precipitated from circulating porewaters during early diagenesis. The most common smectites in fluviatile sandstones are dioctahedral montmorillonite (formed by weathering of feldspar and felsic rocks) and trioctahedral saponite (formed by weathering of mafic minerals/rocks). As diagenesis progresses, these smectites recrystallize to mixed layer clays and eventually illite/chlorite. This transition only becomes volumetrically important as temperatures increase above 70 to 100 °C (Worden & Moran, 2003). As diagenetic temperatures of only 40 – 80 °C were determined for the USM (Mátyás, 1998), smectites are likely still the dominant phase. This is in agreement with the XRD results in Table 3.3 which show that smectites are more abundant than illite - especially as the 6 wt.% determined for Muscovite/Biotite/Illite (Table 3.3) are predominantly muscovite - and chlorite.

As clasts of felsic rocks and feldspars are more abundant in the sample (as well as in the hinterland during the deposition of the USM), montmorillonites are likely more abundant than saponites. Montmorillonites commonly contain Ca and minor Mg and Fe while saponites are rich in Mg and Fe (c.f. Section 3.3.3).

3.3.3 Chemical composition

The chemical composition (major and trace elements as well as carbon, nitrogen and sulphur contents) of sample A is shown in Table 3.4. The composition is close to the average composition of the continental crust (e.g. Wedepohl, 1995). This is in line with the USM representing a well-mixed siliciclastic reservoir derived from the eroding Alps, where at that time, sedimentary, metamorphic as well as igneous Austroalpine and Penninic units were exposed and eroded (von Eynatten, 2003).

Most elements are distributed between various minerals, e.g. Ca is contained within calcite, dolomite as well as different smectites. In addition, many of the minerals identified (e.g. plagioclase or biotite) represent solid solutions. While XRD can distinguish between the pure endmembers (e.g. albite/anorthite or phlogopite/annite), it cannot determine the composition of the solid solution. Chemical analyses of a large number of grains by EMPA and point counting are thus needed in order to link the chemical data to the mineralogy. This requires considerable time and resources and will thus only be attempted once drill core material from the Forsthaus site is available.

However, using the TIC content determined from CNS, the carbonate mineral content (calcite + dolomite) determined by XRD can be verified. Carbonate minerals are the only source of inorganic carbon in the drill sample. The measured TIC of 1.14 wt.% and the mass ratio of calcite/dolomite of 2.67 as determined by XRD imply that the sample should contain 6.8 wt.% of calcite and 2.5 wt.% of dolomite. While these values are lower than the values determined by XRD (Table 3.3), they fall within the analytical uncertainty of XRD analyses as well as the range of carbonate content determined by Keller et al. (1990) (Table 3.3)..

Table 3.4: *Analysis of major and trace elements (by XRF) as well as carbon, nitrogen and sulphur contents (by CNS analyser) performed at the University of Bern on powdered drill core sample material from P7. No chemical data are available from other USM samples for comparison.*

	Uni Bern (sample A)		**Uni Bern (sample A)**
XRF (major, wt.%)		*XRF (trace, µg/g)*	
SiO_2	64.25 ± 0.29	Sc	12.2 ± 3.2
TiO_2	0.33 ± 0.01	V	46.9 ± 5.6
Al_2O_3	10.81 ± 0.09	Co	31.7 ± 3.1
Fe_2O_3	2.70 ± 0.07	Ni	26.2 ± 3.1
MnO	0.08 ± 0.00	Cu	18.4 ± 3.0
MgO	1.58 ± 0.08	Zn	45.5 ± 2.9
CaO	6.98 ± 0.05	Ga	11.7 ± 1.7
Na_2O	2.22 ± 0.05	Cr	34.9 ± 5.5
K_2O	2.73 ± 0.02	Rb	111.7 ± 2.3
LOI[1]	7.08 ± 0.04	Sr	181.9 ± 4.0
CNS analyser (wt.%)		Y	18.4 ± 1.6
TC	1.27 ± 0.02	Zr	111.6 ± 6.3
TOC	0.14 ± 0.02	Ba	371.0 ± 19.8
TIC	1.14 ± 0.02	La	32.2 ± 10.9
TN	<0.01	Nd	22.5 ± 9.5
TS	<0.05	W	199.7 ± 5.2

[1]LOI = loss on ignition, i.e. volatiles (H_2O from hydrated minerals and CO_2 from carbonate minerals) lost during heating of the sample to 1050 °C over 2 h (Section 3.2.3).

When looking at the composition of individual carbonaceous lithic fragments or carbonate cements determined by EMPA, it can be seen that magnesium is completely absent from all analyses (Figure 3.5), suggesting that either dolomite is overrepresented in XRD or no dolomitic grain was selected for analysis by coincidence. An overrepresentation by XRD is possible. Firstly, the value of 3 wt.% is relatively high when compared to the values from Keller et al. (1990). Secondly, when looking at the XRD pattern, nearly all peaks for dolomite overlap with peaks of other, more abundant phases (e.g. albite or ill/mus/bt), affecting the accuracy

of dolomite quantification. In addition, despite staining of the samples (Section 3.2.1), dolomite should remain colourless. However, no colourless carbonate grains were found in the stained half of this section, suggesting a low abundance of dolomite in the present sample. This suggests that overrepresentation of the dolomite content by XRD is the more likely issue.

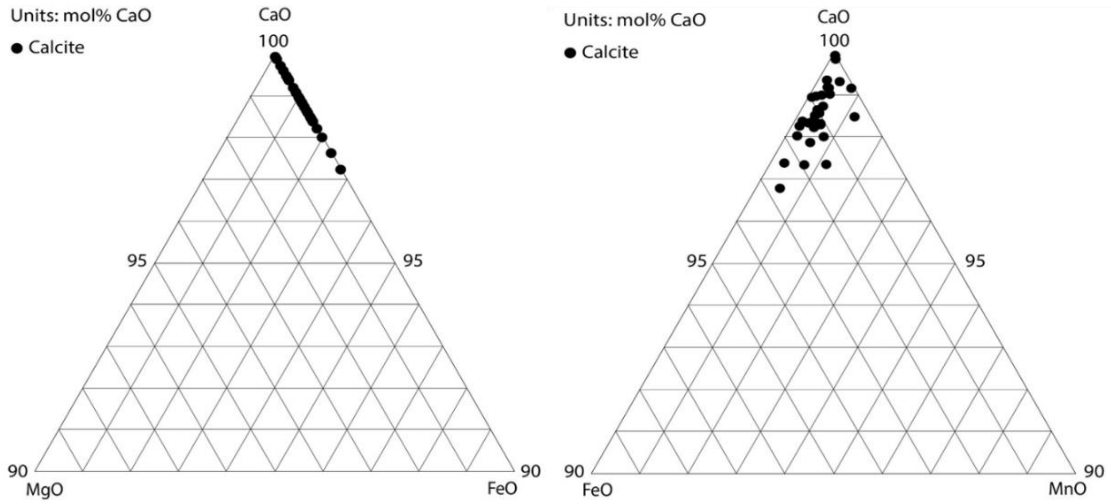

Figure 3.5: *Composition of carbonate minerals and carbonaceous lithic fragments (not distinguished) as determined by EMPA (n=30).*

3.3.4 Porosity and permeability

The petrophysical properties of the samples are shown in Table 3.5. The measurements done on the two different core sections are in good agreement, suggesting a relatively low degree of heterogeneity with respect to porosity and permeability, at least at the m-scale. This suggests that the fine-grained parts described in Section 3.3.1 either represent surficial contamination (e.g. due to drilling mud) which did not affect the petrophysical properties of the entire sample or that these more-fine grained sections were avoided by both teams when selecting the subsamples for analyses.

3.4 Characterisation of USM formation waters

The groundwater analyses obtained from the six monitoring wells around the RBS station Bern are shown in Table 3.6. All samples show a low mineralization with total dissolved solid (TDS) concentrations ranging from 480 to 750 mg/L. Despite their close proximity and the fact that they all originate from within the USM, the measured compositions are quite variable. As all samples were collected from shallow wells, mixing with surface waters and/or anthropogenic contamination can have an effect on water composition. One common indicator of this surficial

influence is elevated nitrate (NO_3) contents. All samples except GW3 show nitrate concentrations of > 10 mg/L, which are likely inherited from mixing with waters influenced by anthropogenic activities. Other parameters, e.g. elevated TDS in GW2 or elevated DOC in GW6 also indicate modification of USM waters by surficial sources. Based on these criteria, composition GW3 (highlighted in Tables 3.1, 3.2 and 3.6) seems to represent the most natural, or least modified, USM groundwater.

Table 3.5: *Porosities, grain densities and Klinkenberg-corrected permeability results from the two drill core samples from P7. For comparison, the median and quartile values (Q25 and Q75) for porosity, grain density and permeability of MBs from the Langenthal wells, as measured by Keller et al. (1990), are given.*

	Uni Bern (sample A)	**Wintershall (sample B)**	**Median/Q25/Q75 (Keller et al., 1990)**
Porosity (vol.%)	18.3	17.6	19.6/13.9/20.7
Grain density (g/cm³)	2.67	2.69	2.65/2.64/2.66
Permeability (mD)	370	369.4	486/79/664

The observed presence or absence of surficial contamination can be explained based on the rock types encountered in the different wells (Table 3.2). The least contaminated groundwater (GW3) originates from the well with the lowest proportion of sandstones (25.5%) and the highest abundance of silts and marls. This section thus represents a relatively impermeable section of the USM, which likely limited the penetration of waters from the surface. Therefore the groundwater composition is dominated by USM formation waters. The other wells have substantially higher proportions of sandstones, especially at the contact with the unconsolidated Quaternary deposits. This facilitated the ingress of waters from the surface (and/or the Quaternary itself), resulting in the observed mixture of waters influenced by anthropogenic activities and the USM formation waters.

The slight supersaturation with respect to calcite (Table 3.6) indicates that the samples were degassing during sampling or storage as they should be in equilibrium with respect to calcite ($SI_{calcite} = 0$) under *in-situ* conditions. In order to correct the reported analyses for this artefact, the *in-situ* composition at 25 °C (assumed reservoir temperature) was calculated by thermodynamic modelling using PHREEQC version 3.0 (Parkhurst and Appelo, 2013) and the wateq4f database. The corrected composition for GW3 is reported in Table 3.7 with values affected by the degassing indicated in italics. This composition was used as the starting point for the preparation of the artificial porewater (APW) which was then used in the experiments described below (Section 4.2.1).

Table 3.6: *Chemical composition of USM groundwaters collected near the main railway station of Bern (Figure 3.1)*

		GW1	GW2	GW3	GW4	GW5	GW6
Water table	m a.s.l.	515	522	523	518	513	510
Temperature	°C	15.6	15.3	13.7	14.1	13.4	13
EC (sampl.)	µS/cm	633	1,110	580	714	660	641
*p*H (sampl.)	-	7.79	7.76	8.05	7.51	7.90	8.33
Ca2+	mg/L	71.5	118	26.6	72.6	62.9	17.5
Mg2+	mg/L	29.5	37.5	19.7	41.7	36.2	10.9
Na+	mg/L	13.3	49.3	75.7	23	21.3	108
K+	mg/L	1.8	3.7	2.8	3.1	2.6	2.6
HCO3-	mg/L	231	190	298	244	237	243
Cl-	mg/L	43.7	151	30.8	104	65.5	56
NO3	mg/L	59.1	123	0.4	20.7	23.3	12.2
SO42-	mg/L	28.2	80	22.5	39.3	48.2	41.6
DOC	mg/L	< 1.0	1.3	< 1.0	< 1.0	2.3	3.5
TDS	mg/L	478	753	476	548	497	492
Simplified water type1		Ca-HCO3	Ca-Cl	Na-HCO3	Ca- HCO3	Ca-HCO3	Na-HCO3
S.I. calcite (sampling)		0.2	0.3	0.3	0.2	0.3	0.1

[1]Only major cation and anion are given.

3.5 Comparison with regional data

3.5.1 Distribution of meander belt sandstones in the Forsthaus area

The profiles of 10 wells penetrating 5 m or more into the USM in the Forsthaus/Inselspital/Länggasse area were compiled (Figure 3.6). The results show that most sandstone units are relatively thick (> 10 m) and likely represent amalgamated units. In well B, several such sequences occur and the sandstone to marl + clay ratio is about 1:1. At the same time, the data also show that thick intervals (up to 150 m) without any sandstone units present are common in the area. Thus, the distribution model developed by Platt and Keller (1992), assuming a random but regular distribution of all architectural elements (Figure 2.8), is not necessarily representative of the internal structure of the USM in the area of interest. The results also show that even at the smallest scale (e.g. between wells B, C and D or G/H and I), there is a high degree of lateral heterogeneity, making predictions of where sandstone layers occur very difficult.

Table 3.7: *Composition of the GW3 sample as analysed and corrected for degassing of CO_2 during sampling or storage using PHREEQC.*

		GW3 (analysed)	**GW3 (corrected)**
T (field)	°C	13.7	*25*
pH (sampling)	-	8.05	n/a
pH (lab)	-	7.92	n/a
pH (calc)	-	n/a	*7.60*
Ca^{2+}	mg/L	26.6	*25.5*
Mg^{2+}	mg/L	19.7	19.7
Na^{+}	mg/L	75.7	75.7
K^{+}	mg/L	2.8	2.8
HCO_3^{-}	mg/L	297.8	*307.7*
Cl^{-}	mg/L	30.8	30.8
NO_3	mg/L	0.4	0.4
SO_4^{2-}	mg/L	22.5	22.5
DOC	mg/L	< 1.0	< 1.0
$SI_{calcite}$	-	0.31	*0.00*
$SI_{dolomite}$	-	0.67	*0.24*
Log pCO_2	bar	-2.66	*-2.15*

Over the coming months, the compilation of these borehole profiles will be expanded across the entire City of Bern and surrounding areas as part of an ongoing MSc thesis at the Institute of Geological Sciences, University of Bern. The compilation will be visualised in 3D using MatLab to identify (a) where data is available and where it is not and (b) which areas are rich/poor in sandstones. This will help with the understanding of the 3D architecture of the USM in the Bern area as well as the evolution of the paleofluviatile system. Once the compilation of the Bern area has been completed, more borehole profiles from other areas (e.g. the more distal realm in the area Aarberg-Lyss-Schüpfen to link up with observations made by Keller et al. (1990) in clay pits) can be compiled and visualised. The MSc thesis will be completed in summer 2022.

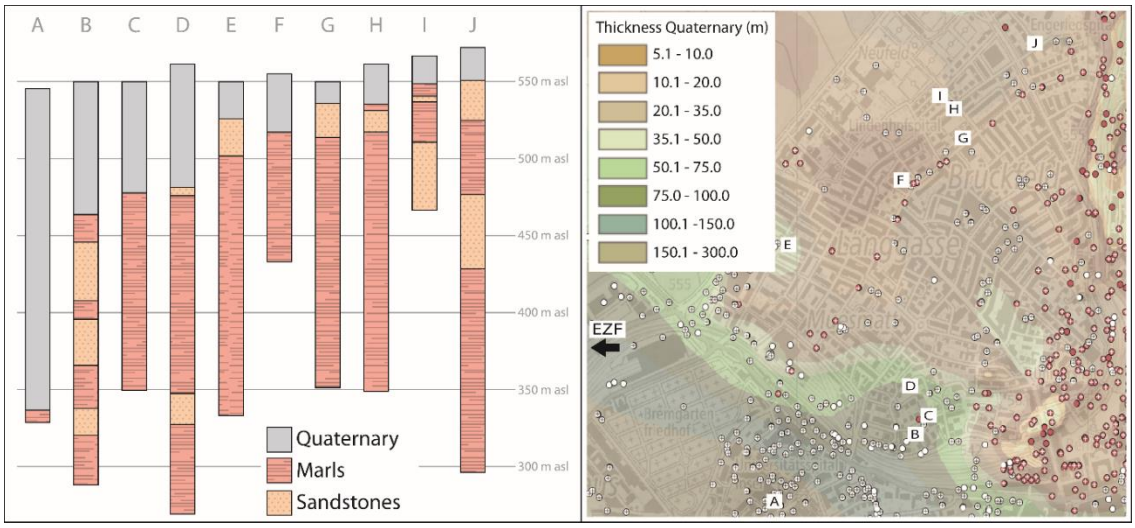

Figure 3.6: *Profiles of all wells penetrating >5 m of USM in the area between the Energiezentrale Forsthaus (EZF) to the west, the Inselspital to the south, Bern train station to the southeast, Engeried hospital to the northeast and the forest of Bremgarten to the north(west). In the immediate area of the EZF and further to the east or south, few wells have been drilled and none have reached the bedrock due to the glacially overdeepened valley in this area filled with a thick (up to 300 m) Quaternary sequence.*

3.5.2 Composition and properties of meander belt sandstones

The thin section observations of the P7 core material are in good agreement with those of USM sandstones by Mátyás (1998) (Section 2.2.4.1). Not just the types of grains are similar in the P7 samples compared to the USM in general, but also their abundance. The mineralogical composition falls within the compositional range determined by Keller et al. (1990) for MBs of the USM (Table 3.3). When comparing to the mean value reported, the drill cores analysed for this study are more quartz-rich, while containing less calcite and fewer clay minerals. The similarities between the samples studied here and the USM in general is not surprising. It has been shown that even the other, more fine-grained lithotypes show similar mineralogical compositions throughout the USM (Keller et al., 1990). These similarities reflect the composition of the eroding Alps in the hinterland, supplying the SMB with a feed of well-mixed debris of relatively constant composition, which was then sorted into different grain size fractions during the deposition of the different lithotypes. Chemical compositions are not available for other USM samples. Thus we cannot compare the XRF and CNS results to previous studies.

Based on thin section analyses, we know that most minerals appear in more than one form (i.e. calcite in rock fragments and as cement or clay minerals in rock fragments, as matrix and authigenic minerals). The XRD data on the other hand represent bulk analyses, which do not allow to distinguish between the different occurrences of a single mineral. However, due to differences in grain size (and reactive surface area) as well as level and type of impurities,

the different mineral reservoirs might show different reaction rates. Thin section analyses allowing to differentiate between the different forms of a single mineral (e.g. point counting) will thus be beneficial for detailed site characterisation as they allow to better assess the reactivity of different minerals or mineral fractions.

The petrophysical data determined for the P7 drill cores also fall within the values previously determined by Keller et al. (1990). While porosity and grain density are slightly higher than the median value, the permeability is lower (Table 3.5). The spread of porosity values is relatively narrow. The measured permeabilities, however, vary widely, indicating that the interconnectedness of pores and pore sizes have a major effect. However, this has not been studied in detail for the P7 samples nor the USM in general. For site characterisation, additional measurements assessing pore types (inter- vs. intragranular porosity) by fluorescence microscopy and pore size distributions by CT or NMR spectroscopy could be of great interest to better constrain both the reactive surfaces and tortuosity of the flow path.

3.5.3 Hydrogeology and hydrochemistry

The following discussion focuses on comparing GW3, which shows the least modified and most representative composition for USM formation waters, with values from previous studies. The water is of the general Na-HCO_3 type, typical of that found at depths of several tens to hundreds of meters in the SMB (Section 2.2.5). When GW3 is plotted into a Schoeller diagram showing other shallow USM waters (Figure 3.6), the pattern agrees well with the other displayed Na-HCO_3 water (light blue). However, GW3 shows substantially higher Cl-concentration. There are two possible explanations for this behaviour: The Cl is derived from (a) mixing with a shallower Ca-HCO_3-type water (yellow) with similar Cl concentrations to GW3 or (b) with a deeper, more Cl-rich Na-Cl water (red). The second option seems more likely as dilution with a Ca-HCO_3 water would result in an increase with respect to Ca and a decrease with respect to Na, which is not observed in the GW3 composition. Rather, the Na concentration of GW3 is higher than the other Na-HCO_3 waters, further supporting the second option. It is thus possible that the Na-Cl-type formation waters with TDS above 1000 mg/L occur at depths of only a few tens of meters in the area shown in Figure 3.1. A direct transition from shallow Ca-(Mg)-HCO_3- to Na-Cl-type waters was observed in both the Weiach and Eglisau wells (Nagra, 1988). This shows that, at least in the northwest of Switzerland, Na-Cl waters do indeed occur at very shallow depths (Figure 2.8). Besides major ions, the GW3 water also shows a DOC concentration (< 1.0 mg/L) in agreement with values from USM-hosted springs and the Eglisau well (0.4 to 2.2 mg/L) as reported by Schmassmann (1990).

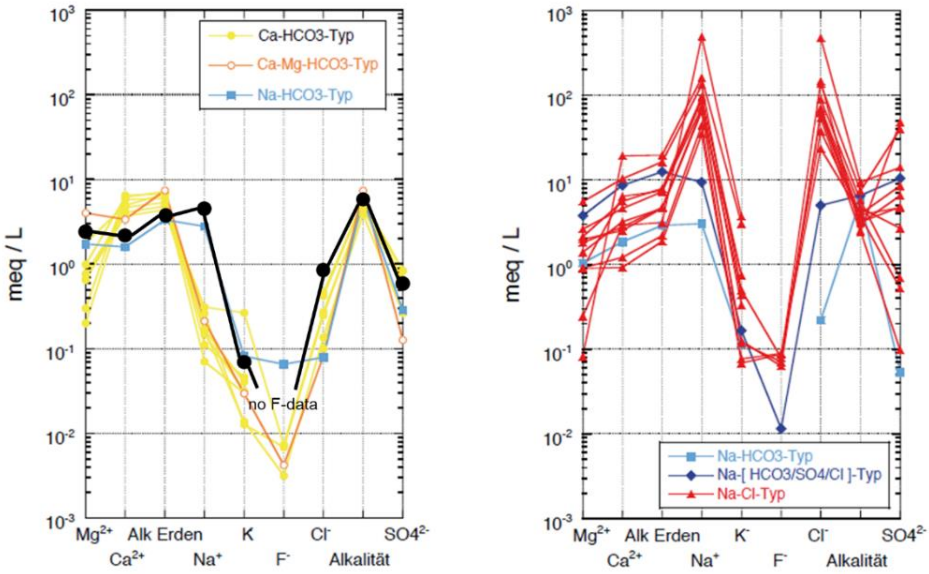

Figure 3.7: *Schoeller diagrams showing shallow (left) and deep (right) USM formation waters from the northeastern part of the SMB (Waber et al., 2014). Sample GW3 (black) is shown for comparison.*

3.6 Implications for the *Geospeicher Forsthaus*

The characterisation of the samples from the shallow wells in the area of the Bern train station shows that the general trends defined for the geology and hydrogeology of the USM (Section 2.2) appear valid in the Bern area. However, the investigated samples were not collected at the Forsthaus site but originate from around 2 km to the east (Figure 3.1). In addition, they were obtained from much shallower depths (max. 40 m deep, corresponds to around 500 to 525 m a.s.l.), compared to the planned maximum reservoir depth of 500 m below surface or 50 m a.s.l. While the lateral distance between the samples studied in this chapter and the planned Forsthaus site are unlikely to have a major effect on the properties studied, the effect of increasing depth is more difficult to assess.

The mineralogical composition of the MBs of the USM is not expected to change with depth as it was primarily determined by the depositional environment and the sediment supply during formation. The depositional environment led to a separation with respect to grain size and the formation of the different lithotypes. However, apart from an increasing clay content in the more fine-grained elements (i.e. LS and OPS), the mineralogical composition of all lithotypes across the SMB is relatively constant (Keller et al., 1990). This indicates that the sediment supply remained relatively constant throughout the deposition of the USM. Similar mineralogical compositions were also reported for the OMM (Mátyás, 1998), indicating that the composition of the debris washed into the SMB remained more or less constant over Millions of years even when depositional conditions drastically changed. Post-depositional changes

during burial and later uplift can potentially affect the composition of the deposited sediments. Mátyás (1998) showed that diagenesis led to the dissolution of certain components (e.g. detrital volcanic fragments) and precipitation of authigenic cements (primarily calcite and clay minerals). This could potentially lead to compositional variations. However, the same volumes and types of cements were found across the SMB in both the USM and the OMM, indicating that the diagenetic processes did not introduce substantial compositional heterogeneities.

Diagenesis took place during burial and compaction of the USM by the deposition of younger Molasse formations (OMM and OSM). Mátyás (1998) showed that calcite cementation took place early on during compaction. It thus helped to preserve a substantial proportion of intergranular porosity in the MB (median porosity of 20 vol.%) despite the formation being buried to up to 5 km. However, a decrease in seismic velocities with increasing depth suggests that porosities decrease towards the base of the USM (Büchi and Bodmer, 1983), either due to increased compaction before calcite cementation or a higher degree of overall cementation. It was also observed that the uppermost few tens of meters of the USM (where most samples studied by Keller and co-workers are from) show elevated porosities and permeabilities due to partial dissolution of calcite cement by recent infiltration of CO_2-rich meteoric waters (Küpfer, 2005). It is therefore possible that the porosity (and likely permeability) at the planned reservoir depth for the *Geospeicher Forsthaus* is lower than the reported median values for the MB samples (Table 3.4).

Besides the properties of the reservoir formation, the expected hydrogeological conditions are also likely to be affected by the increase in depth. The possible presence of Na-Cl waters at a depth of only a few tens of meters is of great importance for the *Geospeicher Forsthaus* project as it makes it very likely that Na-Cl-type waters will be present at the planned reservoir depth. Na-Cl-type waters are expected to be more corrosive and could affect the solubility of minerals and gases. Therefore, more saline formation waters at reservoir depth could possibly aggravate some of the problems (i.e. corrosion and scaling) foreseen during operation of the *Geospeicher Forsthaus*.

A more relevant issue might be the hydrogeological connection between the USM and the overlying Quaternary deposits. During erosion of the Molasse sequence, deep channels were cut into the bedrock, which were then filled by a variety of unconsolidated Quaternary sediments (Figure 2.5), many of which represent highly permeable aquifers. This results in a lateral contact between the Quaternary units and some of the relatively permeable MBs, potentially allowing for mixing between the formation waters of the two units (Figure 3.8). If both the permeability and the degree of vertical interconnectedness between the MBs is high, this could lead to (a) the infiltration of young formation waters deep into the USM or (b) flow

of USM groundwater into the unconsolidated deposits, depending on which deposit is more permeable. In the latter case, the outflow of USM groundwater could lead to lateral groundwater movement within the MB sandstones. For the *Geospeicher Forsthaus* this possible hydrogeological connection and the resulting effects are likely of little importance. The target depth of the reservoir (500 m) is much greater than the maximum thickness of the Quaternary deposits known in the area (200 m tick, 500 m southeast of the planned site). Thus, the reservoir will be overlain by up to 300 m of USM deposits. In addition, it appears that in the USM, at least in the Länggasse area to the east of the planned *Geospeicher Forsthaus*, the fine-grained LS and OPS deposits are much more abundant than the sandstone units, effectively limiting the vertical permeability of the unit and isolating the reservoir formation (Figure 3.6). While this is advantageous from a hydrogeological point of view, such a low abundance of sandstone units in the target area could be problematic as a total thickness of around 20 to 30 m of permeable sandstones (within the 300 m thick USM) are required for efficient HT-ATES storage at Forsthaus.

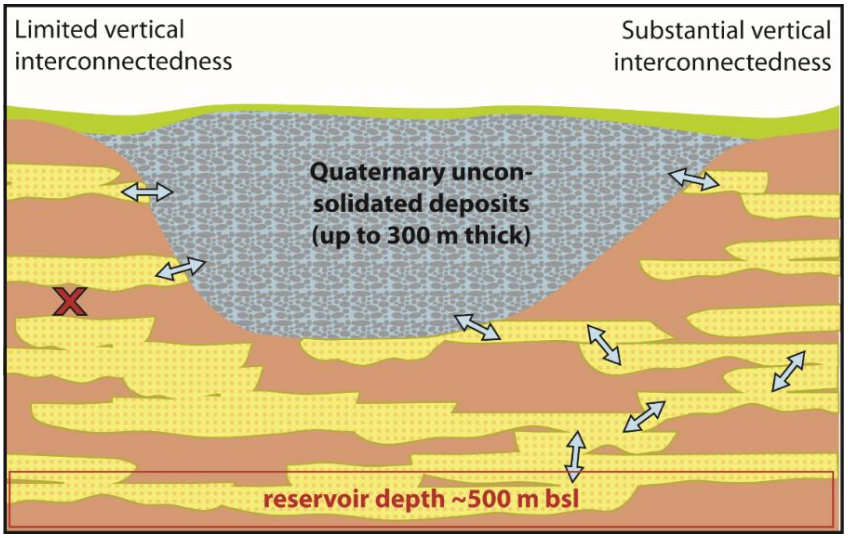

Figure 3.8: *Schematic illustration of the possible hydrogeological connection between the unconsolidated Quaternary deposits and the MBs of the USM, down to reservoir level.*

4 Experimental work – Assessing mineral reactions during heat storage in MB sandstones of the USM

4.1 Motivation of experimental work

In Section 2.3, a range of mineral reactions potentially occurring during operation of the *Geospeicher Forsthaus* was identified by comparing problems encountered in previous HT-ATES with the expected geological and hydrogeological conditions in the USM. The reactions are primarily expected to occur in two locations: in the reservoir during the storage period and in the heat exchanger during heating of formation water (= loading). In order to investigate these reactions in more detail, three types of experiments - core, batch and precipitation experiments - were devised using the core material from well P7 and the USM formation water analyses described in Chapter 3.

4.1.1 Assessing mineral reactions in the reservoir

Based on previous studies (Section 2.1), the following mineral reactions are expected to occur in the reservoir during HT-ATES:

(1) Dissolution of silicate minerals
(2) Dissolution/precipitation of carbonates
(3) Ion exchange on clay minerals

Generally, formation water is used as the working fluid in the operation of a HT-ATES. The water is therefore saturated with respect to the minerals present in the reservoir under *in-situ* physico-chemical conditions. Upon extraction from the formation and heating in the heat exchanger, the water becomes undersaturated with respect to minerals with a normal (prograde) solubility, such as most silicates. Thus, upon reinjection, the hot water is capable of dissolving

any silicate minerals in the reservoir until saturation with respect to that mineral or with respect to more stable minerals is reached. Carbonates, on the other hand, become supersaturated during heating due to their retrograde solubility. Depending on the precipitation rates of the carbonate minerals, on the residence time of the fluid in the surface installation and on the injection rates, the fluid may be in a supersaturated or saturated state upon injection. If the precipitation rate is too low to induce precipitation in the surface installations, the fluid remains supersaturated upon entering the reservoir and after an induction time carbonates might precipitate close to the well. As the water cools upon moving further into the reservoir it may dissolve carbonates in the sandstones. The same is true when carbonate scaling occurs in the surface installations and the water is saturated with respect to carbonated when pumped into the reservoir formation.

In principle, silicates and carbonates may precipitate either in solution (via homogeneous nucleation) or on a surface, e.g. the wall of a pipe or heat exchanger or pre-existing mineral surfaces (via heterogeneous nucleation). Heterogeneous nucleation is generally more common and faster due to the lower energy barrier for precipitation and the abundance of nucleation sites (rough surfaces etc.) in real-world systems. Irrespective of how the nucleation occurs, mineral particles that have precipitated in the wells and surface installations can be transported into the reservoir and potentially clog the formation.

Besides mineral dissolution and precipitation, ion exchange reactions with clay minerals can potentially play an important role. The net negative charge of clay surfaces leads to spontaneous adsorption of cations in the interlayers of their structure. The adsorption capacity depends on the type of clay mineral present. Kaolinites with their 1:1 layer structure generally have very low surface charges and thus ion exchange capacities close to zero. In 2:1 layer clay minerals (e.g. illites, chlorites and smectites), the surface charge and hence the ion exchange capacity are higher. Smectites, especially those in the montmorillonite group, show the highest ion capacities. Exchanger sites are always occupied but the identity of the adsorbed cations depends on the selectivity coefficient, the solution composition (e.g. the concentrations of the different species competing for adsorption sites) and *pH*. Generally speaking, multivalent ions are preferentially adsorbed over monovalent ions, especially in dilute waters (Carroll, 1959). In clay-rich lithologies, the amount of cations adsorbed is typically higher than their concentrations in solution. In addition, such exchange reactions are faster than mineral dissolution or precipitation rates.

In order to evaluate which of these mineral reactions are likely to occur in the reservoir of the *Geospeicher Forsthaus*, we have devised two types of laboratory experiments. The first type are the so-called core experiments. For these, a drill core sample was taken and mounted

in an experimental set-up which allows the core to be saturated with an artificial pore water (APW) and then heated to simulate storage of hot waters in the MB sandstones of the USM. Examination of the change in water composition before and after interaction with the drill core allows the likely mineral reactions to be inferred. The advantage of this type of experiment is that an intact drill core is used. Due to the minimal sample preparation, the microtexture of the sample is not affected and thus mineral surface areas and pore spaces are as present in the reservoir formation. Because mineral surface areas affect mineral reaction rates, the rates in the core experiments are likely most representative of those in the reservoir during HT-ATES. At the same time, this realism constitutes a major drawback of the core experiments. The slow reaction rates necessitate experimental durations of many months which were found to be afflicted by serious experimental artefacts (back diffusion from the core into the infiltration canister, mixing with confining water and microbial activity in the infiltration canister). Therefore the experimental results and the thus derived mineral reactions are not necessarily representative of the actual processes occurring in the reservoir of the *Geospeicher Forsthaus*. All information regarding the core experiments were thus removed from the main part of the Pre-Study report and moved to Appendix B.

For the second type of experiments, the batch experiments, rock fragments were placed with APW in 12 titanium vessels and heated to the desired temperature. The vessels were sampled after six time steps, allowing changes in fluid composition to be monitored as a function of time. The mineral reactions taking place were again identified by comparing the composition of the solution before and after the experiments. Due to the higher surface area of the rock fragments and the much higher liquid-to-solid-ratio (batch experiments 9:1 vs. core experiments 1:5), equilibration is reached more quickly, necessitating experimental times of weeks rather than months. The drawback of the batch experiments is that the rock has to be disaggregated beforehand, either via SelFrag, crushing and/or milling. This destroys the texture of the rock and potentially introduces artefacts (e.g. higher reactive surface area).

4.1.2 Assessing mineral reactions in the heat exchanger

The aim of the precipitation experiments is to assess the amount and rate of carbonate precipitation in the heat exchangers. While precipitation of carbonates from compositionally simple waters can be quantified easily by geochemical modelling, the more complex chemical compositions of real groundwaters can lead to unexpected behaviour. Examples are the preferential precipitation of more soluble Ca-carbonate polymorphs (Ueckert et al., 2020) or the inhib-

itory effect of phosphate, organic acids, magnesium or sulphate, preventing precipitation despite high supersaturation (e.g. de Kanel and Morse, 1978, Griffioen and Appelo, 1993). These observations are difficult to predict by geochemical modelling as the thermodynamic or kinetic data are largely missing. While simple experiments, like those done as part of this study, will not provide a complete thermodynamic and kinetic dataset, they allow quick assessment of the precipitation behaviour of carbonates over a range of different physico-chemical conditions. The observed behaviour can then be implemented into the geochemical models by modifying the parameters already given in the database, e.g. to factor in the inhibitory effect due to other ions present.

4.2 Experimental approach

4.2.1 Mixing of artificial pore water

For all types of experiments described below, a USM water was needed to react with the core materials. Thus, an artificial USM porewater (APW) was designed based on the composition of GW3 (Table 4.1). The APW was prepared according to the instructions in Wersin et al. (2013). The following chemicals were used (all Merck, ACS reagent grade):

- Sodium bicarbonate ($NaHCO_3$, M = 84.01 g/mol)
- Calcium chloride dihydrate ($CaCl_2 \cdot 2H_2O$, M = 147.01 g/mol)
- Potassium chloride (KCl, M = 74.55 g/mol)
- Magnesium sulfate heptahydrate ($MgSO_4 \cdot 7H_2O$, M = 246.51 g/mol)
- Magnesium chloride hexahydrate ($MgCl_2 \cdot 6H_2O$, M = 203.31 g/mol).

In order to prevent the formation of metastable salts that are difficult to dissolve, three separate initial solutions were prepared:

(1) The Na- and K-salts were dissolved in 1/2 of the final volume of ultrapure water (Solution 1).
(2) The Mg-salts were dissolved in 1/4 of the final volume of ultrapure water (Solution 2).
(3) The Ca-salts were dissolved in 1/4 of the final volume of ultrapure water (Solution 3).

Solution 2 was then added to solution 1 and shaken well before adding of Solution 3. As the different ions cannot be added individually but only as salts, it was not possible to mix an APW with the exact composition of GW3. Instead, a solution with a higher chloride concentration resulted (Table 4.1). However, as Na-Cl-type waters are expected to be encountered at reservoir depth at the Forsthaus site (Section 2.2.5), this is not a major drawback. The APW was mixed under atmospheric pressure conditions ($pCO_2 = 10^{-3.5}$ bar) for practical reasons. The

solution was then bubbled with N_2 for 30 min while stirring to remove the dissolved oxygen. In a second step the solution was bubbled for 1 h with a CO_2/Ar mixture ($pCO_2 = 10^{-2.2}$ bar) while stirring and the head space of the bottle was filled with the same gas mixture to impose its higher partial pressure of CO_2 on the solution. An aliquot of the finished solution was taken and analysed (Section 4.2.4).

Over time, the solution was slowly degassing ($pCO_2 = 10^{-2.2}$ bar to $pCO_2 = 10^{-3.5}$ bar) which led to a slight oversaturation with respect to calcite and precipitation as evidenced by the formation of small white crystals on the inside of the bottle during storage. This increases the *pH* of the solution to ~ 8.6 and led to a lower concentration of HCO_3 (~ 145 mg/L) as calculated by PHREEQC. Thus, the prepared APW was bubbled again with the CO_2/Ar mixture to re-establish the desired CO_2 content before the start of every experiment.

Table 4.1: *Composition of GW3 (from Table 3.7) and the APW used for the core and batch experiments. Different batches of APW were prepared for different experiments. The values reported represent the average concentrations. The error values given indicate max/min concentrations. The values given in italics highlight the concentrations which differ with respect to the calculated composition due to the way the sample was prepared. The saturation indices and* pCO_2 *were calculated using PHREEQC version 3.0 (Parkhurst and Appelo, 2013) and the ThermoChimie database, Version 10a.*

		GW3 (corr.)	**APW (anal., n=4)**
T (field)	°C	25	20
pH (sampling)	-	n/a	7.89 ± 0.4
pH (calc)	-	7.60	n/a
Ca^{2+}	mg/L	25.5	21.0 ± 8.6
Mg^{2+}	mg/L	19.7	18.9 ± 2.1
Na^{+}	mg/L	75.7	77.3 ± 0.7
K^{+}	mg/L	2.80	2.84 ± 0.21
Cl^{-}	mg/L	30.8	*84.4 ± 16.0*
SO_4^{2-}	mg/L	22.5	22.3 ± 0.2
HCO_3^{-}	mg/L	307.7	*214.8* ± 8.0
$SI_{calcite}$	-	0.00	-0.32 to -0.06
$SI_{dolomite}$	-	0.24	-0.40 to 0.23
Log pCO_2	bar	-2.15	-2.63 to -2.25

4.2.2 Set-up and sampling of batch experiments

Batch experiments were performed in 50 cm^3 titanium reactor vessels (Figure 4.1 A) originally constructed for the hydrothermal experiments reported by Chermak and Rimstidt (1990). In

order to sample fluids without opening of the vessels, new lids containing two sampling ports were designed and fabricated. PEEK capillaries and micrometering valves were installed. Care was taken the capillaries did not reach the bottom of the vessel so as to limit swirling up of the rock fragments during sampling (Figure 4.1 B). Before filling the vessels, all parts were cleaned with 5 vol. % HNO_3 and subsequently rinsed with ultrapure water and ethanol and dried at 110 °C.

The SelFrag rock material (Section 3.1.1) was heated to 110 °C for 3 hours before loading of the vessels in order to destroy microorganisms potentially present in the samples. Once cooled, three vessels were loaded with 13.25 g of rock fragments. This corresponds to 5 cm^3 of sample, based on the median grain density of 2.65 g/cm^3 for MB sandstones of the USM (Keller et al., 1990). Adding of 45 mL APW resulted in a solid-to-liquid-ratio of 1:9.

The APW was prepared according to Section 4.2.1 to each vessel, 45 mL of APW were added. Once the containers were filled, they were closed and tightly sealed. A clamp was attached to the outside of the vessels and they were mounted onto a rotisserie unit (~ 10 rpm) inside an oven set to the desired experimental temperature. The first set of vessels was left to react at 60 °C, followed by an experiment at 90 °C and one at room temperature (ca. 20 °C) which were run simultaneously. All experiments were run for 12 weeks.

At the end of the experiment, the samples were detached from the rotisserie unit and placed upright inside the running oven for a few minutes. This was done in order to allow the rock fragments to settle and reduce clogging of capillaries during sampling. In order to sample the solutions as close to the reaction temperature as possible, the vessels were only removed from the oven immediately before sampling. Sampling of each vessel took in the order of 10 minutes and it is assumed that, due to the thick-walled design of the vessels, the temperature of the solution did not drop substantially during sampling. To facilitate fluid sampling, an Ar pressure line (~ 2 bar) was attached to one of the valves while a syringe was attached to the second valve. The Ar pressure allowed for easy sampling of solutions without the ingress of any air. For most samples, the obtained solution was relatively clear and clogging was not an issue. However, a few samples could not be taken through the capillaries and the entire vessels had to be opened in order to obtain a sample. When compared to their duplicate, such samples did not show any difference in composition, indicating that fluid composition is not very sensitive to changes in sampling.

At the same time as the 90 °C experiment, an experiment at room temperature (20 °C) was also run. Instead of titanium vessels, 50 mL centrifuge tubes were filled with rock fragments and APW. They were then placed into an end-over-end shaker at roughly 10 rpm. The samples were taken at the same time as for the 90 °C experiment. However, sampling was

done by simply opening the centrifuge tubes and extracting the fluid using a syringe.

For all samples, suspended solids were removed by filtering through 0.2 µm syringe filters immediately after sampling. Different aliquots (~ 20 mL) were taken: one, non-acidified for analysis of anions, alkalinity and TIC/TOC, and another one acidified to *pH* ~ 2 for analysis of cations by adding 1-2 drops of concentrated HNO_3. For all non-acidified samples, the *pH* was measured immediately after sampling. The samples were analysed for *p*H, alkalinity and TIC/TOC on the same day while analyses of anions and cations were performed up to 4 weeks later. In the meantime, samples were stored at 5 °C. For details of solution analyses see Section 4.2.4.

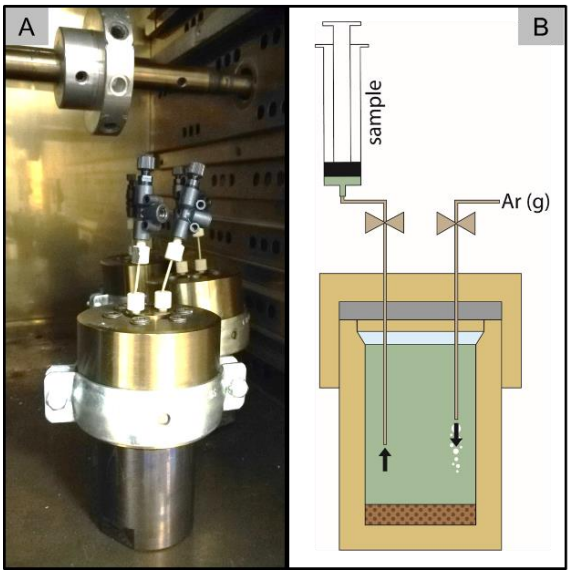

Figure 4.1: *Experimental set-up of batch experiments: Ti-vessel with holder inside rotisserie oven (A). One of the disks to which the samples are attached can be seen in the background above the vessels. The inside of the vessels and the sampling set-up (Ar on one side and syringe on the other) is shown schematically (B). The same conditions are established in all vessels and they are opened at different times to establish a time series.*

4.2.3 Set-up of precipitation experiments

Two types of precipitation experiments were designed: (1) Nucleation experiments (di Lorenzo et al, 2017) to identify the degree of supersaturation needed for the onset of calcium carbonate precipitation through homogeneous nucleation at different temperatures and different solution compositions (i.e. with or without Mg being present). This is important information as geochemical modelling codes generally assume the onset of precipitation at *SI*=0

and thus potentially overestimate the degree of carbonate precipitation. (2) Growth experiments to determine growth rates by growing calcite seed crystals under constant solution composition (Tomson et al, 1978. Beck et al, 2013).

The experiments were performed using a Metrohm Omnis Titration System equipped with the OMNIS software (version 2.4) for method development and data collection. For all experiments, 150 mL of $CaCO_3$-saturated reactor solution (achieved through allowing ultrapure MilliQ water to equilibrate with an excessive amount of calcium carbonate powder over a week) was poured into a double walled beaker and a magnetic stirrer was added. By pumping warm water through the gap, the reactor solution can be heated and kept at constant temperature throughout the entire experiment. For all experiments, solutions were prepared by dissolving analytical grade reactants provided by Merck in ultrapure MilliQ water.

For the nucleation experiments (Figure 4.2 A), a conductivity electrode and an optical conductivity electrode (optrode), measuring the electrical conductivity and the optical transmittance at 660 nm of the solution, were placed into the reactor. A 0.2 M solution of a mixture of $NaHCO_3$ and Na_2CO_3 (*p*H 9) was then added from a burette to the solution at a constant rate (0.5 mL per minute), increasing the saturation of $CaCO_3$ until particles nucleate. The point of nucleation was determined as 95% of the starting transmittance of the solution as determined by the optrode. The conductivity electrode also records the onset of nucleation as the conductivity slope changes with nucleation. Nucleation experiments were performed at 25, 30, 35, 40 and 60 °C. Higher temperatures were not possible due to the maximum temperature of operation of the conductivity electrode. The maximum temperature of the optrode is even lower (40 °C). Nucleation experiments were repeated several times, firstly changing the reactor solution from a pure calcium carbonate solution to the GW3 artificial porewater (Section 4.2.1) to replicate the system more closely. In a next step, the APW was modified to obtain both a Mg- and SO_4-free solution. This was done by replacing the Mg-/SO_4- bearing salt with a Na-bearing salt to keep the composition with respect to the other ions as well as ionic strength constant. These modified APW were used to assess the inhibitory effect of Mg and SO_4 on nucleation. For all experimental runs, saturation indices at the time of nucleation were calculated using PHREEQC v3.5 (Parkhurst & Appelo, 2013) and the phreeqc database.

For the growth experiments, the set-up described above was slightly modified (Figure 4.2 B). The initial $CaCO_3$ reactor solution (100 mL, *p*H 8.5) was supersaturated with respect to calcite (SI = 0.81). After heating to the desired temperature, 15 mg of calcite seed crystals (66 µm < ∅ < 240 µm) were added to the beaker. As the crystals grew, the *p*H of the system decreased, following the reaction

$$Ca^{2+} + HCO_3^- \leftrightarrow CaCO_3 + H^+ \qquad (4.1)$$

The *p*H decrease was counteracted by the controlled addition of $CaCl_2$ and a $NaHCO_3/Na_2CO_3$ mix at *p*H 9 through two burettes. The Omnis titration system was specifically calibrated to add concentrations of the two solutions that would maintain the *p*H at 8.5 and a constant SI of $CaCO_3$ in solution of 0.81. The curve produced measured *p*H vs time. This curve oscillates due to the instrumental delay between *p*H recording and the reactant addition through the titration device as a response to the *p*H reading. Experiments ended when the growth rate of calcite was too fast to allow *p*H to be kept constant, increasing the addition rate from the burettes, and creating a run-away effect of homogeneous nucleation in the beaker. To investigate the inhibition effects of other ions on the growth rate of calcium carbonate, the growth experiment was repeated using a reactor solution which in addition contained 0.1 mol of Mg^{2+} (added as $MgCl_2$).

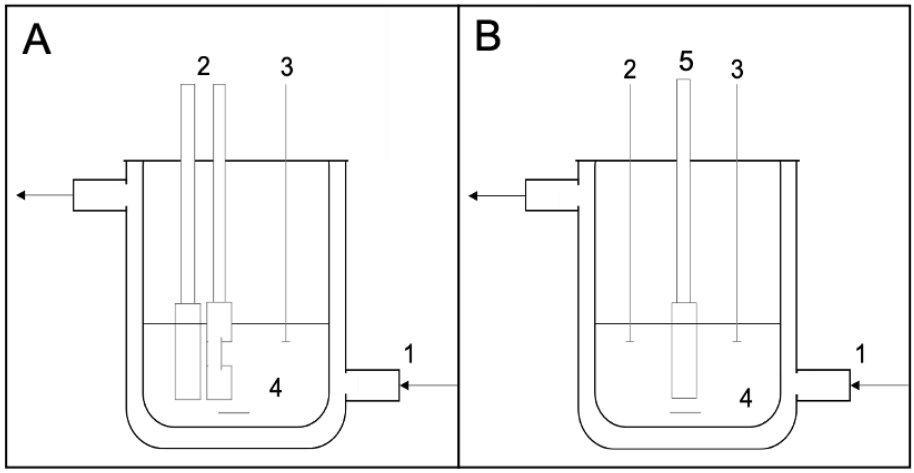

Figure 4.2: *Set up of (A) nucleation experiments and (B) constant composition growth experiments. For nucleation experiments: 1) Water flow into double walled beaker controls temperature of system, 2) Optrode and conductivity electrodes, 3) Burette containing HCO_3/CO_3 mixture, 4) $CaCO_3$ reactor solution. For Growth experiments: 1) Water flow into double walled beaker controls temperature of system, 2) Burette containing HCO_3/CO_3 mixture, 3) Burette containing $CaCl_2$, 4) $CaCO_3$ solution, with* p*H of 8.5 and* SI *of 0.81, 5) pH electrode.*

Growth rates were also determined using observations made by atomic force microscopy. Using a Cypher ES Asylum microscope the growth rate of a calcite crystal submerged in the above reactor solution used for the constant composition experiments (*SI* $CaCO_3$ = 0.81) was determined along the crystallographic 104 axis with and without the presence of 0.1 mol/L Mg^{2+} in the solution. Growth rates were determined through image processing of topography over time using the open source Gwydion software (Version 2.58).

4.2.4 Fluid analyses

Main cation and anions were analysed by ion chromatography (IC) using a Metrohm 850 Professional IC and the MagIC Net 3.3 (2019) software. For cation analyses, the IC is equipped with a Metrosep C4-150/4.0 separation column, combined with a Metrosep C4 Guard/4.0 pre-column and an upstream Metrosep RP 2 Guard/3.5 column. The eluent is composed of a 1.7 mM HNO_3^- and 0.7 mM dipicolinic acid solution. For anion analyses, the IC is equipped with a Metrosep ASupp7-250/4.0 column, combined with a Metrosep ASupp 4/5 Guard/4.0 pre-column and an upstream Metrosep RP 2 Guard/3.5 column (Nr. 6.1011.030). The eluent is composed of 3.6 mM Na_2CO_3. For the preparation of the eluent solutions, ultrapure reagents from commercial producers are used. From the same suppliers, certified calibration and check standards were used. For cations, the quantification limit is 0.1 mg/L with an analytical error of ± 6 % for Na, ± 9 % for K, ± 4 % for Mg and ± 8 % for Ca. For anions, the quantification limit is 0.016 mg/L with an analytical error of ± 5 % for Cl and ± 6 % for SO_4.

Additional cations (Si, Al, Fe) were analysed by inductively-coupled plasma optical emission spectrometry (ICP-OES) using an Varian 720 ES equipped with an autosampler Varian SPS-3 and supported by the ICP Expert II Ver. 1.1.2 software and Varian Spectroscopy Database Administrator Ver. 1.6.0.20. For Si and Al, the quantification limit is 0.05 mg/L with an analytical error of ± 7 % for Si and ± 9 % for Al.

Alkalinity (as mol/L HCO_3^-) and *p*H were determined using a Metrohm OMNIS Titrator supplied with the OMNIS titration-software. The analytical error for HCO_3^- is ± 3%. Total, total inorganic and total organic carbon concentrations (TC/TIC/TOC) were determined using an Analytic Jena multi N/C 2100S equipped with an infrared NDIR-detector and supported by the Software multiWin (aj). TOC was determined indirectly by analysing TC and TIC of the sample and calculating the difference. The quantification limits for these technologies are 1 mg/L with an analytical uncertainty of ± 5 (TC, TIC) and 7% for TOC.

4.3 Results

4.3.1 Batch experiments

The batch experiments were run using SelFrag material at 20, 60 °C and 90 °C. Twelve vessels were filled with the same material and APW and two each were opened at six different time steps up to 3 months, providing time-resolved data on the evolution of fluid composition and mineral reactions. The measured composition and the initial APW composition were used to

calculate the net gain/loss of ions at the end of the experiments (Figure 4.3). A net gain represents addition of the element through mineral dissolution while a net loss represents removal by mineral precipitation.

Over all temperatures, we see an increase in Si, K and Ca. At 20 °C we also see a slight increase in Mg while at elevated temperatures, the Mg concentration is reduced compared to the APW. The concentrations of Na show the opposite behaviour: An increase in Na is observed at elevated temperature while at room temperature the concentration of Na in the experimental solution is lower than in the APW. As all elements can be involved in multiple reactions (dissolution, precipitation and even ion exchange), none of the observed changes can be associated reliably with a single mineral reaction. However, by investigating the evolution of elemental concentrations as a function of time (Figure 4.4), a more detailed understanding can be gained.

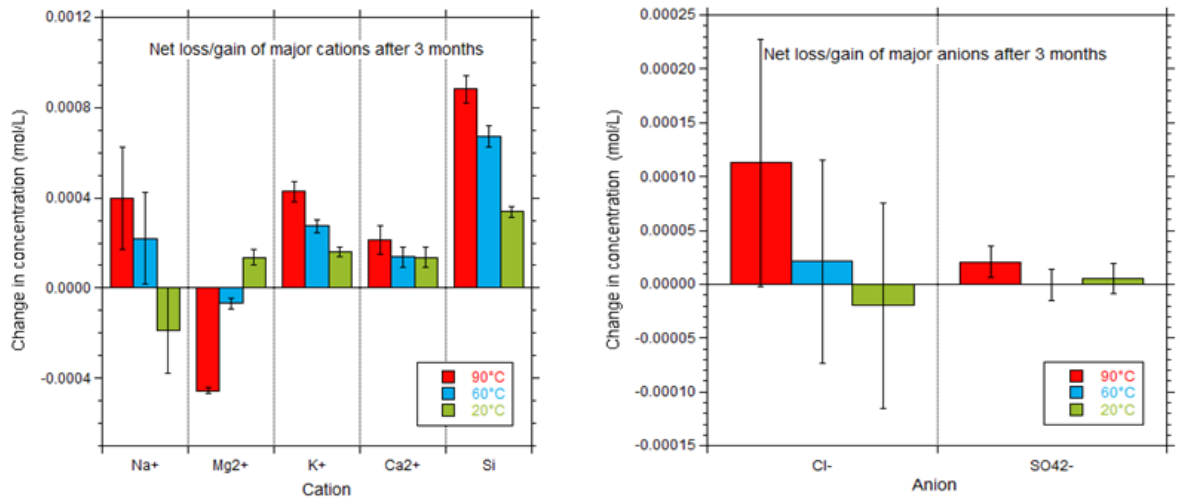

Figure 4.3: *Composition of final experimental solution (after 3 months) in comparison to the initial composition (APW). A positive value indicates a net gain (= released during mineral dissolution) and a negative value a net loss (= removal by precipitation). Values at zero indicate no change in composition. The error bars indicate the analytical uncertainties associated with fluid analyses (see Section 4.2.4).*

The Na concentrations for all time steps and at all temperatures (except the last sample at 90°C) are identical to the original APW concentration within the analytical uncertainties of ±6%. However, they suggest a weak trend to slightly increasing Na concentrations as a function of time at all temperatures. The final concentration of Na is highest at 90 °C suggesting a positive correlation of Na increase with temperature. A potential source for Na is the dissolu-

tion of plagioclase (albite) or Na-bearing sheet silicates. The dissolution of these silicate minerals is faster at higher temperatures which is in line with the higher concentration of Na in the 90 °C experiment compared to the others.

Potassium (K) and silicon (Si) Si show similar trends at all temperatures with a logarithmic-type increase in their concentrations. This increase is more substantial at higher temperatures. The concentrations of both cations in solution seem to be approaching equilibrium, but neither have reached a plateau value within the 3-month period at any temperature. Over the 3 months K concentrations increases by ~600% at 90 °C, by ~400% at 60 °C and 200% at 20°C. The concentration of Si in solution shows the largest increases of all the analysed ions. Starting at a concentration of effectively 0 mmol/L Si in solution, it increases to 0.89 mmol/L (or 25 mg/L) at 90 °C, to 0. 67 mmol/L at 60 °C and to 0.033 mmol/L at 20 °C. The increase of these two ions in the porewater indicate addition through dissolution of silicate minerals. Based on XRD results (Table 3.3), the minerals present in the reservoir system that could influence the concentration of K and Si in solution are: quartz and albite (Si only) as well as K-feldspar, micas, illites and smectites (Si and K). Most of these minerals exhibit normal prograde solubility, meaning that more of these reservoir materials are likely to dissolve at higher temperatures. This is in line with the observed higher concentrations of Si and K in solution at higher temperatures. Although other processes such as ion exchange, where K is preferentially exchanged in preference for bivalent cations (e.g. Ca) on the surface of clays could increase the K-concentration, the similarly shaped curves of Si and K are indicative of linked dissolution behaviour.

The evolution of Ca in solution is slightly different: after a rapid initial increase within the first week, a decrease is observed at elevated temperatures. At 90 °C the decrease is slight and occurs between 2 and 4 weeks. At 60 °C, the dip is more pronounced and occurs between 3 weeks and 2 months. In the room temperature experiment, no clear decrease was observed. The increase in Ca concentration in the 20 and 60 °C experiments is similar at 0.15 mmol and slightly higher (0.21 mmol) in the 90 °C experiments. This corresponds to a 32% increase for Ca in solution at 20 and 60 °C and a 36% increase for the 90 °C run.

Magnesium is the only major ion that undergoes a marked decrease in concentration within the solution at any temperature, decreasing notably by 60% at 90 °C. This decrease happens predominantly within the first 2 weeks. It appears that the concentration of Mg at 90 °C is approaching an equilibrium plateau value after 3 months. Magnesium behaviour at lower temperatures is more complicated.

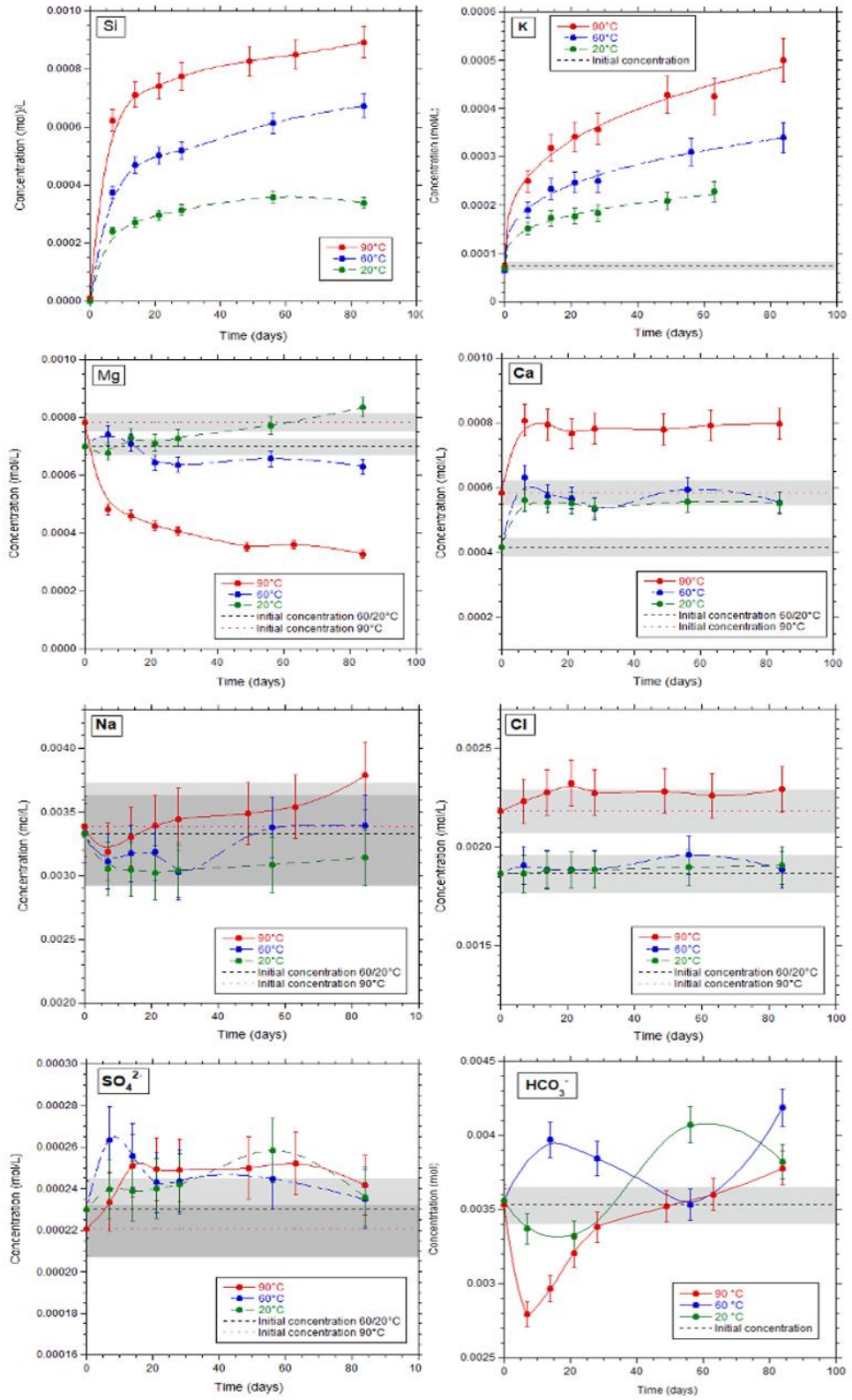

Figure 4.4: *Temporal evolution of solution composition during the batch experiments at 20, 60 and 90°C. Each point is the average of two analyses which overlapped within analytical uncertainties (error bars). Curves joining points are drawn simply to guide the eye. The initial APW composition is given as shaded grey areas. For Si the value in the initial APW was zero.*

When the concentration of the ion over time is examined at 60°C (Figure 4.4) an immediate small increase of Mg in solution is observed, followed by a subsequent decrease within the following weeks resulting in an overall lower (by 9%) value approaching equilibrium. Although this erratic behaviour at the beginning is obvious on the graph, values remain within the analytical uncertainty within the first month. It is therefore difficult to assess whether this is the true evolution of Mg over time, representative of mineral reactions or simply due to analytical uncertainties. At 20°C, the concentration of Mg gradually increases and does not reach equilibrium after 3 months with the increasing trend continuing. After 3 months the concentration of Mg in solution has increased by 19% to 0.83 mol/L.

Calcium is contained in carbonates (calcite and dolomite) as well as the anorthite-component of plagioclase and clay minerals. Magnesium is contained within dolomite, micas, clay minerals and chlorites. The anorthite-content in the rock is likely very low as plagioclase is mostly sericitised (Section 3.3.1) and thus anorthite has largely been replaced. The Ca- and Mg-contents of sheet silicates are unknown and likely highly variable as their exact identity and chemical composition cannot be inferred from XRD (Section 3.2.3). The rapid equilibration of Ca at 90 °C and less prominently at 60 °C suggests that carbonate dissolution dominate the observed evolution of Ca concentrations rather than the dissolution of silicates. This is in line with the ratio of hardness (concentration of Mg+Ca) to bicarbonate in solution. The initial APW has a ratio of 3.5:1.4 but this ratio shifts close to the 2:1 value expected for a pure carbonate system in the first days of the experiment (Figure 4.5) due to calcite dissolution as the initial APW is slightly undersaturated. In the later stages, the ratio shifts further away from the "carbonate line" suggesting that silicate reactions become dominant while calcite is dissolving concurrently (bicarbonate is increasing as a function of time). A likely reaction taking place, is the precipitation of an unidentified, possibly poorly crystalline or amorphous Mg-(alumo)silicate. Such phases precipitated in Icelandic district heating systems under similar chemical conditions and temperatures over the course of a few hours (Harder, 1972; Gunnlaugsson & Einarsson, 1989; Hauksson et al., 1995). At 20 °C, no Mg-bearing phase is precipitating as evidenced by the increasing Mg concentration (Figure 4.4). The observed increase is likely due to continued dolomite dissolution as supported by the evolution of the solution composition parallel to the 2:1 bicarbonate –hardness line in Figure 4.5.

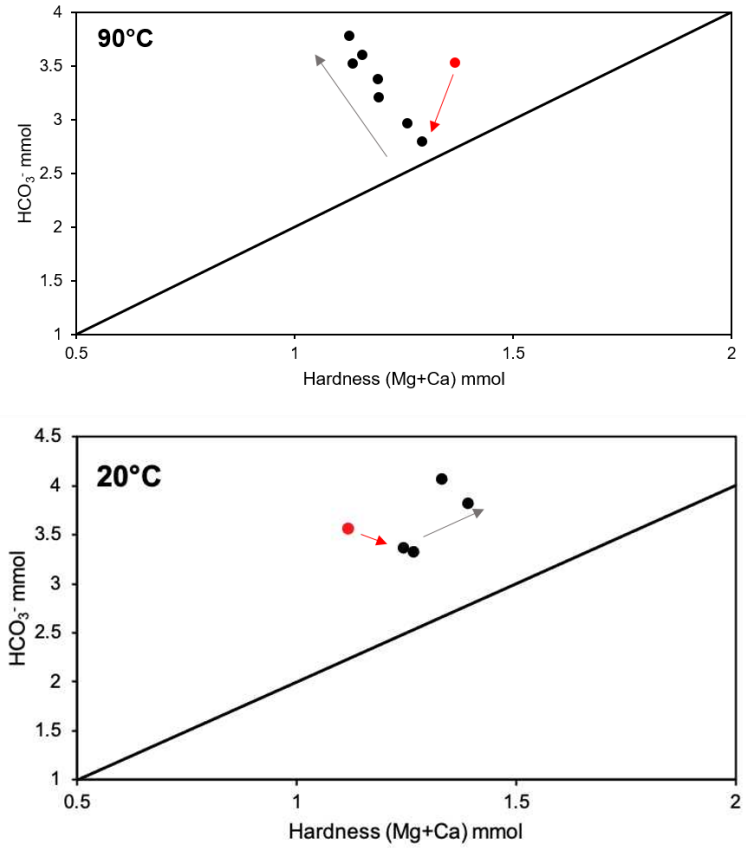

Figure 4.5: *Hardness (Mg+Ca concentration) versus bicarbonate concentration as measured for the experimental solutions (black dots) at 90°C. Carbonate dissolution and precipitation should yield solutions which evolve parallel to the 2:1 bicarbonate to hardness (Mg+Ca) ratio (black continuous line). Deviation from this trend suggests the contribution of silicate reactions. The red point is the composition of the initial APW. The first experimental solution plots close to the 2:1 bicarbonate to Mg:Ca line suggesting carbonate reactions are responsible for initial modification of the APW (red arrow). Over time the experimental solutions evolve away from the carbonate line (grey dashed arrow) as silicate reactions become dominant.*

Similarly to Na, the concentrations of Cl falls within the analytical uncertainty of the initial APW analysis but a weak increase at 90 °C might be inferred. However, no known source of Cl is present in the sample: Any potential remnants of the *in-situ* porewater were removed during the disaggregation of the sample by SelFrag (Section 4.2.2) and none of the minerals is expected to contain a significant amount of Cl which could be released during dissolution.

For sulphate, the analytical uncertainties of concentration measurements also overlap with the concentrations measured in the APW (within analytical uncertainties). However, there is no trend visible and the behaviour appears completely erratic. There are several possibilities for this observation: The concentration of SO_4 could be affected by microbial activity

as microbes consume SO_4 in order to produce H_2S (Section 4.3.1). During sampling and setting up of the experiments, no care was taken to keep the material or solutions sterile. It is thus possible that microbes were introduced to some samples but not others. However, the consistently high concentration of SO_4 and the absence of a "rotten egg smell" during sampling suggests that microbial activity was minor or absent in all samples. The presence of accessory sulphides (e.g. pyrite) has been reported for some samples in the USM (Keller et al., 1990). As each vessel contained a small aliquot of SelFrag material, it is possible that some contained more pyrite than others, resulting in a slightly elevated concentration of SO_4.

4.3.2 Precipitation experiments

4.3.2.1 Nucleation experiments

Pure system

In the context of possible calcite scaling in the wells and surface installations of the Forsthaus project, the aim of the nucleation experiments was to determine the degree of supersaturation needed for onset of spontaneous homogeneous nucleation of calcite under different conditions. Figure 4.6 shows the type of data obtained from the Omnis Titration System for a nucleation experiment done at 25 °C using a pure $CaCO_3$ solution. Further nucleation experiments conducted with the pure $CaCO_3$ solution show that increasing the temperature of the system decreases the time taken for homogeneous nucleation to occur in the solution from 2780 s of carbonate addition at 25 °C to 870 s at 40 °C based on a transmittance value of 95% (Figure 4.7). Two additional nucleation experiments were run at 60 °C. For these experiments the onset of nucleation could only be assessed based on the kink in the conductivity data (Figure 4.8) as the optrode cannot be used at 60 °C. The kinks in the conductivity curves were observed at 950 and 1100 s respectively. As the initial Ca^{2+} concentration in solution is the same at all temperatures, the volume of bicarbonate/carbonate mixture added from the burette can be used to calculate the degree of supersaturation of calcite at nucleation using PHREEQC. At 25 °C a values of 1.74 was determined (Figure 4.9). This is higher than the value of 1.66 previously measured using the same set-up (di Lorenzo et al., 2017). This is likely due to the composition of the solution which was added. In the previous study, it was a Ca-bearing solution while we added a bicarbonate/carbonate solution. Another reason could be that different databases were used for the calculation of the saturation index using PHREEQC.

The saturation indices determined for higher temperatures were lower, decreasing linearly to around 1.4 at 60 °C (R^2 = 0.99; Figure 4.9). In view of the excellent linear fit of the data, the supersaturation needed for the onset of nucleation at 90 °C (planned injection temperature of the *Geospeicher Forsthaus*, Section 1.3) could be confidently calculated by extrapolation. Two extrapolations based on the two values determined at 60 °C were performed. For the higher value at 60 °C, a saturation index of 1.04 was calculated at 90 °C. The lower value at 60 °C yields a saturation index at 90 °C of 0.99. At the same time a third extrapolation was performed, based solely on the data up to 40 °C, yielding an *SI* of 0.91. This was done because the experimentally determined saturation indices at 60 °C are less reliable. At temperatures below 40 °C the onset of nucleation can be determined based on the data from the optrode as well as the conductivity data (Figure 4.6), producing more reliable and reproducible data. At temperatures between 40 and 60 °C, we have to rely on the conductivity data alone. The results shown in Figure 4.8 show that the quality and reproducibility of the conductivity data are poorer.

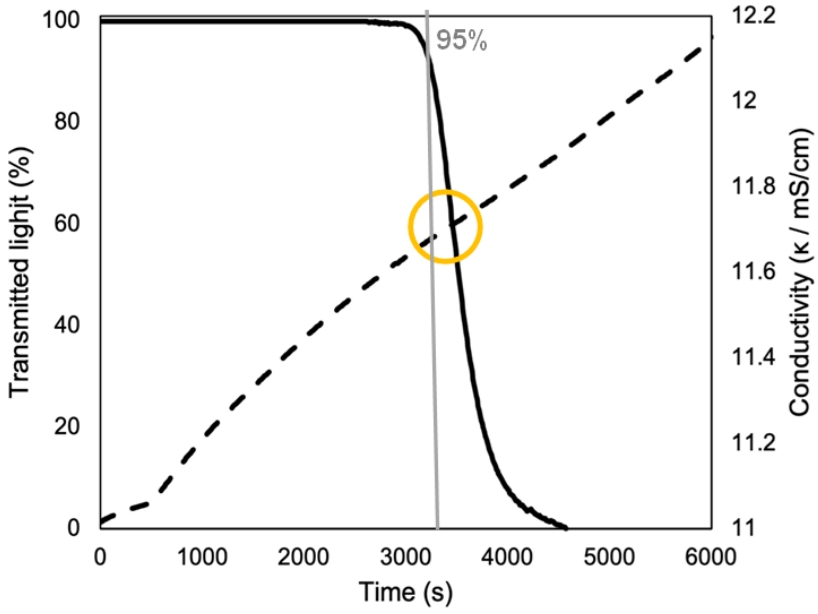

Figure 4.6: *Calcite nucleation experiment at 25 °C. The red curve shows the transmittance obtained by the optrode. A value of 100 % corresponds to the pure solution. As more carbonate/bicarbonate solution is added, the saturation increases until the saturation threshold is crossed and transmittance rapidly decreases. A transmittance value of 95% (grey line) was chosen to define the onset of nucleation. The addition of carbonate/bicarbonate solution increases the conductivity (blue curve) over time as more ions are in solution. The onset of nucleation is evidenced by a slight kink in the conductivity curve where it intersects the grey line.*

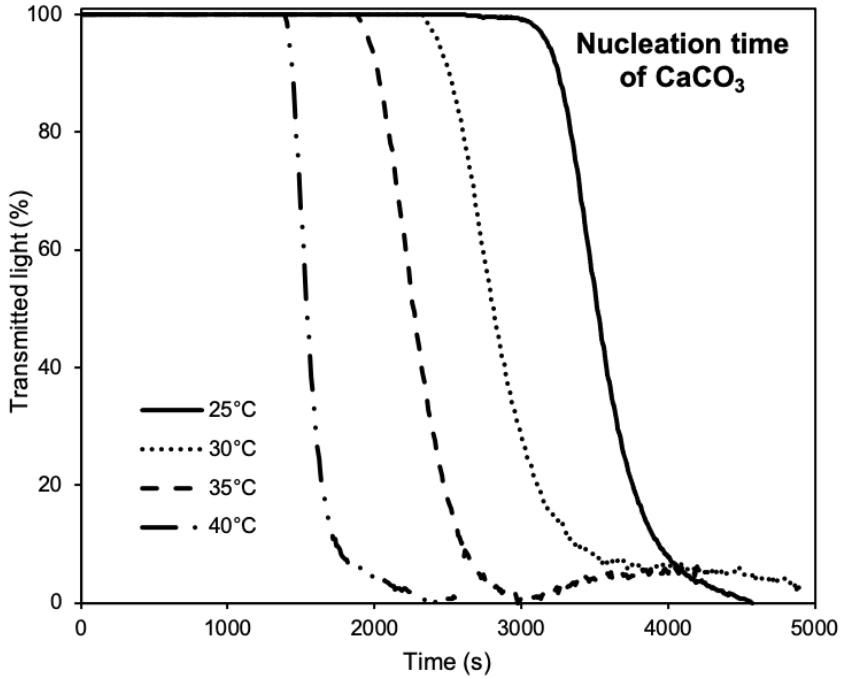

Figure 4.7: *Transmittance data for calcite nucleation experiments at 25, 30, 35 and 40 °C in a pure calcium carbonate solution showing a faster onset of homogeneous nucleation with increasing temperature.*

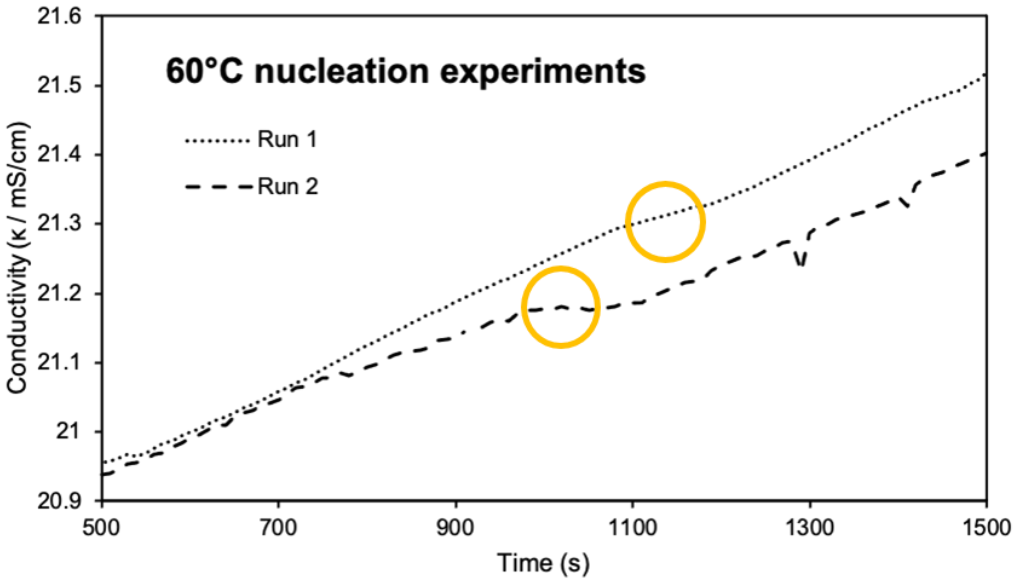

Figure 4.8: *Evolution of the conductivity in solution as a function of time for two different calcite nucleation experiments performed at 60 °C. The kinks observed at 950 and 1100 s respectively indicate the onset of nucleation.*

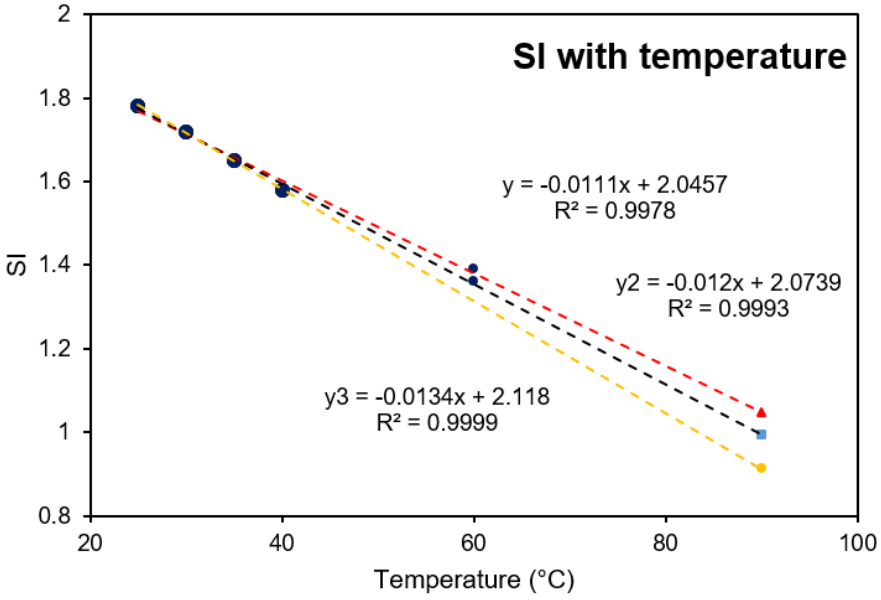

Figure 4.9: *Saturation index (SI) of calcite in solution at the moment that homogeneous nucleation (i.e. precipitation) starts. Up to 40 °C the SI was determined based on the amount of carbonate solution added to reach a transmittance value of 95% as measured by the optrode. At 60 °C, the onset of nucleation was determined based on the kink in conductivity data. For higher temperatures, different extrapolation scenarios were applied.*

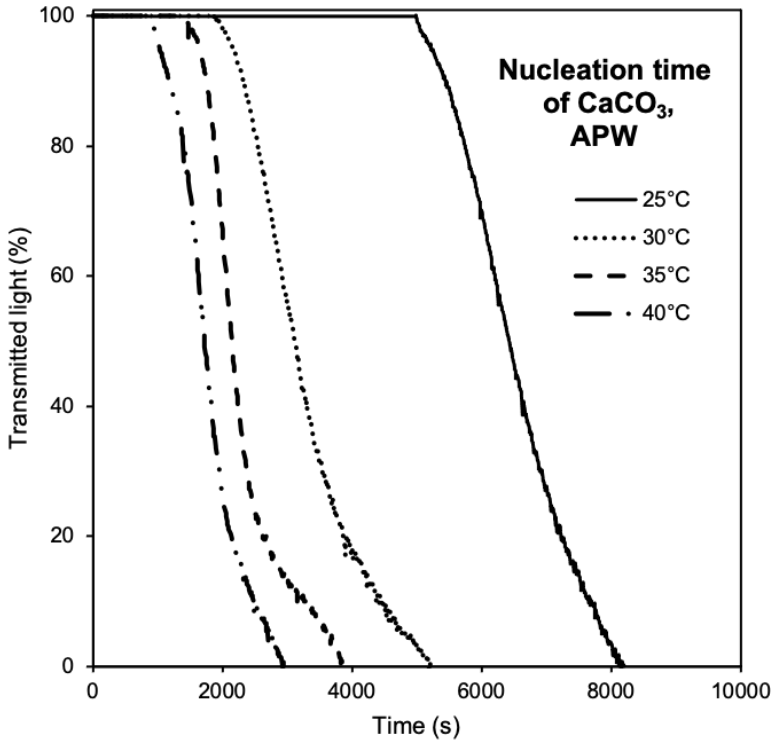

Figure 4.10: *Transmittance data for nucleation experiments at 25, 30, 35 and 40 °C in the APW-system showing a decrease in the onset of homogeneous nucleation with increasing temperature.*

The decreasing saturation needed for the onset of nucleation as temperature increases is because at higher temperatures the activation energy barrier for nucleation is lower and because higher diffusion rates increase the nucleation rate. While this behaviour is well understood, there are a couple of scenarios which could lead to the onset of precipitation at lower degrees of saturation. The extrapolation to calcite precipitation at 90 °C is based on the assumption that the linear trend of decreasing critical supersaturation with increasing temperature remains constant.

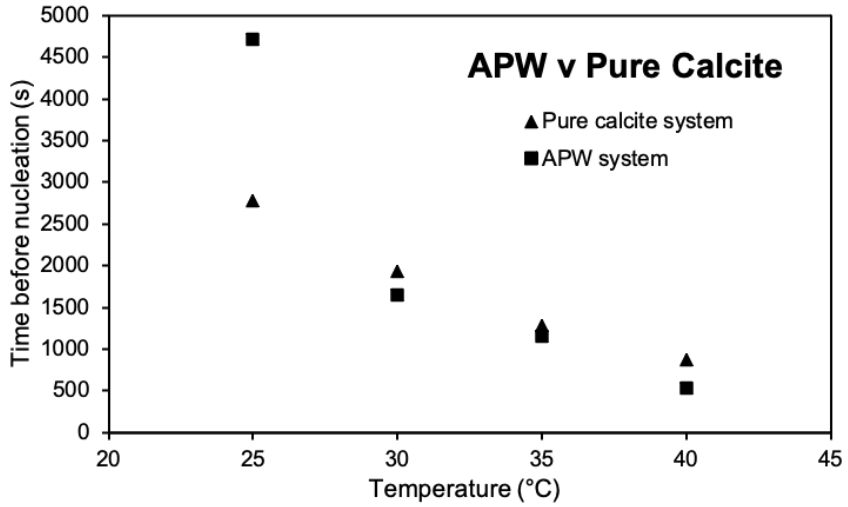

Figure 4.11: *Time between the start of dissolved carbonate addition until the onset of homogeneous nucleation (i.e. precipitation) in the pure $CaCO_3$ (circles) and the APW system (diamonds) as determined by the optrode.*

Another simplification made is the assumption of instantaneous nucleation. The designed experiments are set up to determine the saturation index needed to cause instantaneous nucleation of calcite in a supersaturated solution at a certain temperature. Theoretically, however nucleation of calcite can occur at that same temperature at a lower degree of supersaturation after a longer induction time. This is because a longer time frame creates a greater chance that nuclei can grow larger than the critical nucleus size and thus particles form (Henzler et al., 2018). However, due to the expected short residence time of the fluid in the surface installations of the *Geospeicher Forsthaus*, this scenario is likely of minor importance. A more serious limitation of our results is that we have not tested the effects of heterogeneous nucleation. The experiments only assess the formation of nuclei in solution, where they can be "seen" by the optrode. However, heterogeneous nucleation on available surfaces, especially on rough ones can still occur when the kinetic rate of homogenous nucleation is essentially zero. This can be understood through classical nucleation theory (Sear, 2007), considering that

the surface area of the growing nucleus creates a free energy barrier to nucleation. Whilst a nucleus forming homogenously in a solution is spherical in shape, a nucleus of the same mass adsorbed on a substrate presents a smaller surface area to the solution. Depending on the contact angle of the nucleus and the substrate, this reduced surface area reduces the free energy barrier and thus results in faster nucleation.

System using an artificial USM porewater

While the above experiments provide interesting data, they are not representative of the planned HT-ATES at Forsthaus where the *in-situ* USM groundwater will be used. The groundwater will be saturated with respect to calcite but in addition it will contain ions (e.g. Mg and SO_4) which are known to affect carbonate precipitation (Section 2.1.1.4). Therefore, the nucleation experiments at 25 to 40 °C were repeated using the APW (Section 4.2.1) instead of a pure carbonate solution in the reactor. Similarly to the pure system, a decrease in the onset time of homogeneous nucleation with increasing temperature was observed (Figure 4.10). When comparing to the pure system (Figure 4.11), it is obvious that nucleation in the APW is retarded at 25 °C. The time for calcite to nucleate in the APW was 4710 seconds compared to 2780 s in the pure system. This retardation effect disappears at higher temperatures such that the onset times of nucleation in the APW and pure systems are likely to be comparable between 60 and 90 °C.

No SI value could be determined for the APW as its composition was unknown. The APW prepared for the experiment (Section 4.2.1) had to be modified (e.g. dilution and pH adjusted) in order to have the same properties as the pure CacO3 solution previously used.

In order to assess the retardation effects of Mg and SO_4 separately, two more solutions were prepared (Section 4.2.3). Each of these modified APWs was used to run experiments at temperatures between 25 and 40 °C. In comparison to the non-modified APW, nucleation occurs much sooner in the SO_4-free APW and even sooner in the Mg-free APW at 25 °C (Figure 4.12 and 4.13). This suggests that both ions retard calcite nucleation but that Mg is a more efficient inhibitor than SO_4. The difference between Mg and SO_4 disappears at 40 °C and the retarding effect in general is much lower.

The observed retardation in the APW system due to Mg is in line with previous studies that showed inhibition of calcite nucleation with increasing magnesium concentration (Bischoff, 1968). The same was also observed for calcite growth (Nancollas & Sawada, 1982; Compton & Brown, 1994). Those studies attributed the inhibitory effect to the small size of the Mg^{2+} ion, which leads to stronger hydration and therefore allows it to bond to calcite growth sites which are then no longer available for the addition of larger Ca^{2+} ions.

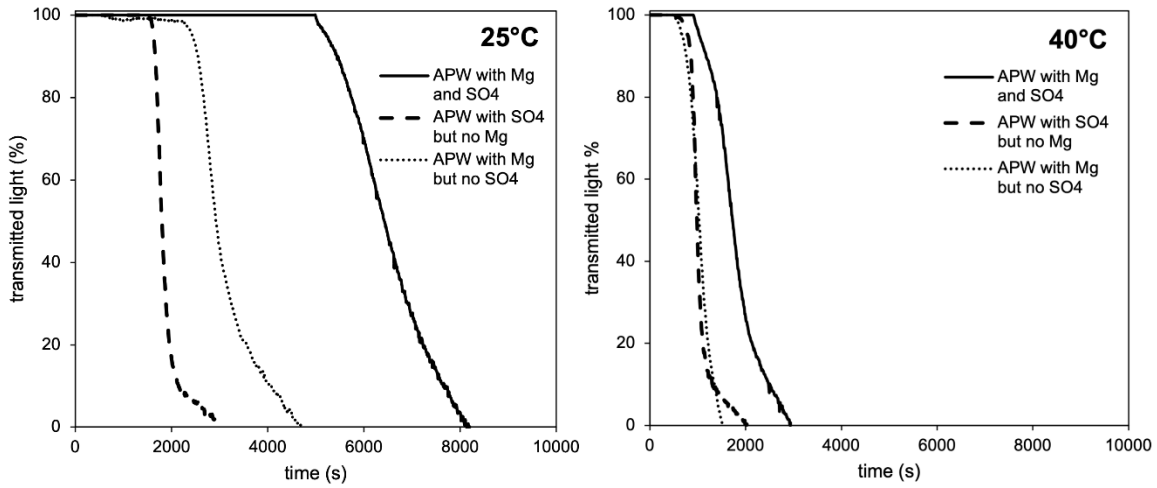

Figure 4.12: *Transmittance data for nucleation experiments at 25 (left) and 40 °C (right) using the original APW, a Mg-free APW and a SO_4-free APW. Both, Mg and SO_4 act as strong inhibitors at 25 °C with Mg slowing down the onset of nucleation more strongly. At 40 °C the difference between Mg and SO4 disappears and the inhibitory effect is strongly reduced.*

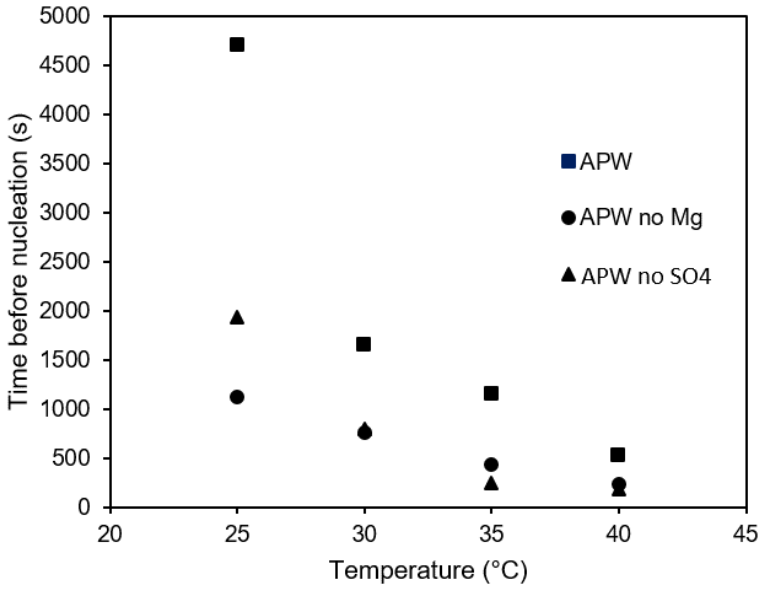

Figure 4.13: *Time between the start of carbonate addition until the onset of homogeneous nucleation (i.e. precipitation) in the original APW system (blue), a Mg-free system (orange) and a SO4-free system (grey) as determined by the optrode.*

Our observation that Mg is a stronger inhibitor than SO_4 (Figure 4.12 and 4.13) is in line with Dobberschütz et al. (2018) and Mjeri et al. (2014), who found that SO_4 had a weak inhibitory effect on its own but enhanced the Mg-inhibition when present. This is in contrast to the

results of the Mg-free experimental data shown here. Figure 4.17 suggests that in the solution free of Mg but containing SO_4, calcite nucleation was still inhibited at 25 °C. It is possible that the observed delay is not due to the presence of SO_4 (or at least not solely) but (also) related to the different CO_3^{2-}/HCO_3^- concentration between the APW and the pure calcium carbonate system introduced by the different preparation of the solutions.

The decrease in inhibition of calcite by ions in solution with increasing temperature was also observed by Mejri et al. (2014). In their study the authors invoked calcium carbonate precipitation by degassing of dissolved CO_2 in the presence of SO_4 and Mg at different temperatures. For SO_4 they found that inhibition was constant across the entire temperature range from 30 to 60 °C. For Mg they found that elevating the temperature from 30 to 60°C weakened the inhibitory effect. This behaviour was attributed to the increased likelihood of aragonite forming instead of calcite. This is because Mg is preferentially incorporated into the aragonite structure compared to the calcite structure, thereby reducing the inhibitory effect.

4.3.2.2 Growth experiments

In the growth experiments, a solution was prepared that was supersaturated with respect to calcite but at a low enough supersaturation state to avoid spontaneous nucleation (Section 4.3.4.1). Calcite seed crystals were then added to this solution to initiate growth (i.e. heterogeneous nucleation of new calcite). Additional Ca^{2+} and CO_3^{2-} were added throughout the experiment to keep the solution composition and thus growth conditions constant. Growth rates were calculated from the linear segments of curves showing the amount of Ca^{2+} and CO_3^{2-} added over time (Figure 4.14). The experiment was done at 25 °C with and without the presence of Mg.

The results show that in the pure system, the growth rate was 0.0082 ± 0.0001 mL/s whilst in presence of 0.1 mol Mg^{2+} the growth rate was reduced by 5% to 0.0078 ± 0.0001 mL/s (Figure 4.14).

4.4 Implications for the *Geospeicher Forsthaus*

4.4.1 Mineral reactions in the reservoir

Using the batch experiments, we tried to assess which mineral reactions in the reservoir are most important in controlling the composition of the reservoir water during HT-ATES.

The experiments suggest that the mineral reactions in the reservoir of the *Geospeicher Forsthaus* are complex. The observed evolution of the solution composition and the modelling

of the results suggest the dissolution of different silicates (quartz, K-feldspar, muscovite, K- and Na-clays) and carbonates (dolomite, calcite (only initially)). At the same time, calcite and a not yet identified Mg-silicate are assumed to precipitate. Based on the undersaturation of the artificial porewater (APW) with respect to most minerals before the experiment and the supersaturation at the end of the experiment, dissolution seems to outweigh precipitation. This suggests that permeability reduction during heat storage due to mineral reactions is likely not a major concern. It also suggests that precipitation is somehow inhibited as the solution would otherwise be saturated with respect to most minerals rather than supersaturated. This can be due to slow reaction rates or actual inhibition by organic acids or other ions (Section 2.1.1.2) preventing mineral precipitation. Unfortunately, based on the experimental results described in this study, not all mineral reactions could be identified and none could be quantified. However, the results (solution composition at the end of the experiments and the mineral reactions identified, can be used to improve the numerical modelling (Chapter 5).

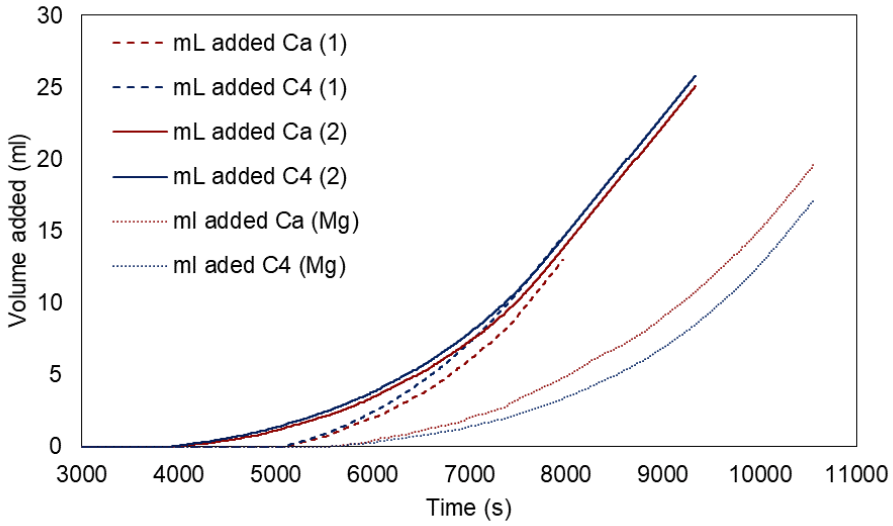

Figure 4.14: *Volume of Ca^{2+}–CO_3^{2-} solution added over time to maintain a constant solution composition during calcite growth.*

4.4.2 Mineral reactions in the heat exchanger

Our results show that in a pure $CaCO_3$ system at ambient temperature, calcite nucleation and growth do not occur instantaneously as the solution becomes saturated (i.e. a saturation index of 0 is reached) but a degree of oversaturation is needed. The degree of oversaturation needed depends on temperature and decreases from 1.7 to 1.4 as temperature increases to 60 °C. If the

linear correlation is extrapolated to 90 °C, a saturation index of around 1 is predicted. However, these values could be substantially lower as the experiments do not take into account heterogeneous nucleation. In wells, pipelines and the heat exchanger there is an abundance of (rough) surfaces onto which precipitation of calcite via heterogeneous nucleation is likely to occur. The importance of this process can be assessed for operational systems (e.g. Wanner et al., 2017; van den Heuvel et al., 2018) but is nearly impossible to predict using experiments due to the interplay of flow conditions and surface properties. In any case, the maximum amount of scales that can form is determined by saturation. Thus, the onset of precipitation as soon as saturation was reached was assumed for the simulations in Chapter 5.

The onset of nucleation also depends on the presence of other ions, e.g. Mg or SO_4. However, our data suggest that the inhibition of Mg and SO_4 decreases with increasing temperature and will be negligible at 90°C, the planned operating temperature of the *Geospeicher Forsthaus*. Besides Mg and SO_4, organic substances could also inhibit calcite scaling. However, as there is no data on the amount and type of organic acids present in the *in-situ* groundwater, this could not be investigated as part of the present study. Overall, no inhibitory effects will be included in the numerical model in Chapter 5.

5 Numerical simulations of a two-year operation of the *Geospeicher Forsthaus*

5.1 Conceptual model for simulations

As the reservoir of the *Geospeicher Forsthaus* is a sequence of permeable sandstones and low-permeability clayrocks (Section 2.2.4). It is expected that fluid-rock reactions take place primarily in the more permeable, sand-rich layers of the USM. The less permeable clay-rich units play an important role in storing heat. Reactions in the permeable units are driven by fluid

motion in response to injection or extraction cycles in combination with temperature changes. In addition to short-time variations related to pumping, there will be long-term, gradual or cumulative changes in reservoir properties. For instance, the reservoir will heat up over time as heat is conducted into the low-permeability clay units. Between injection and extraction cycles there are periods of rest without flow but with ongoing diffusion of heat. Mineral dissolution and precipitation reactions resulting from these changes in the reservoir affect the porosity and permeability of the aquifer material. If at any point in the reservoir the volume of minerals precipitating exceeds the volume of minerals dissolving, the permeability will be reduced. If this clogging of the reservoir rock becomes significant, additional, potentially costly, measures have to be taken to reverse this process and re-enhance permeability. In the worst case the operation can no longer be sustained.

Mineral precipitation or scaling may also occur in the wells and the heat exchanger due to changes in temperature and pressure. Aside from a potential re-dissolution of scales, no mineral dissolution reactions take place within the installation. To predict mineral precipitation in the installation, temperature and pressure conditions, the residence time of the fluid, as well as the rate at which minerals precipitate have to be known. The latter in turn is a function of temperature. Predicting mineral precipitation rates and hence of the distribution of mineral scale formation in the system is a difficult task because of a lack of published precipitation rate data, heterogeneities in the flow field, temperature and pressure conditions that cannot be captured at the scale of the model. In the wells, the precipitation rate may be limited by the low ratio of surface area to fluid flux that prevent minerals to effectively crystallize and grow on the inside wall of the well casing (i.e. heterogeneous nucleation).

In the heat exchanger, water undergoes significant heating or cooling very rapidly, typically under pressures lower than those in the reservoir. These steep gradients in physical conditions imply a strong potential for mineral scaling. Given that the heat exchanger is used for heating and cooling, the amounts and composition of mineral scales may change in time. Because the design of the heat exchanger used in the Forsthaus system is yet unknown, making reliable predictions about the implication of mineral scales on its performance is difficult at this point.

Corrosion of the casing or the surface installation is a risk that could induce significant additional operational cost. Corrosion is favoured by certain chemical conditions, such as a low *p*H, dissolved gases such as O_2 or CO_2 or high TDS (total dissolved solids) in the production fluid or by bacterial activity in the system. Physical corrosion may occur when flow rates are high, in particular in the presence of suspended such as sand, sediment, corrosion by-

products. Incipient chemical corrosion, however, can be detected by monitoring the composition of the circulating water. The risk of chemical corrosion and the implications of incipient corrosion on the water composition can be assessed with coupled THC simulations (e.g. Diamond and Alt-Epping, 2014), but corrosion is not considered in the examples presented below.

Chemical reactions between a fluid and a rock or between a fluid and a gas phase such as CO_2(g) are a function of composition, temperature and pressure. In simulations involving the injection/extraction of waters into/from deep reservoirs, the effects of temperature and pressure on the equilibrium state and kinetic rates of reactions have to be considered explicitly. (Note that the effect of pressure on reactions can often be neglected as it is outweighed by the effect of temperature). To fully comprehend feedbacks between the flow of water, the thermal evolution and chemical reactions, a full-scale model of the ATES system needs to be constructed that includes and couples fluid flow, solute transport (diffusion and advection), heat transport (conduction and convection) and a chemical reaction network including all system-relevant reactions.

We use the high performance reactive transport code PFLOTRAN (www.pflotran.org) to carry out simulations flow and heat transport coupled with reactive transport. In PFLOTRAN, mass conservation equations have the form

$$\frac{\partial}{\partial t}(\varphi s \eta) + \nabla \cdot (\eta \boldsymbol{q}) = Q_w \qquad (5.1)$$

and the energy conservation equation can be written as

$$\frac{\partial}{\partial t}\left(\varphi s \eta U + (1-\varphi)\rho_r C_p T\right) + \nabla \cdot (\eta \boldsymbol{q} H - \kappa \nabla T) = Q_e \qquad (5.2)$$

The Darcy flow velocity $\boldsymbol{q}$ is given by

$$\boldsymbol{q} = \frac{k k_r}{\mu} \nabla (P - \rho g z) \qquad (5.3)$$

Here, φ denotes porosity, s saturation, ρ, η mixture mass density and molar density, respectively, of the brine, q Darcy flux, k intrinsic permeability, k_r relative permeability (here set to unity as only one fluid phase is expected), μ viscosity, P pressure, g gravity, and z the vertical component of the position vector. Water density and viscosity are computed as a function of temperature and pressure through an equation of state for water. The quantity ρ_r denotes the

rock density, c_p, and κ denote the heat capacity and thermal conductivity of the porous medium-fluid system. The molar internal energy and molar enthalpy of the fluid, U and H, are obtained from an equation of state for pure water. These two quantities are related by the thermodynamic expression

$$U = H - \frac{P}{\eta} \tag{5.4}$$

Thermal conductivity κ is determined from the equation

$$\kappa = \kappa_{dry} + \sqrt{s_l}\left(\kappa_{sat} - \kappa_{dry}\right) \tag{5.5}$$

where κ_{dry} and κ_{sat} are dry and fully saturated rock thermal conductivities and s_l is liquid saturation. Here we consider fully saturated conditions at all times, hence the thermal conductivity is always κ_{sat}. Like in most continuum-based simulators, in PFLOTRAN thermal equilibrium is assumed between the liquid and solid within each cell of the model grid.

The governing mass conservation equations for the geochemical transport mode for a multiphase system is written in terms of a set of independent aqueous primary or basis species with the form

$$\frac{\partial}{\partial t}\left(\varphi \sum_a s_a \boldsymbol{\Psi}_j^a\right) + \nabla \cdot \sum_a \boldsymbol{\Omega}_j^a = Q_j - \sum_m v_{jm} I_m - \frac{\partial S_j}{\partial t} \tag{5.6}$$

and

$$\frac{\partial \varphi_m}{\partial t} = V_m I_m \tag{5.7}$$

for minerals with molar volume V_m, reaction rate I_m and volume fraction φ_m referenced to a single grid cell. The term involving S_j describes sorptive processes that are not considered here. Sums over α are over all fluid phases in the system, which in this study is only liquid H_2O. The quantity $\Psi^{\alpha}{}_j$ denotes the total concentration of the j^{th} primary species A_j in the α^{th} fluid phase defined by

$$\Psi_j^a = \delta_{la} C_j^l + \sum_{i=1}^{N_{sec}} v_{ji}^{\alpha}\, C_i^{\alpha} \tag{5.8}$$

In this equation the index l represents the aqueous electrolyte phase from which the primary species j with concentration C^l_i are chosen. The secondary species concentrations C^{α}_i are obtained from mass action equations corresponding to equilibrium conditions of the reactions

$$\sum_j v^{\alpha}_{ji} A^l_j \rightleftarrows A^{\alpha}_i \tag{5.9}$$

yielding the mass action equations

$$C^{\alpha}_i = \frac{K^{\alpha}_i}{\gamma^{\alpha}_i} \prod_j \left(\gamma^l_j C^l_j\right)^{v^{\alpha}_{ji}} \tag{5.10}$$

with equilibrium constant K^{α}_i and activity coefficients γ^{α}_k. Activity coefficients are calculated from the extended Debye-Hückel formulation.

The reaction rate I_m is based on transition state theory taken as positive for precipitation and negative for dissolution, with the form

$$I_m = -A_m \left(\sum_l k_{ml}(T) P_{ml} \right) \left| 1 - (K_m Q_m)^{\frac{1}{\sigma_m}} \right|^{\beta_m} sign(1 - K_m Q_m) \tag{5.11}$$

where the sum over l represents contributions from parallel reaction mechanisms such as pH dependence etc., and where K_m denotes the equilibrium constant of the mineral, σ_m refers to Temkin's constant which is defined as the average stoichiometric coefficient of the overall reaction (Lichtner, 1996b), β_m denotes the affinity power, A_m refers to the specific mineral surface area, and the ion activity product Q_m is defined as

$$Q_m = \prod_j \left(\gamma_j m_j\right)^{v_{jm}} \tag{5.12}$$

with molality m_j of the j^{th} primary species. The rate constant k_{ml} is a function of temperature given by the Arrhenius relation

$$k_{ml}(T) = k^0_{ml} exp\left[\frac{E_{ml}}{R}\left(\frac{1}{T_0} - \frac{1}{T}\right)\right] \tag{5.13}$$

where k^0_{ml} refers to the rate constant at the reference temperature T_0 taken as 298.15 K, with T in units of Kelvin, E_{ml} denotes the activation energy (J/mol).

Permeability, tortuosity and mineral surface area may be updated optionally due to mineral precipitation and dissolution reactions through the change in porosity. The porosity φ is updated according to

$$\varphi = 1 - \sum_m \varphi_m \qquad (5.14)$$

where φ_m is the mineral volume fraction. Thus, although possible in principle, the full feedback between chemically induced porosity change and permeability is not included in the simulations presented below. In this study only the coupling between reactive surface area and porosity is considered and implemented as

$$A_m = A_m^0 \left(\frac{\varphi_m}{\varphi_m^0} \right)^n \qquad (5.15)$$

where φ^0_m is the initial mineral volume fraction. It should be noted, however, that this result only applies to primary minerals because of the restriction $\varphi^0_m > 0$.

5.2 Pre-processing workflow

Uni Bern is in the process of deriving experimental constraints for the pore fluid composition, mineralogical composition and for mineral reactivities of the rocks of the USM. These data will be used to construct the reaction network and the thermodynamic database and to constrain the input parameters for the chemical model. For each homogeneous and heterogeneous reaction included in the simulation the equilibrium constant has to be known as a function of temperature and pressure. We use the default PFLOTRAN database that is part of the installation package, complemented by equilibrium constant will be computed from the thermodynamic databases SUPCRT92 (Johnson et al., 1992).

As the true stratigraphic succession of sand and clay layers and their hydraulic and thermal properties are not yet known for the Forsthaus site, model values are taken from previous thermal-hydraulic simulations of the Forsthaus system (e.g. Driesner et al. 2017).

5.3 Computational approach and software

We use the open source, state-of-the-art massively parallel subsurface flow and reactive transport code PFLOTRAN (*www.pflotran.org*) to carry out these simulations. PFLOTRAN

solves a system of generally nonlinear partial differential equations describing multiphase, multicomponent and multiscale reactive flow and transport in porous materials. The code is designed to run on massively parallel computing architectures as well as workstations and laptops. Parallelization is achieved through domain decomposition using the PETSc (Portable Extensible Toolkit for Scientific Computation) libraries. PFLOTRAN has been developed from the ground up for parallel scalability. The reactive transport equations are solved using a fully implicit Newton-Raphson algorithm.

PFLOTRAN uses a law-of-mass-action (LAM) approach for solving the chemical state of the system. The LAM approach is computationally efficient but it has limitations in terms of flexibility in that it is difficult to handle the effect of dynamic changes in both pressure and temperature on chemical conditions. PFLOTRAN can simulate 2-phase (gas and liquid) systems but here we assume fully liquid saturated conditions at all times. It is still possible to simulate processes such as degassing of CO_2 by using the approach proposed by Alt-Epping et al. (2013) in which the effect of CO_2 degassing was implemented via a pseudo-mineral precipitation reaction.

Two different model geometries are used to represent the Forsthaus system. The first model, presented in Section 5.5.1, involves an axisymmetric model representing a single sequence of clay-sandstone-clay in the reservoir. Although the model geometry is simple, by modifying material properties and scaling parameters it is possible to increase realism and to consider processes that occur elsewhere in the system (e.g. in the heat exchanger). The simplicity of the model allows for the implementation of geochemical complexity and detail without limitations concerning computational performance. These axisymmetric simulations typically can be run on laptop PCs within less than one hour.

The second model (Section 5.5.2) is a full scale 3D representation of the Forsthaus system. It spans the entire vertical and lateral extent of the system, comprising the main well and five supporting wells surrounding it. The model is designed, among other things, to test different well arrangements. It is constructed on the basis of a cartesian coordinate system and it is not limited by any symmetry constraints. This means that lateral heterogeneity in the stratigraphic sequence and hence in hydraulic conditions can be implemented easily. The model achieves perfect water balance between the flux through main well and total flux through all supporting wells by imposing a flux constraint for each supporting well.

5.4 Model Analysis

The models presented here are an extension of previous thermal-hydraulic models carried out

by various groups, in that we couple flow and heat transport with solute transport and chemical reactions. The outcome of these simulations provide insights into geochemical processes that are expected to occur during the operation and an assessment of the risk of geochemical processes for a sustained operation.

The simple axisymmetric model, because of its short running time, is useful for sensitivity studies and parameter optimization. These are particularly useful to assess 1) processes or parameters affecting fluid-rock reactions in the reservoir and their implications for the transmissivity of individual sandstone layers, 2) processes related to cooling of water buffered by the reservoir rock, and 3) the implication of injecting water that is in thermal and geochemical disequilibrium with the reservoir rock.

The full scale 3D model is useful for design and performance optimization (e.g. well spacing, number of wells and pumping schedule) and to address issues related to spatial heterogeneity or asymmetries in the system (e.g. lateral pinching out of strata, background groundwater flow) .

5.5 Scenarios and results

5.5.1 Simplified models of the Forsthaus system

The simplified simulations presented below were originally designed as benchmark problems for reactive transport codes (Alt-Epping and Mindel, 2020). These simulations, despite their simplicity, are highly relevant for the Forsthaus system and are useful as a basis for the full scale 3D model presented in Section 5.5.2.

5.5.1.1 1D simulation to constrain hot fluid composition at injection wellhead

This 1D flowpath simulation constitutes a preparatory step for the subsequent axisymmetric and 3D simulations. It models the closed-system chemical and thermal evolution of previously extracted USM groundwater as it passes through the surface heat exchanger, ready for pumping into the injection well during a heat storage cycle (Figure 5.1). The computed water composition is essential input for all models presented below. In the simulation USM groundwater at 15 °C is fed into a 1D flowpath and heated to 90 °C.

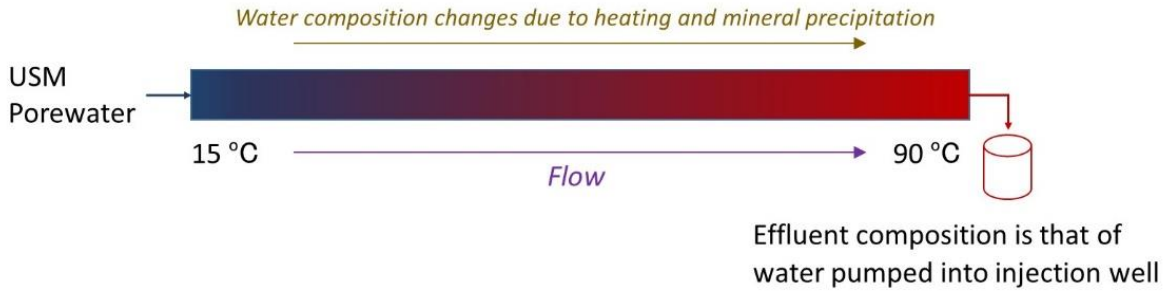

Figure 5.1: *Model of a 1D flowpath used to constrain the composition of the fluid injected into the injection well. Cold USM porewater (Table 5.1) enters on the left and is heated to 90 °C while reactions along the flowpath modify the water composition. The water extracted on the right has the temperature and composition of the water injected into the injection well in the scenarios presented below (Table 5.1).*

The flowpath is arbitrarily 38 m long and discretized into 152 cells, each having a length of 0.25 m. At the inlet of the surface installation (production wellhead) the fluid composition is that of the USM sandstone porewater summarized in Table 5.1. A linear temperature gradient of 2 °C /m is imposed along the flowpath and the fluid composition at 90 °C is read out of the model. There are no dissolving minerals along the flowpath, only mineral precipitation is allowed. Mineral thermodynamic properties are summarized in Table 5.2. Fluid flow along the flowpath is slow enough to maintain local equilibrium. The total simulation time is 730 days.

Heating of the USM groundwater to 90 ºC leads to a slight decrease in *p*H, an increase in pCO_2 and to the oversaturation of carbonate minerals calcite and "dolomite" due to their retrograde solubility with temperature (Figures 5.2 to 5.4). Dolomite is allowed to precipitate in the simulations despite its known kinetic inhibition (Section 2.1.1.4) in lieu of other metastable Mg carbonates or silicates, for which thermodynamic data are not available. The composition of the water extracted at 90 °C is shown in Table 5.1. A comparison of columns 2 and 3 in that Table reveals the compositional changes of the water due to heating and carbonate precipitation.

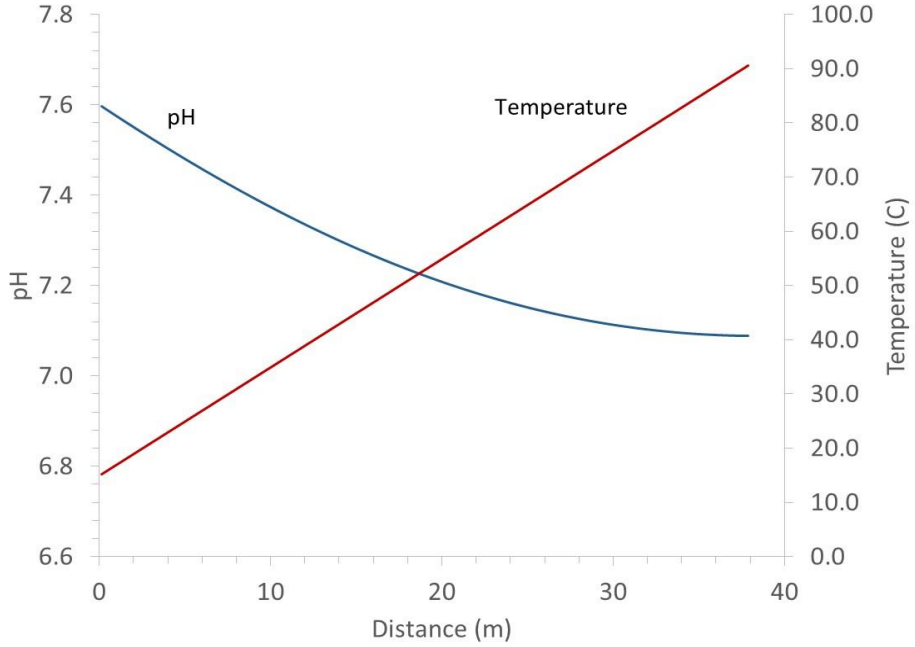

Figure 5.2: *Profiles of temperature and pH*

Mass balance calculations reveal that for a model through flow of 4215.5 kgH_2O/yr, $1.01 \cdot 10^{-4}$ m^3 of carbonate scales (calcite plus dolomite) precipitate in total. If the flow rate in the real system amounts to 25 l/s or $7.89 \cdot 10^8$ kg/yr (using a density at 15 ºC of 1001.21 kg/m^3_H_2O) then the total volume of carbonate scales produced could be as high as 18.9 m^3 per year. Assuming that a volume equivalent of 216 days or 0.59 years of pumping at 25 l/s has to be extracted from the aquifer and heated, the total amount of carbonate scales is 11.15 m^3. Taking into account the gradual heating of the aquifer and assuming that the injected temperature is actually 50 ºC (instead of 15 ºC) the total volume of carbonate minerals amounts to 6.57 m^3 for a fluid volume equivalent of 216 days of pumping at 25 l/s.

The simulations and mass balance calculations show that during loading cycles there is a substantial risk of carbonate precipitation with potentially serious consequences for a sustained operation when reservoir water is heated.

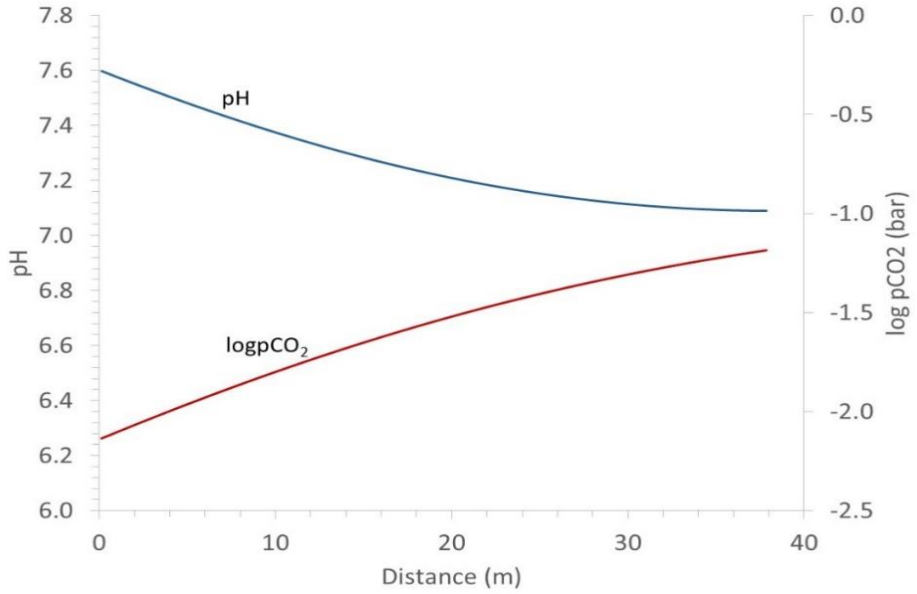

Figure 5.3: *Profiles of temperature and* pCO_2.

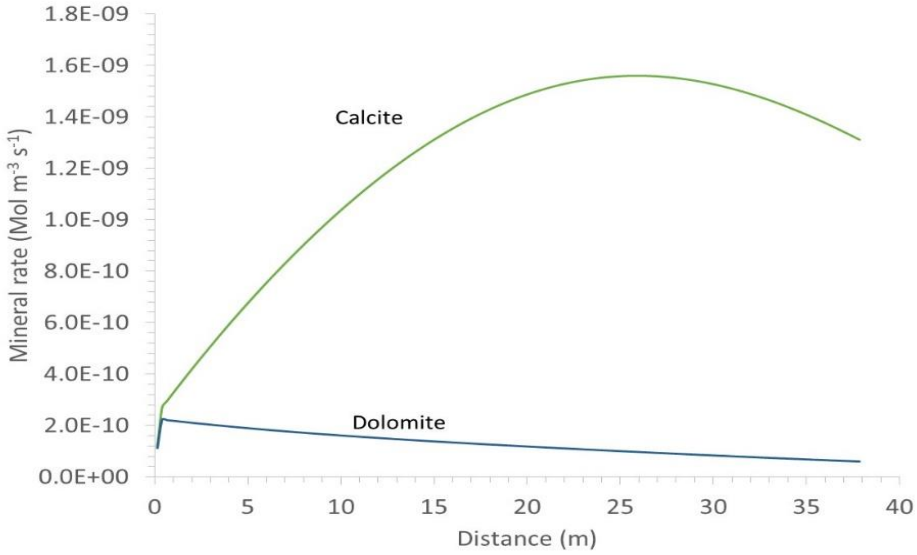

Figure 5.4: *Profiles of carbonate mineral reaction rates. Heating the USM groundwater leads to precipitation of carbonate minerals due to their retrograde solubility with respect to temperature. Dolomite is included in the simulation here despite its slow kinetics in lieu of other metastable Mg carbonates or silicates.*

Table 5.1: *Initial USM pore water compositions expressed as total concentrations and buffering mineral or gas phase, if applicable. The sandstone porewater corresponds to the water entering the flowpath in Figure 5.1. The composition of the 90 ºC water is that of the outlet water in Figure 5.1, corresponding to the composition of the water injected at the well heads.*

	Clay (15 °C)	**Sandstone (15 °C)**	**Inj. water at well head (90 °C)**
Tracer	1e-5	1e-5	1.0
SiO_2,aq	6.04e-5 (Quartz eq.)	6.04e-5 (Quartz eq.)	6.04e-5
*p*H	7.6	7.6	7.014
Na^+	Charge	Charge	Charge
Cl^-	8.69e-4	8.69e-4	8.69e-4
Ca^{++}	7.53e-5 (Calcite eq.)	7.53e-5 (Calcite eq.)	3.18e-4 (Calcite eq.)
Mg^{++}	5.68e-6 (Dolomite eq.)	5.68e-6 (Dolomite eq.)	1.3e-5 (Dolomite eq.)
K^+	7.16e-5	7.16e-5	7.16e-5
Al^{+++}	1e-12	1e-12	1e-12
log(*p*CO_2) (bar)	-2.15	-2.15	-1.1236
SO_4--	2.34e-4	2.34e-4	2.34e-4

Table 5.2: *Mineral kinetic properties.*

	Log rate constant (neutral) mol m^{-2} sec^{-1}	**Activation energy (J/mol) (neutral)**	**Log rate constant (acid) mol m^{-2} sec^{-1}**	**Prefactor (H^+)**	**Activation energy (J/mol) (acid)**	**Reactive surface area m^2/m^3_{bulk}**
Quartz	-13.4	90	-	-	-	1
Calcite	-5.81	14.4	-0.3	1	23.5	1
Dolomite	-7.53	52.2	-3.19	0.5	36.1	1
Albite	-12.56	70	-10.16	0.457	14.4	1
K-feldspar	-12.41	38	-10.06	0.5	51.5	1
Illite	-13.55	22	-11.85	0.37	22	1
Muscovite	-13.55	22	-11.85	0.37	22	1
Ca-Smectite	-12.78	35	-10.98	0.34	12.6	1
Na-Smectite	-12.78	35	-10.98	0.34	12.6	1
Kaolinite	-13.18	22.2	-11.31	0.777	65.9	1
Mg-chlorite	-12.52	88	-11.11	0.5	88	1
Gypsum	-2.79	0	-	-	-	1
Anhydrite	-3.19	14.3	-	-	-	1
SiO_2(am)	-9.42	49.8	-	-	-	100
CO_2(s)	-6	50	-	-	-	100

5.5.1.2 Injection/extraction scenarios with heat and tracer transport in an axisymmetric model

An important feature of regulatory and energetic concern is the spatial extent of the thermal and the geochemical plumes around the injection well. This is defined as the distance over

which compositional changes of the original porewater induced by the operation are detectable around the well. An axisymmetric model of the reservoir (Figures 5.5 and 5.6) is used to simulate the injection and extraction schedule summarized in Table 5.3. Simulations are carried out for an operation period of 10 years. The model comprises a vertical sequence of clay-sandstone-clay layers, each having a thickness of 5 m. The physical properties of the materials are summarised in Table 5.4. Because of the symmetry of the reservoir in the upper panel of Figure 5.5 with respect to the horizontal plane at mid-depth, we only consider the lower half of the model in the simulation. Injection and extraction are performed alternately through the single well located in the centre (i.e. along the centre axis) of the cylindrical model. The injection/extraction rate is 25 l/s scaled by a factor that corresponds to the model thickness over the total thickness of the system. No reactions are included in this simulation yet, only solute and heat transport are considered. Solute transport is implemented via a non-reactive tracer dissolved in the injected water. No natural fluid flow in the reservoir is assumed. Outward transport of the tracer occurs due to this pressure differential upon injection and to diffusion and dispersion through the porewater. Heat is transported by advection and conduction.

Table 5.3: *Annual schedule of injection/extraction cycles (note: PFLOTRAN requires a temperature condition at the extraction well which is set to be 50 ºC).*

Time (d)	Q (L/s)	T (°C)	Inject	Extract
0-216	25	90	x	
216-365	25	50		x

Table 5.4: *Physical properties if the material.*

	Sandstone	Clay-stone	Screen	Well
Porosity	0.1	0.05	0.5	1.0
Tortuosity	0.05	0.05	0.05	1.0
Permeability (m^2)	3.45e-13	2.6e-17	1e-10	1e-10
Dispersivity (transverse and longitudinal) (m)	1e-3	1e-3	0.0	0.0
Heat capacity (J kg^{-1} K^{-1})	750	750	750	818
Thermal conductivity (W m^{-1} K^{-1})	2.67	2.67	1e-5	1.6
Density (kg/m^3)	2743	2743	2780	2000

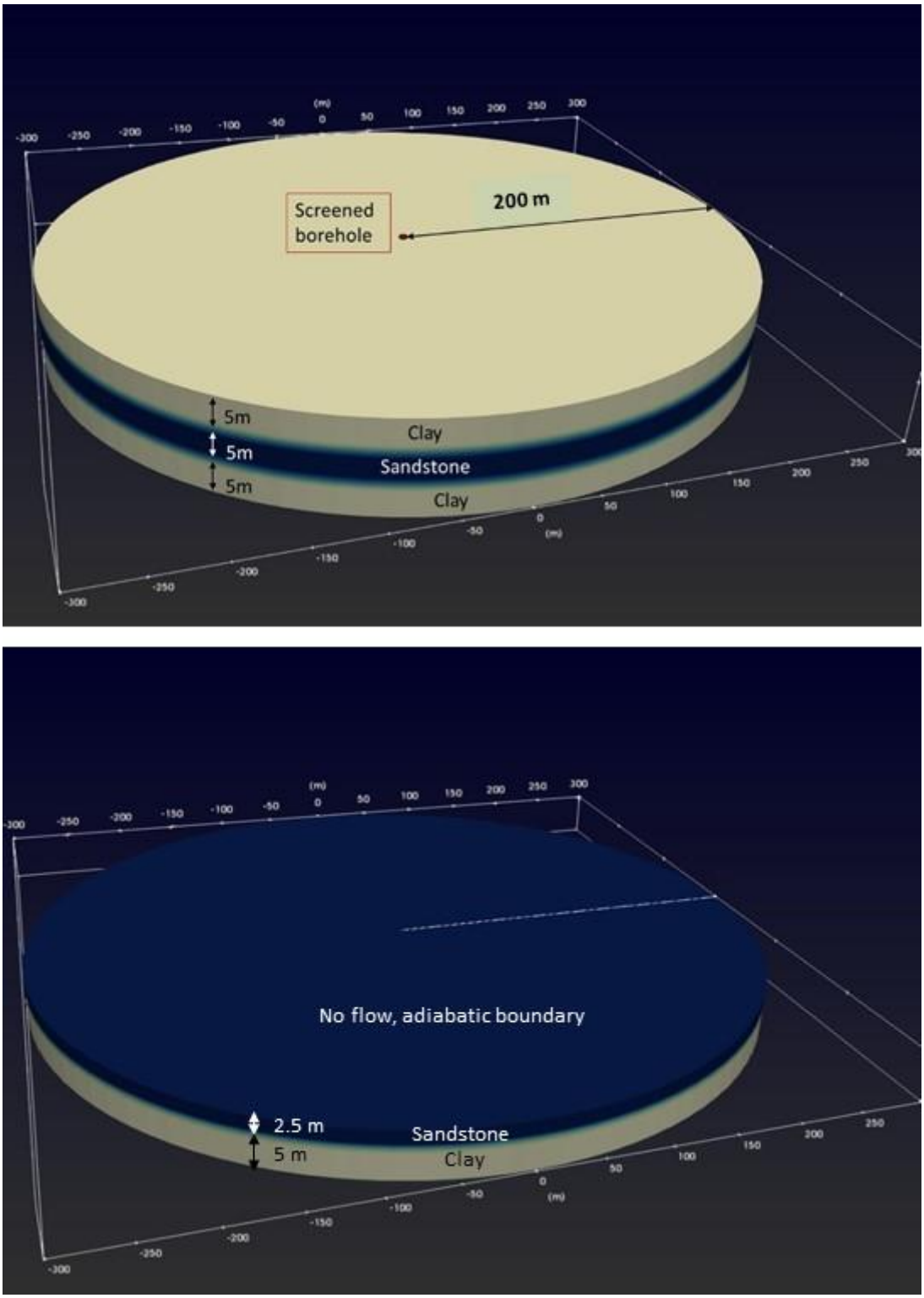

Figure 5.5: *Simplified model of the Forsthaus system with a single permeable sandstone unit sandwiched between low-permeability clays (upper panel). Lower panel: actual model domain making use of the horizontal plane of symmetry at mid-depth.*

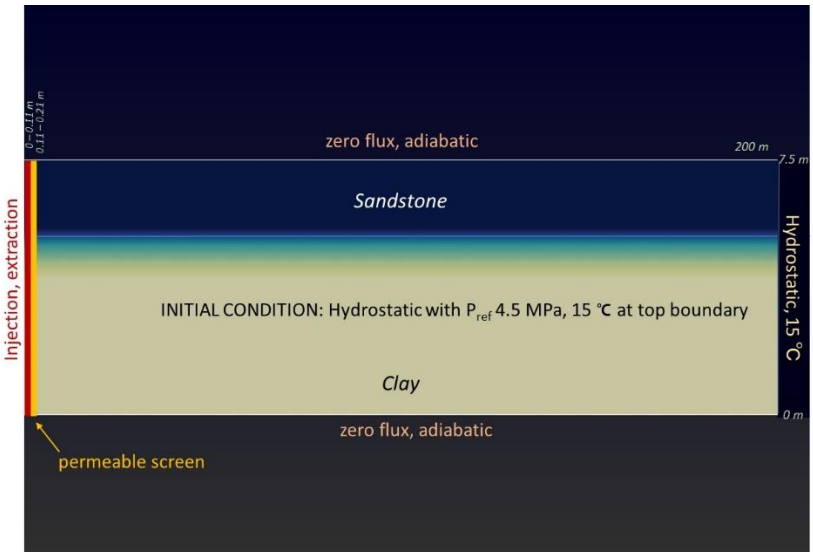

Figure 5.6: *Model dimensions (not to scale) and boundary and initial conditions for flow and heat transport.*

The simulation output shows regular fluctuations of pressure according to injection/extraction cycles. The amplitude of these pressure fluctuations decreases with increasing distance from the well but the perturbation of fluid pressure due to pumping extends well beyond a distance of 100 m from the well (5.7).

The temperature increases and decreases upon injection and extraction, respectively, according to the pumping schedule in Table 5.3. While in close vicinity of the injection well the temperature of the sandstone aquifer acquires and maintains the injection temperature of 90 °C over each injection cycle, the extraction temperature increases over time. Likewise, further away from the well (e.g. at 50.25 m, Figure 5.7) the temperature exhibits a gradual increase over time. This temperature increase indicates a gradual heating of the reservoir (which involves both the sandstone and the clay units). Thermal effects becomes weaker with increasing distance from the injection site – there is virtually no change in temperature at a distance of 100 m from the injection/production well over a period of 10 years.

In contrast, the tracer moves much faster and penetrates deeper into the reservoir than the temperature. This is because tracer transport is confined to the connected porosity while heat transport occurs through the bulk medium, consisting of liquid and solid. Hence, in PFLOTRAN for a given Darcy flux (i.e. volume of liquid per unit area per time) the tracer flow velocity scales inversely with porosity, while the thermal front moves at the rate of the Darcy flux. At observation points close to the well, the injection concentration of 1 mol/kg is attained rapidly and maintained during the 10 year operation period. During the first injection a fraction of the tracer migrates beyond 100 m into the reservoir.

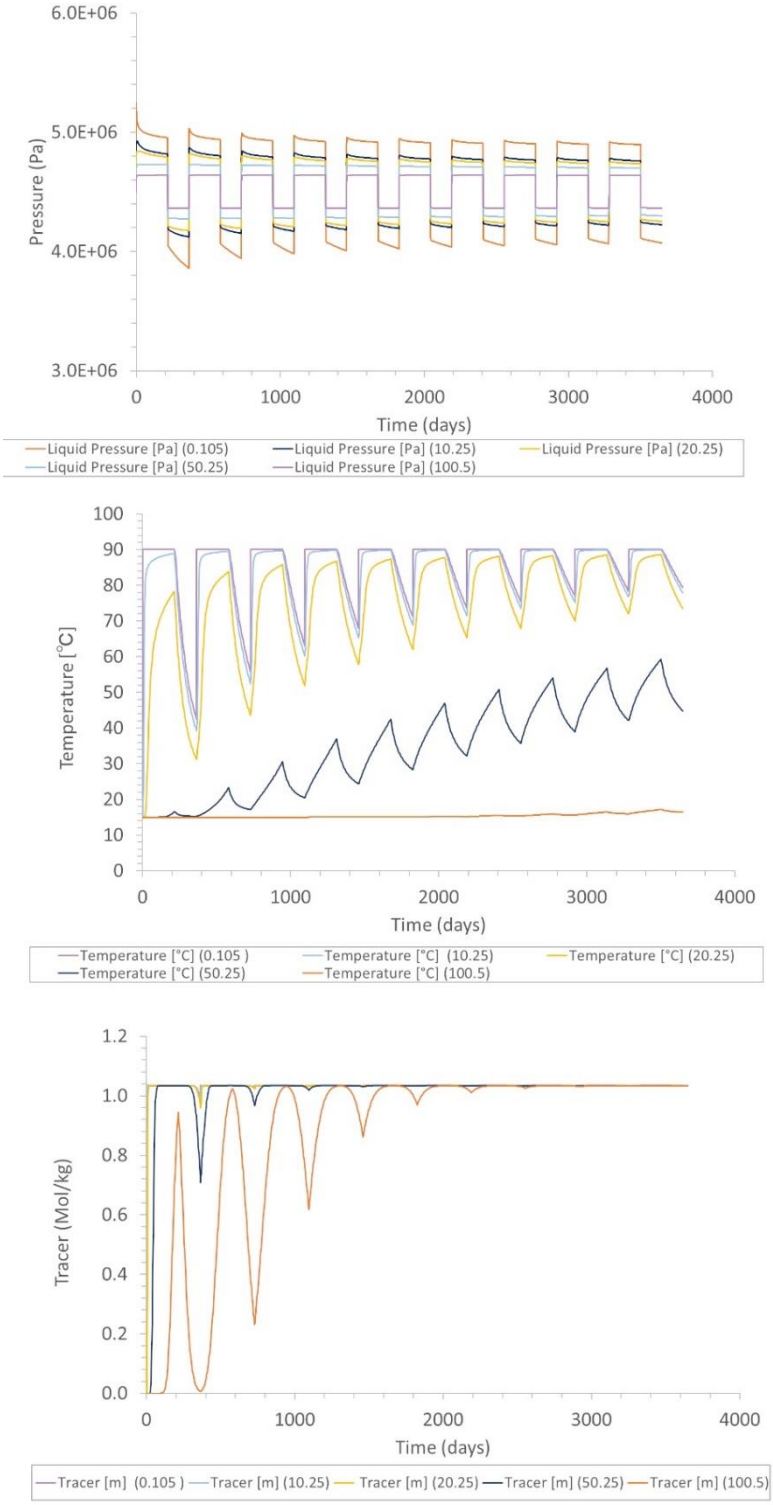

Figure 5.7: *Time series of pressure, temperature and tracer concentration at different distances from the well. While the pressure fluctuates regularly (upper panel), the system heats up over time (e.g. temperature panel at 50.25 m). The thermal plume does not extend beyond 100 m after a 10 year period (middle panel). In contrast, solute transport (lower panel) affects a much larger region that extends well beyond 100 m (although it takes about 5 injection cycles to establish constant tracer concentrations at 100 m).*

In the following extraction cycle much of the tracer mass is flushed out of the sandstone, as dilute water is drawn from the more distal part of the aquifer (note, the observation point at 100 m is not affected by the influx of water across the right-hand boundary). Because the injection period is longer than the extraction period, with each injection-extraction cycle, the tracer migrates deeper into the aquifer so that, ultimately, at r = 100 m the tracer attains the injected concentration of 1 mol/kg at r = 100 m (Figure 5.7).

The results from this simulation are important because they demonstrate that the "radius of influence" of the operation, if defined on the basis of solute transport, far exceeds that defined by the thermal plume. This effect becomes even more pronounced if the volume of the injected water exceeds that of the extracted water.

5.5.1.3 Implementing complex chemistry into axisymmetric model

We use the same injection-extraction schedule, temperature constraints and domain geometry as in the previous simulation case. Here we couple the previous simulation with a full reaction network. The composition of the injected water is taken from Table 5.1. The primary mineralogy of the clay and sandstone units are given in Table 5.5. In Table 5.6 all species (primary and secondary) as well as all gases and minerals considered in the model are given. Note that the minerals amorphous silica and "CO_2(s)" are omitted here as these minerals are specifically used to assess processes in the heat exchanger which are addressed in the next section.

Table 5.5: *Mineral composition (volume fraction) of the clay and sandstone units in the USM.*

	Clay	**Sandstone**
Quartz	0.18	0.35
Calcite	0.15	0.12
Dolomite	0.05	0.02
Albite	0.10	0.18
K-feldspar	0.07	0.11
Illite	0.10	0.05
Muscovite	0.10	0.05
Ca-Smectite	0.10	0.05
Na-Smectite	0.10	0.05
Kaolinite	0.00	0.00
Mg-chlorite	0.05	0.02
Gypsum	0.00	0.00
Anhydrite	0.00	0.00
SiO_2(am)	-	-
CO_2(s)	-	-

Table 5.6: *Full list of component (primary) species, secondary species, minerals and gases:*

Component species	Secondary species	Gases
$SiO_2(aq)$	OH^-	$CO_2(g)$
H^+	$CO_2(aq)$	
Na^+	CO_3^{--}	Minerals
Cl^-	$H_3SiO_4^-$	Quartz
Ca^{++}	$HSiO_3^-$	Calcite
Mg^{++}	$MgOH^+$	Dolomite
K^+	$MgCO_3(aq)$	Albite
Al^{+++}	$MgHCO_3^+$	K-Feldspar
HCO_3^-	$MgCl^+$	Illite
SO_4^{--}	$MgSO_4(aq)$	Muscovite
	$CaCO_3(aq)$	Smectite-Na
	$CaHCO_3^+$	Smectite-Ca
	$CaCl_2(aq)$	Kaolinite
	$CaSO_4(aq)$	Clinochlore-14A
	KCl(aq)	Gypsum
	NaCl(aq)	Anhydrite
	NaOH(aq)	Amorphous silica
	$NaCO_3^-$	"$CO_2(s)$"[1]
	$NaHCO_3(aq)$	
	$AlOH^{++}$	
	$Al(OH)_2$	

[1]Dummy mineral representing $CO_2(g)$ solubility at 3 bar.

Spatial profiles through the sandstone layer showing the tracer composition, temperature, pH and the rates of calcite and dolomite dissolution/precipitation after 214 days (at the end of the first injection period) and 363 days (at the end of the first extraction period) are shown in Figures 5.8 to 5.10. The spatial profiles of the tracer and temperature in Figure 5.8 are consistent with the conclusion from the previous section, that the tracer front propagates much deeper into the aquifer than the thermal front.

Mineral reactions are dominated by calcite dissolution and precipitation (Figure 5.9), consistent with experimental results presented in Chapter 4. All mineral reactions are confined within a radius of about 50 m from the well (Figures 5.9 and 5.10). During injection, strong calcite and minor dolomite dissolution occurs while during extraction both minerals precipitate. This alternation between carbonate dissolution and precipitation also takes places at greater distance from the well, only at lower rates and with a certain time lag, as the injection zone (i.e. the zone affected by thermal or compositional changes due to injection) grows in size.

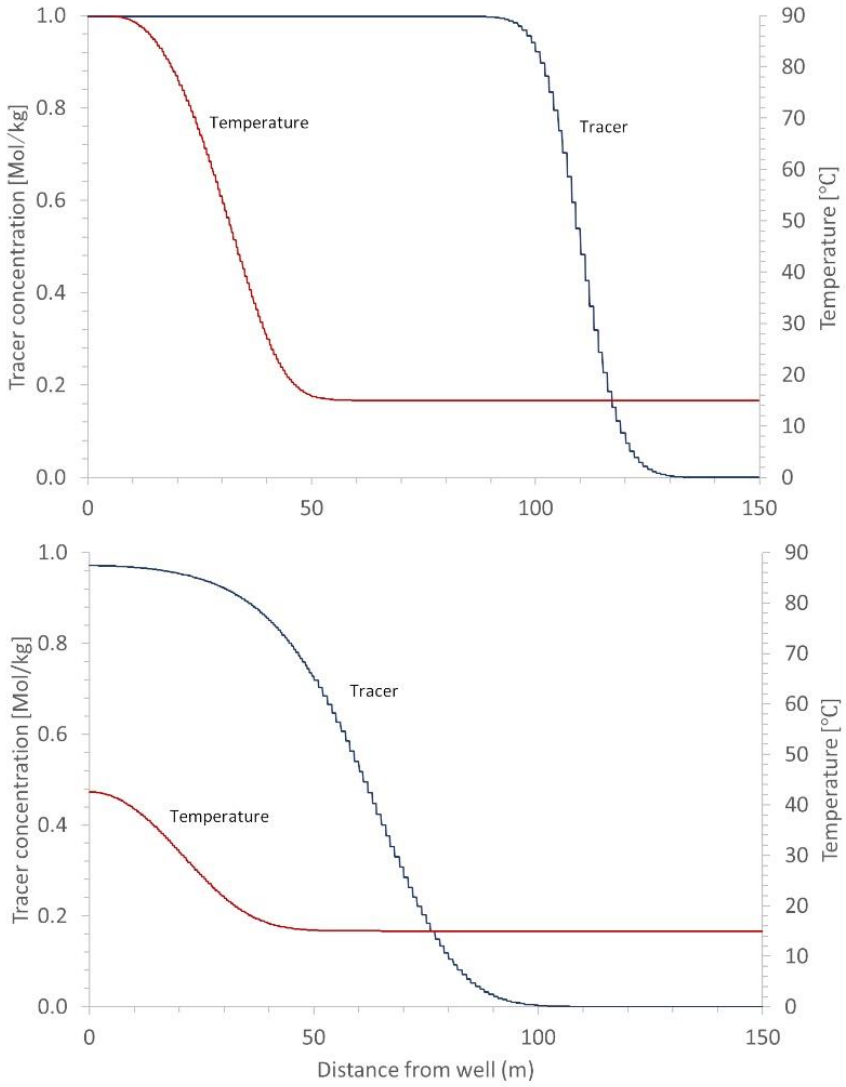

Figure 5.8: *Spatial profiles of the tracer, temperature and pH after 214 days (end of first injection, upper panel) and 363 days (end of first extraction, lower panel. Tracer and pH perturbations advance and retract upon injection and extraction cycles. Owing to the fact that the injected water volume exceeds the extracted volume, over time the thermal and chemical fronts are pushed progressively deeper into the system. Note the slower breakthrough of the thermal plume compared with the tracer breakthrough.*

In contrast, the *p*H shows a slight drop towards the well, because the injected water is very slightly more acidic than the water in the reservoir (Table 5.1). There is little difference in the *p*H profiles between injection and extraction periods. The behaviour of carbonate minerals is most likely controlled by thermal conditions, more specifically, by the slow evolution of the thermal conditions compared to solute transport. During injection, solutes are transported beyond the thermal front, implying that injected water undergoes cooling as it moves deeper into the aquifer. As the injected fluid is increasingly undersaturated with respect to carbonates

at all temperatures below 90 °C, it dissolves carbonates as it cools. Upon extraction, cooler water from the distal parts of the aquifer is pumped towards the well, where the rock is relatively warm from the previous injection cycle. As a consequence, carbonate minerals precipitate due to their retrograde solubility with respect to temperature.

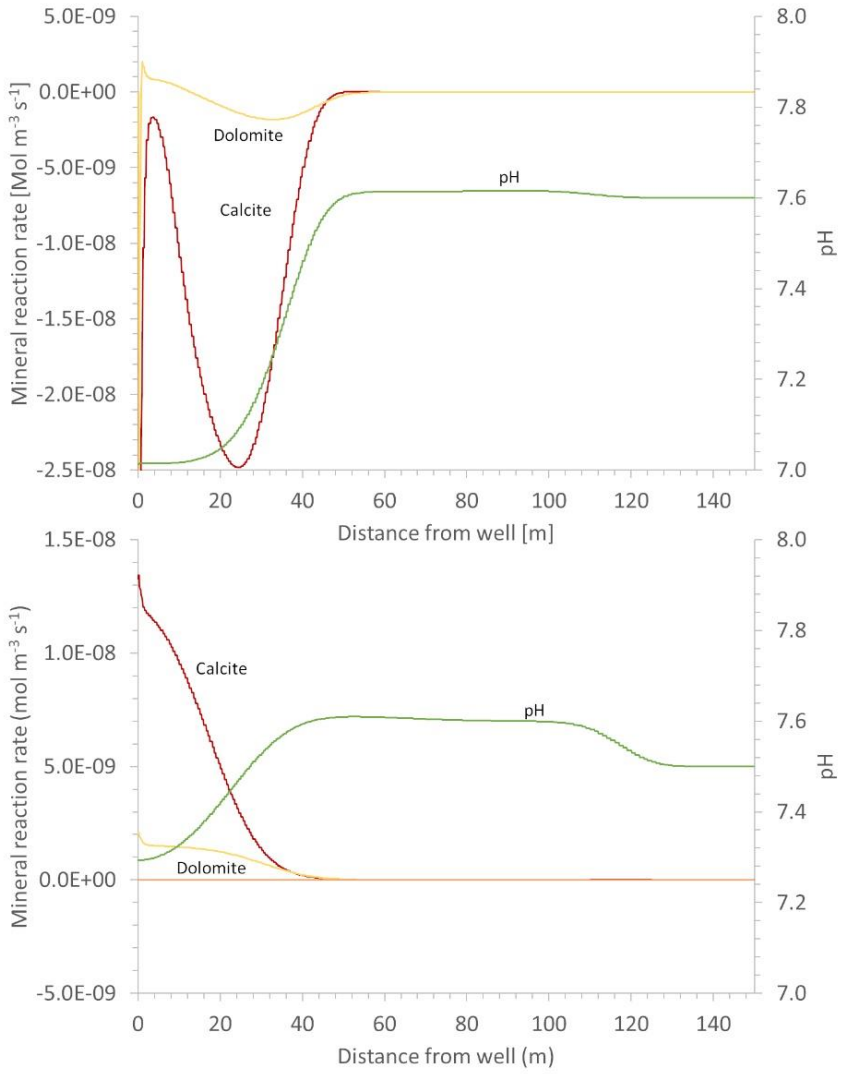

Figure 5.9: *Carbonate mineral reaction rates after 214 days (end of first injection, upper panel) and 363 days (end of first extraction, lower panel. Both carbonate minerals precipitate dissolve and precipitate upon injection and extraction, respectively, within a radius of about 50 m. These reactions are controlled primarily by the direction of flow across isotherms: During injection the water is cooled as it moves away from the well inducing carbonate undersaturation. During extraction the water is heated as it moves towards the well inducing carbonate oversaturation.*

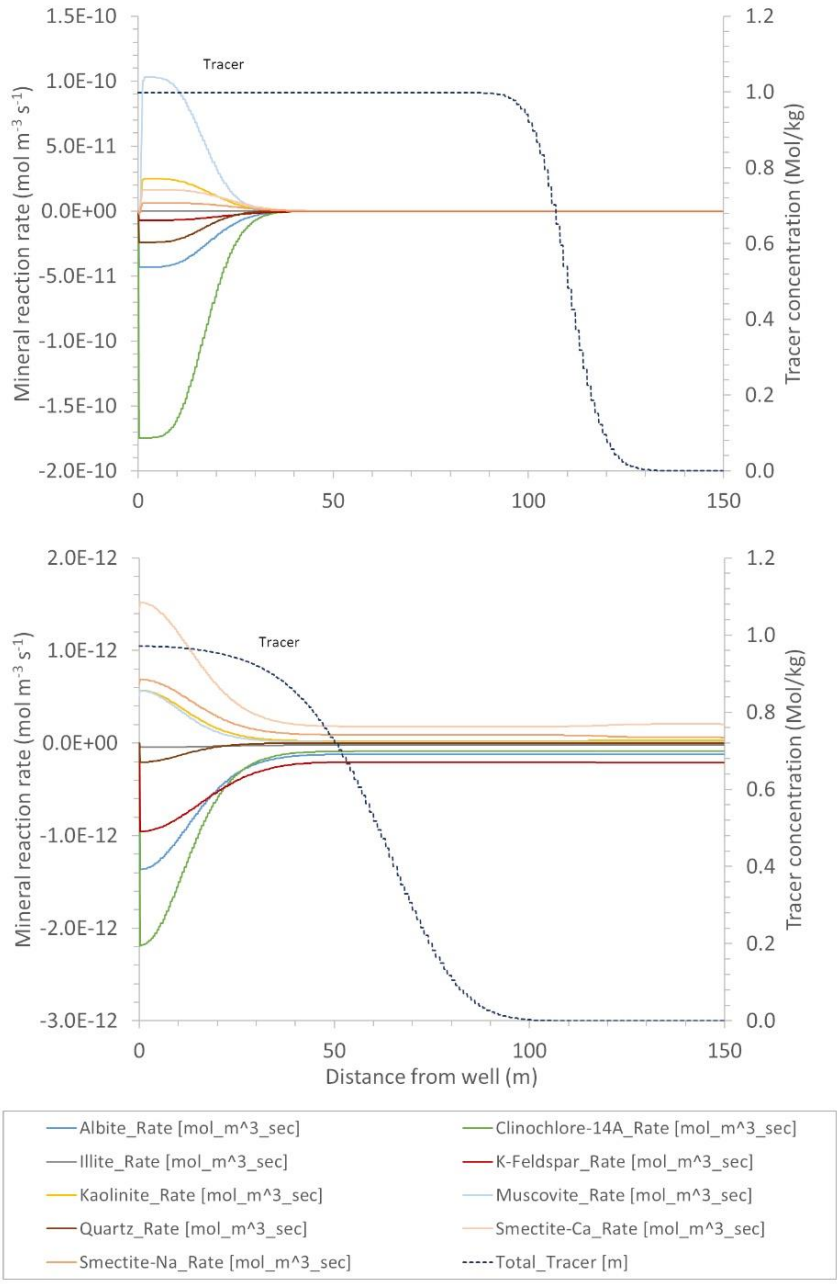

Figure 5.10: *Reaction rates of alumino-silicates after 214 days (end of first injection, upper panel) and 363 days (end of first extraction, lower panel. Profiles show that kaolinite is the main alteration phase near the well, and muscovite occurs in small amounts. Kaolinite precipitates following the hydration of feldspars. Minor smectite forms during extraction and re-dissolves upon injection.*

The reactivity of silicate minerals is orders of magnitude lower than that of the carbonate minerals (Figure 5.10). It is dominated by the hydration of feldspars to an assemblage of clay minerals. While all primary minerals dissolve continuously, regardless of whether water is pumped in or out, the composition of the clay assemblage is sensitive to the pumping

conditions. During injection, the clay assemblage is dominated by muscovite, during extraction by smectite (Ca- and Na-endmembers).

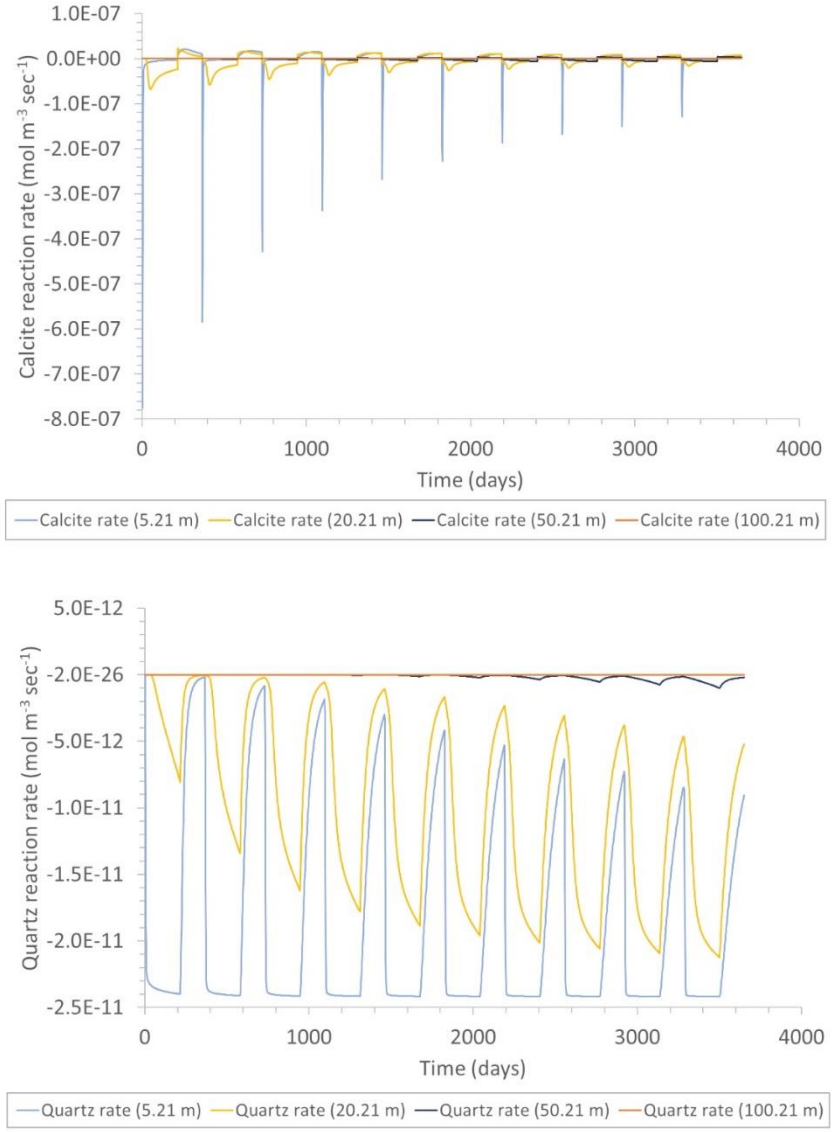

Figure 5.11: *Upper panel: The alternating dissolution and precipitation of calcite upon injection and extraction as can be seen in Figure 5.8 can be seen here as well. Notable is the very short period of calcite dissolution at the beginning of each injection period. Lower panel: quartz dissolves in the vicinity of the injection site. Quartz undersaturation follows from the fact that the injected water constitutes heated USM groundwater. The dependence of the quartz reactivity on temperature is evident from the increasing dissolution rate at 20.21 m and 50.21 m.*

Quartz dissolves at all times. The reason for this is that the injected water constitutes heated USM pore-water that has had no contact with quartz after leaving the reservoir. Because of its prograde solubility, quartz is strongly undersaturated in the hot injected water and

hence it dissolves in the injection zone within the reservoir. During extraction relatively cool water is drawn from the distal parts of the reservoir towards the well where temperatures are higher (Figure 5.8). Here too, owing to its prograde solubility with temperature, quartz becomes undersaturated and dissolves from the reservoir rock.

Time series at observation points at different distances from the well (Figures 5.11 and 5.12) show that at 100 m away from the injection well no mineral reactions take place over the simulated 10 year period. Very small fluctuation in the *p*H can be seen (Figure 5.12). At shorter distances from the well (20 - 50 m), chemical conditions change gradually over time. Superimposed on these gradual changes are fluctuations related to alternating periods of injection and extraction. For instance, the rate of quartz dissolution increases gradually (Figure 5.11), while the *p*H decreases (Figure 5.12). These gradual changes are caused by the heating of the reservoir. The thermal plume around the injection zone extends to a distance beyond 50 m but never reaches 100 m within the 10 year period (Figure 5.7, middle panel). The increase in quartz dissolution over time is an indication of its prograde solubility with respect to temperature and/or the temperature dependence of the rate constant (Equation 5.13).

Closer to the well, the amplitude of pumping-related fluctuations in chemical conditions increases compared to the fluctuations in the more distal parts of the reservoir. However, the amplitude tends to decrease over time. For quartz (Figure 5.11), this decrease in amplitude is related to an increase in the dissolution rate during extraction. The behaviour of quartz correlates with the temperature evolution in Figure 5.7, middle panel, indicating that the rate of quartz dissolution is temperature controlled.

One of the risks for a sustained operation related to chemical processes is that of clogging pore space and reducing permeability in the reservoir due to fluid-rock reactions. Porosity changes due to mineral reactions are readily predicted and they provide an indication of the expected change in permeability provided that a relation between porosity and permeability exists. Similarly, the dissolution of calcite cement may lead to the release of sandgrains that may clog flowpaths downstream or lead to physical corrosion in the wells or the surface installation. Although the behaviour of calcite can be readily assessed with the THC model presented here, the potential release of sand as suspended load and its implication for the reservoir permeability or corrosion are more difficult to predict and are beyond the scope of this modelling study.

Figures 5.9 and 5.10 show the mineral dissolution and precipitation reactions that occur in the injection zone. Carbonate minerals are orders of magnitude more reactive than the silicate minerals. Aside from their low reactivity, the effect of reactions involving silicate minerals

on porosity is negligible because the volume of dissolved primary minerals is partly compensated by the volume of precipitated clay minerals.

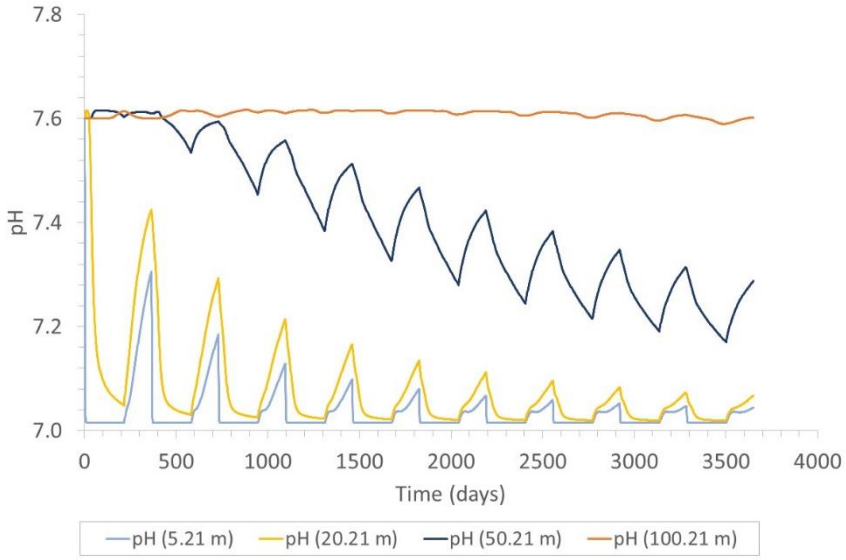

Figure 5.12: *The pH of the initial, undisturbed sandstone is set to 7.6. This value is maintained (with slight fluctuations) in the distal parts of the domain (e.g. at 100.21 m). Closer to the injection well the pH decreases over time, consistent with a lower pH (7.09) of the injected water.*

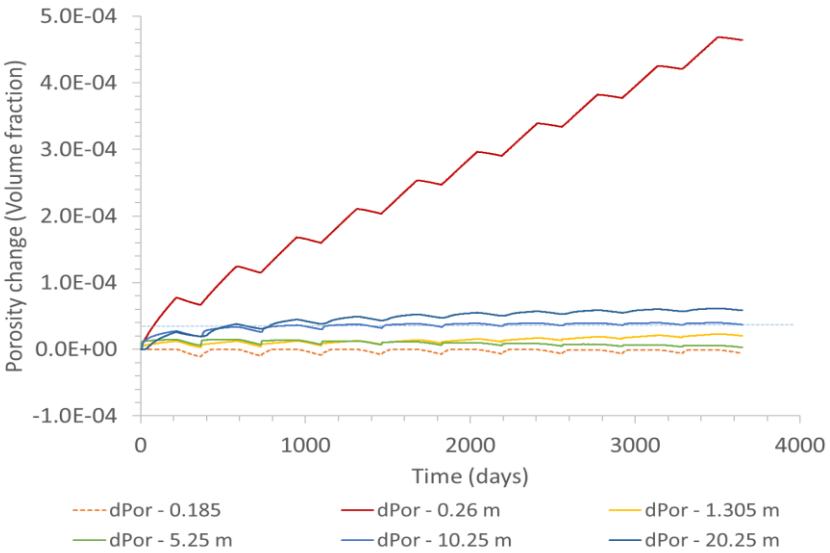

Figure 5.13: *Porosity evolution at different observation points along the aquifer. Most of the porosity changes are due to carbonate dissolution/precipitation reactions. The porosity changes are very small and not likely to affect aquifer permeability and hence the operation of the system.*

While silicate reactions are only mildly affected by alternating pumping scenarios, calcite and dolomite precipitate during extraction and (re)dissolve during injection. Although their reaction rates are high, because of alternating precipitation/dissolution the time-integrated effect of carbonate reactions on porosity is small (Figure 5.13) and there is virtually no risk of clogging. In fact, all reactions in the injection zone combined lead to a porosity increase. It follows that a serious decrease in permeability within the reservoir is very unlikely.

5.5.1.4 Implementing a heat exchanger into the axisymmetric model

Given the simplified geometry of the model, implementing the ascent of the water from the reservoir and its cooling in the heat exchanger can only be a crude approximation of reality. The heat exchanger constitutes a region where the fluid undergoes rapid cooling and heating during unloading and loading cycles, respectively. Here we only consider cooling in the heat exchanger during extraction. During injection we impose the same injection conditions, temperature and water composition, as in the previous section. A heat exchanger that accounts for these alternating conditions during injection and extraction is implemented by changing the properties of the well from an injection well to an extraction well in combination with a heat exchanger at the beginning of each injection and extraction cycle, respectively. The heat exchanger (the red area in Figure 5.14) is implemented in the model as follows:

(1) The thermal conductivity of the well is purposefully increased to an arbitrary high value.
(2) The temperature along the section where the well meets the upper model boundary is set to the desired lowest temperature in the heat exchanger, which is assumed to be 20 ºC
(3) The well attains the desired temperature of the heat exchanger throughout
(4) The heat capacity is set to an arbitrary high value
(5) Mineral precipitation reactions are turned on
(6) Mineral precipitation rates are increased by a factor of 100 to achieve mineral equilibration within the short interval of the model heat exchanger

Between each change from extraction to injection there is one day during which all properties of the well and heat exchanger are reset to injection conditions. To preserve those minerals that precipitated in the well and in the heat exchanger during extraction and to allow them to accumulate in time, during each injection period the reactivity of these minerals is is set to zero.

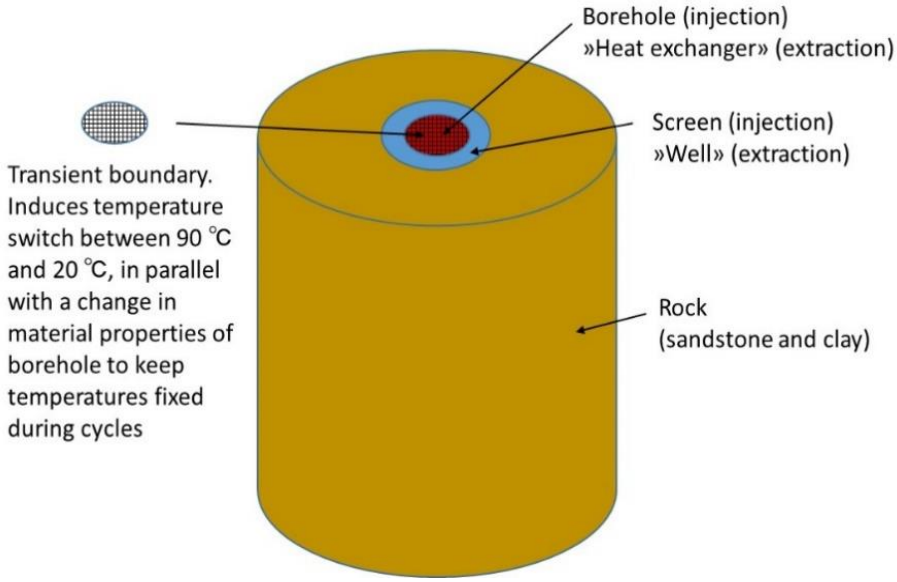

Figure 5.14: *Concept of switching boundary conditions and material properties to approximate conditions in the installations (well and heat exchanger) in the real system.*

In addition, the well screen (the blue area in Figure 5.14) is used to mimic an extraction well. During extraction in the real system, water enters the well where it is no longer buffered by any dissolving minerals but undergoes pressure and temperature changes while ascending to the surface. Analogously to the real system, in the model screen the water moves from rock buffered conditions to unbuffered conditions. In the screen only mineral precipitation is allowed during extraction periods, mimicking the formation of scales in the real extraction well. Mineral precipitation rates are increased by two orders of magnitude to achieve instantaneous mineral equilibration within the interval of the screen which is much shorter than the real wells.

However, because of the much shorter interval of the screen, we cannot model the pressure and temperature changes within a well in detail. Instead, we assume that the water ascends fast enough to maintain its reservoir temperature during ascent. Pressure changes are not accounted for.

We focus on processes in the immediate vicinity of the well, in the region $r < 10.21$ m. The innermost observation point ($r = 0.105$ m) is located within the region in which properties alternate between an injection well and a heat exchanger during injection and extraction cycles, respectively. The temperature–time series illustrates this behaviour (Figure 5.15). During injection, the temperature of the well is that of the injected water (i.e. 90 ºC). During extraction the well is cooled to 20 ºC, assumed to be the lowest water temperature in the heat exchanger.

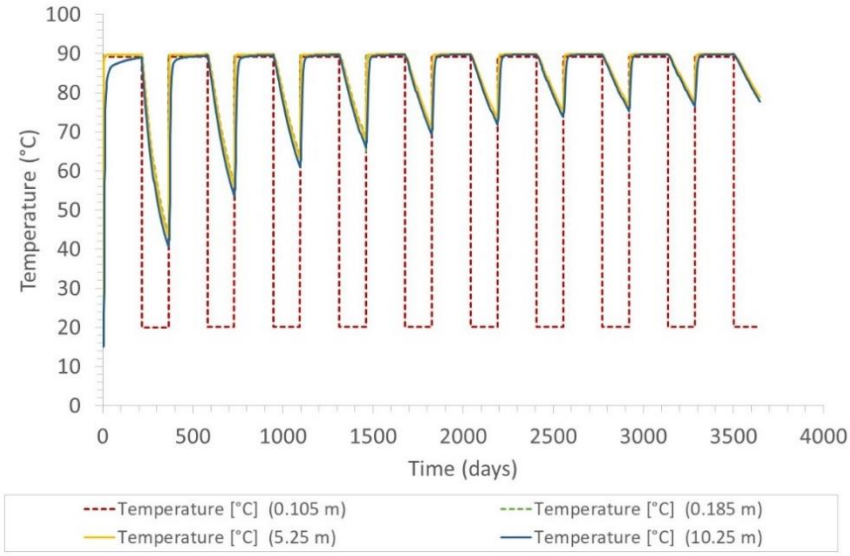

Figure 5.15: *Temperature evolution in the injection well/heat exchanger (0.105 m) and at greater distance from the well.*

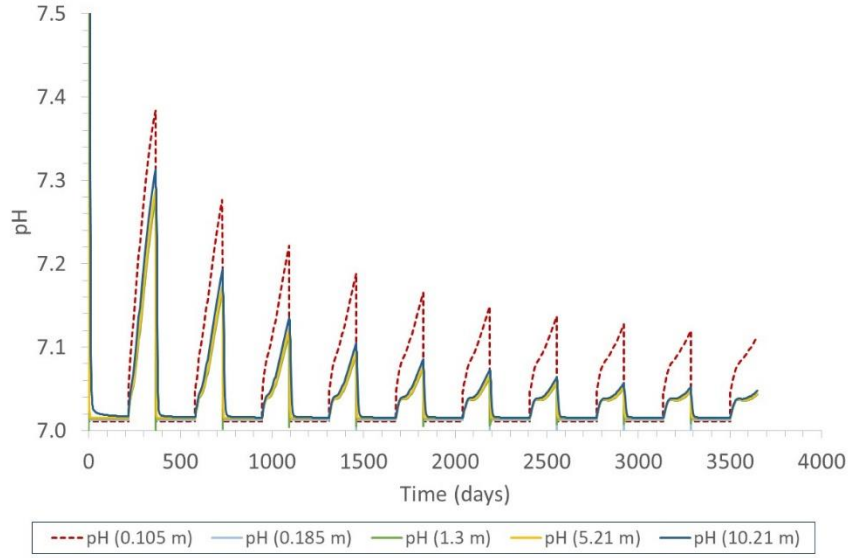

Figure 5.16: *The pH shows fluctuations between that of the injected water (pH = 7.01) and that of the rock buffered water during injection and extraction cycles respectively.*

The observation point at r = 0.185 m is located in the "screen" representing the well. The screen is thermally isolated from the heat exchanger, and the temperature is solely controlled by the movement of water (Figure 5.15). Chemical conditions are analogous to the well in the real system in that there are no primary minerals that can dissolve; only mineral precipitation is considered. The screen thus represents an interval in which the groundwater moves from rock buffered to unbuffered conditions. Precipitating minerals accumulate, mimicking the formation of scales.

Figure 5.16 shows the constant *p*H during injection periods (i.e. the *p*H of the injected water, Table 5.1) and the *p*H of the water extracted from the reservoir during extraction periods. The *p*H shows a general decrease in time, but there is a *p*H increase related to cooling in the heat exchanger (0.105 m). Calcite precipitation occurs in the "well" (i.e. the screen, 0.185 m). The water entering the screen is slightly oversaturated with calcite, owing to relatively high flow velocities in combination with heating in the vicinity of the well. The high precipitation rates in the screen that were imposed to scale the amounts of minerals precipitating in the screen to those precipitating along the length of the real well, lead to high rates of calcite precipitation. This indicates that calcite scaling in the well has to be expected during extraction (Figures 5.17 and 5.18). There is no calcite precipitation in the heat exchanger during extraction due to its retrograde solubility. In the reservoir surrounding the well, calcite dissolution occurs during injection, consistent with Figure 5.9.

Cooling the water in the heat exchanger lowers the solubility of alumino-silicates leading to the precipitation of small amounts of clay minerals in the heat exchanger (Figure 5.19). It is interesting to note that neither quartz nor amorphous silica attain saturation. There may be two reason for this: 1) the extracted water is undersaturated with respect to quartz because the water temperature increases as the water is drawn towards the well, and 2) the precipitation of clay minerals consumes SiO_2(aq) such that it is no longer available for the formation of quartz.

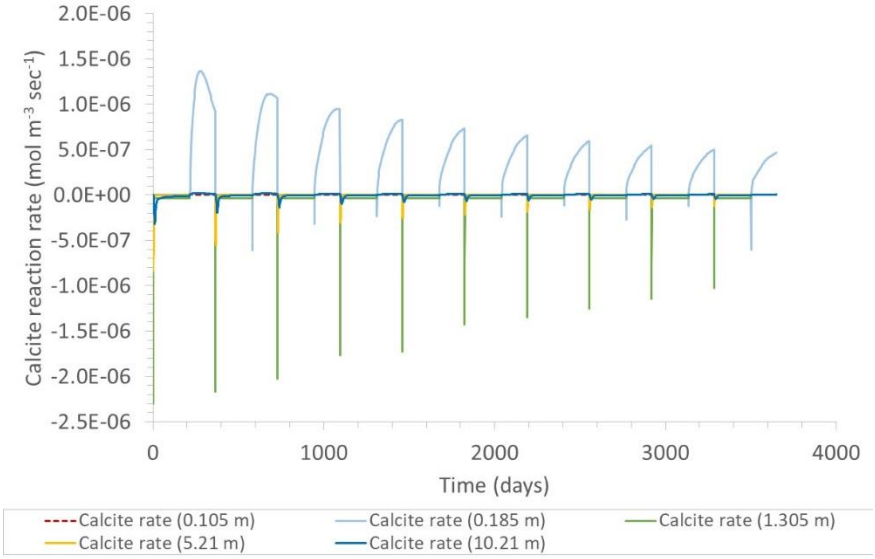

Figure 5.17: *Calcite precipitates in the screen (representing the well in the real system) at r = 0.185 m during extraction and dissolves in the reservoir during injection.*

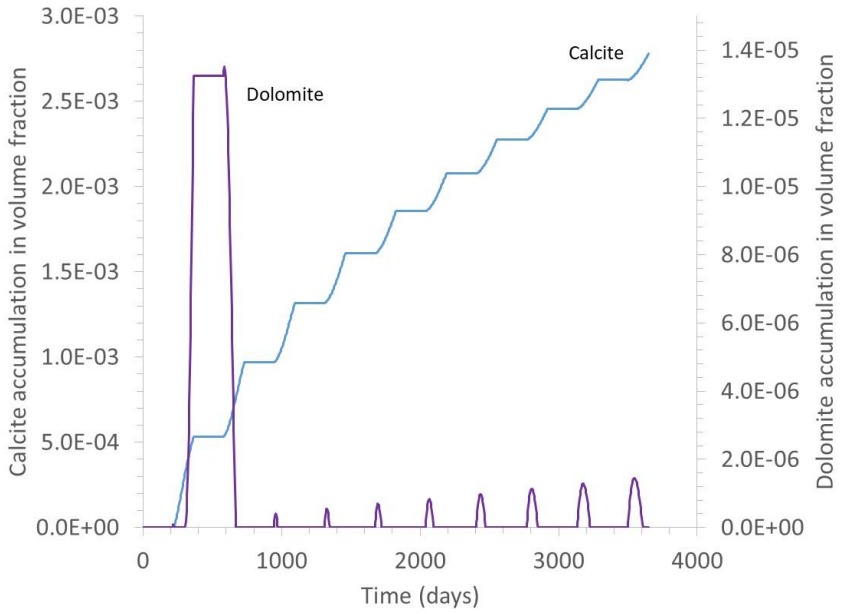

Figure 5.18: *Accumulation of calcite and dolomite in the screen (representing scale formation in the well).*

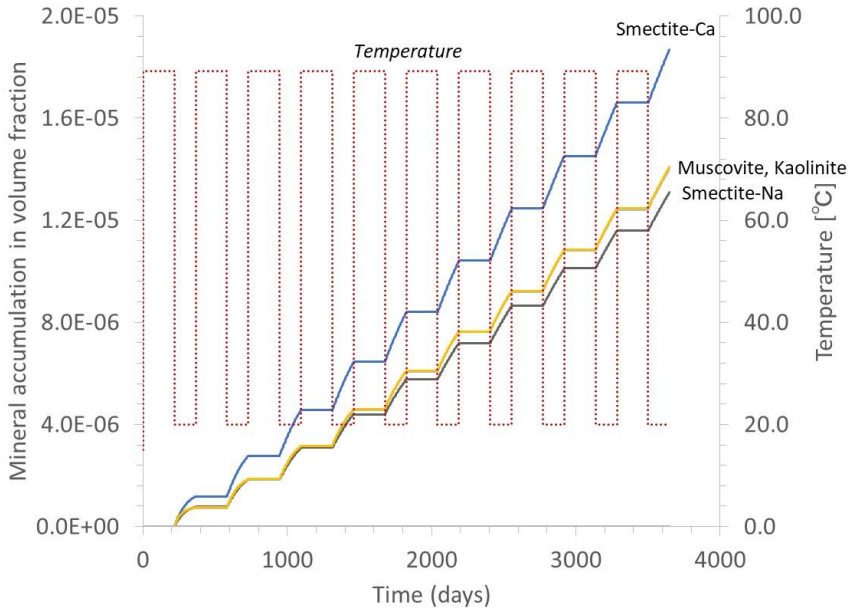

Figure 5.19: *Minerals forming in the heat exchanger. Consistent with their prograde solubility with respect to temperature, clay minerals are the dominant scale-forming mineral phases.*

The computed amounts of minerals in the "well" and the "heat exchanger" (i.e. the model screen and the model well, respectively), need to be scaled to the dimension of the real system to have any quantitative meaning. That is, model volume fractions have to be scaled by the extraction rates and bulk volumes in the real system. For instance, a volume fraction of

$3.75 \cdot 10^{-3}$ of calcite accumulating in the screen over a period of 10 years (Figure 5.18) implies an absolute volume of about 0.078 m^3 for the 7.5 m vertical extent of the model. Recalculating for the entire thickness of the real system (350 m) yields a total volume of scales of 0.36 m^3 per year for the real system.

The simulations included a dummy pseudo-mineral ($CO_2(s)$) to track the saturation state of the water with respect to CO_2 gas. The results suggest that degassing of CO_2 is not likely occur in the system. The computed reservoir pCO_2 and the assumed pressure drop to 3 bar overpressure in the surface installation are too low to cause CO_2 exsolution.

5.5.2 3D model of the Forsthaus system

5.5.2.1 Model design

A full scale 3D model of the Forsthaus heat storage system was constructed, which explicitly accounts for the envisaged arrangement of wells comprising the main injection/extraction well surrounded by supporting or auxiliary wells (Figure 5.20). However, because the Forsthaus project is still in its planning stage, the design of the model (specifically the stratigraphic succession, the lateral extent of individual strata or the distance between the wells) is still somewhat arbitrary. The main well is used to inject hot water into the reservoir during the warm months of the year and extract warm water during periods of demand. The supporting wells are used to regulate the flow, to maintain the desired reservoir pressure and to provide a connection to the surface installation, so that the reservoir, the wells and the surface installation (e.g. the heat exchanger) form a closed circulation system. The heat exchanger and closed-system circulation is not yet included in the simulations presented below.

To keep the model generic and allow for greatest flexibility in terms of updating the design or parameterization, it is constructed using a structured grid in a 3D cartesian coordinate system. Unlike axisymmetric models, which are in fact a 2D representation of the system, a Cartesian model is truly three-dimensional. The main advantage of a 3D model is to be able to include each well explicitly and to provide flexibility in terms of well design modifications, the implementation of geological heterogeneity in the reservoir and to account for asymmetric processes such as background groundwater flow.

The main disadvantage of a Cartesian coordinate system is that round features, such as the circular cross-section of the well, are represented by rectangles or blocks. The model wells for instance exhibit a square cross-section, whereby the cross-sectional area is scaled to match that of the real well. Similarly, because of regulatory constraints, the wellheads will be

slightly offset from the target reservoir such that the wells will be slightly inclined (2 – 22°). This inclination is difficult to implement using a structured grid hence it is not considered here. All wells are assumed to be vertical. We do not expect that this affects the results significantly.

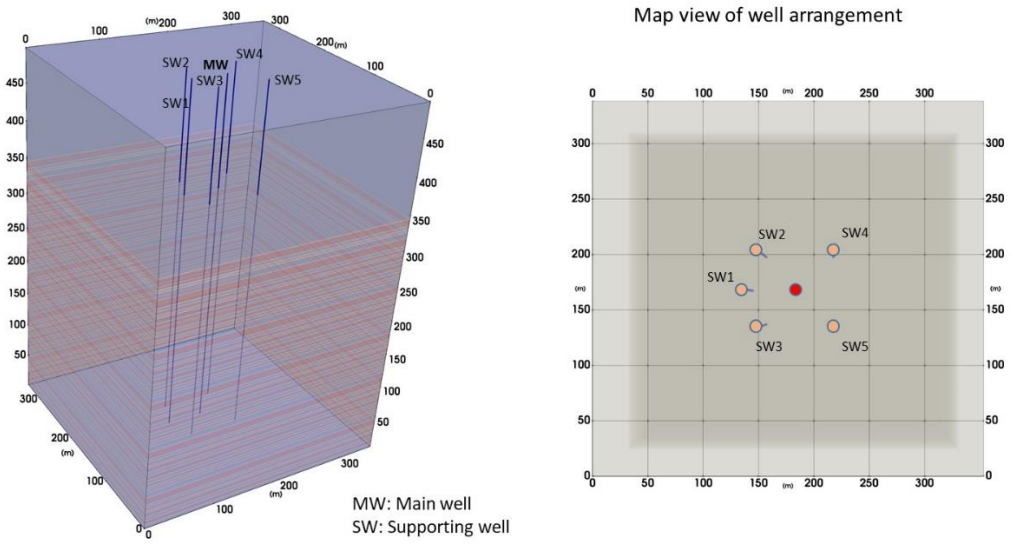

Figure 5.20: *Model domain with stratigraphy and wells (left panel) and a map view of the well arrangement (right panel).*

The model consists of a main well surrounded by five supporting wells at a distance of 50 m (Figure 5.20). The main and supporting wells have square cross-sectional areas of 0.09 m^2 and 0.058 m^2 corresponding to a diameter of an equivalent circular well of 13'' and 11'', respectively. We do not account for changes in diameter with depth. A more accurate representation of the wells (e.g. with decreasing diameter with depth) is planned in future simulations.

The domain extends to a depth of 495 m and horizontally more than 100 m beyond the circle of supporting wells (Figures 5.20 and 5.21). The added lateral extent serves as a buffer to reduce the impact of the side boundaries, which are "open" with respect to flow and heat transport, on processes within the circle of wells. Open side boundaries are implemented using a constant hydrostatic pressure and a fixed thermal gradient of 35 °C/km. A constant background heat flux into the domain resulting in a geothermal gradient of 35 °C /km under conductive conditions is assigned to the bottom boundary of the domain. Note that a gradient of 35 ºC/km is at the high end of estimated average gradients in the Molasse Basin. We assume a constant surface temperature of 15 °C which implies a temperature of 32.5 °C at a depth of 500 m, which is slightly above the estimated temperature range of 29 to 31 °C from the Swisstopo (www.swisstopo.admin.ch) GeoMol15 Temperature Model for the region of Bern. This

slightly higher temperature gradient in the model should not significantly affect the results of this study.

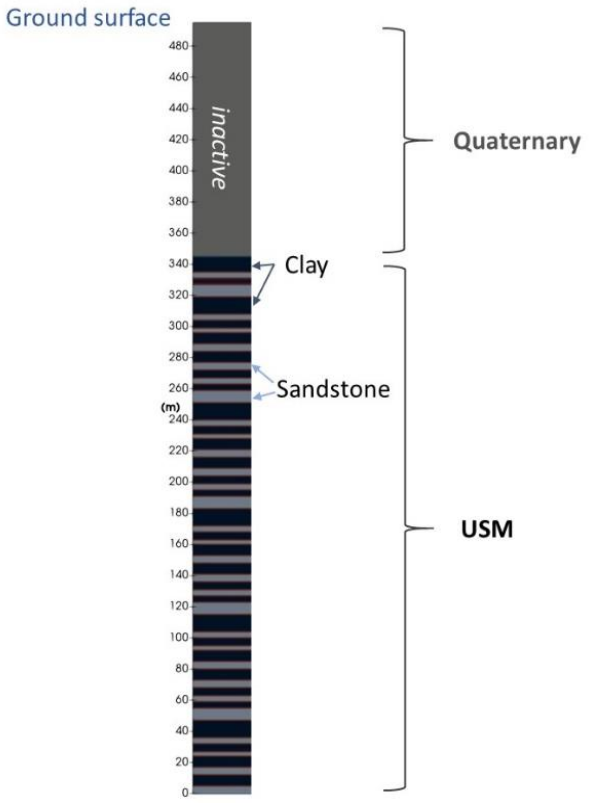

Figure 5.21: *Stratigraphy of the model domain. The Quaternary is considered inactive, that is it is impermeable, adiabatic and inert. In this model, all sandstone and clay units in the USM are horizontal and laterally continuous. The thickness of individual layers ranges from 3 to 11 m.*

The stratigraphy of the USM is based on previous modelling studies (e.g. Driesner et al., 2017) (Figure 5.21). It comprises alternating clay and sandstone layers of varying thickness. The thickness of individual layers ranges from 3 to 11 m. Each layer is horizontal, laterally continuous and of constant thickness. Given the generic design of the model, a more complex stratigraphic sequence representing the different lithotypes of the USM at the Forsthaus site more accurately will be easy to implement.

Thermal and hydraulic properties of the rock units are summarized in Table 5.6. Because the wells are planned to be cased throughout the Quaternary, all Quaternary rocks are considered "inactive", meaning that they are excluded from the simulation (Figure 5.21). In other words, Quaternary rocks are impermeable, adiabatic and inert. This assumption has a small impact on the distribution of heat in the system, because it prevents conductive heat loss into the Quaternary. We expect that this assumption has no impact on the results.

Injection and extraction follow the schedule presented in Table 5.7. The total simulated time is 2 years, spanning 2 injection-extraction cycles. Between periods of injection and extraction there are 2 days of resting.

The main well constitutes the injection and extraction well through which active pumping occurs. Along with the supporting wells a water balance will be established so that the total volume of water in the reservoir remains constant. To achieve this in the model, the supporting wells are also "activated", that is, water balance is enforced by active pumping in these wells. Given a total of 5 supporting wells and assuming the same flow rate through each of them, the pumping rate through each well has to be 5 l/s to achieve water balance.

The domain is composed of a total of 3.2 Mio grid cells yielding a spatial resolution of less than 2 m within the circle of wells. All simulations were run on UBELIX, the HPC cluster at the University of Bern, with runtimes of up to 2 days.

Table 5.7: *Thermal and hydraulic properties of the rock*

	Quaternary	Sandstone	Clay
Porosity	**inactive**	0.1	0.05
Tortuosity		0.1	0.05
Dispersivity [m]		1e-3	1e-3
Density [kg/m^3]		2743	2743
Wet thermal conductivity [W m^{-1} K^{-1}]		2.67	2.67
Heat capacity [J kg^{-1} K^{-1}]		764	764
Permeability [m^2]		3e-13	2.3e-17

Table 5.8: *Schedule of injection/extraction periods.*

Time (d)	Q (L/s)	T (°C)	Inject	Extract
0-216	25	90	x	
216-365	25	50		x
365-581	25	90	x	
581-730	25	50		x

5.5.2.2 Results

The fluxes through the wells (Figure 5.22) and the temperature at the wellheads (Figure 5.23) are consistent with the pumping schedule in Table 5.7. The injection temperature is 90 °C. The temperature of the extracted water decreases during withdrawal as more distal, cooler water is drawn from the reservoir. The lowest temperature at the end of the first and second extraction periods is 59 °C and 68.3 °C, respectively, indicating that the reservoir heats up over time.

This gradual heating of the reservoir can also be seen in the water extracted from the supporting wells. The temperature of the water discharging from the supporting wells increases with each successive period of injection through the main well.

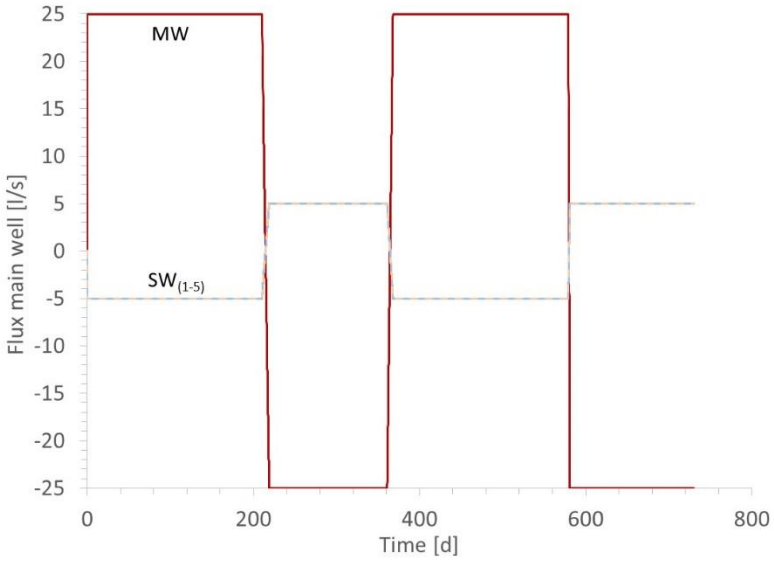

Figure 5.22: *Pumping rates through the main well (MW) and supporting wells (SW) according to the schedule in Table 5.7. Pumping rate > 0 denotes injection and < 0 denotes extraction. It is assumed that the flow rate through each supporting well is the same, amounting to 5 l/s to achieve global water balance.*

After the first injection, the thermal plume extends along the permeable sandstone layers driven by preferential flow along those layers (Figure 5.24, left panel). The edge of the thermal plume in the most transmissive layers extends to the supporting well SW1 which is 50 m away from the main well. This implies that there is a slight "thermal short circuit" causing the loss of heat that is being injected through the main well at the same time. This loss of heat is not very significant: during the injection through the main well the temperature of the water discharging through the supporting wells increases by 2-3 ºC (Figure 5.23), but it could be easily avoided by increasing the distance between main and supporting wells. Figure 5.25 confirms that the circle of supporting wells with a radius of 50 m from the main well is situated at the very edge of the thermal plume. Increasing the radius by another 5 – 10 m would probably contain the thermal plume entirely even over a longer life times of the system.

Over time, heat diffuses vertically into the clay layers and the temperature distribution in the reservoir becomes more homogeneous and the reservoir as a whole heats up (Figure 5.24, right panel). The figure illustrates that, given the assumptions of the model, the concept of thermal storage in the *Geospeicher Forsthaus* works very well.

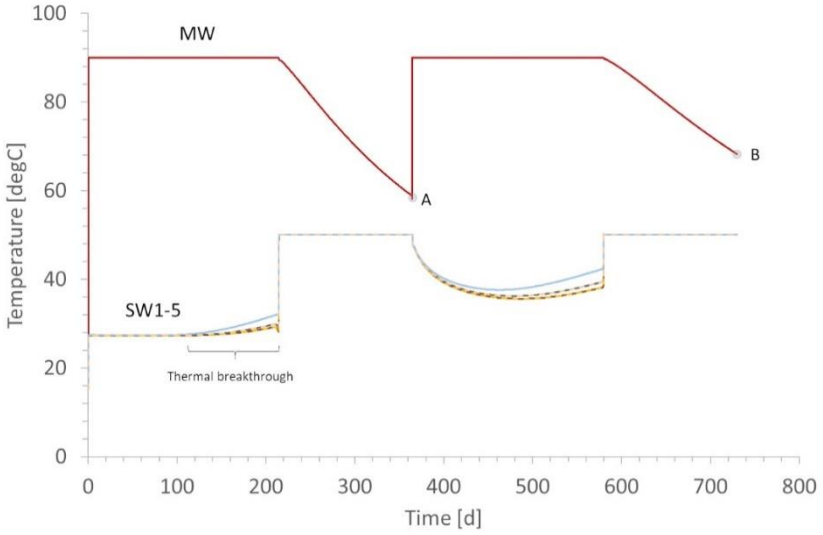

Figure 5.23: *Temperature evolution at the wellheads. The temperature of the water extracted through the main well increases over time (see points A and B marking the ends of two successive extraction cycles) and so does the water discharging from the supporting wells in response to injection through the main well. This behaviour indicates a gradual heating of the reservoir. Note the temperature increase of the water discharging from the supporting wells during injection into the main well, marking the thermal breakthrough. This is indicative of an unwanted "thermal short circuit".*

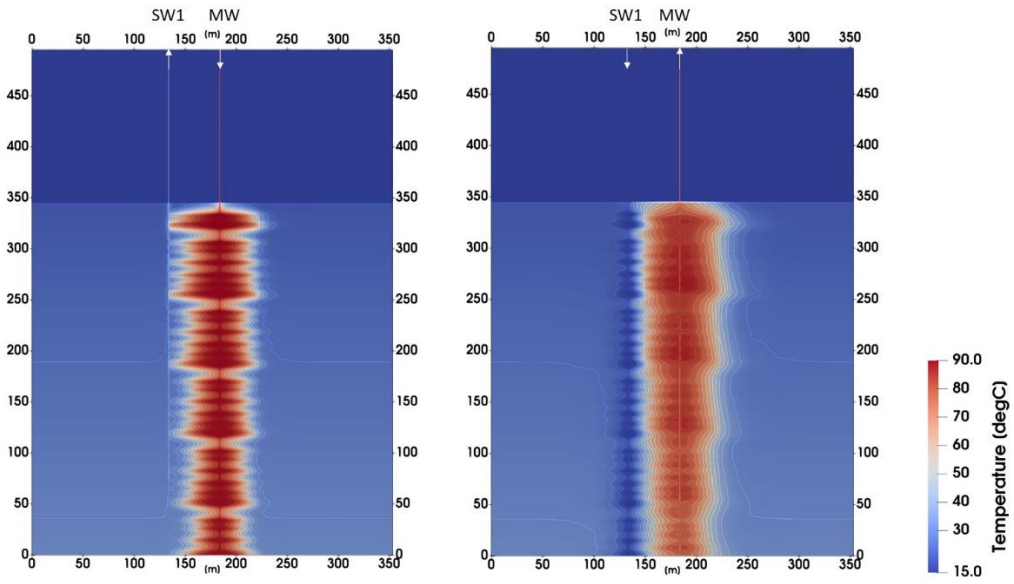

Figure 5.24: *2D section through SW1 and MW showing the extent of the thermal plume after the first injection period (left panel) and after the second extraction period (right panel).*

A tracer was added to the injected water at a concentration of 1 mol/g. Figure 5.26 shows the arrival of the injected tracer at the wellhead of the supporting wells. Homogeneous conditions lead to a breakthrough of the tracer front in each supporting well at about the same

time. In analogy to the (very weak) thermal "short circuit" discussed above (Figure 5.23 and 5.24), the breakthrough of the tracer indicates a "short circuit" of water mass currently injected into the well head. Whereas the former is unwanted, the second is consistent with the design of the system. It takes 77 days for the breakthrough of 50% of the tracer concentration in the supporting wells. Unlike heat, there is little diffusive exchange of tracer mass between the transmissive sandstone layers and the over- and underlying clay units (Figure 5.27).

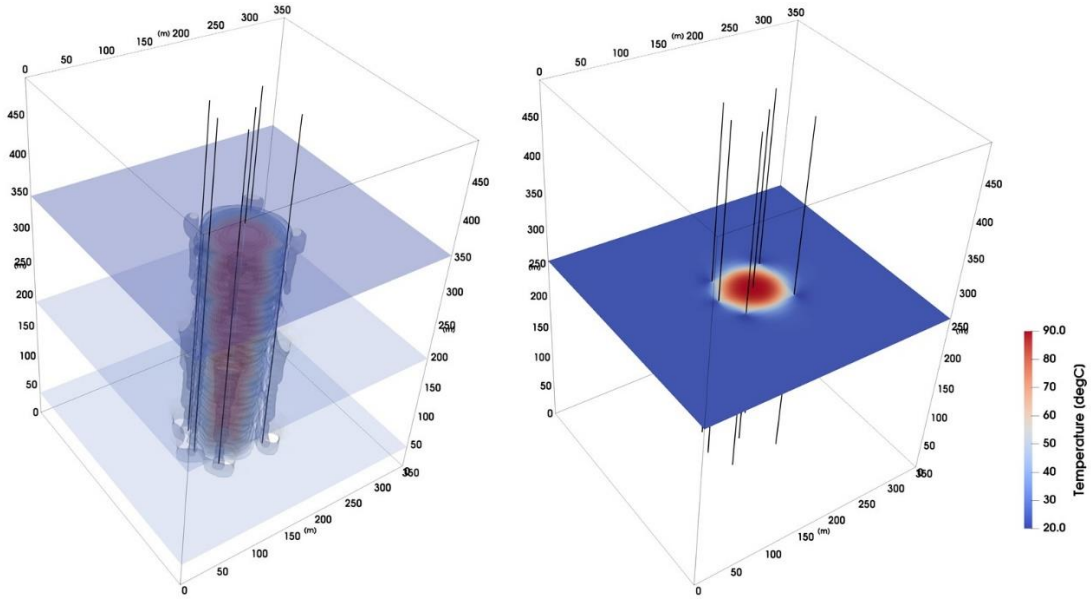

Figure 5.25: *Extent of the thermal plume during the second injection period. The thermal plume stays within the circle of supporting wells, 50 m away from the main well.*

Consistent with the rapid breakthrough of the tracer is a much larger lateral extent of the tracer plume (Figure 5.27 and 5.28). Figure 5.8 shows that a significant amount of tracer mass "escapes" the ring of supporting wells and migrates along the transmissive layers beyond the edge of the model domain, 175 m away from the main well. This escape can be prevented if the spacing between supporting wells is decreased. The spacing between supporting wells SW1-3 is closer than between SW4 and SW5 (Figure 5.20). The close arrangement of SW1-3 prevents the escape of the tracer as can be seen on the opposite side of the main well between SW4 and SW5 (Figure 5.28, right panel). In general, the tighter the ring of supporting wells, the more contained becomes the system.

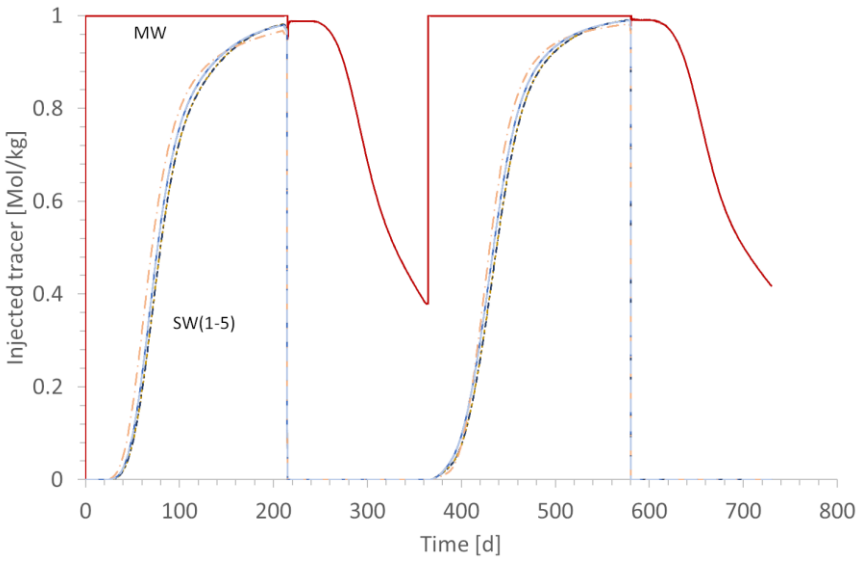

Figure 5.26: *Injection of a tracer into the main well (MW) and breakthrough of the tracer in water discharging from the supporting wells. The breakthrough of 50 % of the tracer concentration takes about 77 days.*

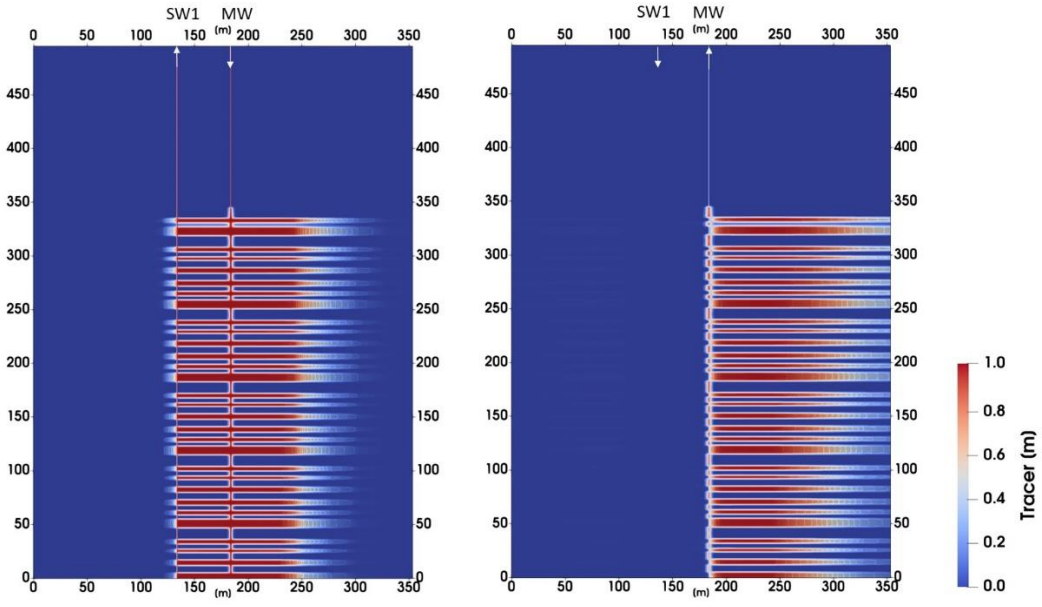

Figure 5.27: *2Dsection through SW1 and MW showing the concentration of the injected tracer after the first injection and second extraction period (left and right panels, respectively). The tracer distribution shows preferential flow and transport along the permeable sandstone layers and the extent of the tracer plume to the boundary of the model.*

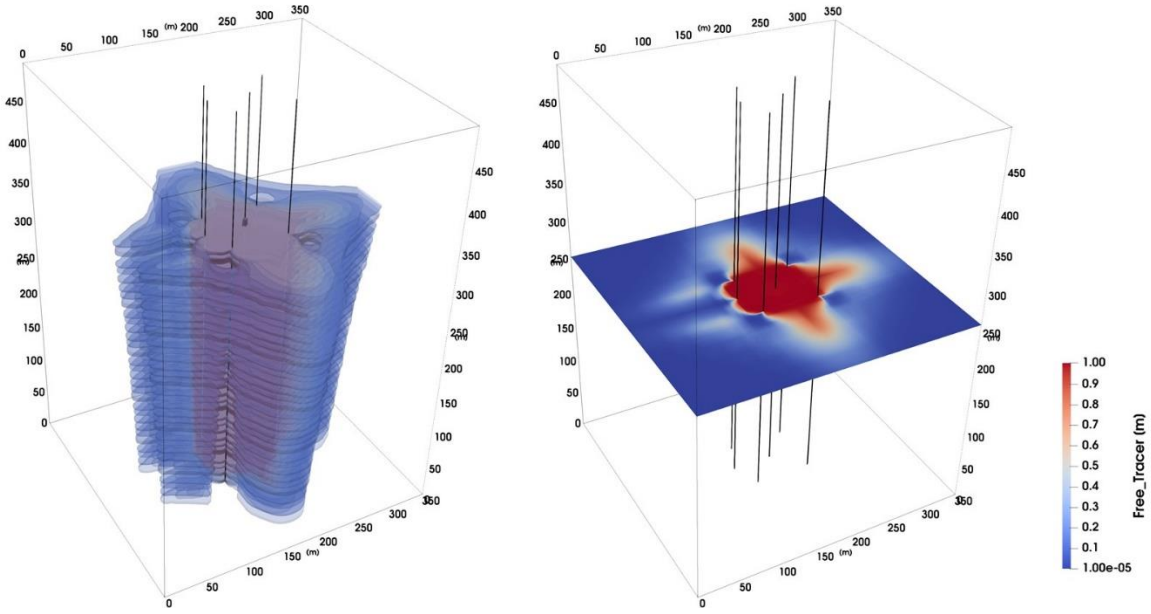

Figure 5.28: *3D distribution of the tracer during the second injection period (left panel). Unlike the thermal plume, the tracer is not contained within the circle of supporting wells (right panel).*

The *p*H distribution after 2 years of operation shows a similar pattern as that of the tracer. Changes in *p*H are restricted to the transmissive layers and within these layers, changes in the pH extend beyond the model boundary. Unlike the tracer, the *p*H is affected by chemical reactions between the water and the rock. Hence the *p*H changes as a function of the pumping scenario and temperature, so that, after 2 years, the *p*H of the reservoir water around the main well is highly heterogeneous as a result of time-integrated, overlapping processes (Figure 5.25). However, for conditions as they apply to the Forsthaus system, spatial and temporal changes in *p*H are very small (Figure 5.25 and Figure 5.26, respectively) and these are not likely to cause problems such as enhanced mineral reactions or corrosion.

The behaviour of mineral reactions is consistent with that described for the axisymmetric model. Significant mineral reactions are restricted to the region within the circle of supporting wells, that is within a radius of 50 m around the main well (Figures 5.31 and 5.32), which corresponds roughly to the extent of the thermal plume (Figure 5.24). Carbonate minerals calcite and dolomite dissolve during injection and precipitate during extraction (cf. Figure 5.9 and Figure 5.32), while quartz and other primary silicate minerals dissolve, regardless of the pumping scenario. The size of the zone involving silicate alteration (or the local intensity of silicate reactions) increases and decreases during injection and extraction periods, respectively, consistent with the fluctuations in the quartz reaction rate seen in Figure 5.11.

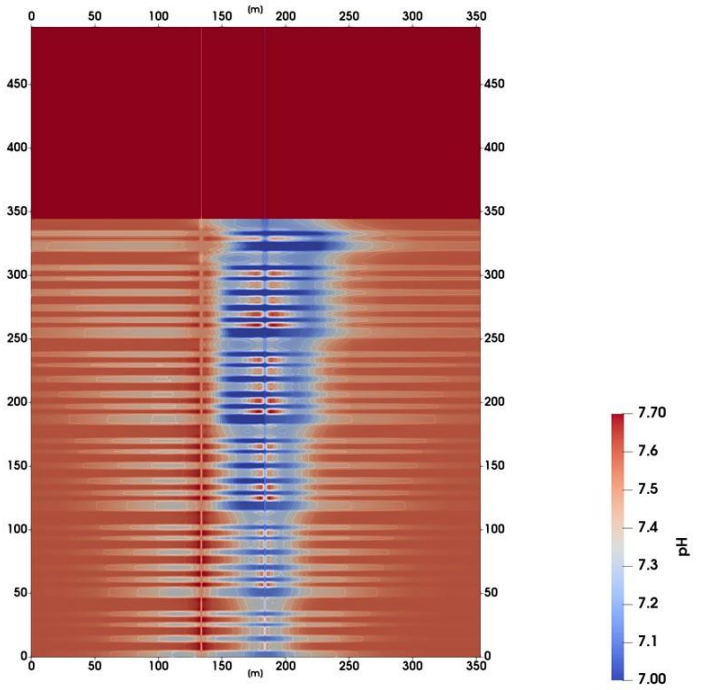

Figure 5.29: *The pH after 730 days, at the end of the second extraction cycle.*

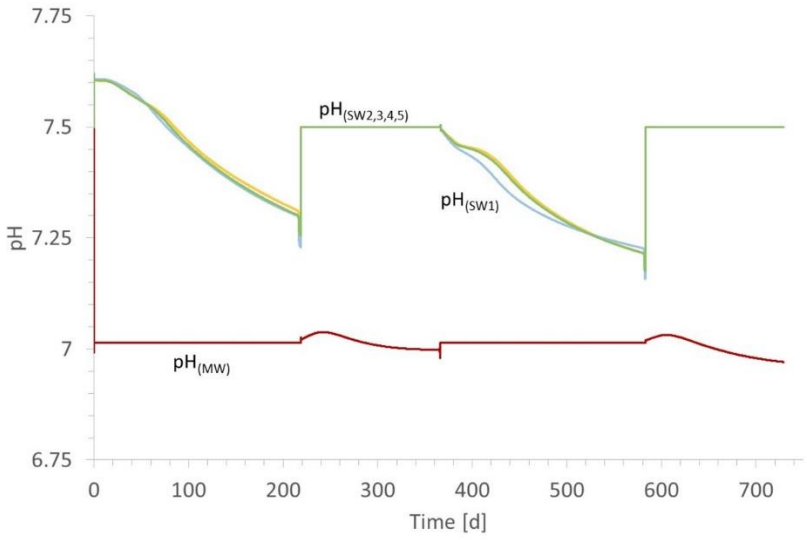

Figure 5.30: *The pH evolution at the wellheads.*

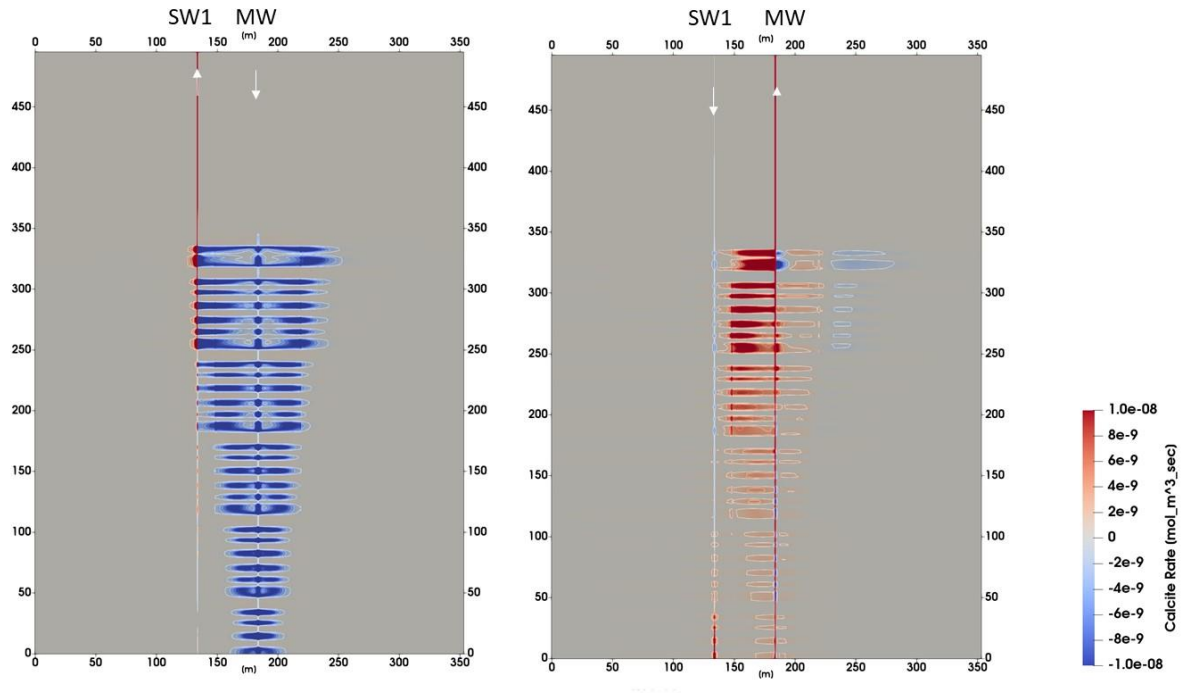

Figure 5.31: *Calcite reaction rate (<0: dissolution; >0 precipitation) after the first injection and second extraction period (left and right panel, respectively).*

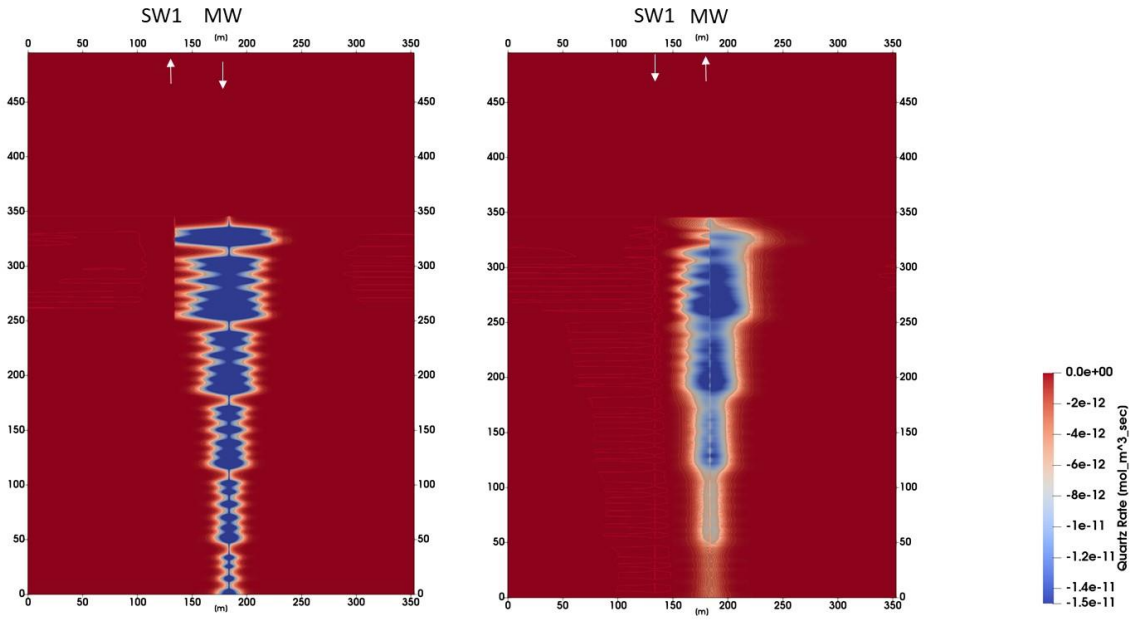

Figure 5.32: *Quartz reaction rate after the first injection and second extraction period (left and right panel, respectively)) showing only dissolution. During injection: the injected water is undersaturated with respect to quartz (as it is* in-situ *pore water heated to 90 ºC). During extraction distal, cooler reservoir water is drawn towards the relatively warm injection zone, thereby heating up and becoming undersaturated with respect to quartz.*

Consistent with the axisymmetric model, carbonate minerals calcite and dolomite precipitate in the wells, whereby the amounts forming in the main well far exceed those in the supporting wells (Figure 5.34). Clay minerals may also form as accessories (Figure 5.35). Scale forms in the wells only during periods of extraction (Figure 5.34) but these scales are largely preserved during subsequent injection periods (Figure 5.33). However, the total amount of scales remains low (Figure 5.35) and there is little risk of rapid clogging of the well. Even if scale formation in the well turns out to be a problem (for instance if mineral precipitation occurs rapidly within a short interval of the well or if it results in turbulent flow and thus reduced flow rates), given that scales are predominantly composed of calcite and dolomite, the formation of these scales could be prevented with relatively little effort by injecting appropriate inhibitors.

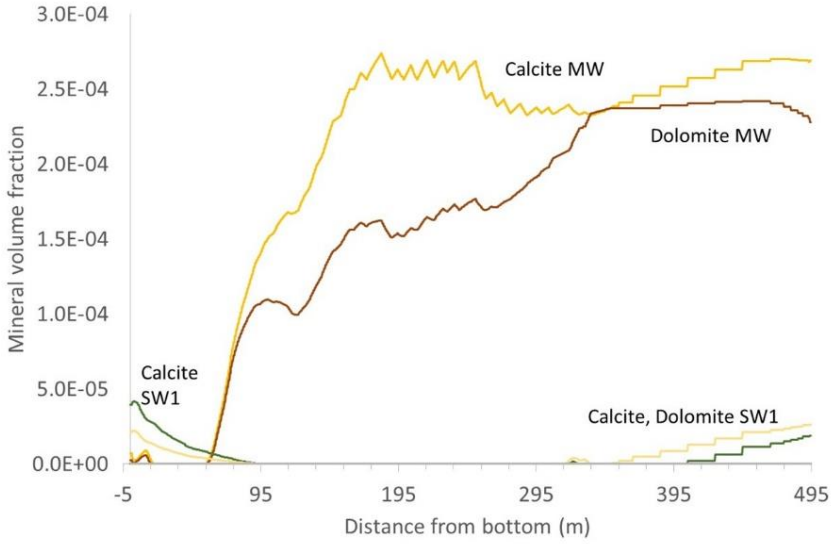

Figure 5.33: *Snapshot of mineral scales along the main well (MW) and supporting well 1 (SW1) after 486 days (second injection).*

5.6 Analysis and discussions

We use two modelling approaches to gain insight into processes that may occur in the *Geospeicher Forsthaus* during the operation stage. One approach is to use a simple axisymmetric model with a single injection and extraction well in the centre that includes a single permeable sandstone layer sandwiched between two clay layers. The reduced dimension, simplified geometry and reduced complexity of the flow system allows for the implementation of a relatively large and complex chemical reaction network without compromising computational performance. The purpose of this simple model is to run suites of parameter and scenarios

tests. The other approach is that of a full-scale 3D model of the system. The model is designed to allow for easy adaptation of the well design, operation schedule and implementation of geological heterogeneity as soon as new information becomes available.

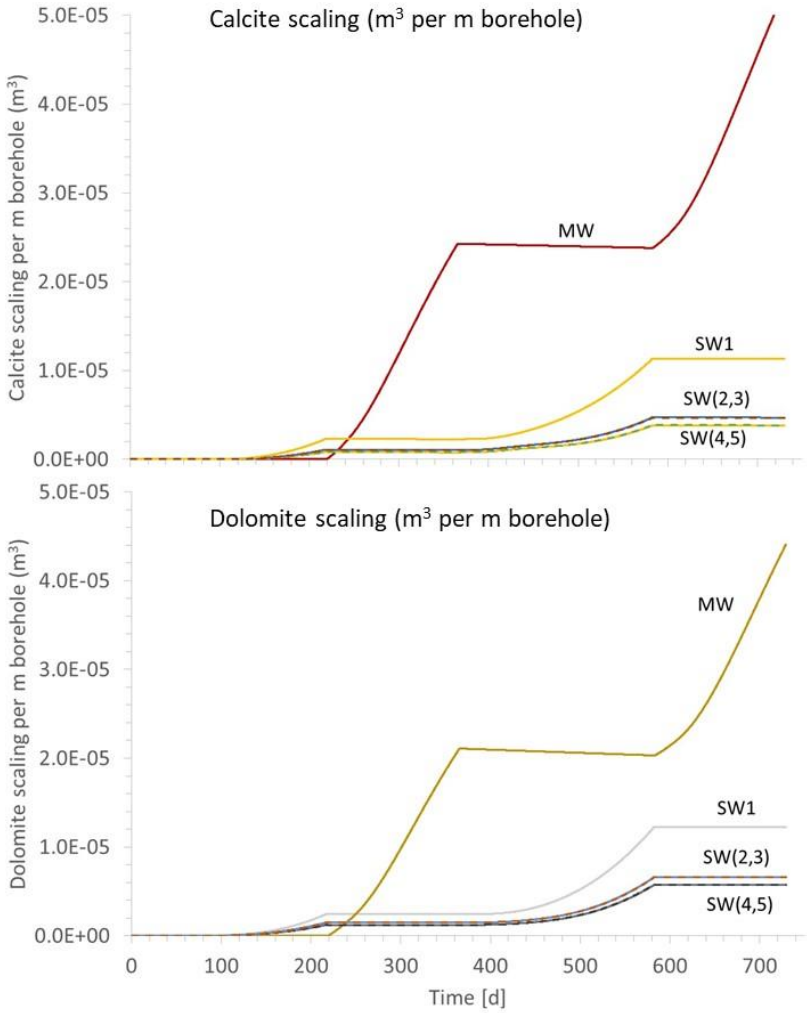

Figure 5.34: *Carbonate scale formation at the wellhheads.*

These two approaches complement one another because they operate on different scales and on different levels of detail. Furthermore, results from the simple model, in particular those concerning the chemical system or geochemical processes, e.g. the optimal composition and parameterization of the chemical reaction network, can be used to constrain input for the large scale simulations.

With simple modifications of the axisymmetric model, realism can be greatly enhanced. We conducted a study in which we use the simple axisymmetric model to address critical geochemical issues in various parts in the system. The simulations show that the "radius of influence" of the Forsthaus operation may exceed 100 m during a 10 year period if it is

defined in terms of solute transport. Chemical constituents injected or released from the aquifer material can travel far beyond the radius of the thermal plume and up to several hundreds of meters away from the Forsthaus site. This could be a problem if unwanted constituents are released and transported into aquifer systems outside the Forsthaus site, which are utilized for other purposes. However, these considerations neglect the effect of the supporting wells, which may limit the spread of a solute plume, provided that the spacing between these wells is sufficiently close. Hence, this assessment requires confirmation with simulations involving the large scale model and appropriate well arrangements.

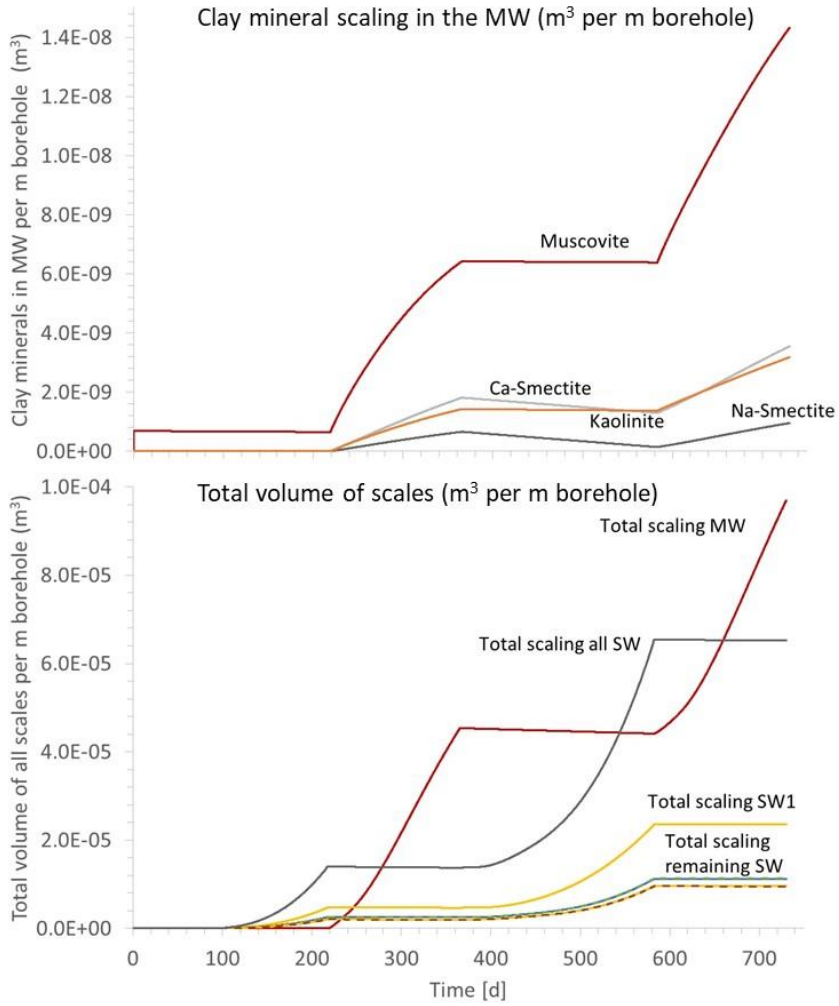

Figure 5.35: *Formation of silicate scales (upper panel) and total volume of mineral scales (lower panel).*

Although solutes may travel relatively large distances, the region of fluid-rock reactions where noticeable mineral dissolution and precipitation reactions take place, is restricted to a radius of less than 50 m. The zone of strong mineral alteration is limited to a radius of about 20 m. It is not likely that these zones will expand significantly if the operation time of

the system increases beyond the simulated 2 years. One reason for this is the circular geometry of the plume which implies lower flow velocities and stronger dilution of the chemical perturbation induced by the injection with increasing distance from the well. This in turn implies a relatively rapid dissipation of chemical disequilibrium and transition to a rock buffered water composition with increasing distance from the well. Geochemical processes within the 50 m radius are controlled by two overlapping processes: the long-term heating of the reservoir and short-term reversals in the direction of flow in combination with heating and cooling due to pumping. Heating of water in the injection zone occurs during periods of extraction when water is drawn from distal, cooler parts of the reservoir towards the well, where temperatures are still high owing to the preceding injection. Cooling occurs during injection when the direction of flow is reversed and warm water is pumped into cooler regions of the aquifer.

One of the main concerns regarding geochemical processes in the reservoir is that of permeability reduction due to mineral precipitation. Results suggest that this is not likely to be a problem in practice. Mineral reactions involving alumino-silicates are slow and porosity changes are small as volume changes due to the precipitation of secondary clay phases is balanced by those caused by the dissolution of primary minerals. Similarly, the precipitation of carbonates, which is a major concern in the installation, does not seem to greatly affect reservoir permeability because carbonate precipitation during extraction is followed by a carbonate re-dissolution during injection. Hence, the behaviour of carbonate minerals is strongly dependent on the pumping scenario and the pumping schedule. It is possible, in principle, to influence the distribution of carbonate reactions in the reservoir by designing an appropriate pumping schedule.

Carbonate precipitation during extraction occurs in the vicinity of and within the main well. It is caused by the higher temperature around the injection/extraction well in combination with retrograde solubility. That is, carbonate enriched water that is drawn towards the well becomes oversaturated with respect to calcite or dolomite which subsequently precipitate. Given that flow velocities increase as the water approaches the well, it is likely that the water entering the production well is oversaturated with respect to calcite. This leads to the formation of carbonate scales on the inside wall of the production well.

There is little risk of carbonate precipitation in the heat exchanger when the produced warm water is cooled. Instead, silicate minerals which have prograde solubility with temperature precipitate, albeit in small amounts. The dominant minerals that form in the heat exchanger upon cooling are clay minerals. This conclusion is based solely on the assumption of thermodynamic equilibrium. It is not known if precipitation kinetics will play a role, in which case the amounts of clay minerals forming in the heat exchanger could be even lower.

One important result of these simulations is that quartz or amorphous silica scaling does not seem to be an issue during extraction and cooling in the heat exchanger. Apparently, the same process causing calcite oversaturation in the production well, that is heating of the water approaching the well in combination with fast flow velocities near the well, also lead to quartz undersaturation in the production fluid and thus prevent quartz (or amorphous silica) precipitation in the heat exchanger. The suite of simulations involving the simple axisymmetric model did not reveal any obvious problem or risk related to geochemical processes that would hinder a sustained operation.

The 3D model is a much more accurate representation of the geometry of the system. Nevertheless, it is reassuring that the results from the 3D simulations of the Forsthaus system are largely consistent with the insights gained from the simpler axisymmetric model in particular concerning those of chemical processes near the main well. Even the composition and the amount of scales that may precipitate in the main well during extraction could be predicted with the simpler model with reasonable accuracy.

Results from the 3D simulations show that based on the extent of the thermal plume, a radius of 50 m for the circle of supporting wells is an absolute minimum and should not be any lower. In fact, for an optimal heat exploitation this radius should be increased if possible. The optimal distance is yet to be determined, but the results suggest that an additional 5 meters would be sufficient to eliminate the "thermal circuit" that occurs in the most transmissive sandstone layers.

With the current design of the system it is not possible to contain the chemical plume, that is compositional changes to the original reservoir water induced by the operation, within the circle of supporting wells. To achieve chemical containment the spacing between the supporting wells need to be reduced, meaning that more wells are required. Because this is not feasible, it is important to assess the implications of the operation for the composition of the groundwater and how these changes may affect any groundwater usage within a radius of hundreds of meters around the Forsthaus system. Currently, there is no groundwater usage in the vicinity of Forsthaus and the USM groundwater is not classified as drinking water. Experimental results and the simulations presented here suggest that these compositional change are small. The *p*H changes only slightly and there is no indication that unwanted compounds could be released from the aquifer rock into the groundwater.

Consistent with the results from the axisymmetric model, the risk of significant scaling in the wells or clogging of the reservoir is low. Carbonate minerals are far more reactive than silicate minerals and dominate the composition of scales in the wells and volume changes in the reservoir rock. The amount of carbonate scales in the main well is small over 2 injection

extraction cycles. The effect of carbonate reactions on porosity and permeability in the reservoir is reduced due to opposing behaviour during injection and extraction: carbonate minerals dissolve during the former and precipitate during the latter.

The simulations presented here use insights gained from the experiments presented in chapter 4 and integrate these into a thermal-hydraulic model to assess their implications for the operation stage at Forsthaus. Hence, the geochemical model used here still includes many of the uncertainties summarized in Section 4.4.1. For instance, at this stage the selection of clay minerals included in the simulations is based on geological realism and an assessment of thermodynamic data, rather than actual field or experimental observations.

The aim of the model presented here is not to resolve the issues presented in Section 4.4.1 but rather to focus on thermal-hydraulic processes and their geochemical implications that have not and probably cannot be captured by lab-scale experiments. For instance, the simulations reveal that the thermal evolution near the main well is far more complex than assumed in the simple heating experiments, involving repeated heating and cooling cycles and a gradual heating over time. Fluid compositions change locally, depending on whether water is injected or extracted. As a consequence, permeability changes ensuing from mineral reactions are a time-integrated effect of geochemical conditions that vary in space and time. The model presented here provides the theoretical framework for analysing these time and space dependent processes.

The simulations have verified the feasibility of the heat storage principle in deep aquifers of the sandstones in the USM (Figure 5.24). From a geochemical perspective and with the current knowledge, there is little risk for failure. Perhaps the greatest risk for the operation are the unknown geological and hydraulic conditions in the subsurface. The stratigraphy used for the USM in this model is based on data from the Nagra drilling campaign at Burgdorf near Bern and not the specific stratigraphy at Forsthaus. Likewise, the pore water composition is from another site. Furthermore, little is known about active groundwater flow in the USM. All modelling results are based on the assumption that natural groundwater flow does not occur. The models presented here will be adapted as soon as site-specific data or information become available.

6 Conclusions – Problems expected in the operation of the *Geospeicher Forsthaus*

In the absence of any subsurface data from the site itself, our conclusions are based on five sources of information: (1) scientific literature on previous aquifer thermal storage projects; (2) scientific literature on the regional geology; (3) analyses of drill cores and formation waters from shallow existing wells 2 km from the Forsthaus site; (4) laboratory experiments involving heating of the sandstones in contact with a best-guess artificial formation water; (5) heating experiments to nucleate to calcite scaling; and (6) numerical simulations of the coupled thermal–hydraulic–chemical processes expected during the heat loading and unloading cycles at the reservoir scale.

Spatial heterogeneities:

Our review of the geological literature has highlighted the spatial heterogeneities in the target meander belt sandstones with respect to properties that are central to the behaviour of the planned *Geospeicher Forsthaus*. The important unknowns are:

- presence or absence of the sandstones in any given vertical section of the USM
- 3D geometries and dimensions of the sandstones
- porosity, permeability, mineral content and degree of calcite cementation in the sandstones
- extent to which individual sandstone layers are hydraulically connected (versus hydraulically compartmentalised by interlayered silt- and claystones);
- velocity and direction of groundwater flow
- groundwater properties: salinity, solute composition (especially pCO_2) and microbial activity

- concentrations in the groundwater of the corrosion-inducing components H_2S, SO_4, Cl and microbes

The heterogeneous nature of these properties within the reservoir formation implies that they are all strongly site-specific, and so we must wait for drilling and hydraulic testing at Forsthaus before their specific values can be determined. At present, without this site-specific information, it is impossible to make reliable predictions of the injectability, permeability and mechanical integrity of the sandstones, and of the mobility of the thermal plume that the *Geospeicher Forsthaus* will generate.

Issues critical to the success of the *Geospeicher*:

Beyond the above site-specific uncertainties, we have so far not discovered any further geological, thermal, hydraulic or chemical features that suggest the *Geospeicher* will fail or that a completely different storage strategy is required. Our investigations have reinforced our optimism for the project and we fully support the planned drilling and hydraulic testing campaign.

Cautionary issues:

Based on issues encountered in previous heat-storage projects and on our experimental and modelling results, several cautionary issues have been identified:

- Dissolution and precipitation of silicate minerals will occur in the reservoir sandstones (e.g., steady replacement of feldspars by various clays), but they will have no significant consequences for reservoir porosity and permeability. However, considerable amounts of calcite, which occurs naturally in the sandstones as rock fragments and as cement, will dissolve and precipitate as a function of the water injection/extraction cycles (owing to their linked variations in fluid temperature and composition). Consequently, the distribution of calcite in the reservoir will become increasingly heterogeneous with time, leading to regions where calcite accumulates and regions where it becomes depleted. Regions of calcite accumulation will become less permeable and may become isolated from the induced injection/extraction flow regime. Regions of calcite depletion will become more permeable and may channel flow and reduce the volume of reservoir rock that is swept by the injected hot water, thereby reducing heat storage efficiency. Regions of calcite depletion may also lose their mechanical integrity and undergo compaction.

- In addition to the above inorganic processes, degradation of naturally occurring organic matter within the reservoir and possibly microbial activity may impact the mineral reactions. Organic compounds may coat mineral surfaces and thus slow down mineral–water reactions or form complexes with ions in solution enhancing mineral solubilities. While this will likely have no adverse effects on the system, it is difficult to quantify this process in our simulations and hence it may have led to overestimations of reaction products. On the other hand, microbes may enhance corrosion and if they form biofilms, they may lead to clogging, especially if injection temperatures are well below 90 °C. It can be assumed that microbial activity will strongly diminish as the reservoir heats up towards 90 °C.
- Dissolution reactions and mechanical disintegration of mineral and organic particles during repeated water injection and production cycles may mobilise fines and clog pore throats, reducing permeability. This has been neither modelled nor investigated in our experiments but appears likely to occur owing to the observed friability of the sandstones near Bern. Its possible occurrence away from the immediate vicinity of the wells and its impact on the flow regime remain unknown.
- Regarding hydrological problems, rise of a bouyant thermal plume to the top of the reservoir is not expected, owing to the probable modest thicknesses of individual sandstone layers. However, it is conceivable that discrete, preferential flow paths will develop between the main and supporting wells within one or several sandstone layers, owing to their heterogeneous permeability distributions. Such short-circuits could reduce the volume of reservoir rock swept by the injected hot water and reduce storage capacity.
- The thermal plume and the reaction zone around the main well is predicted to remain within a 50 m radius from the well. However, the zone of influence of the entire heat storage reservoir, if defined by the distance to which non-reactive solutes injected or released from the rock can travel in the USM groundwater system, is much larger. There is therefore a possibility that unwanted chemical compounds are transported over large distances.
- Based on the simulated extent of the thermal plume, a radius of 50 m for the circle of supporting wells is an absolute minimum and should not be any lower. For optimal heat exploitation this radius should be increased if possible. Even an additional 5 meters would be sufficient to eliminate the “thermal circuit” that occurs in the most transmissive sandstone layers.

- Significant carbonate scaling is expected in the surface installations during the heat loading cycle. This could impede flow and exchange of heat in the surface installations. Its extent may potentially be mitigated by the natural occurrence of inhibiting ions in solution (Mg, SO_4, organic acids).

While it is difficult to make predictions without site-specific data, the above list of issues highlights which phenomena to focus on during drilling and hydraulic testing. Moreover, the insight gained and the methods developed during this pre-study serve as an excellent preparation to interpret the site-specific data as they become available. This understanding should enable formulation of creative solutions to problems that arise during the testing and operational phases of the *Geospeicher Forsthaus*.

7 References

Adinolfi, M. and Ruck, W. (1992) Microbiological and Environmental Effects of Aquifer Thermal Energy Storage. SAE Technical Paper, No. 929155, .

Allenbach, R., Baumberger, R., Kurmann, E., Michael, C. S. & Reynolds, L. (2017) GeoMol: Geologisches 3D-Modell des Schweizer Molassebeckens – Schlussbericht. Bundesamt für Landestopographie swisstopo, Bern, p. 128.

Alt-Epping, P., Waber, H. N., Diamond, L. W., & Eichinger, L. (2013). Reactive transport modeling of the geothermal system at Bad Blumau, Austria: implications of the combined extraction of heat and CO_2. Geothermics, 45, 18-30.

Ammann, M., Birkhauser, P., Bläsi, H., Lavanchy, J.-M. and Löw, S. (1993) Untere Süsswassermolasse im Erdsondenfeld Burgdorf - Charakterisierung mittles Geologie, Petrophysik und Fluid Logging, Nagra Technischer Bericht 92-03, Nagra, Wettingen, p. 108.

Amy, P. (1997) Microbial dormancy and survival in the subsurface, in: Amy, P., Haldeman, D. (Eds.), The Microbiology of the Terrestrial Deep Subsurface. CRC, Lewis Publishers, NY, pp. 185-204.

Anderson, G.M. (2005) Thermodynamics of natural systems. Cambridge University Press.

Andersson, O. and Sellberg, B. (1992) Swedish ATES applications: experiences after ten years of development. SAE Technical Paper, No. 929019.

Arnórsson, S. (1975) Application of the silica geothermometer in low temperature hydrothermal areas in Iceland. American Journal of Science 275.

Beck, R., Seiersten, M., & Andreassen, J. P. (2013). The constant composition method for crystallization of calcium carbonate at constant supersaturation. Journal of Crystal Growth, 380, 187-196.

Becker, D. and Rauber, G. (2007). Esquisse de l'histoire des mammifères et gisements fossilifères de Suisse. Société Neuchâteloise des Sciences Naturelles 130, 5-48.

Beckingham, L. E., Mitnick, E. H., Steefel, C. I., Zhang, S., Voltolini, M., Swift, A. M., Yang, L., Cole, D. R., Sheets, J. M. Ajo-Franklin, J. B., DePaolo, D. J., Mito, S. & Xue, Z. (2016). Evaluation of mineral reactive surface area estimates for prediction of reactivity of a multi-mineral sediment. Geochimica et Cosmochimica Acta, 188, 310-329.

Berger, J.-P., Kälin, D. and Kempf, O. (2010) Swiss Molasse lithostratigraphy, 8th Swiss Geoscience Meeting, Fribourg, Nov. 19–20, pp. 127.

Berger, J.-P., Reichenbacher, B., Becker, D., Grimm, M., Grimm, K., Picot, L., Storni, A., Pirkenseer, C., Derer, C. and Schaefer, A. (2005) Paleogeography of the upper Rhine Graben (URG) and the Swiss Molasse basin (SMB) from Eocene to Pliocene. International Journal of Earth Sciences, 94, 697-710.

Berner, R., Westrich, J., Graber, R., Smith, J. and Martens, C. (1978) Inhibition of aragonite precipitation from supersaturated seawater; a laboratory and field study. American Journal of Science 278, 816-837.

Bischoff, J. L. (1968). Kinetics of calcite nucleation: magnesium ion inhibition and ionic strength catalysis. Journal of Geophysical Research, 73(10), 3315–3322.

Brons, H., Griffioen, J., Appelo, C. and Zehnder, A. (1991) (Bio) geochemical reactions in aquifer material from a thermal energy storage site. Water Research 25, 729-736.

Buatois, L. A., Wetzel, A., & Mángano, M. G. (2020). Trace-fossil suites and composite ichnofabrics from meandering fluvial systems: The Oligocene Lower Freshwater Molasse of Switzerland. Palaeogeography, Palaeoclimatology, Palaeoecology, 558, 109944.

Büchi, U. and Bodmer, P. (1983) Der Tiefenverlauf der seismischen Geschwindigkeiten in den Molassesedimenten des schweizerischen Mittellandes. Bulletin Vereinigung Schweizer Petroleum-Geologen und -Ingenieure 49, 3-13.

Buscheck, T.A., Doughty, C. and Tsang, C.F. (1983) Prediction and analysis of a field experiment on a multilayered aquifer thermal energy storage system with strong buoyancy flow. Water Resources Research 19, 1307-1315.

Caliskan, H., Dincer, I. and Hepbasli, A. (2012) Thermodynamic analyses and assessments of various thermal energy storage systems for buildings. Energy Conversion and Management 62, 109-122.

Carroll, D. (1959) Ion exchange in clays and other minerals. Geological Society of America Bulletin 70, 749-779.

Chermak, J.A. and Rimstidt, J.D. (1990) The hydrothermal transformation rate of kaolinite to muscovite/illite. Geochimica et Cosmochimica Acta 54, 2979-2990.

Chevalier, G., Diamond, L.W. and Leu, W. (2010) Potential for deep geological sequestration of CO 2 in Switzerland: a first appraisal. Swiss Journal of Geosciences 103, 427-455.

Cody, R. (1991) Organo-crystalline interactions in evaporite systems; the effects of crystallization inhibition. Journal of Sedimentary Research 61, 704-718.

Collignon, M., Klemetsdal, Ø.S., Møyner, O., Alcanié, M., Rinaldi, A.P., Nilsen, H. and Lupi, M. (2020) Evaluating thermal losses and storage capacity in high-temperature aquifer thermal energy storage (HT-ATES) systems with well operating limits: insights from a study-case in the Greater Geneva Basin, Switzerland. Geothermics 85, 101773.

Collinson, J. (1978) Vertical sequence and sand body shape in alluvial sequences, in: Miall, A. (Ed.), Fluvial sedimentology. Canadian Society Petroleum Geology, Memoir pp. 577-586.

Compton, R. G., & Brown, C. A. (1994). Inhibition of calcite dissolution/precipitation: Mg^{2+} cations. In Journal of Colloid And Interface Science, 165(2), 445–449.

Costerton, J.W., Lewandowski, Z., Caldwell, D.E., Korber, D.R. and Lappin-Scott, H.M. (1995) Microbial biofilms. Annual Review of Microbiology 49, 711-745.

de Kanel, J. and Morse, J.W. (1978) The chemistry of orthophosphate uptake from seawater on to calcite and aragonite. Geochimica et Cosmochimica Acta 42, 1335-1340.

Diamond, L. W., & Alt-Epping, P. (2014). Predictive modelling of mineral scaling, corrosion and the performance of solute geothermometers in a granitoid-hosted, enhanced geothermal system. Applied Geochemistry, 51, 216-228.

Dijkstra, H., de Boer, C., Griffioen, J., & Koenen, M. (2020). Workflow to evaluate the risk of mineral scaling in a HT-ATES system and application to a potential site in Middenmeer, The Netherlands. TNO Report 2020 R10437, TNO, Utrecht, p. 56.

di Lorenzo, F., Burgos-Cara, A., Ruiz-Agudo, E., Putnis, C. V., & Prieto, M. (2017). Effect of ferrous iron on the nucleation and growth of $CaCO_3$ in slightly basic aqueous solutions. CrystEngComm, 19(3), 447-460.

Dincer, I. and Rosen, M. (2010) Energy storage systems, Thermal Energy Storage: Systems and Applications. John Wiley & Sons, Ltd Chichester, UK.

Dobberschütz, S., Nielsen, M. R., Sand, K. K., Civioc, R., Bovet, N., Stipp, S. L. S., & Andersson, M. P. (2018). The mechanisms of crystal growth inhibition by organic and inorganic inhibitors. Nature Communications, 9(1), 1–6.

Doughty, C., Hellström, G., Tsang, C.F. and Claesson, J. (1982) A dimensionless parameter approach to the thermal behavior of an aquifer thermal energy storage system. Water Resources Research 18, 571-587.

Drever, J. and Stillings, L. (1997) The role of organic acids in mineral weathering. Colloids and Surfaces A: Physicochemical and Engineering Aspects 120, 167-181.

Driesner, T., L. Manatschal and J. Mindel (2017) Finaler Bericht numeriche Simulationen «Geospeicher Forsthaus», ETH Zürich Department Erdwissenschaften, ETH, Zürich.

Fielding, C. and Crane, R. (1987) An application of statistical modelling to the prediction of hydrocarbon recovery factors in fluvial reservoir sequences, in: Etheridge, F., Flores, R., Harvey, M. (Eds.), Recent Developments in Fluvial Sedimentology. Special Publication of the Society of Economic Paleontologists and Mineralogists (SEPM), pp. 321-328.

Fleuchaus, P., Godschalk, B., Stober, I. and Blum, P. (2018) Worldwide application of aquifer thermal energy storage–A review. Renewable and Sustainable Energy Reviews 94, 861-876.

Galloway, W.E. (1981) Depositional architecture of Cenozoic Gulf coastal plain fluvial systems, in: Etheridge, F., Flores, R. (Eds.), Recent and Ancient Non-marine Depositional Environments : Models for Exploration. Special Publication of the Society of Economic Paleontologists and Mineralogists (SEPM), pp. 127-155.

Galloway, W.E. and Hobday, D.K. (2012) Terrigenous clastic depositional systems - Applications to fossil fuel and groundwater resources. Springer-Verlag New York.

Gallup, D. (1989) Iron silicate scale formation and inhibition at the Salton Sea geothermal field. Geothermics 18, 97-103.

Gallup, D.L. (1998) Aluminum silicate scale formation and inhibition (2): Scale solubilities and laboratory and field inhibition tests. Geothermics 27, 485-501.

Gautier, Q., Bénézeth, P., & Schott, J. (2016). Magnesite growth inhibition by organic ligands: An experimental study at 100, 120 and 146 °C. Geochimica et Cosmochimica Acta, 181, 101-125.

Giffaut, E., Grivé, M., Blanc, P., Vieillard, P., Colàs, E., Gailhanou, H., ... & Duro, L. (2014). Andra thermodynamic database for performance assessment: ThermoChimie. Applied Geochemistry, 49, 225-236.

Gnos, E., Kurz, D. and Eggenberger, U. (2006) Elelectrodynamic disaggregation of geologic material, 4th Swiss Geoscience Meeting, Bern, Nov. 24–25.

Gold, P.B. (1987) Textures and geochemistry of authigenic albite from Miocene sandstones, Louisiana Gulf Coast. Journal of Sedimentary Research 57, 353-362.

Gregg, J. M., Bish, D. L., Kaczmarek, S. E., & Machel, H. G. (2015). Mineralogy, nucleation and growth of dolomite in the laboratory and sedimentary environment: A review. Sedimentology, 62(6), 1749-1769.

Griebler, C. and Lueders, T. (2009) Microbial biodiversity in groundwater ecosystems. Freshwater Biology 54, 649-677.

Griebler, C., Mindl, B., Slezak, D. and Geiger-Kaiser, M. (2002) Distribution patterns of attached and suspended bacteria in pristine and contaminated shallow aquifers studied with an in situ sediment exposure microcosm. Aquatic Microbial Ecology 28, 117-129.

Griffioen, J. and Appelo, C.A.J. (1993) Nature and extent of carbonate precipitation during aquifer thermal energy storage. Applied Geochemistry 8, 161-176.

Grim, R.E. (1942) Modern concepts of clay materials. The Journal of Geology 50, 225-275.

Gunnarsson, I. and Arnórsson, S. (2000) Amorphous silica solubility and the thermodynamic properties of H_4SiO_4 in the range of 0 to 350 C at P_{sat}. Geochimica et Cosmochimica Acta 64, 2295-2307.

Gunnlaugsson, E., & Einarsson, A. (1989). Magnesium-silicate scaling in mixture of geothermal water and deaerated fresh water in a district heating system. Geothermics, 18(1-2), 113-120.

Hamilton, W.A. (1985) Sulphate-reducing bacteria and anaerobic corrosion. Annual Review of Microbiology 39, 195-217.

Hammond, G.E., P. C. Lichtner, C. Lu, and R.T. Mills (2012) Pflotran: Reactive flow and transport code for use on laptops to leadership-class supercomputers. In Fan Zhang, G.T. Yeh, and Jack C. Parker (eds.), Groundwater Reactive Transport Models,. Bentham Science Publishers, Sharjah, UAE, p. 141-159.

Harder, H. (1972). The role of magnesium in the formation of smectite minerals. Chemical Geology, 10(1), 31-39.

Hauksson, T., Pórhallsson, S., Gunnlaugsson, E., & Albertsson, A. (1995, May). Control of magnesium silicate scaling in district heating systems. In World Geothermal Congress 1995.

Hellstrom, G., Tsang, C.F. and Claesson, J. (1979) Heat storage in aquifers: buoyancy flow and thermal stratification problems. Lawrence Berkley Laboratory Technical Report, LBL-14246.

Henzler, K., Fetisov, E. O., Galib, M., Baer, M. D., Legg, B. A., Borca, C., Xto, J. M., Pin, S., Fulton, J. L., Schenter, G. K., Govind, N., Siepmann, J. L., Mundy, C. J., Huthwelker, T. & De Yoreo, J. J. (2018). Supersaturated calcium carbonate solutions are classical. Science Advances, 4(1), eaao6283.

Hewitt, C.H. (1963) Analytical techniques for recognizing water-sensitive reservoir rocks. Journal of Petroleum Technology 15, 813-818.

Hicks, R. and Stewart, D.L. (1988) Environmental assessment of the potential effects of aquifer thermal energy storage systems on microorganisms in groundwater. Pacific Northwest Lab., No. PNL-6492.

Holm, T.R., Eisenreich, S.J., Rosenberg, H.L. and Holm, N.P. (1987) Groundwater geochemistry of short-term aquifer thermal energy storage test cycles. Water Resources Research 23, 1005-1019.

Howsam, P. (1988) Biofouling in wells and aquifers. Water and Environment Journal 2, 209-215.

Hoyer, M., Eisenreich, S., Almendinger, J., Perlinger, J., Miller, R., Lauer, J., Splettstoesser, J. and Walton, M. (1991) University of Minnesota aquifer thermal energy storage (ATES) project - Report on the first long-term cycle, Pacific Northwest Laboratory Report, PNL–7817.

Hoyer, M., Hallgren, J., Uebel, M., Delin, G., Eisenreich, S. and Sterling, R. (1994) University of Minnesota Aquifer Thermal Energy Storage (ATES) - Project Report of the Third Long-Term Cycle, Pacific Northwest Laboratory Report, PNL–9811.

Huang, P. M., & Violante, A. (1986). Influence of organic acids on crystallization and surface properties of precipitation products of aluminum. Interactions of Soil Minerals with Natural Organics and Microbes, 17, 159-221.

Huenges, E. (2011) Thermische Untergrundspeicher in Energiesystemen: Optimierung der Einbindung der Aquiferspeicher in die Wärme-und Kälteversorgung der Parlamentsbauten im Berliner Spreebogen - Abschlussbericht, Helmholtz-Zentrum Potsdam GFZ Deutsches Geoforschungszentrum, Potsdam.

Inskeep, W.P. and Bloom, P.R. (1986) Kinetics of Calcite Precipitation in the Presence of Water-Soluble Organic Ligands 1. Soil Science Society of America Journal 50, 1167-1172.

Isler, A. (2005) Blatt 1166 Bern. – Geol. Atlas Schweiz 1: 25 000, Erläut. 100.

Javaherdashti, R. (2008) Microbiologically influenced corrosion (MIC). Microbiologically Influenced Corrosion: An Engineering Insight, 29-71.

Javaherdashti, R. (2011) Impact of sulphate-reducing bacteria on the performance of engineering materials. Applied Microbiology and Biotechnology 91, 1507.

Jenne, E., Andersson, O. and Willemsen, A. (1992) Well, hydrology, and geochemistry problems encountered in ATES systems and their solutions. SAE Technical Paper No. 929153.

Jenne, E., McKinley, J. and Smith, R. (1989) Geochemical research for high-temperature aquifer thermal energy storage. Pacific Northwest Lab., No. PNL-SA-16706.

Jollien, L., Remonnay, S. and Miserez, F. (1992) Heat Storage at SPEOS (Swiss ATES Pilot Plant): Chemical and Microbiological Aspects and Problems. SAE Technical Paper, No. 929052.

Jost, J., Kälin, D., Börner, S., Vasilyan, D., Lawver, D. and Reichenbacher, B. (2015). Vertebrate microfossils from the Upper Freshwater Molasse in the Swiss Molasse Basin: Implications for the evolution of the North Alpine Foreland Basin during the Miocene Climate Optimum. Palaeogeography, Palaeoclimatology, Palaeoecology, 426, 22-33.

Kälin, B., Rybach, L. and Kempter, E. (1992) Rates of deposition, uplift and erosion in the Swiss molasse basin, estimated from sonic and density logs. Bulletin der Vereinigung Schweizerischer Petroleum-Geologen und-Ingenieure 58, 9-22.

Karamalidis, A.K., Torres, S.G., Hakala, J.A., Shao, H., Cantrell, K.J. and Carroll, S. (2013) Trace metal source terms in carbon sequestration environments. Environmental Science & Technology 47, 322-329.

Keller, B. (1992) Hydrogeologie des schweizerischen Molasse-Beckens: aktueller Wissensstand und weiterführende Betrachtungen. Eclogae Geologicae Helvetiae 85, 611-652.

Keller, B., Blasi, H.-R., Platt, N., Mozley, P. and Matter, A. (1990) Sedimentäre Architektur der distalen Unteren Süsswassermolasse und ihre Beziehung zur Diagenese und den petrophysikalischen Eigenschaften am Beispiel der Bohrungen Langenthal. Nagra Technischer Bericht 90-41, Nagra, Wettingen, p. 129.

Kharaka, Y.K., Thordsen, J.J., Hovorka, S.D., Nance, H.S., Cole, D.R., Phelps, T.J. and Knauss, K.G. (2009) Potential environmental issues of CO_2 storage in deep saline aquifers: Geochemical results from the Frio-I Brine Pilot test, Texas, USA. Applied Geochemistry 24, 1106-1112.

Koch, M. and Ruck, W. (1992) Injection of CO_2 for the Inhibition of Scaling in ATES Systems. SAE Technical Paper, No. 929154.

Kristmannsdóttir, H. (1989) Types of scaling occurring by geothermal utilization in Iceland. Geothermics 18, 183-190.

Kristmannsdóttir, H., Ó1afsson, M. and Thórhallsson, S. (1989) Magnesium silicate scaling in district heating systems in Iceland. Geothermics 18, 191-198.

Küpfer, T. (2005) Hydrogeologie der Unteren Süsswassermolasse, Nagra Arbeitsbericht NAB 04-09, p. 52.

Kwong, K. N. K., & Huang, P. M. (1979). Nature of hydrolytic precipitation products of aluminum as influenced by low-molecular weight complexing organic acids. In Developments in Sedimentology (Vol. 27, pp. 527-536). Elsevier.

Lebron, I., & Suarez, D. L. (1996). Calcite nucleation and precipitation kinetics as affected by dissolved organic matter at 25 °C and pH > 7.5. Geochimica et Cosmochimica Acta, 60(15), 2765-2776.

Lee, W., Lewandowski, Z., Nielsen, P.H. and Hamilton, W.A. (1995) Role of sulfate-reducing bacteria in corrosion of mild steel: A review. Biofouling 8, 165-194.

Leenheer, J. A., Malcolm, R. L., McKinley, P. W. and Eccles, L. A. (1974). Occurrence of dissolved organic carbon in selected ground-water samples in the United States. Journal of Research US Geological Survey, 2(3), 361-369.

Lerm, S., Westphal, A., Miethling-Graff, R., Alawi, M., Seibt, A., Wolfgramm, M. and Würdemann, H. (2013) Thermal effects on microbial composition and microbiologically induced corrosion and mineral precipitation affecting operation of a geothermal plant in a deep saline aquifer. Extremophiles 17, 311-327.

Leu, W., Megel, T. and Schaerli, U. (2006) Geothermal properties of Swiss Molasse Basin (depth range 0-500 m) - 2006 upgrade of the thermal conductivity, heat capacity, rock density and porosity data base, BFE Technical report SFOE-260067, Bern, p. 80.

Li, G. (2016) Sensible heat thermal storage energy and exergy performance evaluations. Renewable and Sustainable Energy Reviews 53, 897-923.

Lorenz, J.C., Heinze, D.M., Clark, J.A. and Searls, C.A. (1985) Determination of widths of meander-belt sandstone reservoirs from vertical downhole data, Mesaverde Group, Piceance Creek Basin, Colorado. AAPG bulletin 69, 710-721.

Lu, J., Partin, J.W., Hovorka, S.D. and Wong, C. (2010) Potential risks to freshwater resources as a result of leakage from CO 2 geological storage: a batch-reaction experiment. Environmental Earth Sciences 60, 335-348.

Matter, A., Homewood, P., Caron, C., van Stuyvenberg, J., Weidmann, M. and Winkler, W. (1980) Flysch and Molasse of Western and Central Switzerland. Exkursion no. 5, Geology of Switzerland - A Guide Book. Schweizerische Geologische Kommission, Wepf & Co., Basel.

Mátyás, J. (1998) Carbonate cements in the Tertiary sandstones of the Swiss Molasse basin: relevance to palaeohydrodynamic reconstruction, Carbonate Cementation in Sandstones: Distribution Patterns and Geochemical Evolution. Blackwell Publishing Ltd. Oxford, UK, pp. 141-162.

McBride, E.F. (1963) A classification of common sandstones. Journal of Sedimentary Research 33, 664-669.

Mejri, W., Korchef, A., Tlili, M., & Ben Amor, M. (2014). Effects of temperature on precipitation kinetics and microstructure of calcium carbonate in the presence of magnesium and sulphate ions. Desalination and Water Treatment, 52(25–27), 4863–4870.

Mennecart, B., Yerly, B., Mojon, P. O., Angelone, C., Maridet, O., Böhme, M. and Pirkenseer, C. (2016). A new Late Agenian (MN2a, Early Miocene) fossil assemblage from Wallenried (Molasse Basin, Canton Fribourg, Switzerland). Paläontologische Zeitschrift, 90(1), 101-123.

Mercer, J., Faust, C., Miller, W. and Pearson Jr, F. (1982) Review of simulation techniques for aquifer thermal energy storage (ATES), Advances in Hydroscience. Elsevier, pp. 1-129.

Miller, R.T. and Delin, G.N. (2002) Analysis of thermal data and nonisothermal modeling of short-term test cycles. US Geological Survey, Professional Paper 1530–B.

Mohan, K.K., Reed, M.G. and Fogler, H.S. (1999) Formation damage in smectitic sandstones by high ionic strength brines. Colloids and Surfaces A: Physicochemical and Engineering Aspects 154, 249-257.

Molz, F., Melville, J., Güven, O. and Parr, A.D. (1983a) Aquifer thermal energy storage: an attempt to counter free thermal convection. Water Resources Research 19, 922-930.

Molz, F., Melville, J., Parr, A.D., King, D. and Hopf, M. (1983b) Aquifer thermal energy storage: a well doublet experiment at increased temperatures. Water Resources Research 19, 149-160.

Molz, F., Parr, A.D. and Andersen, P. (1981) Thermal energy storage in a confined aquifer: Second cycle. Water Resources Research 17, 641-645.

Molz, F., Parr, A.D., Andersen, P., Lucido, V. and Warman, J. (1979) Thermal energy storage in a confined aquifer: Experimental results. Water Resources Research 15, 1509-1514.

Molz, F.J., Warman, J.C. and Jones, T.E. (1978) Aquifer storage of heated water: Part I—a field experiment. Groundwater 16, 234-241.

Morse, J.W. (1983) The kinetics of calcium carbonate dissolution and precipitation. Carbonates: Mineralogy and Chemistry, Reviews in Mineralogy 11, 227-264.

Muecke, T.W. (1979) Formation fines and factors controlling their movement in porous media. Journal of Petroleum Technology 31, 144-150.

Müller, D.R. and Regenspurg, S. (2017) The element-release mechanisms of two pyrite-bearing siliciclastic rocks from the North German Basin at temperatures up to 90° C under oxic and anoxic conditions. Geothermal Energy 5, 25.

Mungan, N. (1989) Discussion of an overview of formation damage. Journal of Petroleum Technology 41.

Nagra (1988) Sedimentstudie - Zwischenbericht 1988: Möglichkeiten zur Endlagerung langlebiger radioaktiver Abfälle in den Sedimenten der Schweiz, Nagra Technischer Report NTB 88-25, Nagra, Wettingen.

Nancollas, G. H., & Sawada, K. (1982). Formation of Scales of Calcium Carbonate Polymorphs: the Influence of Magnesium Ion and Inhibitors. JPT, Journal of Petroleum Technology, 34(3), 645–652.

Nehrke, G., Reichart, G. J., Van Cappellen, P., Meile, C., & Bijma, J. (2007). Dependence of calcite growth rate and Sr partitioning on solution stoichiometry: Non-Kossel crystal growth. Geochimica et Cosmochimica Acta, 71(9), 2240–2249.

Oelkers, E. H., Golubev, S. V., Pokrovsky, O. S., & Bénézeth, P. (2011). Do organic ligands affect calcite dissolution rates?. Geochimica et Cosmochimica Acta, 75(7), 1799-1813.

Palandri, J. and Y.K. Kharaka (2004) A compilation of rate parameters of water–mineral interaction kinetics for application to geochemical modeling. US Geol. Surv. Open File Report 2004-1068. 64 pp.

Parkhurst, D.L. and Appelo, C. (2013) Description of input and examples for PHREEQC version 3: a computer program for speciation, batch-reaction, one-dimensional transport, and inverse geochemical calculations, US Geological Survey (No. 6-A43). US Geological Survey, p. 519.

Paulus, B. (1963) Zur Stratigraphie und Fazies der oligozänen und miozänen Molasse im südlichen Oberbayern. Bulletin der Vereinigung Schweiz. Petroleum Geologen und Ingenieure 30, 53-97.

Perdikouri, C., Putnis, C. V., Kasioptas, A., & Putnis, A. (2009). An atomic force microscopy study of the growth of a calcite surface as a function of calcium/total carbonate concentration ratio in solution at constant supersaturation. Crystal Growth and Design, 9(10), 4344–4350.

Perlinger, J.A., Almendinger, J.E., Urban, N.R. and Eisenreich, S.J. (1987) Groundwater geochemistry of aquifer thermal energy storage: Long-term test cycle. Water Resources Research 23, 2215-2226.

Platt, N.H. and Keller, B. (1992) Distal alluvial deposits in a foreland basin setting—the Lower Freshwater Miocene), Switzerland: sedimentology, architecture and palaeosols. Sedimentology 39, 545-565.

Plummer, L., Parkhurst, D. and Wigley, T. (1979) Critical review of the kinetics of calcite dissolution and precipitation, Chemical Modeling in Aqueous Systems - ACS Symposium Series, Vol 93. ACS Publications, pp. 537-573.

Plummer, L.N. and Busenberg, E. (1982) The solubilities of calcite, aragonite and vaterite in CO_2-H_2O solutions between 0 and 90 °C, and an evaluation of the aqueous model for the system $CaCO_3$-CO_2-H_2O. Geochimica et Cosmochimica Acta 46, 1011-1040.

Pokrovsky, O. S., Golubev, S. V., & Jordan, G. (2009). Effect of organic and inorganic ligands on calcite and magnesite dissolution rates at 60 °C and 30 atm pCO_2. Chemical Geology, 265(1-2), 33-43.

Poppe, L., Paskevich, V., Hathaway, J. and Blackwood, D. (2001) A laboratory manual for X-ray powder diffraction, US Geological Survey Open-File Report 01-041 pp. 1-88.

Potter, J., Nur, A. and Dibble Jr, W. (1980) Effect of Temperature and Solution Composition on the Permeability of St. Peters Sandstone: Role of Iron (III), in: Ramey, H., Kruger, P. (Eds.), 6th Workshop Geothermal Reservoir Engineering. Stanford University, Stanford CA, pp. 316-321.

Rosenbrand, E., Haugwitz, C., Jacobsen, P.S.M., Kjøller, C. and Fabricius, I.L. (2014) The effect of hot water injection on sandstone permeability. Geothermics 50, 155-166.

Rybach, L. (1992) Geothermal potential of the Swiss Molasse basin. Eclogae Geologicae Helvetiae 85, 733-744.

Sanner, B. and Knoblich, K. (1999) Advantages and problems of high temperature underground thermal energy storage. Bull. Hydrogeol. 17, 341-348.

Schegg, R. (1992). Thermal maturity of the Swiss Molasse Basin-indications for paleogeothermal anomalies. Eclogae Geologicae Helvetiae;(Switzerland), 85(3).

Schlunegger, F., Matter, A., Burbank, D. and Klaper, E. (1997) Magnetostratigraphic constraints on relationships between evolution of the central Swiss Molasse basin and Alpine orogenic events. Geological Society of America Bulletin 109, 225-241.

Schmassmann, H., Balderer, W., Kanz, W. and Pekdeger, A. (1984) Beschaffenheit der Tiefengrundwässer in der zentralen Nordschweiz und angrenzenden Gebieten, Nagra Technischer Bericht NTB 84-21, Nagra, Wettingen, p. 398.

Schmassmann, H. (1990). Hydrochemische Synthese Nordschweiz: Tertiär-und Malm-Aquifere. Nagra Technische Bericht NTB, 88-07.

Schout, G., Drijver, B., Gutierrez-Neri, M. and Schotting, R. (2014) Analysis of recovery efficiency in high-temperature aquifer thermal energy storage: a Rayleigh-based method. Hydrogeology Journal 22, 281-291.

Sjöberg, S. (1996) Silica in aqueous environments. Journal of Non-Crystalline Solids 196, 51-57.

Small, J.S., Hamilton, D.L. & Habesch, S. (1992) Experimental simulation of clay precipitation within reservoir sands 2: mechanisms of illite formation and controls on morphology. Journal of Sedimentary Petrology, 62, 520–529.

Sousa, M.F., Signorelli, F. and Bertran, C.A. (2016) Fast evaluation of inhibitors for calcium carbonate scale based on *pH* continuous measurements in jar test at high salinity condition. Journal of Petroleum Science and Engineering 147, 468-473.

Stumm, W. and Morgan, J.J. (2012) Aquatic chemistry: chemical equilibria and rates in natural waters. John Wiley & Sons.

Subcasky, W.J. (1978) Petroleum Industry Experience in Water Injection, Thermal Energy Storage in Aquifers Workshop CONF-7805140. National Technical Information Service, Springfield VA, Berkeley CA, p. 14.

Thórhallsson, S., Ragnars, K., Arnórsson, S. and Kristmannsdóttir, H. (1975) Rapid scaling of silica in two district heating systems, In: Second United Nations Symposium on the Development and Use of Geothermal Resources, San Francisco, pp. 1445-1449.

Thurman, E. M. (1985). Organic geochemistry of natural waters (Vol. 2). Springer Science & Business Media.

Tomson, M. B., & Nancollas, G. H. (1978). Mineralization kinetics: a constant composition approach. Science, 200 (4345), 1059-1060.

Traber, D., Gautschi, A., Marschall, P., Becker, J. and Waber, N. (2014) Geologische Grundlagen - Dossier V: Hydrogeologische Verhältnisse, Nagra Technischer Bericht NTB 14-02, Nagra, Wettingen, p. 129.

Trümpy, R. (1985) Die Plattentektonik und die Entstehung der Alpen. Neujahrsblatt herausgegeben von der Naturforschenden Gesellschaft in Zürich 129.

Ueckert, M. and Baumann, T. (2019) Hydrochemical aspects of high-temperature aquifer storage in carbonaceous aquifers: evaluation of a field study. Geothermal Energy 7, 1-22.

Ueckert, M., Wismeth, C. and Baumann, T. (2020) Crystallization of calcium carbonate in a large-scale push–pull heat storage test in the Upper Jurassic carbonate aquifer. Geothermal Energy 8, 7.

Ullman, W.J., Kirchman, D.L., Welch, S.A. and Vandevivere, P. (1996) Laboratory evidence for microbially mediated silicate mineral dissolution in nature. Chemical Geology 132, 11-17.

Usdowski, E. (1989). Synthesis of dolomite and magnesite at 60° C in the system Ca^{2+}-Mg^{2+}-CO_3^{2-}-$C1_2^{2-}$-H_2O. Naturwissenschaften, 76(8), 374-375.

Vail, L., Jenne, E. and Eary, L. (1992) H20TREAT: An Aid for Evaluating Water Treatment Requirements for Aquifer Thermal Energy Storage. SAE Technical Paper No. 929195.

Valdez, B., Schorr, M., Quintero, M., Carrillo, M., Zlatev, R., Stoytcheva, M. and de Dios Ocampo, J. (2009) Corrosion and scaling at Cerro Prieto geothermal field. Anti-Corrosion Methods and Materials, 56(1), 28-34

van den Heuvel, D.B., Gunnlaugsson, E., Gunnarsson, I., Stawski, T.M., Peacock, C.L. and Benning, L.G. (2018) Understanding amorphous silica scaling under well-constrained conditions inside geothermal pipelines. Geothermics 76, 231-241.

van Loosdrecht, M., Eikelboom, D., Gjaltema, A., Mulder, A., Tijhuis, L. and Heijnen, J. (1995) Biofilm structures. Water Science and Technology 32, 35.

van Lopik, J.H., Hartog, N. and Zaadnoordijk, W.J. (2016) The use of salinity contrast for density difference compensation to improve the thermal recovery efficiency in high-temperature aquifer thermal energy storage systems. Hydrogeology Journal 24, 1255-1271.

Veetil, S. P., Mucci, A., & Arakaki, T. (2018). Dolomite dissolution kinetics in aqueous solutions in the presence of organic and inorganic additives at 25 °C and pCO_2~ 1 atm. Chemical Geology, 483, 98-110.

von Eynatten, H. (2003). Petrography and chemistry of sandstones from the Swiss Molasse Basin: an archive of the Oligocene to Miocene evolution of the Central Alps. Sedimentology, 50(4), 703-724.

Vuataz, F.-D., Czernichowski-Lauriol, I., Fouillac, C. and Detoc, S. (1989) Chemical study of a low temperature geothermal fluid in a triassic sandstone aquifer: Scaling potential and fluid treatment (Melleray, France). Geothermics 18, 313-320.

Waber, H., Heidinger, M., Lorenz, G. and Traber, D. (2014) Hydrochemie und Isotopenhydrogeologie von Tiefengrundwässern in der Nordschweiz und im angrenzenden Süddeutschland, Nagra Arbeitsbericht NAB 13-63, Nagra, Wettingen, p. 276.

Wang, S. and Jaffe, P.R. (2004) Dissolution of a mineral phase in potable aquifers due to CO_2 releases from deep formations; effect of dissolution kinetics. Energy Conversion and Management 45, 2833-2848.

Wanner, C., Eichinger, F., Jahrfeld, T., & Diamond, L. W. (2017). Causes of abundant calcite scaling in geothermal wells in the Bavarian Molasse Basin, Southern Germany. Geothermics, 70, 324-338.

Wedepohl, K. H. (1995). The composition of the continental crust. Geochimica et Cosmochimica Acta, 59(7), 1217-1232.

Wersin, P., Mazurek, M., Waber, N., Mäder, U., Gimmi, T., Rufer, D. and De Haller, A. (2013) Rock and porewater characterisation on drillcores from the Schlattingen borehole, Nagra Arbeitsbericht NAB 12-54, Nagra, Wettingen, p. 343.

Westphal, A., Lerm, S., Miethling-Graff, R., Seibt, A., Wolfgramm, M. and Würdemann, H. (2016) Effects of plant downtime on the microbial community composition in the highly saline brine of a geothermal plant in the North German Basin. Applied Microbiology and Biotechnology 100, 3277-3290.

Wolthers, M., Nehrke, G., Gustafsson, J. P., & Van Cappellen, P. (2012). Calcite growth kinetics: Modeling the effect of solution stoichiometry. Geochimica et Cosmochimica Acta, 77, 121–134.

Zhang, X.N., Wu, W.L., Li, D.M. and Zhao, G.J. (2012) A new evaluation method of scale inhibitors for controlling CaCO3 scale in reverse osmosis system based on *pH* measurement, Advanced Materials Research. Trans Tech Publ, pp. 2146-2152.

Zhao, K., Wang, M., Wang, X., Wu, C., Xu, H., & Lu, J. R. (2013). Crystal growth of calcite mediated by ovalbumin and lysozyme: Atomic force microscopy study. Crystal Growth and Design, 13(4), 1583–1589.

Zotzmann, J., Vetter, A. and Regenspurg, S. (2018) Evaluating efficiency and stability of calcite scaling inhibitors at high pressure and high temperature in laboratory scale. Geothermal Energy 6, 1-13.

Zullig, J.J. and Morse, J.W. (1988) Interaction of organic acids with carbonate mineral surfaces in seawater and related solutions: I. Fatty acid adsorption. Geochimica et Cosmochimica Acta 52, 1667-1678.

Appendix A Previous HT-ATES projects

List of previous HT-ATES systems

Table A-1 *List of previous HT-ATES systems, many of them early test sites that have been decommissioned by now, including aquifer type, injection temperature, problems encountered and, if applicable, mitigation strategies. The projects from the 70s have been summarised by Tsang (1980), Tsang and Hopkins (1982) and (Mercer et al., 1982) and the Dutch projects by Drijver et al. (2019).*

		Years active	Aquifer type	Injection parameters	Problems encountered	Mitigation strategies
Switzerland	University of Neuchâtel (Mathey, 1977; Mathey and Menjos, 1978)	1974 (term.)	Shallow, phreatic Columbier-Robinson aquifer consisting of three sand and gravel layers	51 °C, 37 L/min, 9 days injection	Strong thermal stratification Large heat loss to the environment through the unconfined upper layer	None
	SPEOS, Lausanne-Dorigny (Hadorn, 1997; Jollien et al., 1992; Mäder, 1998; Saugy et al., 1984)	1982 – 1994 (term.)	Permeable glaciofluviatile unconfined aquifer at a depth of 7 – 24 m b.s.l.	70 -80 °C	Carbonate scaling in heat exchanger (and reservoir at times) Corrosion due to increased Cl concentration Increase in number of thermophiles (and potentially pathogenic) microbes Lack of interest by owners	Acidification by HCl and CO_2 and periodic cleaning Not successful to prevent carbonate scaling: electromagnetic conditioning, self-scrubber balls, Teflon coating, adding of NaOH to spatially control precipitation

Germany	Krefeld (Meyer, 1978; Werner and Kley, 1977)	1973 – 1974 (term.)	Shallow, phreatic aquifer with an effective porosity of 23 Vol.%	45 °C at 0.3 m^3/h for 64 days	Large heat loss to the environment through the unconfined upper layer	None
	Reichstag Berlin (Kranz and Bartels, 2010; Sanner et al., 2005; Sanner and Knoblich, 2004)	1999 – now	Lower Sinemurian sandstone aquifer > 300 m b.s.l. with up to 30% porosity and 29 g/L TDS Clay-rich aquitard above	80 °C at 100 m^3/h, production at 30 – 65 °C	None	
	Neubrandenburg (Kabus et al., 2009; Lerm et al., 2013; Westphal et al., 2016; Wolfgramm and Seibt, 2006)	2004 – now	Late Triassic sandstone aquifer (Rhätkeuper) 1200 – 1300 m b. s. l. with up to 130 g/L TDS (Na-Cl water) Used for geothermal production (~55 °C) until 1998	75 – 80 °C at 100 m^3/h, produced at 65+ °C	Minor formation of carbonates (pressure reduction in surface installations), iron/nickel/copper sulphides (microbial activity) and amorphous silica (if the injection temperature is raised, caused by dissolution of clay minerals) Mobilisation of detrital particles from the reservoir Mobilisation of (heavy) metal ions, likely from metal installations Microbially-induced corrosion	Filtration in surface installations

	Research well Landshut (Ueckert and Baumann, 2019; Ueckert et al., 2020)	2014 – ?	Malm aquifer between 250 and 475 m b.s.l. consisting of limestones (top, potentially karstified) and dolomite and dolomitic breccia Freely flowing groundwater (19.4 L/s)	Up to 110 °C	Carbonate scaling in heat exchanger High rates of mixing with *in-situ* groundwater lead to strongly reduced energy recovery	Addition of CO_2 to prevent scaling; caused carbonate dissolution in the aquifer
France	Plaisir-Thiverval-Grignon	1987 – ? (term.)	Wealdien aquifer (alternation of unconsolidated sand and clay) of 16 m thickness at a depth of 500 m b.s.l aquifer was targeted as it is known for its alternation of clay (impervious cap rock) and sand	Inject at 180 °C, return at 80 °C 40 m^3/h	Carbonate precipitation and Si-Al-precipitates in heat exchanger during loading and unloading respectively. Pump damage due to suspension load and reservoir clogging due to mobilisation of clay particles Corrosion of steel parts as waters interacted with air in the surface installations.	Addition of lime and iron chloride to decarbonise water before heating Addition of lime, iron chloride and sodium aluminate to de-silicate water before cooling.
Netherlands	Utrecht University (Drijver et al., 2019; van	1991 – 1999	Oosterhout formation (medium- to fine grained sands)	Inject at 90 °C and 100 m^3/h,	Carbonate scaling in heat exchanger	Ion exchange resins (Ca ↔ Na)

	Loon and Van der Heide, 1992)	(term.)	at 220 to 260 m b.s.l containing brackish water	return at 90 °C and 50 m^3/h Cooling to 50 °C	Limited storage efficiency due to high return temperatures Damage to hot well	
	Hooge Burch Zwammerdam (Drijver et al., 2019)	1998 – 2003 (term.)	131 to 151 m deep	~20'000 m^3/yr at 71 – 82 °C; extraction at 54 – 72 °C	Economically not viable	None
USA	Auburn University, Mobile (Buscheck et al., 1983; Molz et al., 1983a; Molz et al., 1983b; Molz et al., 1981; Molz et al., 1979; Molz et al., 1978)	1975 – ? (term.)	Sandstone aquifer with 15 wt.% silt and clay minerals (kaolinite & smectites) at a depth of 40 to 61 m b.s.l.	55 – 80 °C; 1350 m^3/day; injection over 79 days	Reduction of permeability due to clogging of pores by clay particles which led to an increase in injection pressure causing breaching of the aquitard Swelling of clay (= surface uplift of up to 1.24 cm in early tests) Thermal stratification	Regular backwashing to unclog particles Injection of saline water to reduce swelling of clays
	University of Minnesota, St. Paul (Hoyer et al., 1991; Hoyer et al., 1994; Miller and	1982 – ? (term.)	Franconia-Ironton-Galesville (FIG) aquifer: highly stratified and anisotropic fine- to medium-grained sandstone +	Up to 109 °C; temperature difference across the	Reduction of permeability due to clogging of pore throats by small grains and by precipitation of calcite)	Use of ion-exchange water softening before heating of the groundwater to eliminate carbonate scaling in surface installations

	Delin, 2002; Perlinger et al., 1987)		thin intercalated shale beds; 61 m thickness; 180 to 240 m deep; Hydralic conductivity <0.01 to 1.5 m/d	heat exchangers 66 °C; 18 L/s		
	Stony Brook	1976 – ? (term.)	Sandstone aquifer with 15 wt.% silt and clay minerals (kaolinite & smectites) at a depth of 40 to 61 m b.s.l. ($T_{insitu} \approx 20$ °C)	55 – 80 °C;	Reduction of permeability due to clogging of pores by clay particles, increase of injection pressure lead to breaching of aquitard Swelling of clay (= surface uplift of up to 1.24 cm in early tests) Thermal stratification	Filtration to remove particles Injection of saline water to reduce swelling of clays

References

Buscheck, T.A., Doughty, C. and Tsang, C.F. (1983) Prediction and analysis of a field experiment on a multilayered aquifer thermal energy storage system with strong buoyancy flow. Water Resources Research 19, 1307-1315.

Drijver, B., Bakema, G. and Oerlemans, P. (2019) State of the art of HT-ATES in The Netherlands, European Geothermal Congress 2019, 11-14 June, Den Haag, The Netherlands.

Hadorn, J. (1997) Status of Seasonal Heat Storage in Switzerland, Proceedings of the Megastock '97, 7th International Conference on Thermal Energy Storage, June 18, University of Hokkaido, Sapporo, Japan, pp. 972 – 976.

Hoyer, M., Eisenreich, S., Almendinger, J., Perlinger, J., Miller, R., Lauer, J., Splettstoesser, J. and Walton, M. (1991) University of Minnesota aquifer thermal energy storage (ATES) project - Report on the first long-term cycle, Pacific Northwest Laboratory Report, PNL–7817.

Hoyer, M., Hallgren, J., Uebel, M., Delin, G., Eisenreich, S. and Sterling, R. (1994) University of Minnesota Aquifer Thermal Energy Storage (ATES) - Project Report of the Third Long-Term Cycle, Pacific Northwest Laboratory Report, PNL–9811.

Jollien, L., Remonnay, S. and Miserez, F. (1992) Heat Storage at SPEOS (Swiss ATES Pilot Plant): Chemical and Microbiological Aspects and Problems. SAE Technical Paper, No. 929052.

Kabus, F., Wolfgramm, M., Seibt, A., Richlak, U. and Beuster, H. (2009) Aquifer thermal energy storage in Neubrandenburg: monitoring throughout three years of regular operation, Proceedings of 11th International Conference on Energy Storage EffStock, Stockholm, Sweden.

Kranz, S. and Bartels, J. (2010) Simulation and data based optimisation of an operating seasonal aquifer thermal energy storage, Proceedings of the World Geothermal Congress, 25–30 April 2010, Bali, Indonesia.

Lerm, S., Westphal, A., Miethling-Graff, R., Alawi, M., Seibt, A., Wolfgramm, M. and Würdemann, H. (2013) Thermal effects on microbial composition and microbiologically induced corrosion and mineral precipitation affecting operation of a geothermal plant in a deep saline aquifer. Extremophiles 17, 311-327.

Mäder, U. (1998) Contributions to Thermodynamic Models of Complex Geologic and Sysnthetic Systems: Solid Solutions and Mineral-Fluid Systems, Habilitationsschrift, Institute of Geological Sciences,. University of Bern.

Mathey, B. (1977) Development and resorption of a thermal disturbance in a phreatic aquifer with natural convection. Journal of Hydrology 34, 315-333.

Mathey, B. and Menjos, A. (1978) Underground heat storage: Choice of a geometry and efficiency, Proceedings Thermal Energy Storage in Aquifers Workshop, Lawrence Berkeley Laboratory LBL-8431, pp. 80-87.

Mercer, J., Faust, C., Miller, W. and Pearson Jr, F. (1982) Review of simulation techniques for aquifer thermal energy storage (ATES), Advances in Hydroscience. Elsevier, pp. 1-129.

Meyer, C. (1978) Large-scale thermal energy storage for cogeneration and solar systems, Proceedings 5th Energy Technology Conference and Exposition, Wahington DC.

Miller, R.T. and Delin, G.N. (2002) Analysis of thermal data and nonisothermal modeling of short-term test cycles. US Geological Survey, Professional Paper 1530–B.

Molz, F., Melville, J., Güven, O. and Parr, A.D. (1983a) Aquifer thermal energy storage: an attempt to counter free thermal convection. Water Resources Research 19, 922-930.

Molz, F., Melville, J., Parr, A.D., King, D. and Hopf, M. (1983b) Aquifer thermal energy storage: a well doublet experiment at increased temperatures. Water Resources Research 19, 149-160.

Molz, F., Parr, A.D. and Andersen, P. (1981) Thermal energy storage in a confined aquifer: Second cycle. Water Resources Research 17, 641-645.

Molz, F., Parr, A.D., Andersen, P., Lucido, V. and Warman, J. (1979) Thermal energy storage in a confined aquifer: Experimental results. Water Resources Research 15, 1509-1514.

Molz, F.J., Warman, J.C. and Jones, T.E. (1978) Aquifer storage of heated water: Part I—a field experiment. Groundwater 16, 234-241.

Perlinger, J.A., Almendinger, J.E., Urban, N.R. and Eisenreich, S.J. (1987) Groundwater geochemistry of aquifer thermal energy storage: Long-term test cycle. Water Resources Research 23, 2215-2226.

Sanner, B., Kabus, F., Seibt, P. and Bartels, J. (2005) Underground thermal energy storage for the German Parliament in Berlin, system concept and operational experiences, Proceedings World Geothermal Congress. , Antalya, Turkey, pp. 1-8.

Sanner, B. and Knoblich, K. (2004) Thermische Untergrundspeicherung auf höherem Temperaturniveau: Begleitforschung mit Messprogramm Aquiferspeicher Reichstag (Schlussbericht Projekt 0329809B), Institut für Angewandte Geowissenschaften der Justus-Liebig-Universität Gießen.

Saugy, B., Doy, R., Mathey, B., Aragno, M., Geister, M., Rieben, C., Miserez, J., Parriaux, A., Tissieres, P. and Vuilleumier, F. (1984) Accumulateur de chaleur en nappe souterraine SPEOS. Bilan de deux ans d'exploitation, Société des éditions des associations techniques universitaires, SEATU.

Tsang, C.F. (1980) A review of current aquifer thermal energy storage projects, Energy Storage. Elsevier, pp. 279-293.

Tsang, C.F. and Hopkins, D.L. (1982) Aquifer Thermal Energy Storage: A Survey. Recent Trends in Hydrogeology 189, 427.

Ueckert, M. and Baumann, T. (2019) Hydrochemical aspects of high-temperature aquifer storage in carbonaceous aquifers: evaluation of a field study. Geothermal Energy 7, 1-22.

Ueckert, M., Wismeth, C. and Baumann, T. (2020) Crystallization of calcium carbonate in a large-scale push–pull heat storage test in the Upper Jurassic carbonate aquifer. Geothermal Energy 8, 7.

van Loon, L. and Van der Heide, K. (1992) High-Temperature ATES at the University of Utrecht, the Netherlands. SAE Technical Paper.

Werner, D. and Kley, W. (1977) Problems of heat storage in aquifers. Journal of Hydrology 34, 35-43.

Westphal, A., Lerm, S., Miethling-Graff, R., Seibt, A., Wolfgramm, M. and Würdemann, H. (2016) Effects of plant downtime on the microbial community composition in the highly saline brine of a geothermal plant in the North German Basin. Applied microbiology and biotechnology 100, 3277-3290.

Wolfgramm, M. and Seibt, A. (2006) Geochemisches Monitoring des geothermalen Tiefenspeichers in Neubrandenburg, Proceedings of GtV conference, Karlsruhe, Germany.

Appendix B Core experiments

Set-up and sampling

For the core experiments, two 25 cm long pieces from sample A and B respectively were used Section 3.1.1). The core surfaces were found to be wet upon opening of the PVC bags, indicating that evaporation during storage was successfully prevented and that the drill core still contained *in-situ* porewater. The core was then cut with a tap-water-cooled rock saw to create flat ends perpendicular to its long axis and then immediately prepared for the experiment. The core for the 60 °C experiment thus contained a mixture of porewater, drilling fluid as well as water from sawing and air. The core used for the 90 °C experiment was additionally rinsed with deionised water for a couple of minutes to replace as much of this unknown water mix present in the porespace.

The cores were prepared by first placing titanium filter discs (Ø = 5 cm, 0.5 mm tick) on the top and bottom ends of the cores. In order to cover the ends entirely, two Teflon rings were cut and placed around the filter disc (Figure B.1 A). Cone-shaped titanium pieces (inner caps) with small holes at the centre (to attach the capillaries needed for infiltration and sampling) were placed over the filter disks (Figure B.1 B). The surface of the cores was then wrapped with Teflon tape (Figure B.1 C), covered with a latex sleeve and the inner caps were fixed in place by electrical tape (Figure B.1 D). The tape and sleeve help to distribute the confining pressure over the entire core sample while sealing the core from contact with of the confining liquid (deionised water) during the experiment.

The wrapped cores were then placed in a vertical orientation into the titanium pressure cylinder (Figure B.1 E) and closed with a titanium cap (outer cap) on either end. The sealed pressure cylinder was filled with water and a confining pressure of around 13 bar was established by filling the remaining volume of a separate pressure vessel with pressurized argon. Two heating bands were placed around the pressure cylinder and covered by an insulating layer several cm thick (Figure B.11 E). Insulation was placed over the top and bottom caps as well (Figure B.1 F). The assembly was then heated to 60 °C and 90 °C respectively. The two experiments were conducted in sequence.

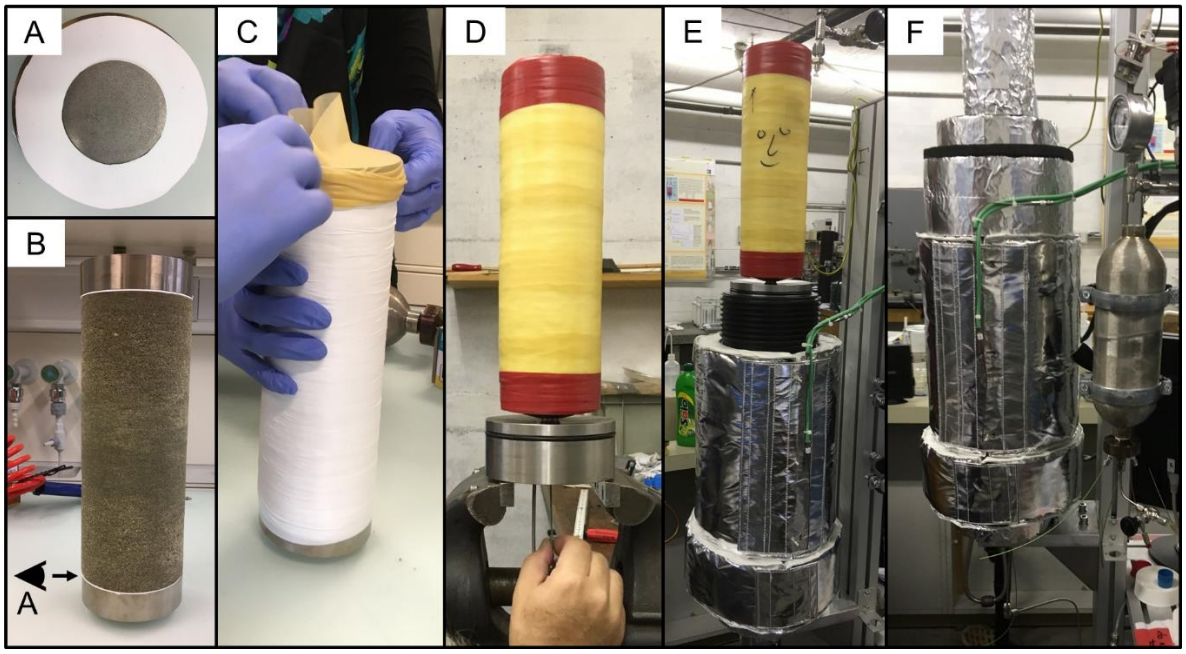

Figure B.1: *Experimental set-up of core experiments: Ti-filter discs and Teflon rings (A) were placed on either side of the drill core sample before being covered by the inner caps (B). The core was then wrapped in Teflon tape (C) and covered in a Latex sleeve, held in place with electric tape (D). The thus prepared core was attached to the outer caps and the capillaries (D) and then attached to the core holder which is surrounded by heating bands (not visible) and a thick insulation layer (E). In a last step the core was placed inside the holder and the top and bottom were covered in additional insulation (F). Infiltration container filled with APW can be seen to the right side of the core (F).*

In order to saturate the drill core with the APW and to obtain water samples during the experiments, capillaries were installed at the in- and outlet (Figure B.1 D). They provide the only access to the inside of the experiment as they are fed through the outer and inner caps and terminate at the titanium filter discs at either end of the core. Once connected, the APW was filled into the stainless steel infiltration container (Figure B.1 F) and an infiltration pressure of 2 to 2.5 bar (60 °C experiment) and 4 to 6.5 bar (90 °C experiment) was established by filling the remaining volume with pressurised argon. Then both inlet and outlet valves were opened to start infiltrating the core with water and forcing out any air bubbles, such that the core attained saturation with water. For the 60 °C experiment, a vacuum pump was attached and periodically switched on to speed up saturation and reduce the amount of mineral reactions happening during saturation. For the 90 °C experiment, it was deemed more important to replace the already present porewater than to prevent mineral reactions (as all minerals should be present in excess). Accordingly, around 1.5 pore volumes (ca. 500 mL) of APW were flushed trough the core before the start of the actual experiment. Once the core was fully sat-

urated, the outlet valve was closed and the experiment was left to run. Confining and infiltration pressures as well as temperatures at the surface of the pressure cylinder were logged at regular intervals. Based on the porosity estimate of around 20 vol.% (Section 3.3.4), the final solid-to-liquid-ratio within the experiment was close to 5:1.

Aliquot of the fluids from the inlet and outlet were periodically taken by syringes attached to the valves. The samples were filtered through 0.2 µm syringe filters and different aliquots were taken: one, non-acidified, for analysis of anions, alkalinity and TIC/TOC, and another one, acidified to *pH* ~ 2 by adding 15 vol.% HNO_3, for analysis of cations. For all samples, the *pH* was measured immediately after sampling as well as 5 minutes and 10 minutes later. The samples were analysed on the same day for alkalinity while analyses of anions, cations and TIC/TOC were performed around 4 weeks later. For details of solution analyses see Section 4.2.4.

Results

The core experiments were conducted at 60 °C and 90 °C and with a confining pressure of ~ 13 bar and an infiltration pressure of 2 to 2.5 bar (60°C experiment) and 4 to 6.5 bar (90 °C experiment). The infiltration pressure decreased slowly over weeks and was readjusted whenever it dropped below 2 bar/4.5 bar by increasing the Ar pressure in the infiltration canister. The injection pressure was maintained to prevent the backflow of porewater from the core into the injection container (Figure B.1), while the outlet valve remained closed and was only opened to obtain fluid samples. The APW and composition of the sampled aliquots analysed at different times are given in Table B.1 (60 °C experiment) and Table B.2 (90 °C experiment). As the 90 °C experiment is constrained better, only these results will be discussed below. The Cl concentration is strongly decreasing at the outlet of the core sample as a function of time (Figure B.2, Table B.2). Such a strong decrease would require the precipitation of large amounts of Cl-bearing minerals. However, all Cl-bearing minerals are undersaturated under the experimental conditions and can thus not precipitate. The concentration of Cl therefore has to remain constant over the duration of the experiment and the strong decrease can only be explained by substantial experimental artefacts. Most likely, the observed decrease is due to the mixing of porewater inside the core with the pure water surrounding the core used to establish the confining pressure. When the experiment was set up, we tried to avoid this by wrapping the core sample in Teflon first and then a latex sleeve (Figure B.1) to isolate it from the surrounding water. This method of sealing the core sample has successfully been used in numerous out-diffusion experiments on claystones in the past. However, the much higher permeability and likely the elevated temperatures (the experiments using claystones are generally

performed at room temperature) have led to the failure of this double barrier and allowed for the mixing of porewater and the confining water.

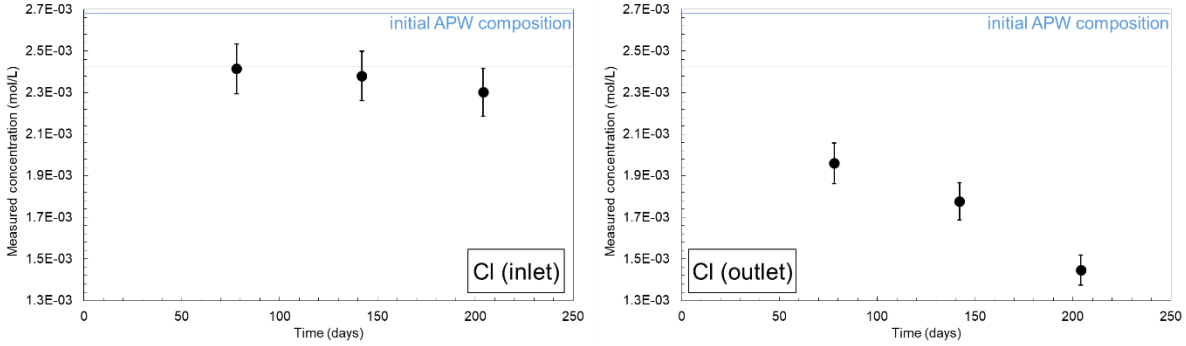

Figure B.2: *Evolution of Cl concentration at the (a) inlet (= infiltration canister) and (b) outlet of the core sample as a function of time during the 90 °C core experiment. As a conservative tracer, Cl is not involved in any mineral reactions and should thus show constant concentrations throughout the experiment. Its depletion at the inlet and especially at the outlet thus suggests experimental artefacts.*

The contamination of the APW in the infiltration canister by back diffusion could also be observed for most other ions analysed: Their concentrations are different from the initial APW and the concentrations increase as a function of time due to the contribution of mineral dissolution which is mirrored by increasing concentrations at the outlet. In Figure B.3 (top panels), Si concentrations are shown as an example. Other ions with the same behaviour are Na, K and HCO_3. The increasing concentrations suggests (1) the continuous dissolution of silica (quartz and/or chalcedony) and silicate minerals (i.e. feldspars, sheet silicates) and (2) that no secondary phase controls the concentration of dissolved Si.

Calcium shows a different behaviour (Figure B.3, centre panels). In the infiltration canister, an initial decrease in concentration is observed. This decrease is related to calcite precipitation as the AOW is slightly supersaturated with respect to calcite. The subsequent increase was due to contamination through back diffusion. The reaching of a constant equilibrium concentration at the outlet indicates that within the core, the solubility of Ca is controlled by the precipitation of a secondary phase, likely calcite. Therefore, not matter how long the experiment is run for the concentration will not increase further unless other parameters (e.g. *p*H or temperature) are changed. Magnesium shows the same behaviour (except for the initial decrease at the inlet). The secondary phase limiting the concentration of Mg in solution is likely the same Mg-(alumo)silicate postulated in the interpretation of the batch experiments as dolomite is not expected to precipitate under these conditions (Section 4.3.1).

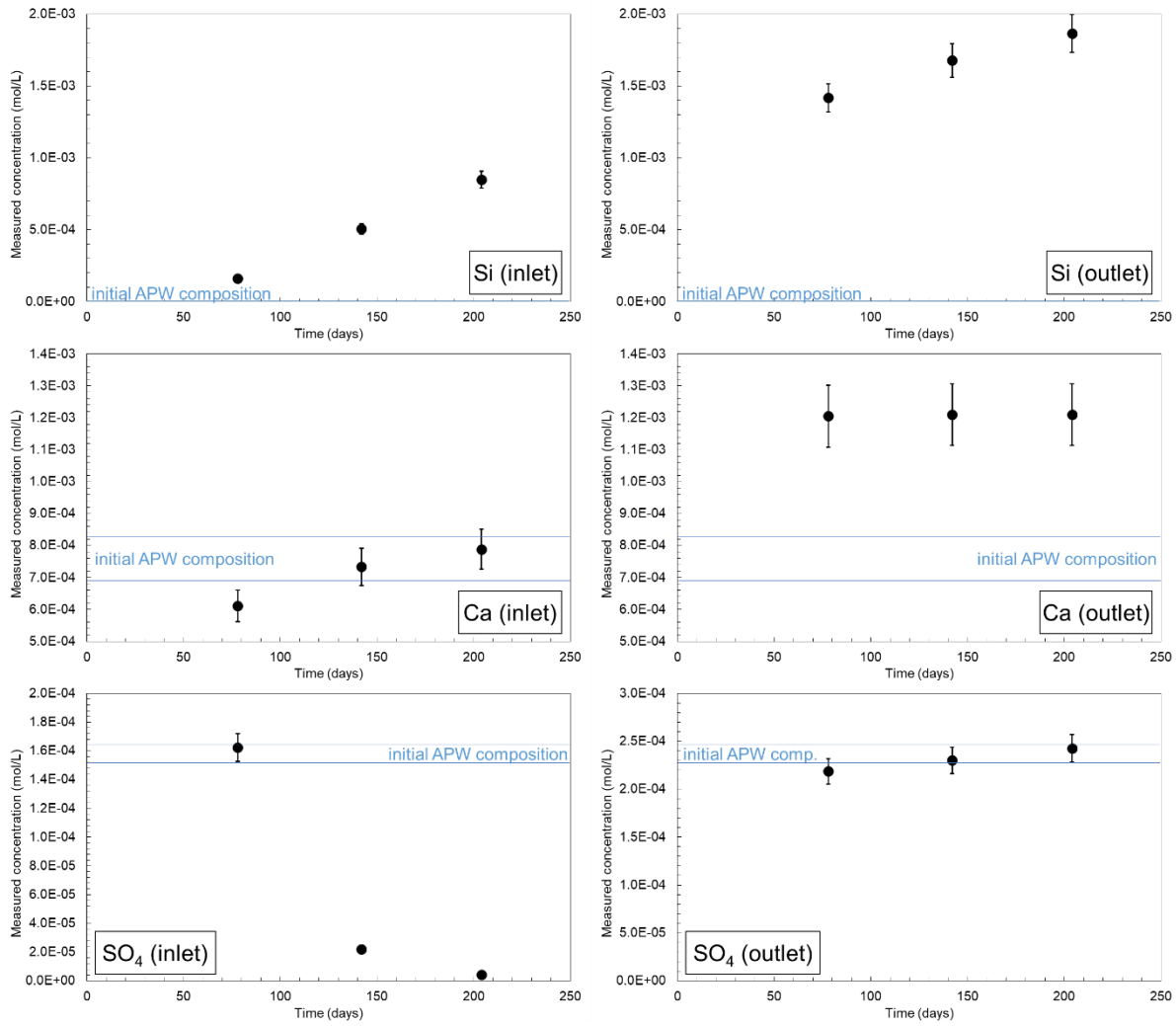

Figure B.3: *Evolution of Si, Ca and SO_4 concentrations at the (a) inlet (= infiltration canister) and (b) outlet of the core sample as a function of time during the 90 °C core experiment. The observed concentrations of Si can be explained by mineral dissolution (outlet) and back diffusion (inlet). For Ca, calcite precipitation is observed at the in- and outlet while the inlet concentration is additionally affected by back diffusion. The concentration of SO_4 at the inlet is controlled by microbial sulphate reduction. At the outlet, pyrite dissolution might be occurring.*

A very different behaviour is shown in the evolution of SO_4 concentrations (Figure B.3, bottom panels). The reason for the decrease at the inlet (down to nearly 10^{-6} mol/L) can be attributed to the presence of sulphate reducing bacteria, which consume SO_4 and produce H_2S. The presence of reduced sulphur was confirmed by a strong "rotten egg" smell whenever the infiltration container was opened. As the reduction of SO_4 in the infiltration canister was only observed during the 90 °C experiment, it is assumed that the microbes introduced during setting up of the experiment and are not related to processes occurring inside the drill core samples. The slight increase at the outlet (albeit within analytical uncertainties) indicated a small contribution from dissolution of S-bearing minerals such as pyrite.

While the trends at the outlet indicate certain mineral reactions, the concentrations cannot be used to assess them quantitatively as they a mixture of contributions from mineral reactions and the mixing with the pure water used to establish the backpressure. For Cl, which is not affected by mineral reactions, the dilution changes from 23 to 43 % over the course of the experiment. However, these numbers cannot be used to correct the outlet concentrations of other ions as the dilution affects the saturation states of different minerals differently. Therefore, the results from the core experiments will not be evaluated any further.

In the absence of experimental artefacts, core experiments are expected to provide the data most representative of the in-situ reservoir (Section 4.1.1). Therefore we will work on improving the experimental set-up (e.g. by using shrink-wrap as an additional barrier between the confining water and the core and testing of a flow-through procedure) so core experiments are possible once core materials from the Forsthaus reservoir are available.

Table B-1 *Chemical composition of the artificial porewater (APW) and analyses of aliquots taken at inlet (= from infiltration tank) and outlet (Figure 4.1) samples for of the 60°C core experiment. All concentrations in mg/L. Highlighted in red are the Cl concentrations that should remain constant between inlet and outlet as well as over time if the experimental set-up worked as planned.*

	APW	June 2019 (200 days)		December 2019 (430 days)	
		Inlet	Outlet	Inlet	Outlet
*p*H	7.51	7.90	7.51	8.09	7.58
Ca^{2+}	24.6 ± 2.0	18.3 ± 1.5	78.3 ± 6.2	20.5 ± 1.6	75.7 ± 6.1
Mg^{2+}	19.6 ± 0.8	20.8 ± 0.8	41.8 ± 1.7	21.1 ± 0.8	39.6 ± 1.6
Na^{+}	77.2 ± 4.6	116 ± 7.0	58.2 ± 3.5	113 ± 6.8	64.8 ± 3.9
K^{+}	2.72 ± 0.25	4.23 ± 0.38	16.0 ± 1.4	6.03 ± 0.54	46.3 ± 4.2
Al^{3+}	< 0.5	n.d.	n.d.	< 0.5	0.04 ± 0.004
Si(aq)	< 0.5	n.d.	n.d.	3.08 ± 0.22	24.1 ± 1.7
Cl^{-}	87.8 ± 4.4	85.0 ± 4.3	75.9 ± 3.8	96.7 ± 4.8	134 ± 6.7
SO_4^{2-}	22.3 ± 1.3	22.5 ± 1.4	45.5 ± 2.7	22.7 ± 1.4	47.5 ± 2.9
HCO_3^{-}	207	282	n.d.	263	391
TOC	n.d.	35.2	395	44.8	354

Table B-2 *Chemical composition of the artificial porewater (APW) and analyses of aliquots taken at inlet (= from infiltration tank) and outlet (Figure 4.1) samples for of the 90°C core experiment. All concentrations in mg/L. Highlighted in red are the Cl concentrations that should remain constant between inlet and outlet as well as over time if the experimental set-up worked as planned.*

	APW	Nov. 2020 (80 days)		January 2021 (140 days)		March 2021 (200 days)	
		Inlet	Outlet	Inlet	Outlet	Inlet	Outlet
*p*H	7.60	7.95	6.71	7.71	7.01	7.31	6.84

Ca^{2+}	30.4 ± 1.8	24.5 ± 2.0	48.3 ± 3.9	29.4 ± 2.4	48.5 ± 3.9	31.6 ± 2.5	44.2 ± 3.5
Mg^{2+}	19.9 ± 0.8	20.8 ± 0.8	41.8 ± 1.7	21.1 ± 0.8	39.6 ± 1.6	21.1 ± 0.8	39.6 ± 1.6
Na^{+}	77.6 ± 4.7	78.2 ± 4.7	57.8 ± 3.5	84.9 ± 5.1	70.1 ± 4.2	84.3 ± 5.1	73.2 ± 4.4
K^{+}	3.30 ± 0.30	4.77 ± 0.43	102 ± 9.2	6.69 ± 0.60	17.1 ± 1.5	9.09 ± 0.82	15.9 ± 1.4
Al^{3+}	< 0.5	< 0.5	< 0.5	< 0.1	< 0.05	< 0.05	< 0.05
Si(aq)	< 0.5	4.54 ± 0.32	39.8 ± 2.8	14.2 ± 1.0	47.1 ± 3.3	23.8 ± 1.7	52.4 ± 3.7
Cl^{-}	90.5 ± 4.5	85.6 ± 4.3	69.5 ± 3.5	84.4 ± 4.2	63.0 ± 6.7	81.6 ± 4.1	51.3 ± 2.6
SO_4^{2-}	22.7 ± 1.4	15.6 ± 0.9	21.0 ± 1.3	2.12 ± 0.13	22.1 ± 1.3	0.42 ± 0.03	23.3 ± 1.4
HCO_3^{-}	228	232	305	259	324	287	339
TOC	15.5	376	253	89.5	324	140	326